Canadian
Journal of Physics

Editor: H. E. DUCKWORTH

ABSOLUTE YIELDS OF THE XENON AND KRYPTON ISOTOPES IN U238 SPONTANEOUS FISSION[1]

B. G. YOUNG[2] AND H. G. THODE

ABSTRACT

The absolute abundances of the isotopes of fission-product xenon and krypton in six uranium minerals have been determined mass spectrometrically using the isotope dilution technique. The fission products were resolved into a U238 spontaneous fission component, a U235 neutron-induced fission component, and a U238 neutron-induced fission component. Internal consistency in the analysis was achieved only when the Xe129 yield used for the U235 thermal neutron fission component was 20% lower than that reported by Purkayastha and Martin at I129. This discrepancy in the mass 129 chain yield measured at I129 and at Xe129 has not been resolved.

Only one of the six minerals, Cinch Lake pitchblende, retained essentially all of its fission product inert gases throughout geological time. Inert gas losses from the remaining five minerals ranged from 20% to 75%. The absolute yields of the stable xenon and krypton fission products in U238 spontaneous fission were determined from an analysis of the inert gases from the Cinch Lake mineral. This analysis showed that 95.9% of the fission gas in this case resulted from the spontaneous fission and only 4.1% from neutron-induced fission.

INTRODUCTION

Soon after the discovery of fission, Petrzhak and Flerov (1940), Maurer and Pose (1943), Scharff-Goldhaber and Klaiber (1946) demonstrated with ionization chambers and boron trifluoride counter tubes that uranium undergoes fission spontaneously and emits neutrons in the process. Later, Segrè (1952) used enriched isotopes of uranium and showed that U238 has a spontaneous fission rate of about 23 times that of U235, the half lives for spontaneous fission of U238 and U235 being 8.04×10^{15} years and 1.87×10^{17} years respectively.

In 1950, Macnamara and Thode, using mass spectrometric methods, identified xenon and krypton fission products in the rare gases extracted from old uranium minerals. The pattern of xenon and krypton isotopes found for natural fission indicated an asymmetric mass yield curve similar to that obtained in the neutron fission of U235 and U238. There were, however, certain marked differences. First, the mass yield curves in the xenon and krypton mass ranges are steeper for natural fission. Since there is much less energy available for

spontaneous fission than for neutron fission, the process is expected to be more selective (steeper curves). This was considered strong evidence that spontaneous fission of U^{238} is involved in natural fission. Secondly, the abnormally high yield at masses 133 and 134 (fine structure in the mass yield curve) found for neutron fission of U^{235} is shifted toward the lower mass for natural fission, which is the same direction of shift found between neutron fission of U^{235} and neutron fission of U^{238}. Finally, the xenon-to-krypton ratio was found to be much higher in the natural fission gases. The low-mass hump of the mass yield curve is shifted toward higher mass with increasing mass of the fissioning nucleus. This results in lower krypton yields in the fission of U^{238} as compared with U^{235} fission. From this and other evidence, Macnamara and Thode concluded that a large part of the fission gases in uranium minerals resulted from the spontaneous fission of U^{238}.

In 1953, Fleming and Thode showed that both neutron fission of U^{235} and spontaneous fission of U^{238} occur in nature. They found that the fission isotope patterns of xenon and krypton varied from one uranium ore to another, depending on the proportions of the two fission processes which have taken place. Wetherill (1953) confirmed the existence of neutron and spontaneous fission in uranium ores. Since the mass 129 chain yield is about 1% for neutron fission of U^{235} and was found to be very nearly zero for spontaneous fission of U^{238}, the yield of this isotope was taken as one index of the proportion of neutron fission of U^{235} and spontaneous fission of U^{238} which has occurred in a given mineral. The fission yield of Xe^{129} in several minerals was less than 0.02% which indicated that at least 98% of the fission gas was due to the spontaneous fission of U^{238}. Other samples showed up to 23% neutron fission of U^{235}. There are two main sources of neutrons for this process, spontaneous fission and (α,n) reactions on light elements.

Recently the absolute yields of Mo^{99} and several iodine isotopes from U^{238} spontaneous fission were reported by Parker and Kuroda (1958) and Ashizawa and Kuroda (1957).

In the present work, absolute abundances of the cumulative yields of xenon and krypton fission products from six uranium minerals were determined mass spectrometrically using isotope dilution techniques. The purpose of this work was to obtain the absolute yields of the stable xenon and krypton fission products for U^{238} spontaneous fission, to determine the leakage of fission gas from the minerals throughout geological time, to assess the spontaneous fission method of mineral age determination, and, finally, to investigate further the various fission processes which occur in nature.

EXPERIMENTAL

The uranium minerals were crushed and sieved to provide a homogeneous aggregate for the extraction and analysis of the fission product gases. The mineral aggregates were concentrated to a density greater than three by gravitational separation with diiodomethane to facilitate the preparation of fission gas samples suitable for mass spectrometric analysis. Chemical analyses were performed on samples of the mineral concentrates to determine uranium

concentrations. Lead isotope ages of the minerals were obtained by Farquhar (1959) and by Collins *et al.* (1954) of the geophysics group at the University of Toronto.

The stable tracer isotopes Xe^{128}, Kr^{80}, and Kr^{82} were prepared by neutron irradiation of iodine and bromine salts in the N.R.X. reactor and standardized by diluting against a standard mixture of normal xenon and krypton.

The apparatus used to extract and purify about 10^{-4} ml^3 at S.T.P. of xenon and krypton from a uranium mineral sample is shown in Fig. 1. The vacuum induction furnace, powered by a 6-kw Ajax Northrup mercury arc converter,
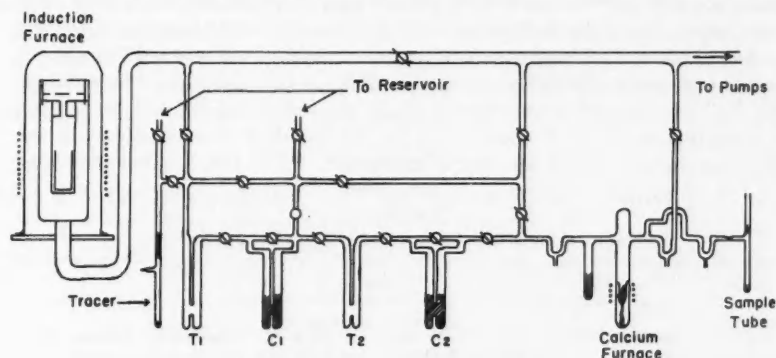
FIG. 1. Inert gas separation system.

could be charged with about 100 g of the crushed mineral concentrate. A 25-liter reservoir was connected at the points shown to receive gases evolved from the heated mineral and to mix them with a sample of tracer isotopes. The open traps T_1 and T_2 together with the activated charcoal traps C_1 and C_2 were used to partially remove the extraneous gases by condensation and preferential adsorption on cooled charcoal. The final purification was by calcium vapor in the calcium induction furnace, which could be isolated by means of mercury ventils. The extraction was considered complete if reheating the mineral to 1400° C for 8 hours evolved less than 0.5% of the fission products extracted in a first heat to 1300° for 8 hours.

The inert gas mixtures were analyzed in a 10-in. directional focusing mass spectrometer using an electron multiplier for a detector. The multiplier output was integrated and amplified by a vibrating reed electrometer and displayed on a recorder. A resolving power of about 625 allowed doublet separation of the hydrocarbon background from the xenon and krypton isotopes. The relative abundances of normal xenon and krypton reported by Nier (1950) were used to correct for instrumental mass discrimination.

RESULTS

The primary mass spectrometric data provide relative and absolute xenon and krypton isotopic abundances. In our analyses of these data, relative

xenon isotopic abundances only are required for the normal xenon correction and for the analysis of the fission products into their components. Absolute abundances, on the other hand, are required to determine absolute yields and to measure any loss of fission product gas from the mineral. The normal xenon and krypton corrections were made on the basis of Xe^{130}, Kr^{80}, and Kr^{82}, since these isotopes are not formed in natural fission in appreciable amounts (Kennett 1956).

The fission product abundances were normalized to 100 at Xe^{136} for comparison and are shown in Table I(1). Table I(2) gives the total number of fission product Xe^{136} atoms in each sample as determined by the isotope dilution method. Since the Xe^{129} abundance relative to Xe^{136} is considered to be a good indication of the percentage of neutron fission in the mineral (see above) the minerals were arbitrarily arranged in order of increasing Xe^{129} abundance. The Xe^{129} is preceded in its mass chain by the long-lived I^{129} and corrections were applied to the Xe^{129} abundances for the retention of a small part of the 129 mass chain as I^{129} at the time of extraction. Table I(6, 7) gives the ratios

TABLE I

Absolute abundances of xenon and krypton fission products

	Mineral					
Fission product	Cinch Lake pitchblende	Jahala Lake uraninite	Beaver Lodge Lake pitchblende	Great Bear Lake pitchblende	Eagle Mine pitchblende	Belgian Congo pitchblende
	(1)					
Kr^{83}	$0.854 \pm .030$	$0.728 \pm .022$	$0.865 \pm .044$	$1.71 \pm .02$	$1.75 \pm .05$	$2.56 \pm .03$
Kr^{84}	$2.52 \pm .15$	$2.45 \pm .09$	$1.98 \pm .21$	$3.94 \pm .09$	$4.23 \pm .18$	$5.40 \pm .13$
Kr^{86}	$15.79 \pm .21$	$12.54 \pm .15$	$14.37 \pm .18$	$16.49 \pm .17$	$15.43 \pm .20$	$17.95 \pm .20$
Xe^{129}	$0.460 \pm .021$	$0.488 \pm .009$	$0.800 \pm .073$	$2.06 \pm .01$	$2.29 \pm .02$	$3.38 \pm .02$
Xe^{131}	$9.88 \pm .06$	$9.77 \pm .07$	$11.41 \pm .11$	$15.43 \pm .12$	$15.85 \pm .11$	$20.51 \pm .15$
Xe^{132}	$57.97 \pm .27$	$58.18 \pm .48$	$58.44 \pm .33$	$59.76 \pm .43$	$59.05 \pm .59$	$61.39 \pm .37$
Xe^{134}	$83.36 \pm .36$	$83.72 \pm .63$	$85.27 \pm .38$	$89.17 \pm .75$	$89.83 \pm .84$	$94.46 \pm .50$
Xe^{136}	$100.00 \pm .42$	$100.00 \pm .94$	$100.00 \pm .41$	$100.00 \pm .95$	$100.00 \pm .83$	$100.00 \pm .65$
	(2)					
Xe^{136} atoms $(\times 10^{14})$	3.312	7.710	1.352	6.033	7.639	4.838
	(3)					
Lead age $(\times 10^6 y)$	1120 ± 50	1740 ± 50	785 ± 60	1400 ± 50	1700 ± 30	635 ± 20
	(4)					
U^{235}, %	$29.0 \pm .3$	$30.4 \pm .4$	41.2 ± 1.4	$43.3 \pm .4$	$45.3 \pm .4$	$56.4 \pm .5$
	(5)					
Sample wt., g	65.1	128.0	103.8	69.7	99.5	115.3
	(6)					
Normal Kr / Fission Kr	.130	.640	.440	.096	.180	.082
	(7)					
Normal Xe / Fission Xe	.0094	.0050	.0240	.0061	.0055	.0066

of normal to fission product gas for krypton and xenon respectively. These ratios show the extent of normal gas contamination in each sample. The errors are the standard deviations based on seven mass spectrometer double scans. Duplicate analyses showed that the absolute abundances were reproducible within this experimental error. Lead ages and uranium contents of the six mineral concentrates are included in Table I(3) and Table I(4, 5) respectively.

Absolute Yields; Spontaneous Fission

The absolute yield calculation depends on the independent determination of the number of fissions which have taken place and the amount of a given fission product which has been formed.

The total number of U^{238} atoms which have undergone spontaneous fission in a mineral sample since deposition was calculated from the U^{238} content, the age, and the rates at which the U^{238} nucleus decays by alpha emission and spontaneous fission according to the relation

$$N = W(\lambda_t/\lambda_a)(e^{\lambda_a T} - 1)$$

where W = the present number of U^{238} atoms in the mineral sample,

λ_t = the U^{238} spontaneous fission decay constant,

= $8.62 \pm .30 \times 10^{-17}/y$ (Segrè 1952),

λ_a = the U^{238} alpha-decay constant = $1.54 \times 10^{-10}/y$ (Kienberger 1949),

T = the period during which fission products accumulated (assumed to be given by the lead age of the mineral).

The fraction of the fission gas (xenon and krypton isotopes) in each mineral sample which resulted from the spontaneous fission of U^{238} was obtained from a breakdown of the results for each natural fission gas sample into its various fission components.

Fleming and Thode (1953) and Wetherill (1953) obtained fairly consistent results by assuming only two fission processes in nature, the spontaneous fission of U^{238} and the neutron fission of U^{235}. Since the mass 129 chain yield is about 1% for neutron fission of U^{235} and very nearly zero for spontaneous fission of U^{238} (the curve for spontaneous fission is much steeper at this point) they used the yield of this isotope as an index of the proportions of neutron fission of U^{235} and the spontaneous fission of U^{238} which have occurred in a given uranium mineral. A preliminary analysis of the data in Table I showed that it was not possible to separate the six mineral patterns into a U^{235} neutron-induced component and a U^{238} spontaneous fission component satisfactorily. However, a satisfactory analysis was obtained when a third component, U^{238} neutron-induced fission, was considered along with the two processes proposed by Fleming and Thode. This analysis made use of the known relative abundances of the xenon and krypton isotopes for the two neutron fission processes separately and a comparison of these with the relative abundances obtained for the fission gases extracted from the various minerals (Table I).

In this connection, the U^{238} spontaneous fission pattern was determined by a successive approximation procedure, in which the Cinch Lake pattern,

corrected for its small neutron fission component on the basis of the Xe^{129} yield as described above, was used as the first approximation. A three-component breakdown, using the Xe^{131}, Xe^{134}, and Xe^{136} relative abundances in the three components and the five remaining mixtures, produced a more exact Xe^{129} relative yield from the neutron fission components.

The criterion for a satisfactory three-component analysis is that each mineral sample gives the same relative abundances of the xenon isotopes after subtraction of the two neutron-induced fission components. In other words, the spontaneous fission pattern (U^{238}) obtained should be the same for each sample. It is seen from Table II that the xenon pattern agreement

TABLE II

Fission product patterns corrected for neutron fission

	Mineral					
Fission product	Cinch Lake pitchblende	Jahala Lake uraninite	Beaver Lodge Lake pitchblende	Great Bear Lake pitchblende	Eagle Mine pitchblende	Belgian Congo pitchblende
Kr^{83}	$0.519\pm.031$	$0.412\pm.023$	$0.175\pm.048$	$0.25\pm.02$	$0.15\pm.06$	$0.00\pm.06$
Kr^{84}	$1.94\ \pm.16$	$1.92\ \pm.09$	$0.74\ \pm.23$	$1.36\pm.11$	$1.47\pm.22$	$0.85\pm.20$
Kr^{86}	$15.10\ \pm.22$	$11.68\ \pm.16$	$12.82\ \pm.20$	$13.41\pm.21$	$11.73\pm.25$	$12.46\pm.29$
Xe^{129}	$0.000\pm.019$	$+0.060\pm.015$	$-0.113\pm.086$	$+ 0.06\pm.06$	$+0.15\pm.06$	$+0.01\pm.13$
Xe^{131}	$8.31\ \pm.10$	$8.31\ \pm.05$	$8.31\ \pm.11$	$8.31\pm.07$	$8.31\pm.12$	$8.31\pm.16$
Xe^{132}	$57.54\ \pm.17$	$57.79\ \pm.21$	$57.58\ \pm.20$	$57.48\pm.15$	$56.54\pm.24$	$57.39\pm.31$
Xe^{134}	$81.54\ \pm.27$	$82.04\ \pm.24$	$81.66\ \pm.14$	$81.54\pm.15$	$81.54\pm.27$	$81.54\pm.23$
Xe^{136}	$100.00\ \pm.24$	$100.00\ \pm.24$	$100.00\ \pm.20$	$100.00\pm.17$	$100.00\pm.27$	$100.00\pm.32$

among samples is excellent. The disagreement among the krypton patterns is discussed below.

The percentages of the three components, spontaneous fission of U^{238}, neutron fission of U^{235}, and neutron fission of U^{238}, obtained from the analysis are given in Table III(1). Included also in Table III(2) are the ratios of the

TABLE III

Absolute yield of Xe^{136} and loss of spontaneous fission products

	Mineral					
Component	Cinch Lake pitchblende	Jahala Lake uraninite	Beaver Lodge Lake pitchblende	Great Bear Lake pitchblende	Eagle Mine pitchblende	Belgian Congo pitchblende
	(1)					
U^{238} spontaneous fission, %	95.86	96.15	91.82	81.65	80.42	68.65
U^{235} neutron fission, %	4.14	3.85	8.18	15.19	17.22	25.23
U^{238} neutron fission, %	0.00	0.00	0.00	3.16	2.36	6.12
	(2)					
$\dfrac{Xe^{136}}{Fissions}\times100$ (U^{238} spontaneous fission)	$6.30\pm.38$	$4.38\pm.18$	$1.59\pm.26$	$4.78\pm.23$	$3.21\pm.13$	$3.51\pm.17$
	(3)					
Xe^{136} loss, %	0.0 ± 6.0	30.5 ± 6.6	74.8 ± 7.3	24.1 ± 7.1	49.0 ± 6.3	44.3 ± 6.5

number of atoms of Xe^{136} produced to the number of fissions (spontaneous fission of U^{238}) for each sample. These ratios, expressed as percentages, can be interpreted as absolute yields only if fission products have not been lost from the mineral. This ratio for the Cinch Lake mineral agrees with other absolute yield estimates (Fleming and Thode 1953; Wetherill 1953) and therefore suggests that inert gas losses from this mineral have been very small. If the lead ages are assumed to be the periods during which spontaneous fission products accumulated, then the low ratios of Xe^{136} to the number of fissions for each of the other five minerals must be due to a loss of the rare gases during geological time, and these losses are given in Table III(3). If we assume little or no loss of gas from the Cinch Lake sample during geological time, the data shown in Tables II and III should give the absolute yields of the xenon and krypton isotopes from the spontaneous fission of U^{238}. These yields are given in Table IV(1).

TABLE IV

Absolute yields in U^{238} spontaneous fission

Mass	Absolute yields (This work)		Absolute yields (*Parker and Kuroda, †Ashizawa and Kuroda)	
	Element	Yield, %	Element	Yield, %
	(1)		(2)	
83	Kr	$0.0327 \pm .0028$		
84	Kr	$0.122 \pm .012$		
86	Kr	$0.951 \pm .057$		
99			Mo*	$6.4 \pm .5$
131	Xe	$0.524 \pm .031$	I†	$0.4 \pm .1$
132	Xe	$3.63 \pm .22$	I†	$3.6 \pm .4$
133			I†	$1.5 \pm .3$
134	Xe	$5.14 \pm .31$	I†	$5.2 \pm .5$
135			I†	$5.1 \pm .5$
136	Xe	$6.30 \pm .38$		

DISCUSSION

Tables I(4) and III(1) indicate that there is a correlation between the percentage of uranium in a mineral concentrate and the percentage of neutron fission. This relationship is shown in Fig. 2. The percentage of uranium in the mineral concentrate should be approximately equal to the percentage of uranium in the mineral itself, since most of the rock matrix was removed by the gravitational separation with diiodomethane.

It had previously been assumed that the presence of the rare earth elements, which have large thermal neutron absorption cross sections, was largely responsible for the low proportion of neutron fission in the uraninites. The occurrence of U^{238} neutron fission in uranium minerals suggests much larger effective neutron energies than had been suspected, and indicates that the rare earths may have had little effect on the amount of neutron fission in a uranium mineral. The fact that the Jahala Lake uraninite and Cinch Lake pitchblende, with about equal uranium concentrations in the concentrates, have the same proportion of neutron fission supports this conclusion.
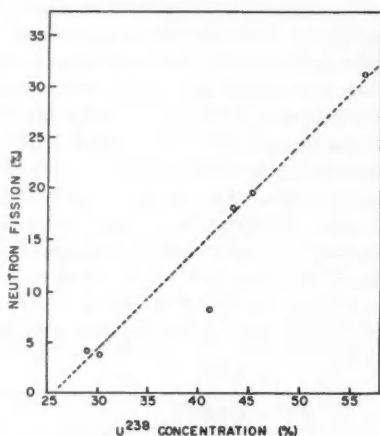
FIG. 2.   Relation between the amount of neutron fission and uranium concentration in a uranium mineral or ore concentrate.

Tables I(4) and III(1) also suggest that the proportion of U^{238} neutron fission in the neutron fission component decreases with decreasing uranium concentration in the mineral concentrate. The presence of two neutron fission processes, each with a very different energy dependence, allows some conclusions regarding the effective energy of the neutrons in a uranium mineral. U^{238} has a neutron fission cross section which is less than 1 barn in the 1-Mev energy region and has a threshold at about 0.5 Mev. U^{235}, on the other hand, has a neutron fission cross section which varies from about 1000 barns in the thermal energy range to about 1 barn in the 1-Mev region. The ratio of U^{238} to U^{235} neutron fission in normal uranium is therefore very sensitive to the effective neutron energy and decreases by a factor of about 10^3 when this energy is reduced from 2 Mev to 0.5 Mev. Because of this sensitivity, and the effects of mineral age on the U^{235}/U^{238} ratio, the correlation between uranium concentration in the mineral and the proportion of U^{238} neutron fission in the neutron fission component is not expected to be quantitative.

It may be concluded from these correlations that the materials which dilute uranium in minerals strongly absorb neutrons, but reduce only slightly their mean energy.

Internal consistency in the spontaneous fission pattern obtained from the analysis of the natural fission patterns into their three components required the use of a Xe^{129} yield in U^{235} neutron fission of 0.71%, which is about 20% lower than the I^{129} yield reported by Purkayastha and Martin (1956). These authors first drew attention to this discrepancy when they extracted the Xe^{129} and I^{129} from two uranium minerals and found that the I^{129} abundance was about 20% lower than would be expected from the Xe^{129} content. No satisfactory explanation for this discrepancy has been found.

The ratio of krypton to xenon fission products from spontaneous fission (Table II) is about 20% higher in the Cinch Lake mineral than in the other five uranium minerals. This discrepancy is attributed to the fractionation of krypton relative to xenon as the rare gases diffuse from a mineral. The ratio of krypton to xenon obtained from the Cinch Lake sample should therefore be a minimum value for U^{238} spontaneous fission. Since the loss of fission gas from this sample must be small we have taken it to be the true ratio. The large losses of these gases by most uranium minerals prevent the general use of accumulated rare gas fission products for age determination. Nevertheless, the fractionation which accompanies loss should be a sensitive test of the validity of a "fission product age", i.e. the period during which fission products have accumulated without loss.

Recently, Parker and Kuroda (1958) and Ashizawa and Kuroda (1957) have reported the absolute yields of Mo^{99} and several iodine isotopes from the spontaneous fission of U^{238}. These yields, along with the absolute yields of xenon and krypton from the present analysis, are shown in Table IV. The good agreement between the xenon and iodine yields at masses 131, 132, and 134 is in accord with the assumption that no fission product xenon and krypton had been lost from the Cinch Lake mineral. Segrè's (1952) value of the U^{238} spontaneous fission half life has been used for all of the absolute yields obtained thus far, and therefore, the reliability of this half life does not enter into the comparison.

ACKNOWLEDGMENTS

REFERENCES

ASHIZAWA, F. T. and KURODA, P. K. 1957. J. Inorg. & Nuclear Chem. **5**, 12.
COLLINS, C. B., FARQUHAR, R. M., and RUSSELL, R. D. 1954. Bull. Geol. Soc. Am. **65**, 1.
FARQUHAR, R. M. 1959. Private communication.
FLEMING, W. H. and THODE, H. G. 1953. Phys. Rev. **92**, 378.
KENNETT, T. J. and THODE, H. G. 1956. Phys. Rev. **103**, 323.
KIENBERGER, C. A. 1949. Phys. Rev. **76**, 1561.
MACNAMARA, J. and THODE, H. G. 1950. Phys. Rev. **80**, 471.
MAURER, W. and POSE, H. 1943. Z. Physik, **121**, 285.
NIER, A. O. 1950. Phys. Rev. **79**, 450.
PARKER, P. L. and KURODA, P. K. 1958. J. Inorg. & Nuclear Chem. **5**, 153.
PETRZHAK, K. A. and FLEROV, G. N. 1940. J. Exptl. Theoret. Phys. U.S.S.R. **10**, 1013.
PURKAYASTHA, B. C. and MARTIN, G. R. 1956. Can. J. Chem. **34**, 293.
SCHARFF-GOLDHABER, G. and KLAIBER, G. S. 1946. Phys. Rev. **70**, 229.
SEGRÈ, E. 1952. Phys. Rev. **86**, 21.
WETHERILL, G. W. 1953. Phys. Rev. **92**, 907.

A $^2\Pi$–$^2\Pi$ ELECTRONIC BAND SYSTEM OF THE FREE NCO RADICAL[1]

R. N. DIXON[2]

ABSTRACT

A series of red-degraded absorption bands has been observed between 2650 Å and 3200 Å and is attributed to a $^2\Pi$–$^2\Pi$ transition of the NCO radical. The bands probably represent a progression of the upper-state stretching vibration ν_1'. The rotational structure of one band has been analyzed. Diffuseness in some of the bands indicates predissociation of the upper state, and is discussed in terms of the dissociation energy of NCO.

INTRODUCTION

A system of violet-degraded emission bands near 4400 Å was observed at low dispersion by Holland and Style in the fluorescence of a number of aliphatic cyanates and isocyanates. These same bands were also observed in absorption during the flash photolysis of similar compounds (Holland, Style, Dixon, and Ramsay 1958), and showed rotational structure under high resolution. The vibrational and rotational analyses of these bands have been carried out (Dixon 1959, hereafter referred to as Paper I), and show that the bands are due to the $A(^2\Sigma^+)$–$X(^2\Pi_i)$ transition of the NCO radical. During this flash photolysis experiment a series of red-degraded bands was observed in the region 2650 Å – 3200 Å. These bands are more complex and less resolved than the 4400-Å bands, but the structure of strong bands in the series suggests that they are $^2\Pi$–$^2\Pi$ bands. They are attributed to the $B(^2\Pi_i)$–$X(^2\Pi_i)$ transition of NCO.

EXPERIMENTAL PROCEDURE

The $^2\Pi$–$^2\Pi$ bands of NCO were observed during the flash photolysis of HNCO vapor, using the same apparatus and experimental conditions as for the $^2\Sigma^+$–$^2\Pi$ bands (Paper I). The bands at wavelengths greater than 2900 Å were photographed on Eastman Kodak I-O plates in the third order of a 21-ft concave grating spectrograph, with 12 traversals through the 50-cm reaction tube. The complete region from 2600 Å to 3200 Å was also photographed in the fourth order of the grating, but lack of light-gathering power necessitated a reduction in the absorption path to two traversals through the reaction tube.

Two plates of the strong sharp features in the spectrum were each measured twice on a comparator equipped with a photoelectric scanning device similar to that described by Tomkins and Fred (1951). The diffuse features were measured from a print of the spectrum. A hollow-cathode iron-arc lamp was used for wavelength calibration.

VIBRATIONAL STRUCTURE

The wavelengths and vacuum wave numbers of the band heads and absorption maxima are given in Table I, and portions of the spectrum are illustrated

TABLE I

Band heads and absorption maxima for the $B(^2\Pi) \leftarrow X(^2\Pi)$ system of NCO, with possible assignments

Feature	λ(air), Å	ν(vac.), cm^{-1}	Assignment
VW	3167.14	31,565.1	
VW	3156.48	31,671.7	
S head	3149.873	31,738.12	R_2 000–000
S head	3148.388	31,753.09	R_1 000–000
VW	3142.34	31,814.3	
VW	3141.99	31,817.7	
W head	3059.642	32,674.06	
S	3051.30	32,763.4	$R_2\ \nu_1'$
S head	3045.877	32,821.72	$R_1\ \nu_1'$
VW head	3038.351	32,903.02	
W b	2973.59	33,619.6	
S head b	2964.31	33,724.8	$R_2\ 2\nu_1'$
M d	2959.50	33,779.7	
S head b	2953.92	33,843.4	$R_1\ 2\nu_1'$
M d	2949.2	33,897	
M d	2936.6	34,043	$R_2\ \nu_3'$
M d	2935.7	34,054	$R_1\ \nu_3'$
W	2873.06	34,795.9	
M b	2866.93	34,870.3	$R\ \ 3\nu_1'$
VW b	2865.50	34,887.7	
VW b	2864.02	34,905.7	
W d	2849.7	35,081	$R_2\ \nu_1'+\nu_3'$
W d	2848.6	35,095	$R_1\ \nu_1'+\nu_3'$
VW }	2843.51	35,157.5	
VW }	2843.30	35,160.1	
W	2786.78	35,873.2	
MW head	2783.27	35,918.4	$R\ \ 4\nu_1'$
W	2780.47	35,954.6	
VW	2712.72	36,852.5	
VW	2702.19	36,996.0	
W	2690.38	37,158.5	
W	2677.24	37,340.8	

NOTE: VW very weak, W weak, M medium, S strong, b broad, d diffuse.

in Fig. 1. It is seen that the bands are grouped in regions about 1000 cm^{-1} apart. These groups most probably arise from the excitation of successive quanta of the upper-state stretching frequency ν_1'. The bands at 3148 Å, 3046 Å, and 2954 Å are approximately equal in intensity, and there is no trace of any bands to the red of the 3150-Å group. The 3148-Å band must therefore be the 000–000 band of the electronic transition.

Upon closer inspection of the features in the groups of bands it is seen that in each of the 2950-Å, 3050-Å, and 3150-Å groups there are two prominent heads which have the appearance of the R_1 and R_2 heads of $^2\Pi$–$^2\Pi$ bands. However, the doublet splitting in these three bands is far from constant, and does not even vary in a linear manner. Furthermore, it is not possible to select a series of band heads in a vibrational progression with a constant second difference. This suggests that there are vibrational perturbations in the upper state. It is not difficult to understand how perturbations leading to such

irregularities could arise. In CO_2 and similar molecules, and in the $A(^2\Sigma^+)$ state of NCO (Paper I), $\nu_1 \simeq 2\nu_2$, and there is a Fermi resonance between those levels v_1,v_2,v_3 and v_1-1,v_2+2,v_3 which are of the same species. This may also be true in the $B(^2\Pi)$ state of NCO. In addition, as this state is a Π state, the electronic angular momentum $\Lambda h/2\pi$ may couple with the angular momentum $lh/2\pi$ of the bending vibration such that Λ and l are no longer good quantum numbers. The resultant angular momentum is then characterized by $K = |\Lambda \pm l|$. The energy levels of such a Π state have been discussed by Renner (1934). In Paper I it was shown that the $X(^2\Pi)$ state of NCO is subject to such an effect, with additional effects due to the coupling of the angular momentum $Kh/2\pi$ with the spin angular momentum $\Sigma h/2\pi$. The levels of this latter system have been investigated theoretically by Pople (1959). It may be shown that the spin doubling in the $^2\Pi$ (vibronic) levels of even v_2 is much smaller than in the zero level. Thus, if there is a Fermi resonance between the levels v_1,v_2,v_3 and v_1-1,v_2+2,v_3 in the $B(^2\Pi)$ state of NCO, this would involve the interaction of levels with different effective spin-coupling constants, and would give a very complicated vibrational pattern. In consequence of these possibilities the vibrational assignments of Table I can be considered as only tentative.

The spectrum shows a number of diffuse features, presumably as a result of predissociation of the upper state. The two pairs of diffuse features near 2936 Å and 2849 Å show doublet splittings similar to that in the 000–000 band. It is unlikely that these are hot bands as there are no similar features near the 3046-Å and 3149-Å bands. They are therefore assigned to ν_3' and $\nu_1'+\nu_3'$.

The following vibration frequencies are derived from the mean values of the frequencies of the R_1 and R_2 heads of the 000–000, 100–000, and 001–000 bands; $\nu_1' = 1047$ cm^{-1}, $\nu_3' = 2303$ cm^{-1}. A complete determination of the stretching force constants in the $B(^2\Pi)$ state of NCO cannot be achieved without data from an isotopic molecule. However, if the above frequencies are substituted into the equations for the bond stretching of a linear XYZ molecule with no interaction force constant k_{12} (Herzberg 1945, p. 173), then either $k_{CN} = 17.3 \times 10^5$ dynes/cm and $k_{CO} = 7.4 \times 10^5$ dynes/cm, or $k_{CN} = 7.0 \times 10^5$ dynes/cm and $k_{CO} = 18.4 \times 10^5$ dynes/cm. If k_{12} is included in the equations it is found that with these vibration frequencies real solutions for the force constants are possible for any $k_{12} > -1.9 \times 10^5$ dynes/cm, at which value $k_{CN} = 11.2 \times 10^5$ dynes/cm and $k_{CO} = 11.9 \times 10^5$ dynes/cm. Thus, either one bond of NCO in the $B(^2\Pi)$ state is much stronger than the other, or there is a negative interaction stretching force constant k_{12} (which implies that the stretching of one bond of NCO in this state weakens the other bond).

ROTATIONAL STRUCTURE

Several of the bands in the spectrum show rotational fine structure. Although the 000–000 band has the two heads expected for a $^2\Pi(a)$–$^2\Pi(a)$ band, a rotational analysis of this band was not possible, as the structure appears to be considerably perturbed. This could be due to perturbation by higher levels of the $A(^2\Sigma^+)$ state, which is only 9000 cm^{-1} below the $B(^2\Pi)$ state. Examina-
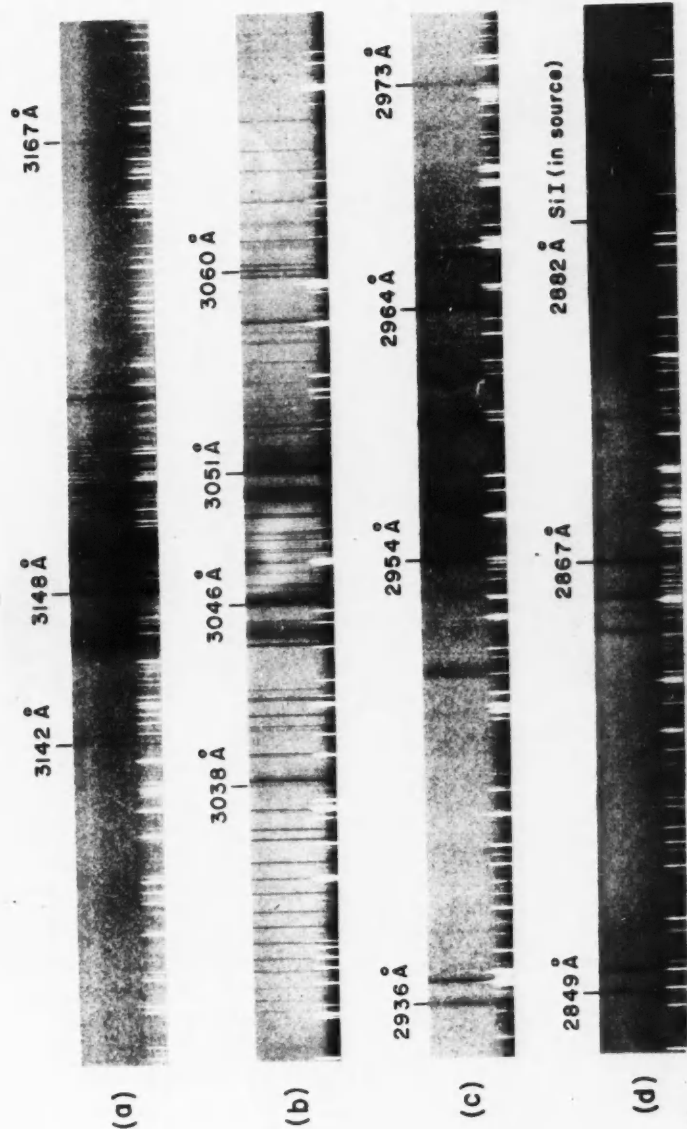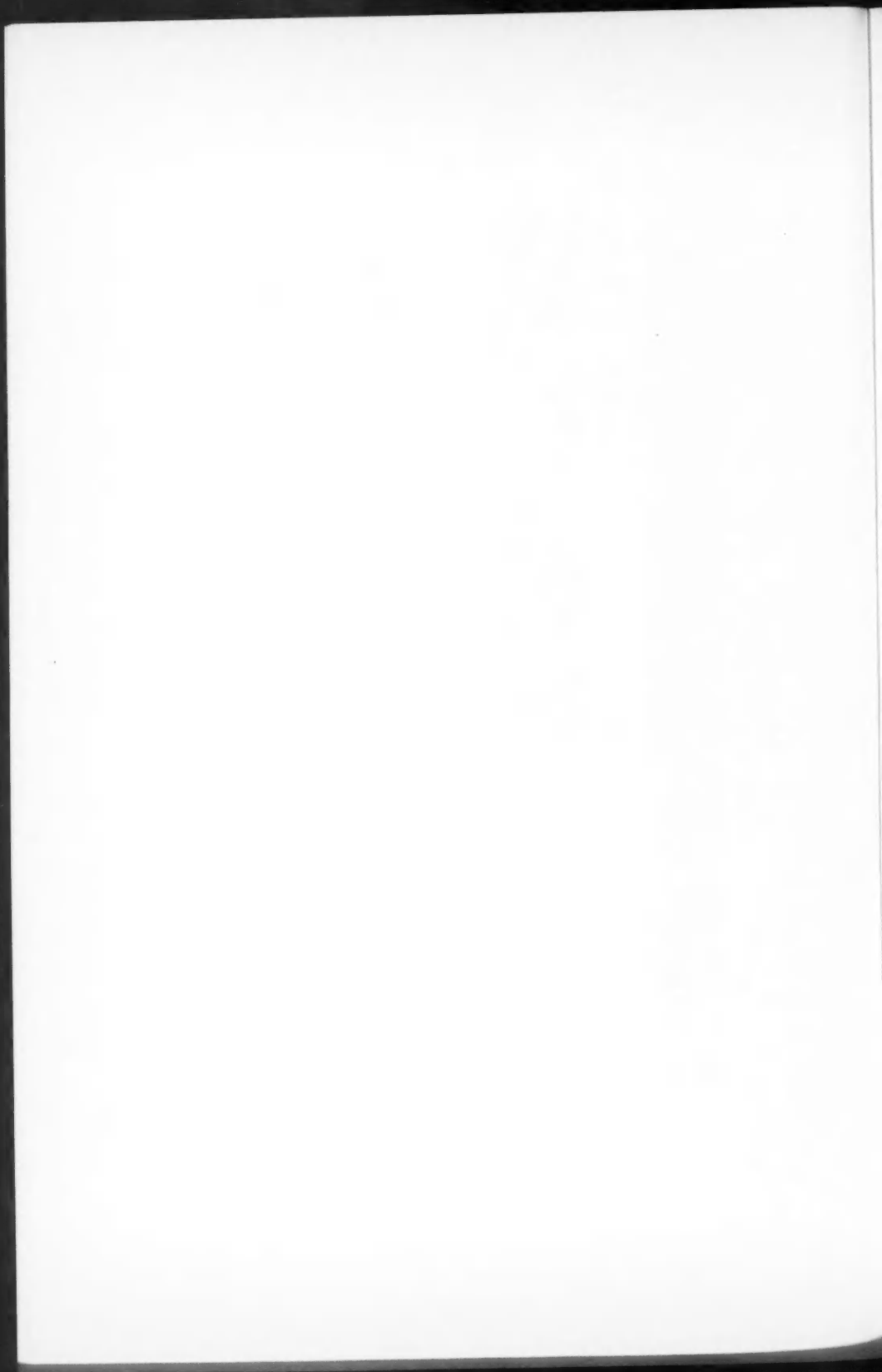
PLATE I

FIG. 1. Absorption bands of NCO: (a), (b), and (c) photographed in the third order of a 21-ft concave grating spectrograph, (d) photographed in the fourth order. The widely spaced lines in (b) are the 1–0 band of the $A(^3\Pi)–X(^2\Sigma^-)$ system of NH.

tion of the other bands in the spectrum showed that only in the 3046-Å band was the fine structure sufficiently extended for a rotational analysis.

The 3046-Å band has two subbands, each with one P and one R branch. The lines in the region of the subband origins are very weak. Consequently it was not possible to determine the J numberings from the positions of the zero gaps, and the J values of Table II were assigned using lower-level combination differences. In columns 6 to 9 of Table II the lower-level combination dif-

TABLE II

Vacuum wave numbers and assignments for the lines of the 3046-Å band of NCO, and lower-level combination differences

J	P_1	R_1	P_2	R_2	$R_1(J-1)$ $-P_1(J+1)$	$R_2(J-1)$ $-P_2(J+1)$	$\Delta_2 F_1''(J)$†	$\Delta_2 F_2''(J)$†
½								
1½		32,815.30					—	3.13
2½	32,811.55	816.11			4.42		4.65	4.69
3½	810.88	816.59		32,752.11	6.31		6.21	6.26
4½	809.80	817.30		752.63	7.68		7.76	7.82
5½	808.91	817.71		753.39	(9.25)	9.31	9.31	9.38
6½	808.05*	818.36	32,743.32	754.09	(10.68)	(10.61)	10.86	10.95
7½	807.03*	818.74	742.78*	·754.77	12.49	(12.45)	12.41	12.51
8½	805.87	819.24	741.64*	755.24	13.90	14.12	13.96	14.07
9½	804.84	819.77	740.65	755.93*	(15.63)	15.59	15.51	15.64
10½	803.61*		739.65	756.51	(17.30)	(17.19)	17.06	17.20
11½	802.47*		738.74	757.06		18.74	18.61	18.76
12½	801.23		737.77	757.68		20.29	20.17	20.33
13½	800.01		736.77	758.24		21.94	21.71	21.89
14½	798.75		735.74	758.76		23.54	23.26	23.45
15½	797.61		734.70	759.31		25.03	24.82	25.02
16½	796.22		733.73	759.68*		26.62	26.37	26.58
17½	794.88		732.69	760.15		(28.11)	27.92	28.14
18½	793.42*		731.57			29.69	29.49	29.73
19½	792.01		730.46				31.02	31.27
20½	790.81	(Head	729.35				32.54	32.81
21½	789.32, 9.13	821.72)	728.06				34.12	34.39
22½	787.85, 8.65		727.02				35.67	35.95
23½	786.30, 6.11		725.87				37.22	37.52
24½	784.89, 4.54		724.84				38.77	39.08
25½			723.68				40.32	40.64
26½	781.46						41.86	42.20
27½	780.31, 9.96						43.41	43.76

*Blended with lines of the 1-0 band of the $A(^3\Pi) \leftarrow X(^3\Sigma^-)$ system of NH.
†Calculated from rotational constants of Paper I.

ferences obtained from this band are compared with values calculated from the rotational constants of Paper I. The combination differences from the subband of longer wavelength are available to sufficiently high J values to prove that this is the subband $^2\Pi_{\frac{3}{2}} \leftarrow {}^2\Pi_{\frac{1}{2}}$ (the ground state is known to be an inverted state).

The rotational term values for doublet states of Hund's coupling case (a) have been calculated by Hill and Van Vleck (1928) for any magnitude of the spin-coupling constant A:

(1) $$F(J) = B[(J+\tfrac{1}{2})^2 - \Lambda^2] \pm [B^2(J+\tfrac{1}{2})^2 + \tfrac{1}{4}A(A-4B)\Lambda^2]^{\frac{1}{2}}.$$

With the addition of a centrifugal stretching term this expression was found adequate for the representation of the rotational term values of a $^2\Pi$ level

(00^{1}0) and a $^2\Delta$ level (01^{2}0) in the ground state of NCO $(X, {}^2\Pi_i)$. Equation (1) shows that the mean energy of the $F_1(J)$ and $F_2(J)$ levels is independent of the magnitude of A:

$$(2) \qquad \tfrac{1}{2}[F_1(J)+F_2(J)] = B[(J+\tfrac{1}{2})^2-\Lambda^2].$$

There are insufficient lines in the R branches of the 3046-Å band for the determination of an accurate B' value from upper-level combination differences. Consequently the upper-level term values were computed by adding the rotational term values of the appropriate lower levels (calculated from the data of Paper I) to the measured frequencies of the lines in the band. The mean value for each J of the resultant $T'_1(J)$ and $T'_2(J)$ was plotted against $[(J+\tfrac{1}{2})^2-1]$. The scatter of the plot was too great to allow a determination of the upper-state centrifugal stretching constant D'. The term values $T'(J)$ were therefore corrected to allow for a value of D' put equal to D'' ($=15\times10^{-8}$ cm^{-1}). Then from the intercept and slope of the line:

$$(3) \qquad \nu_0 = 32{,}781.1_3 \text{ cm}^{-1}, \qquad B' = 0.3765\pm0.0002 \text{ cm}^{-1}.$$

If $A \gg B$, the square root of equation (1) can be expanded to show that

$$(4) \qquad F_2(J)-F_1(J) = \Lambda|A-2B|+(2B^2)/(\Lambda|A-2B|)[(J+\tfrac{1}{2})^2-\Lambda^2]$$

and thus the rotational levels of the two sublevels of a $^2\Pi$ level ($\Lambda=1$) can be represented using effective B values of $B\pm B^2/|A-2B|$. Values of the left-hand side of equation (4) were obtained from the separations of lines in the two subbands and the lower-level combination differences, according to the equations

$$(5) \qquad F'_2(J)-F'_1(J) = [F''_2(J+1)-F''_1(J+1)]-[P_1(J)-P_2(J)]$$

$$(6) \qquad\qquad\qquad\quad = [F''_2(J-1)-F''_1(J-1)]-[R_1(J)-R_2(J)],$$

and were plotted against $[(J+\tfrac{1}{2})^2-1]$. This gave a straight line of intercept 31.6 cm^{-1} and slope $+0.012_0$ cm^{-1}. Thus $A' = -30.8$ cm^{-1}. The value of the slope of the plot calculated according to equation (4) with these values of A' and B' is $2B'^2/|A'-2B'| = +0.0090$ cm^{-1}. Therefore, although $(B'_{2,\text{eff}}-B'_{1,\text{eff}})$ is of the correct sign and order of magnitude, the rotational term values of this upper level cannot be accurately represented by equation (1). Possibly this lack of agreement between observation and calculation is due to a Fermi resonance, as discussed above in the section on the vibrational structure of the bands, but as was pointed out above, even the 000–000 band appears to be perturbed.

The value of $B' = 0.3765$ cm^{-1} determined above cannot be a 'true' B value for the level, as the rotational structure does not obey equation (1). In addition, this B' value is an effective value for an excited vibrational level of the $B(^2\Pi)$ state of NCO. Even so it can be used to give an approximate value of a molecular dimension for NCO in this state. The individual bond lengths r_{NC} and r_{CO} cannot be determined without data from an isotopic molecule, but it is possible to give an upper limit to the distance between the nitrogen and oxygen atoms consistent with this B value. To calculate this limit the carbon atom is placed at the center of gravity of the molecule, and the distance

corresponding to $B' = 0.3765 \pm 0.0030$ cm^{-1} is $(r_{NC} + r_{CO}) \leqslant 2.45 \pm 0.01$ Å. The molecular dimensions determined for the $A(^2\Sigma^+)$ and $X(^2\Pi)$ states of NCO from the values of B_0 given in Paper I are:

(7) $\qquad\qquad\qquad A(^2\Sigma^+),\ (r_{NC} + r_{CO}) \leqslant 2.369$ Å,

(8) $\qquad\qquad\qquad X(^2\Pi),\ (r_{NC} + r_{CO}) \leqslant 2.408$ Å.

DISSOCIATION AND PREDISSOCIATION

The only published kinetic study involving the NCO radical is on the thermal decomposition of potassium cyanate (Shushunov and Serdyuk 1953). The initial states in the pyrolysis are thought to be

$$KNCO \rightarrow K + NCO, \qquad\qquad\qquad (9)$$
$$NCO \rightarrow N + CO, \qquad\qquad\qquad (10)$$
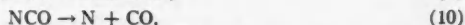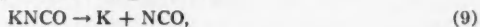
of which the first appears to be the rate-determining step. As potassium cyanate decomposes at about 700° C the activation energy of its decomposition is probably of the order of 70 kcal/mole. Thus the dissociation energy of NCO into N + CO cannot be greater than 70 kcal/mole (3.0 ev). An independent estimate of the dissociation energy of N—CO may be made from the heat of formation of HNCO (36.5 kcal/mole in aqueous solution, Bichowsky and Rossini 1936). If the heat of solution of gaseous HNCO is assumed to be 10 kcal/mole, and the NH bond strength is 100 kcal/mole, then the dissociation energy of N—CO is 64 kcal/mole (2.8 ev), with an error probably no greater than 20 kcal/mole (0.8 ev).

The possible electronic states of linear NCO that can be formed from the low-lying electronic states of N + CO, or O + CN, were discussed in Paper I. These are indicated in Fig. 2, which is a schematic correlation of the three
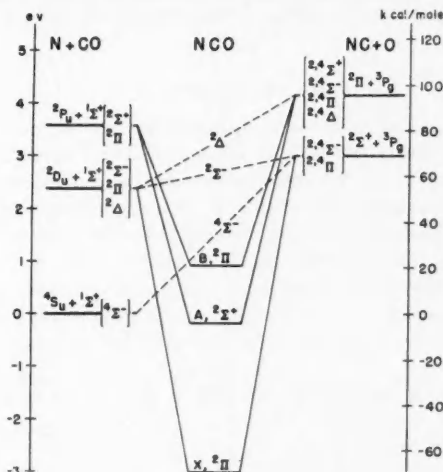
FIG. 2. Correlation diagram for NCO and its dissociation products N + CO or NC + O. The possible electronic states arising from each combination of dissociation products are indicated in braces.

known states of NCO with the dissociation products, taking account of the non-crossing rule. The dissociation energy of N—CO has been arbitrarily made 69 kcal/mole (3.0 ev) in this figure.

The observed diffuseness of some of the bands in the spectrum above 33,700 cm^{-1} (4.2 ev) is presumed to be due to predissociation of the $B(^2\Pi)$ state of NCO, although the possibility that the diffuse features are unresolved groups of lines cannot be ignored, especially as the spectrum appears to be perturbed. If this predissociation is produced by the $^4\Sigma^-$ state, leading to $N(^4S_u) + CO(^1\Sigma^+)$, it follows that the dissociation energy of N—CO $\leqslant$ 96 kcal/mole (4.2 ev). However, it would be surprising if a "forbidden" $^4\Sigma^-, ^2\Pi$ predissociation results in a noticeable diffuseness in the spectrum. On the other hand, if the predissociation is produced by the $^2\Sigma^-$ state, leading to $N(^2D_u) + CO(^1\Sigma^+)$, then the dissociation energy of N—CO is less than or equal to 41 kcal/mole (1.8 ev).

ACKNOWLEDGMENTS

REFERENCES

BICHOWSKY, F. R. and ROSSINI, F. D. 1936. The thermochemistry of the chemical substances (Reinhold Publishing Corp., New York).
DIXON, R. N. 1959. Phil. Trans. Roy. Soc. London. In press.
HERZBERG, G. 1945. Infrared and Raman spectra (D. Van Nostrand Co. Inc., New York).
HILL, E. L. and VAN VLECK, J. H. 1928. Phys. Rev. 32, 250.
HOLLAND, R., STYLE, D. W. G., DIXON, R. N., and RAMSAY, D. A. 1958. Nature, 182, 336.
POPLE, J. A. 1959. Molecular Phys. In press.
RENNER, R. 1934. Physik, 92, 172.
SHUSHUNOV, V. A. and SERDYUK, N. K. 1953. Doklady Akad. Nauk U.S.S.R. 93, 507.
TOMKINS, F. S. and FRED, M. 1951. J. Opt. Soc. Am. 41, 641.

THE SPECIFIC HEAT OF COPPER FROM 20° TO 300° K[1]

Douglas L. Martin

ABSTRACT

The specific heats of commercially pure cold-rolled copper and of annealed and heavily cold-worked 99.999% pure copper have been measured in the temperature range 20° to 300° K. When results are averaged over the whole temperature range of measurement the specific heat of the pure cold-worked copper is about 0.15% above that of the pure annealed sample while results for the commercially pure cold-rolled material lie in an intermediate position. Results on a given sample are reproducible within 0.05%. The entropy of pure annealed copper at 298.15° K is 7.92±0.04 cal/°K g-atom.

INTRODUCTION

Measurements of the specific heat of copper in the temperature region 20° to 300° K are too numerous to detail. Early measurements (see, for example, Regnault 1840) suggested that there was a difference in the specific heats of cold-worked and annealed copper but careful later comparisons (Eucken and Werth 1930; Maier and Anderson 1934) showed that the difference, if any, was not greater than the experimental error ($\sim 0.2\%$). Later work by Giauque and Meads (1941) produced results systematically higher than other recent measurements (loc. cit. and Dockerty 1933, 1937) which they attributed to the perfection of their sample, arguing that since annealed copper is softer than cold-worked material the Debye temperature was lower and the specific heat higher. However, they failed to distinguish between elastic and plastic properties and in fact the elastic constants of cold-worked material are *lower* than those for annealed copper. Hence, on this argument one would expect the specific heat of annealed copper to be lower than that of cold-worked material.

The primary purpose of the present work was to assess the performance of a calorimeter but at the same time it has been possible to resolve the above discrepancy.

EXPERIMENTAL

The measurements were made with a continuous heating semiautomatic adiabatic calorimeter basically similar to that described by Dauphinee *et al.* (1954). This earlier apparatus was constructed so that it could be placed between the pole pieces of an A. D. Little electromagnet, and the cramped design resulting from this requirement greatly hampered the attainment of adiabatic conditions so that above about 150° K it was always necessary to surround the cryostat with a liquid bath maintained within a few degrees of the calorimeter temperature. Figure 1 is a diagram of the redesigned cryostat and it will be seen that the three adiabatic shields are now separated from one

another and the rest of the cryostat. The calorimeter and shields are assembled in a 'cage' which is then screwed onto the bottom of the can and electrical connections established by means of copper 'jumpers' soldered between the two rings of teflon-insulated terminals.

The electronic control of the shields and the measuring circuit are exactly as described previously except that time measurement is now by a stop clock driven from a standard frequency supply and triggered by a cam and micro-switch on the balancing motor shaft of the Leeds and Northrup potentiometer recorder measuring the thermometer resistance.

A slightly different calorimeter vessel from that used previously (Dauphinee *et al.* 1954, 1955) has been used in this work and can be seen in Fig. 1. The
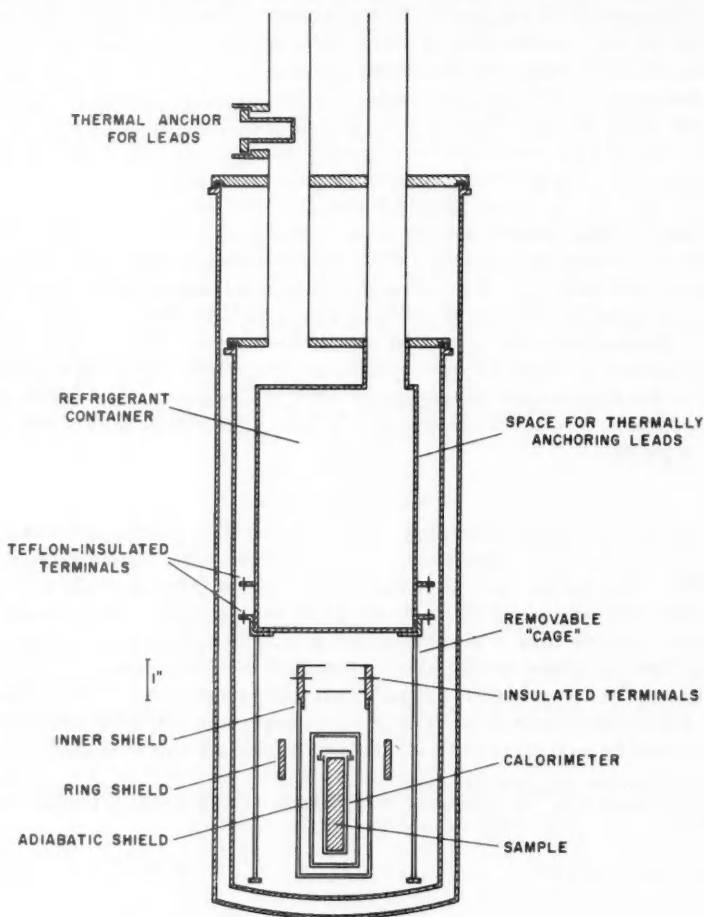
FIG. 1.   The cryostat, shield system, and calorimeter.

sealing of the calorimeter is carried out in a helium atmosphere and the Wood's metal is manipulated with a non-tinning molybdenum spatula, so that the weight of metal remains constant. The only conclusive test for the vacuum tightness of the seal is measurement of the calorimeter equilibrium time after assembly. (The tubular part of the calorimeter was made from copper sheet 0.004 in. thick with a hard-soldered lap joint. For such a thin wall this method is much superior to the customary turning.)

The single thermocouple control of the adiabatic shield presupposes a uniform surface temperature of the calorimeter vessel. The large area of the surface covered by the heater contributes towards satisfying this requirement but it is also necessary to have a specimen which is a good conductor fitting closely the inside dimensions of the calorimeter vessel.

If a suitable specimen is used, the results are independent of heating rate over a range of at least 2 °K/hr to 30 °K/hr. The surrounding bath temperature now has no influence on the results.

The three probable causes of error in these measurements are in the determination of temperature, in the power measurement, and in the non-attainment of adiabatic conditions. The copper temperature scale of Dauphinee and Preston-Thomas (1954) was used. Experience with a larger number of copper thermometers indicates that their original estimate of errors was too optimistic and should be doubled. Resistors and standard cells have been checked against standards. Determination of the calorimeter equilibrium times at various temperatures indicates that errors due to thermal lags in the calorimeter are negligible. Drift checks with the adiabatic shield temperature offset from that of the calorimeter show that errors due to non-attainment of adiabatic conditions during normal operation are unlikely. The limiting factor in shield control is stray thermal voltages in the thermocouple circuits. Hence results above 80° K are expected to be accurate to $\pm 0.2\%$, the accuracy decreasing to $\pm 2.0\%$ at 20° K. The reproducibility of results on a given specimen is of the order of 0.05%, as will be detailed in the next section.

The copper samples were prepared from two different sources of material. Two of the samples were prepared from 99.999% pure copper obtained from the American Smelting and Refining Co., New Jersey. This was melted into graphite crucibles by induction heating under high vacuum. The first sample (the 'annealed sample') was cooled slowly over a period of about four hours and measured in the 'as cast' condition, no machining or other operations having been carried out. After measurements were completed the sample was etched and found to consist of a large crystal with much smaller crystals at its edges. The second sample was heavily cold worked below room temperature, using a hydraulic press, until its length was increased by 50%. It was then turned to shape, care being taken to prevent heating. X-ray measurement showed that the high-angle lines were very weak or absent and low-angle lines showed considerable broadening and some displacement. It is inferred from these results that the lattice is severely distorted as a result of the cold working. By approximate analysis of the line profiles a plot of fraction of sample with a given strain against strain was obtained. From this the *average*

strain in the sample was deduced to be about 0.2%. The weights of these samples were 65.092 g (annealed sample) and 71.424 g (cold-worked sample).

The other samples were turned from commercially pure cold-rolled copper. Spectrographic analysis showed the chief impurities to be silicon and magnesium, both estimated to be less than 0.01%. The first of these samples was solid and the second was hollow (made in two parts) so as to change the mass without altering the external dimensions. The weights of these samples were 71.138 and 38.625 g respectively. After completion of measurements the solid sample was etched and the average grain size found to be of the order 0.05 mm. X-ray measurement on the same stock showed line broadening which, by the analysis indicated above, was found to correspond to an average strain of about 0.1%, indicating considerable cold work.

RESULTS

In this continuous heating apparatus the time elapsed during a comparatively small temperature increment is measured (normally less than 0.5° K in the present work). In this way a great number of 'points' are recorded and, except in regions of special interest, only a sample of these are evaluated and plotted. The smoothed values in Table I are read from large-scale graphs.

Results on the various samples examined during this work are compared by summing the smoothed specific heat results for equal temperature increments for one sample and comparing with a similar sum for another. In this way mean systematic deviations between samples may be found. The method is equivalent to a comparison of enthalpies.

As a check on the reproducibility of the apparatus the heavier commercially pure sample was measured on two occasions and the results independently evaluated and tabulated (columns I(a) and I(b) of Table I). The deviation averaged over the whole temperature range is 0.05%. The lighter commercially pure sample (column II of Table I) is systematically high with a mean deviation of about 0.25%. It is not known whether this is due to the mass difference or to the extra machining operations or both.

The results obtained for the very pure copper are almost the same as those for commercially pure material. Again averaging over the whole temperature range, the cold-worked sample has a systematic average deviation of about 0.15% above the annealed sample and about 0.07% above the commercially pure sample of approximately the same mass.

DISCUSSION

The results for the annealed sample are compared with other work in Table II. Giauque and Meads (1941) remark that Dockerty's work on commercial copper shows an average deviation of 0.018 cal/°K g-atom below their results over the temperature range 50° to 300° K. Satterthwaite et al. (1954) have since found for commercial copper an average deviation of 0.017 cal/°K g-atom below Giauque and Meads' results, thus closely confirming Dockerty's work. The present results for commercial copper deviate (taking the average of I(a) and I(b)) about 0.020 cal/°K g-atom below Giauque and Meads and

TABLE I

Specific heat of copper (units cal/°K g-atom)

| T, °K | Commercially pure cold-rolled copper | | | 99.999% pure copper | | | |
| | I(a) | I(b) | II | Cold-worked | Annealed | | |
					C_p	C_v	θ_D
20	—	—	—	—	0.113	0.113	324
21	0.132	0.132		0.131	0.132	—	—
22	—	—	0.153	—	—	—	—
25	0.230	0.231	0.231	0.229	0.230	0.230	317
30	0.406	0.407	0.408	0.405	0.404	0.404	313
35	0.637	0.636	0.637	0.636	0.634	0.634	311
40	0.896	0.897	0.901	0.896	0.893	0.892	311
45	1.178	1.182	1.185	1.180	1.179	1.178	311
50	1.470	1.471	1.477	1.472	1.467	1.465	313
55	1.769	1.769	1.774	1.770	1.764	1.761	313
60	2.056	2.061	2.064	2.061	2.055	2.051	314
65	2.330	2.342	2.341	2.336	2.334	2.328	314
70	2.592	2.598	2.601	2.597	2.589	2.581	315
75	2.841	2.834	2.848	2.849	2.841	2.831	315
80	3.074	3.071	3.089	3.081	3.074	3.061	316
85	3.289	3.287	3.301	3.291	3.287	3.272	316
90	3.481	3.488	3.496	3.498	3.488	3.470	316
95	3.657	3.662	3.678	3.668	3.665	3.645	315
100	3.811	3.821	3.838	3.824	3.826	3.802	317
110	4.108	4.111	4.118	4.109	4.116	4.086	317
120	4.350	4.358	4.367	4.358	4.354	4.317	318
130	4.563	4.572	4.579	4.572	4.565	4.520	318
140	4.748	4.749	4.763	4.744	4.749	4.697	317
150	4.899	4.902	4.909	4.896	4.903	4.844	316
160	5.030	5.035	5.042	5.031	5.029	4.963	317
170	5.143	5.147	5.156	5.145	5.138	5.064	318
180	5.243	5.245	5.256	5.242	5.237	5.155	318
190	5.325	5.328	5.347	5.331	5.327	5.238	317
200	5.401	5.404	5.420	5.409	5.399	5.302	318
210	5.472	5.471	5.487	5.475	5.466	5.362	318
220	5.535	5.531	5.542	5.534	5.527	5.415	319
230	5.592	5.586	5.593	5.587	5.579	5.460	319
240	5.645	5.632	5.643	5.636	5.625	5.498	321
250	5.687	5.681	5.690	5.685	5.672	5.537	321
260	5.724	5.728	5.737	5.731	5.718	5.571	319
270	5.764	5.772	5.778	5.773	5.761	5.611	318
273.15	5.776	5.784	5.790	5.784	5.773	5.620	—
280	5.798	5.811	5.815	5.807	5.794	5.636	319
290	5.828	—	5.844	5.835	5.824	5.660	320
298.15	5.850	—	—	5.858	5.843	5.673	—
300	5.855	—	—	5.863	5.846	5.675	324

NOTE: Atomic weight = 63.57; J = 4.186.

are therefore within about 0.05% of Dockerty and of Satterthwaite *et al*. Hence it is concluded that the present apparatus yields specific heat results in very close agreement with those obtained elsewhere.

From our experimental results it has been shown that the specific heat of annealed copper is systematically very slightly lower than that of cold-worked material. This conclusion was reached by a comparison of the results obtained from the measurement of a number of *different* samples of copper with the *same* calorimeter and therefore does not depend upon the absolute accuracy of the measurements. Now Giauque and Meads compared their measurements

TABLE II

Comparative values for specific heat of copper
(units cal/°K g-atom)

T, °K	This work 99.999% annealed	Dockerty (1933, 1937)	Giauque and Meads (1941)
20	0.113	—	0.114
25	0.230	—	0.233
30	0.404	0.401	0.412
35	0.634	0.628	0.637
40	0.893	0.900	0.901
45	1.179	1.188	1.191
50	1.467	1.489	1.493
55	1.764	1.791	—
60	2.055	2.076	2.074
65	2.334	2.345	—
70	2.589	2.607	2.615
75	2.841	2.859	—
80	3.074	3.090	3.091
85	3.287	3.304	—
90	3.488	3.498	3.500
95	3.665	3.669	—
100	3.826	3.828	3.847
110	4.116	4.115	4.138
120	4.354	4.364	4.380
130	4.565	4.571	4.580
140	4.749	4.749	4.752
150	4.903	4.904	4.904
160	5.029	5.026	5.042
170	5.138	5.145	5.163
180	5.237	5.242	5.263
190	5.327	5.328	5.350
200	5.399	5.395	5.430
210	5.466	5.459	5.499
220	5.527	5.523	5.558
230	5.579	5.576	5.613
240	5.625	5.622	5.670
250	5.672	5.669	5.719
260	5.718	5.714	5.755
270	5.761	5.752	5.788
273.15	5.773	5.763	—
280	5.794	5.789	5.817
290	5.824	5.824	5.837
298.15	5.843	5.850	5.848
300	5.846	5.857	5.850

on a *single* sample of annealed copper with results of *other* workers and con-
cluded that the specific heat of annealed copper was systematically higher
than that of cold-worked material. It appears therefore that there must have
been some systematic error in Giauque and Meads' results.

Measurements of the effect of strain on elastic constants have been made
by Kawai (1930), Smith (1953), and others. For copper the apparent Young's
modulus decreases for small elongations but increases again for greater strains.
It seems clear that the latter effect is due to the development of preferred
crystallographic orientation as a result of elongation in which case the elastic
anisotropy results in an apparent increase of Young's modulus. Hence the
over-all effect of cold work is a reduction of elastic constants, which Smith
(loc. cit.) attributes to the elastic oscillations of relatively mobile screw
components of dislocation loops.

The effect of this change of elastic constants on the specific heat is only likely to be appreciable at very low temperatures where the dominant vibrational modes are of such long wavelength as to include a number of dislocations. (There is also a contribution to the specific heat due to the vibration of mobile defects (Granato 1958).) Thus in the temperature range covered in these measurements no very large difference in the specific heat of annealed and cold-worked copper is to be expected. Any residual of the low-temperature effects would increase the specific heat of cold-worked material above that of an annealed sample.

The specific heat at constant volume for the annealed copper sample has been calculated using the thermal expansion data of Rubin *et al.* (1954) and the elastic constant data of Overton and Gaffney (1955). From these C_v values Debye temperatures have been evaluated after subtraction of the electronic specific heat (Corak *et al.* (1955). Figure 2 shows the results and also the limiting
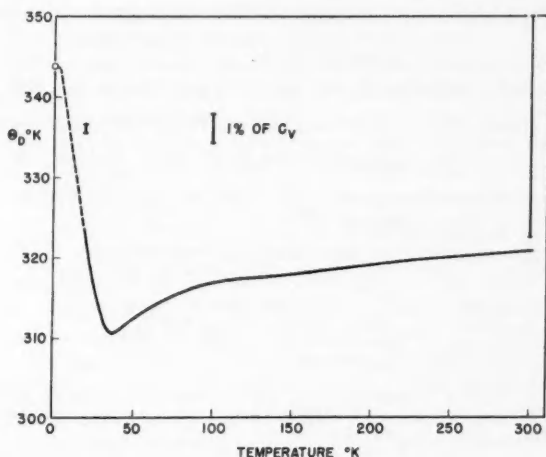
FIG. 2.   The Debye temperature for copper. Smoothed experimental results are represented by the solid line, which has been extrapolated to the θ_0 value of Corak *et al.* and Rayne.

value at the absolute zero taken from calorimetric results below 4.2° K of Corak *et al.* (1955) and of Rayne (1956). (Strictly there is a further correction to be applied to the Debye temperature values due to the thermal expansion of the copper. This may be calculated using the Grüneisen constant for copper and is greatest at the high-temperature end where the Debye temperature values would be increased by about 6° K.) There are two main features of interest in this curve: firstly, the very shallow minimum and, secondly, the fact that there is no sign of a decrease of the Debye temperature at the high-temperature end, indicating a negligible anharmonic contribution to the specific heat even at this temperature.

The entropy at 298.15° K has been calculated from the results for the 99.999% pure annealed sample and is 7.92 ± 0.04 cal/°K g-atom. A value at 20° K was obtained from the extrapolated θ_D plot in Fig. 2 and the electronic specific heat as determined by Corak *et al.* (1955).

CONCLUSION

Averaged over the temperature range 20° to 300° K, the specific heat of heavily cold-worked 99.999% pure copper is about 0.15% above that of the annealed material. The reproducibility of measurements on a given sample is within 0.05%.

ACKNOWLEDGMENTS

REFERENCES

CORAK, W. S., GARFUNKEL, M. P., SATTERTHWAITE, C. B., and WEXLER, A.   1955.   Phys.
    Rev. **98**, 1699.
DAUPHINEE, T. M., MACDONALD, D. K. C., and PRESTON-THOMAS, H.   1954.   Proc. Roy.
    Soc. A, **221**, 267.
DAUPHINEE, T. M., MARTIN, D. L., and PRESTON-THOMAS, H.   1955.   Proc. Roy. Soc. A, **233**,
    214.
DAUPHINEE, T. M. and PRESTON-THOMAS, H.   1954.   Rev. Sci. Instr. **25**, 884.
DOCKERTY, S. M.   1933.   Can. J. Research, **9**, 84.
———   1937.   Can. J. Research, A, **15**, 59.
EUCKEN, A. and WERTH, H.   1930.   Z. anorg. u. allgem. Chem. **188**, 152.
GIAUQUE, W. F. and MEADS, P. F.   1941.   J. Am. Chem. Soc. **63**, 1897.
GRANATO, A.   1958.   Phys. Rev. **111**, 740.
KAWAI, T.   Sci. Repts. Tohoku Imp. Univ. 1930. **19**, 209.
MAIER, C. G. and ANDERSON, C. T.   1934.   J. Chem. Phys. **2**, 513.
OVERTON, W. C. and GAFFNEY, J.   1955. Phys. Rev. **98**, 969.
RAYNE, J. A.   1956.   Australian J. Phys. **9**, 189.
REGNAULT, V.   1840.   Pogg. Ann. **51**, 213.
RUBIN, T., ALTMAN, H. W., and JOHNSTON, H. L.   1954.   J. Am. Chem. Soc. **76**, 5289 (1954).
SATTERTHWAITE, C. B., CRAIG, R. S., and WALLACE, W. E.   1954.   J. Am. Chem. Soc. **76**, 232.
SMITH, A. D. N.   1953.   Phil. Mag. **44**, 453.

THE SPECIFIC HEAT OF A LITHIUM–MAGNESIUM ALLOY.
THE MARTENSITIC TRANSFORMATION[1]

DOUGLAS L. MARTIN

ABSTRACT

The specific heat of an alloy of lithium with 0.95 at.% magnesium has been measured from 20° to 300° K. The specific heat of the body-centered cubic phase is less than that calculated from the Kopp–Neumann rule. A specific heat anomaly, due to the martensitic transformation, is observed and has almost the same heat content as the corresponding anomaly for pure lithium but the high-temperature end is of significantly different shape.

INTRODUCTION

Up to 70% magnesium may be dissolved in lithium without changing the body-centered cubic structure of the pure parent metal. This alloy system therefore provides a means of studying the effect of a solid soluble "impurity" on the physical properties of lithium metal.

Zener (1947, 1948) showed that the rapidly increasing free energy with decreasing temperature for body-centered cubic metals and alloys might lead to a solid-phase transformation. Such a transformation in pure sodium and lithium and some lithium–magnesium alloys was discovered and studied by Barrett and co-workers (1947, 1948, 1950, 1956) using X-ray and metallographic techniques. More recently measurements have been made on the electrical, elastic, and thermal properties of sodium and of lithium of two different isotopic compositions (Dugdale and Gugan 1958, 1959; Verdini 1959; Martin 1958a, b, 1959a, b) in which effects due to the transformation were found. The interpretation of the electrical resistance data on lithium was made difficult by the effects of small impurity concentrations on the residual resistance and measurements were therefore extended to dilute alloys of magnesium in lithium in order to investigate the effect of controlled amounts of impurities (Dugdale and Gugan 1959). The present work examines the effect of a small addition of magnesium on the thermodynamic properties of the transformation.

EXPERIMENTAL

The sample was prepared from the "sodium-free" grade of lithium obtained from the Lithium Corporation of America (principal impurities Na, 0.005%; K, 0.01%; Ca, 0.01%; N, 0.02%; Fe, 0.001%; atomic weight = 6.945) and "spectroscopically pure" magnesium obtained from Johnson Matthey. A master alloy of approximately 10 at.% magnesium was prepared by heating the lithium and magnesium to 800° C in a low carbon steel crucible. The master alloy was then diluted with lithium in a stainless steel container to

make an alloy containing approximately 1 at.% magnesium. The calorimeter sample was extruded from the diluted alloy. The exact composition of the sample was determined as follows. The residual electrical resistances at liquid helium temperature of pieces taken from the ends of the sample were compared with the residual resistances of alloys for which the composition had been determined gravimetrically. The composition was found to be 0.95 ± 0.05 at.% where the tolerance indicates both the uniformity of the specimen and the estimated absolute accuracy of the measurement. From this the "average" atomic weight is 7.110. The weight of the sample, after buoyancy correction, was 4.451 g.

The measurements were made in a continuous heating adiabatic calorimeter (Martin 1959c). The estimated accuracy of the measurements is $\pm0.3\%$ above $80°$ K, decreasing to $\pm2\%$ at $20°$ K, after allowing for the uncertainty in the exact composition of the sample.

RESULTS

Provided that the alloy is not cooled below about $90°$ K the body-centered cubic structure is unaltered; smoothed results of measurements under these conditions are given in column 2 of Table I. On cooling the alloy below this temperature a partial transformation to a faulted hexagonal close-packed phase occurs, the amount transformed increasing as the temperature is lowered. On heating such a partially transformed sample a specific heat anomaly is observed in the region where reversion to the high-temperature phase takes place. Specific heat results obtained after cooling the sample to $20°$ K are given in column 3 of Table I for a sample annealed at about $300°$ K and in column 4 for a sample not annealed following a previous cycle of transformation and reversion.

DISCUSSION

The results for the body-centered cubic (b.c.c.) phase will be considered first. The "calculated" results given in column 5 of Table I have been obtained from specific heat results on lithium (Martin 1959a) and magnesium (Craig et al. 1954) assuming the Kopp–Neumann rule (i.e. that the thermal capacity of the alloy equals the sum of the thermal capacities of its constituent parts). The experimental results are some 2% lower than the calculated results and are also lower than the specific heat of pure lithium. This situation is not at all uncommon in alloys and it is interesting to seek a physical explanation. Assuming that small quantities of magnesium dissolve in lithium in a divalent form and that there is no change in band shape then the electronic specific heat of the alloy would be higher than that of pure lithium. Hence the observed *reduction* in specific heat is most probably due to a change in the lattice contribution. On a simple Debye model the Debye temperature would be *lowered* by the reduction in elastic constants on alloying (Verdini 1959) but it would be *increased* by the accompanying decrease in lattice parameter

TABLE I

Specific heat of a lithium – 0.95 at.% magnesium alloy

| Temp., °K | B.c.c. phase | After cooling to 20° K | | Calculated by Kopp–Neumann rule |
		Annealed	Not annealed	
21	—		.111	—
25	—		.173	—
30	—		.285	—
35	—		.424	—
40	—		.587	—
45	—		.767	—
50	—		.963	—
55	—		1.170	—
60	—		1.388	—
65	—		1.608	—
70	—		1.823	—
75	—		2.040	—
80	—		2.254	—
85	—		2.465	—
90	—	2.667	2.667	—
95	—	2.859	2.864	—
100	3.026	3.045	3.052	3.107
110	3.329	3.552	3.665	3.417
120	3.611	4.047	3.969	3.707
130	3.870	4.005	3.930	3.963
140	4.098	4.141	4.118	4.195
150	4.298	4.316	4.305	4.397
160	4.479	4.482	4.480	4.581
170	4.647	—	—	4.755
180	4.788	—	—	4.900
190	4.918	—	—	5.036
200	5.040	—	—	5.153
210	5.149	—	—	5.256
220	5.243	—	—	5.350
230	5.342	—	—	5.438
240	5.428	—	—	5.521
250	5.499	—	—	5.601
260	5.579	—	—	5.680
270	5.654	—	—	5.752
273.15	5.675	—	—	—
280	5.722	—	—	5.822
290	5.785	—	—	5.889
298.15	5.833	—	—	5.941
300	5.843	—	—	5.952

NOTE: Atomic weight $= 7.110$; $J = 4.186$.

(Herbstein and Averbach 1956). Insufficient detail is available to make a quantitative estimate of the first of these effects. The second would be negligibly small in comparison with the observed change (at 100° K) from a Debye temperature of 393° K for pure lithium to 402° K for the approximately 1% alloy (where these values have been calculated after subtraction of the electronic term but without correction for thermal expansion). The effect must therefore be due to the change in the vibration spectrum on alloying.

Turning now to the experiments relating to the martensitic transformation, Fig. 1 shows the experimental results for a typical anomaly caused by reversion to the high-temperature phase. The shape of this anomaly and another,
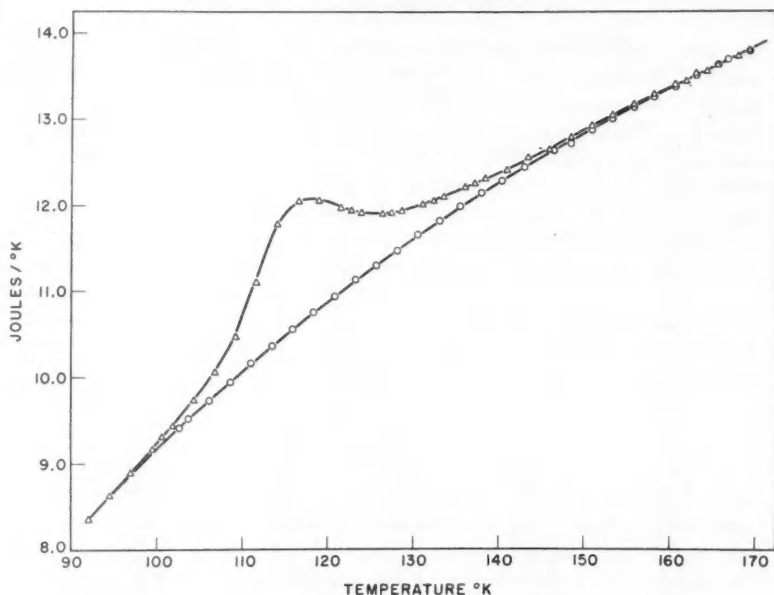
FIG. 1.   Thermal capacity of calorimeter containing 4.451 g lithium−0.95 at.% magnesium alloy.

O body-centered cubic phase;
△ after cooling to 20° K (heating rate 20° K/hr).

obtained under different conditions, are shown in Fig. 2. The heat content of the anomaly observed after cooling an annealed sample to 20° K is 9.3 cal/g-atom. For pure lithium under similar conditions a figure of 9.4 cal/g-atom was observed (Martin 1959a). It seems probable, therefore, that the presence of a small percentage of magnesium in lithium does not significantly alter the course of the martensitic transformation. However, it is already known that the temperature of equilibrium between the two phases is increased with the addition of magnesium and this is reflected in the position of the reversion anomaly. Figure 3 shows the progress of the reversion with increasing temperature and was obtained by integration over the anomaly shown in Fig. 1, thus assuming that equal areas of anomaly contribute equally to the reversion. This may not be so, as discussed elsewhere (Martin 1959a), due to the effects of stored elastic energy and cold work. Figure 2 also shows an anomaly obtained after cooling to 20° K a sample which had been previously transformed and then heated to 170° K, i.e. the sample was in a cold-worked state due to the previous transformation. The heat content of the anomaly is slightly reduced and the peak shifted to a lower temperature, but the general shape remains the same—in contrast to the corresponding results for pure lithium (Martin 1959a). On the whole it might be said that the shape of the anomalies observed
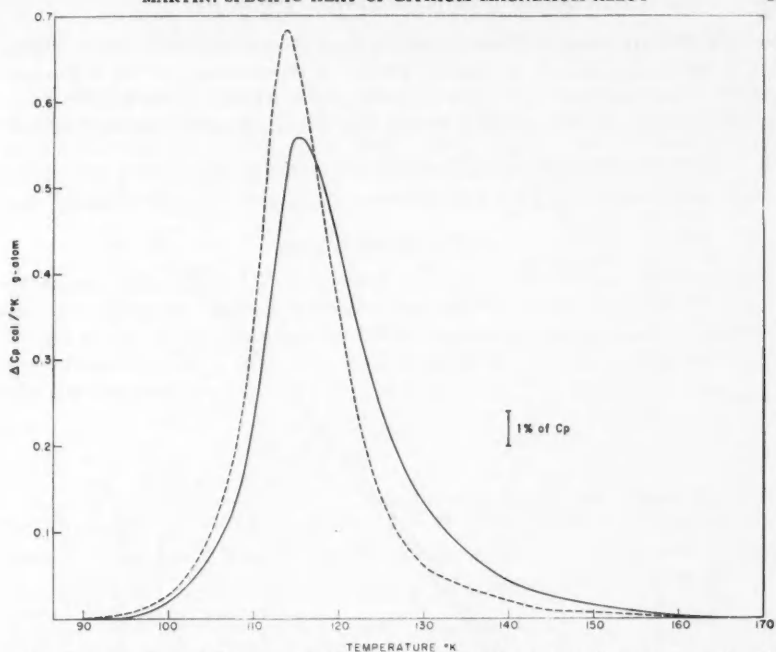
FIG. 2.   Specific heat anomalies in lithium – 0.95 at.% magnesium alloy due to martensitic transformation.

After cooling to:	Heated to:	$\int \Delta C_p . dT$, cal/g-atom
——— 20° K	170° K	9.3
– – – 20° K	300° K	8.9

Measurements made in this sequence.
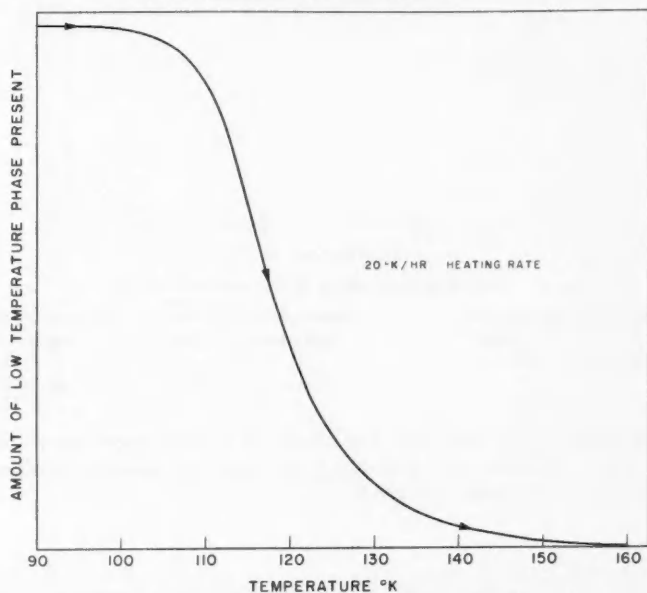
FIG. 3.   Progress of the reversion in lithium–magnesium alloy.

for this alloy are more like those of sodium than those of lithium (Martin 1959a, b). In particular there is no sudden ending of the anomaly at the high-temperature end, but there are some time-dependent effects in the specific heat, as shown in Fig. 4, from which it will be seen that a change in the heating rate
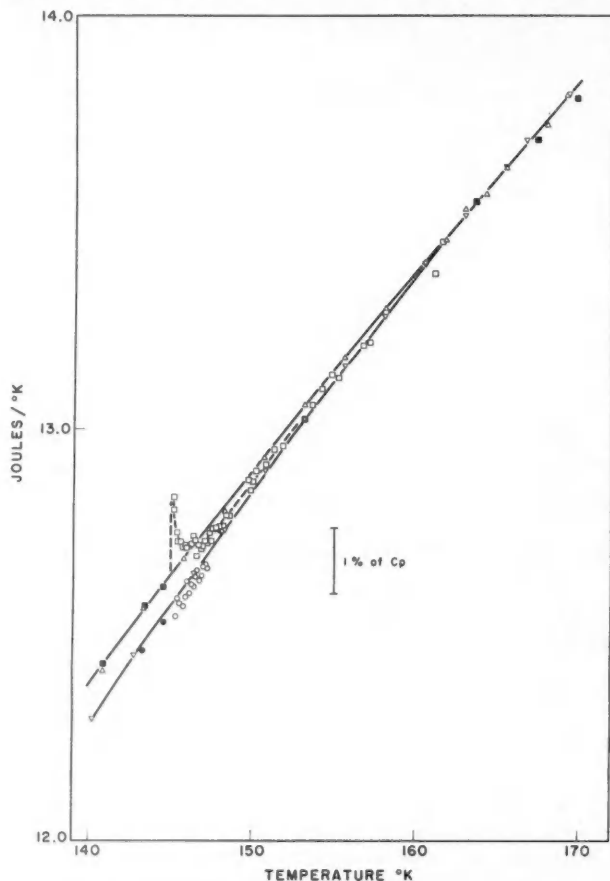
FIG. 4. Time-dependent effects in the reversion region.

Runs at 20° K/hr heating rate:
  ▽ body-centered cubic phase,
  △ after cooling to 20° K.

Runs in which heating rate is changed at 145° K:
  body-centered cubic phase   ● 20° K/hr,
                                      ○ 2° K/hr;
  after cooling to 20° K   ■ 20° K/hr,
                                      □ 2° K/hr.

alters the shape of the anomaly. The results of a check experiment are also given in Fig. 4, showing that a change in heating rate does not significantly affect the results obtained with the b.c.c. phase.

CONCLUSION

The results would be consistent with the fact that the addition of a small amount of magnesium to lithium does not significantly alter the course of the martensitic transformation, apart from raising slightly the temperature of equilibrium between the phases. There is some difference between the alloy and pure lithium in the final stages of the reversion to the high-temperature phase.

ACKNOWLEDGMENTS

REFERENCES

BARRETT, C. S. 1947. Phys. Rev. **72**, 245.
———— 1956. Acta Cryst. **9**, 671.
BARRETT, C. S. and TRAUTZ, O. R. 1948. Trans. Am. Inst. Mining Met. Engrs. **175**, 579.
BARRETT, C. S. and CLIFTON D. F. 1950. Trans. Am. Inst. Mining Met. Engrs. J. Metals, **188**, 1329.
CRAIG, R. S., KRIER, C. A., COFFER, L. W., BATES, E. A., and WALLACE, W. E. 1954. J. Am. Chem. Soc. **76**, 238.
DUGDALE, J. S. and GUGAN, D. 1958. Can. J. Phys. **36**, 1248.
———— 1959. To be published.
HERBSTEIN, F. H. and AVERBACH, B. L. 1956. Acta. Met. **4**, 407.
MARTIN, D. L. 1958a. Phys. Rev. Letters, **1**, 4.
———— 1958b. Phys. Rev. Letters, **1**, 447.
———— 1959a. Proc. Roy. Soc. Submitted for publication.
———— 1959b. Physica. Submitted for publication.
———— 1959c. Can. J. Phys. This issue.
VERDINI, L. 1959. To be published.
ZENER, C. 1947. Phys. Rev. **71**, 846.
———— 1948. Elasticity and anelasticity of solids (University of Chicago Press, Chicago, Illinois).

COMPARISON OF FLOW LINES IN VARIOUS TYPES OF RHEOLOGICAL BODIES[1]

SISIR CHANDRA DAS

ABSTRACT

An attempt has been made to investigate the nature of flow in Bingham bodies compressed by means of parallel rigid approaching plates. The results have been compared with those of plastic and viscous flow under the same conditions. It is shown that the flow lines in all three cases are very similar.

INTRODUCTION

In recent years attentions have been focused on Bingham bodies as an important case of rheological substances, but not much work has been done on its theoretical aspects. The case of Bingham flow through a tube has been discussed by Buckingham (1921) and Reiner (1926), while Reiner and Riwlin (1927) have done the integration in the case of a rotating cylinder. In a series of papers Oldroyd (1947a and 1948) has obtained the solutions for Bingham bodies for cylinders of various shapes moving through each other. He has also discussed the two-dimensional case (1947b) in some specified instances.

In the present paper an attempt has been made to investigate the relation of the Bingham flow in two dimensions in the case of approaching parallel plates with other types of flow (plastic, viscous). A yield condition similar to that valid in plastic flow has been assumed, and the flow lines have been drawn. The result is that the flow lines for a Bingham substance are very much similar to those for plastic and viscous materials.

GEOMETRY OF EXAMPLE. YIELD CONDITION

We consider the case of a plate compressed between planes $y = a$ and $y = -a$; there is no motion in z-direction. Therefore the principal stress in the z-direction is $1/2(\sigma_1 + \sigma_2)$ where σ_1 and σ_2 are the principal stresses in the xy-plane. The criterion of yield is taken as

$$(1) \qquad \sigma_1 - \sigma_2 = 2\nu$$

where ν is the yield stress. It may be noted here that equation (1) satisfies both Tresca's and von Mises's yield criterion.

If σ_x, σ_y, τ_{xy} are the components of stress referred to x and y axes, the equation of equilibrium can be written in the absence of a body force as follows:

$$(2) \qquad \frac{\partial \sigma_x}{\partial x} + \frac{\partial \tau_{xy}}{\partial y} = 0,$$

$$\frac{\partial \tau_{xy}}{\partial x} + \frac{\partial \sigma_y}{\partial y} = 0.$$

The yield criterion (1) becomes

(3) $$1/4(\sigma_x - \sigma_y)^2 + \tau_{zy}^2 = \nu^2.$$

Taking the plates to be rough at the surfaces of contact and ruling out the possibility of their transmitting a shearing stress in excess of the yield stress in simple shear, we can formulate the boundary condition as follows:

(4) $$\tau_{zy} = \pm \nu \qquad\qquad \text{at } y = \mp a.$$

The stresses σ_x and σ_y can be easily eliminated from the equations (2) and (3), and we get an equation for τ_{zy} which is

(5) $$\frac{\partial^2 \tau_{zy}}{\partial x^2} - \frac{\partial^2 \tau_{zy}}{\partial y^2} = \pm 2 \frac{\partial^2}{\partial x \partial y} (\nu^2 - \tau_{zy}^2)^{\frac{1}{2}}.$$

A solution of this equation which satisfies the boundary condition (4) is

(6) $$\tau_{zy} = -\frac{\nu y}{a}.$$

The other stress components in this case are

(7)
$$\sigma_x = -p + \frac{\nu x}{a} + 2\nu \left(1 - \frac{y^2}{a^2}\right)^{\frac{1}{2}},$$

$$\sigma_y = -p + \frac{\nu x}{a},$$

where p is a constant.

The stress deviators (denoted by s) can be written as

(8)
$$s_x = \nu \left(1 - \frac{y^2}{a^2}\right)^{\frac{1}{2}},$$

$$s_y = -\nu \left(1 - \frac{y^2}{a^2}\right)^{\frac{1}{2}},$$

$$\tau_{zy} = -\frac{\nu y}{a}.$$

SOLUTION FOR VARIOUS TYPES OF FLOW

The solution up till now has been quite similar to that in the case of a narrow strip of plastic material if it is squeezed between two rough rigid plates which are kept parallel to each other. We now propose to find the velocity field in the case when the material behaves like a Bingham substance, as the flow starts after the yield stress is reached.

Writing U and V for $\dot{u}$ and $\dot{v}$, we reformulate the equations (8) in the case of a Bingham substance as follows:

(9)
$$s_x = \nu \left(1 - \frac{y^2}{a^2}\right)^{\frac{1}{2}} = 2\phi \frac{\partial U}{\partial x}$$

$$s_y = -\nu \left(1 - \frac{y^2}{a^2}\right)^{\frac{1}{2}} = 2\phi \frac{\partial V}{\partial y}$$

where ϕ is a function of the co-ordinates; the bulk viscosity term has been neglected. Further,

$$(10) \qquad \tau_{zy} = -\frac{\nu y}{a} = \mp \nu + \eta\left(\frac{\partial U}{\partial y} + \frac{\partial V}{\partial x}\right)$$

according to whether both y and $[(\partial U/\partial y) + (\partial V/\partial x)] \gtrless 0$. Here η is the plastic viscosity and ν, η are both taken to be positive.

Here we have retained the stress–strain relations for the normal stress deviators as in the case of plastic flow. Only for the tangential stress we make use of the Bingham law which may be taken as an extension of the law describing a Newtonian fluid with the addition of a yield stress. As we are only interested in the study of flow in a Bingham fluid arising out of shear stress, it may be assumed that the bulk viscosity is negligible in comparison with the shear viscosity. We have also retained Tresca's or von Mises's yield conditions for plastic flow since we do not have sufficient experimental evidence to indicate the contrary. The yield condition arises from simple common sense when the elastic limit is exceeded and the matter begins to flow or tends to flow. In the case of a Bingham substance where some kind of flow also exists, it seems natural to assume that the same condition will hold. Integrating equations (9) and (10) we have

$$V = -\frac{yV_0}{a},$$

$$(11) \qquad U = \frac{V_0 x}{a} + \frac{\nu}{a\eta}\left(ay - \frac{y^2}{2}\right) \qquad \text{if } y > 0,$$

$$U = \frac{V_0 x}{a} - \frac{\nu}{a\eta}\left(ay + \frac{y^2}{2}\right) \qquad \text{if } y < 0,$$

if the plates are approaching with speed V_0.

The flow lines for the above distribution of velocities turn out to be

$$(12) \qquad xy + \frac{S}{6}\left[3y^2 - \frac{y^3}{a}\right] = \text{const.} \qquad \text{for } y > 0,$$

$$xy + \frac{S}{6}\left[3y^2 + \frac{y^3}{a}\right] = \text{const.} \qquad \text{for } y < 0,$$

where, following Oldroyd (1947), we take S as a dimensionless parameter depending on the material and velocity of the boundary as well as the distance between the plates which is given by

$$(13) \qquad S = \frac{\nu a}{\eta V_0}.$$

It is to be noted that to have the boundary condition as specified in the problem, some type of arbitrary normal pressure should be applied in the boundary. This has been roughly shown in Fig. 1.
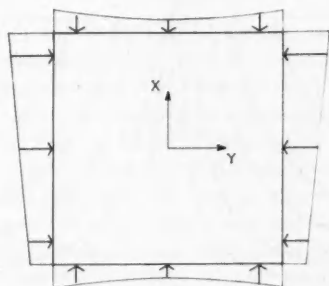
FIG. 1.

We now draw the lines of flow given in (12) with $S = 3$, and obtain the result shown in Fig. 2. In the same condition, the flow lines for a plastic material would be as shown in Fig. 3. Finally, for the sake of comparison, the lines of flow have also been drawn in the case of Newtonian fluid and are shown in Fig. 4.
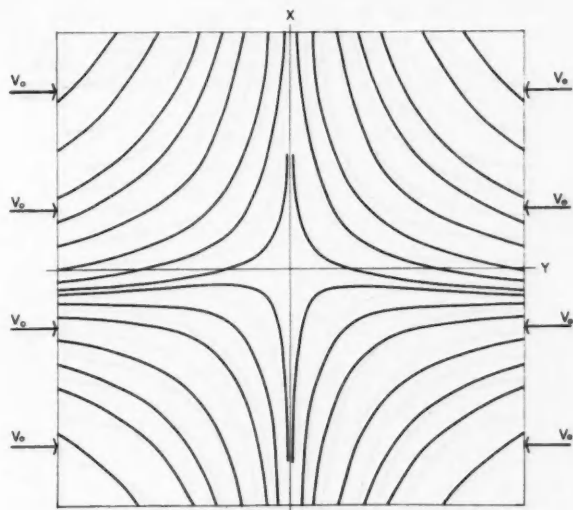
FIG. 2.   Bingham flow.
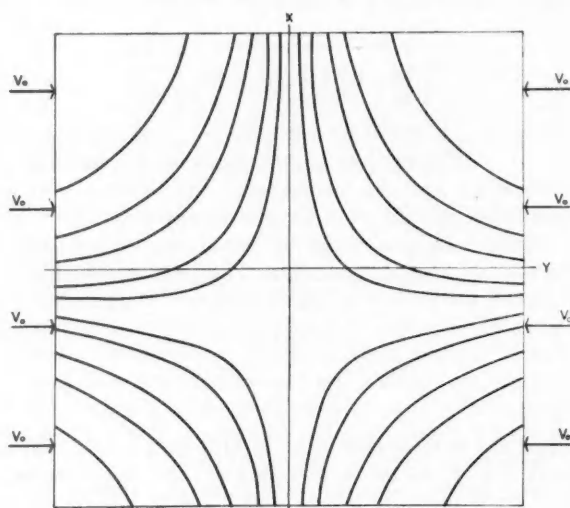
FIG. 3.   Plastic flow.
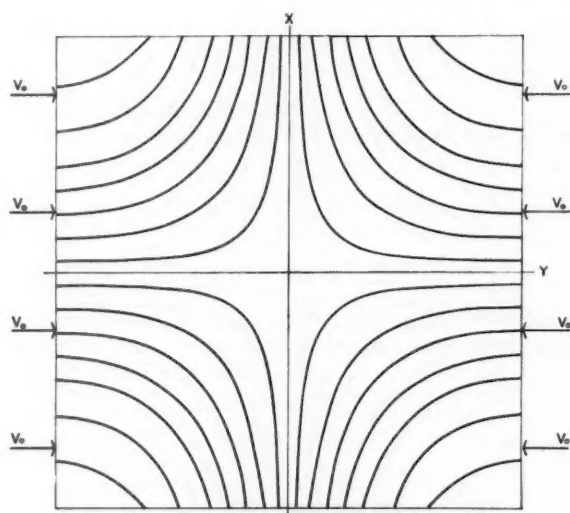
FIG. 4.   Viscous flow.

DISCUSSION

From the diagrams of the flow lines in various cases it is seen that the latter for a Bingham body differ very little from those in a plastic material. The same conclusion was arrived at by Oldroyd from his calculations of the flows within different types of cylinders. It seems that this small difference of flow patterns in the various types of rheological behavior is a general result. This follows from a consideration of the boundary and yield conditions in the case of plastic and Bingham flow. In the above calculations it turned out that these are the same in both these cases, and therefore the separation of flowing and nonflowing parts of such rheological bodies is also the same in the two cases. Equally, the boundary stresses are the same and the only difference lies in a slight change of the shape of the flow lines.

ACKNOWLEDGMENTS

REFERENCES

BUCKINGHAM, E.   1921.   Proc. Am. Soc. Testing Materials for 1921, 1154.
OLDROYD, J. G.   1947a.   Proc. Cambridge Phil. Soc. **43**, 395, 521.
———   1947b.   Proc. Cambridge Phil. Soc. **43**, 383.
———   1948.   Proc. Cambridge Phil. Soc. **44**, 200, 214.
REINER, M. and RIWLIN, R.   1927.   Kolloid-Z. **43**, 1.
REINER, M.   1926.   Kolloid-Z. **39**, 80.

A NOTE ON DIFFRACTION BY AN INFINITE SLIT[1]

R. F. MILLAR

ABSTRACT

The two-dimensional problem of diffraction of a plane wave by a narrow slit is considered. The assumed boundary values on the screen are the vanishing of either the total wave function or its normal derivative. In the former case, a differential–integral equation is obtained for the unknown function in the slit; in the latter, a pure integral equation is found. Solutions to these equations are given in the form of series in powers of ϵ (where ϵ/π is the ratio of slit width to wave-length), the coefficients of which depend on log ϵ. Expressions are found for the transmission coefficients as functions of ϵ and the angle of incidence; these are compared with previous determinations of other authors.

A brief outline is given for the treatment of diffraction of a cylindrical wave by the slit.

INTRODUCTION

The problem of diffraction of a plane wave by the infinite slit separating two half-planes has received considerable attention in recent years. The extreme cases in which the wavelength is much less than, and much greater than, the slit width have been treated in some detail. In the latter circumstances, with the exception of the work of Morse and Rubenstein (1938), Hoop (1955), and Nomura and Katsura (1957), little attention appears to have been given to other than normal incidence.

It is the purpose of this present note to extend previously given results for the long wavelength region to oblique incidence in two dimensions. The method employed is that of Bouwkamp (1953) and Müller and Westpfahl (1953). No new mathematical difficulties are encountered, although the algebraic manipulations are somewhat more tedious.

Expressions are obtained for the first few terms in the series for the transmission coefficients when the wave function or its normal derivative vanish on the screen. A comparison is made with the results of the Mathieu-function analysis of Morse and Rubenstein (1938), the calculations of Hoop (1955), and the short wavelength asymptotic solution (Millar 1958). The diffraction of a cylindrical wave by the slit is briefly considered.

FORMULATION OF THE PROBLEM

Let the diffracting screen occupy the plane $z = 0$ in a rectangular Cartesian co-ordinate system (x,y,z). The edges of the slit (of width $2a$) are parallel to the x-axis, with the origin at the center of the slit. The propagation vector of the plane wave $e^{ik(y \cos \alpha + z \sin \alpha)}$ (incident from $z \leqslant 0$) makes an angle α with the positive y-axis, and lies in the y–z plane; thus all field quantities are independent of x. The total wave function will be denoted by ϕ, the notation employed being essentially that of Bouwkamp (1953). The time-dependence factor $e^{-i\omega t}$ is suppressed throughout.

(i) $\phi = 0$ *on the Screen*

If $\phi = 0$ on the screen, then

$$\phi = \begin{cases} e^{ik(y\cos\alpha + z\sin\alpha)} - e^{ik(y\cos\alpha - z\sin\alpha)} + \phi_1(y,-z), & z \leqslant 0, \\ \phi_1(y,z), & z \geqslant 0. \end{cases}$$

The function $\phi_1(y,z)$, defined only for $z \geqslant 0$, is given by

$$(1) \qquad \phi_1(y,z) = -\frac{1}{2}i\frac{\partial}{\partial z}\int_{-a}^{a}\phi_1(y',0)H_0^{(1)}\{k\sqrt{[(y-y')^2+z^2]}\}\,dy'.$$

Since

$$\frac{\partial}{\partial z}\phi_1(y,z)\Big|_{z=0} = ik\sin\alpha\,e^{iky\cos\alpha}$$

when $-a \leqslant y \leqslant a$, the following differential–integral equation is obtained for the determination of $\phi_1(y',0)$:

$$(2) \qquad \left(k^2+\frac{d^2}{dy^2}\right)\int_{-a}^{a}\phi_1(y',0)H_0^{(1)}(k|y-y'|)\,dy' = 2k\sin\alpha\,e^{iky\cos\alpha}$$

when $-a \leqslant y \leqslant a$.

Equation (2) may be integrated, and the two arbitrary constants determined in terms of the unknown function by consideration of the integral, and its y-derivative, at $y = 0$. Since $\phi_1(-a,0) = \phi_1(a,0) = 0$, it is found that

$$(3) \quad \int_{-a}^{a}\phi_1(y',0)\left\{H_0^{(1)}(k|y-y'|) - \cos ky H_0^{(1)}(k|y'|) + \frac{\sin ky}{k}\frac{d}{dy'}H_0^{(1)}(k|y'|)\right\}dy'$$
$$= 2(e^{iky\cos\alpha} - \cos ky - i\cos\alpha\sin ky)/(k\sin\alpha),$$

where $-a \leqslant y \leqslant a$, and the integral involving the Hankel-function derivative is to be interpreted as a Cauchy principal value. When $\alpha = \frac{1}{2}\pi$, $\phi_1(y',0)$ is an even function of y', and eq. (3) reduces to the form obtained by Sommerfeld (1954).

(ii) $\partial\phi/\partial z = 0$ *on the Screen*

If $\partial\phi/\partial z = 0$ on the screen, then

$$\phi = \begin{cases} e^{ik(y\cos\alpha + z\sin\alpha)} + e^{ik(y\cos\alpha - z\sin\alpha)} - \phi_2(y,-z), & z \leqslant 0, \\ \phi_2(y,z), & z \geqslant 0, \end{cases}$$

where $\phi_2(y,z)$, defined only for $z \geqslant 0$, is determined by

$$(4) \qquad \phi_2(y,z) = -\frac{1}{2}i\int_{-a}^{a}\frac{\partial}{\partial z}\phi_2(y',0)H_0^{(1)}\{k\sqrt{[(y-y')^2+z^2]}\}\,dy'.$$

The equality of ϕ_2 and $e^{iky\cos\alpha}$ in the slit implies that

$$(5) \qquad \int_{-a}^{a}\frac{\partial}{\partial z'}\phi_2(y',0)H_0^{(1)}(k|y-y'|)dy' = 2i\,e^{iky\cos\alpha}$$

for $-a \leqslant y \leqslant a$.

SOLUTIONS OF THE INTEGRAL EQUATIONS FOR $ka \ll 1$

Because the determination of $(\partial/\partial z')\phi_2(y',0)$ is rather more readily accomplished, eq. (5) will be considered first. The substitutions $y = a \cos u$, $y' = a \cos v$, $\epsilon = ka$ transform eq. (5) into

$$(6) \qquad \int_0^\pi F_2(v)\, H_0^{(1)}(\epsilon|\cos u - \cos v|)\, dv = 2i\, e^{i\epsilon \cos \alpha \cos u}$$

where

$$(7) \qquad F_2(v) = a \sin v \frac{\partial}{\partial z}\, \phi_2(a \cos v, z)\Big|_{z=0},$$

and $0 \leqslant u \leqslant \pi$.

For small ϵ, $H_0^{(1)}(\epsilon|\cos u - \cos v|)$ may be written as

$$(8) \qquad H_0^{(1)}(\epsilon|\cos u - \cos v|) = \frac{2i}{\pi}\,(\psi_0 + \psi_1 \epsilon^2 + \psi_2 \epsilon^4 + \psi_3 \epsilon^6 + \dots)$$

where

$$(9) \quad \begin{cases} \psi_0 = p + \log|2(\cos u - \cos v)|, \\ \psi_n = \dfrac{(-1)^n}{2^{2n}(n!)^2}\,(\cos u - \cos v)^{2n}\,[p - 1 - \tfrac{1}{2} \dots - \dfrac{1}{n} + \log|2(\cos u - \cos v)|] \end{cases}$$

for $n \geqslant 1$,

$$(10) \qquad p = \log \tfrac{1}{4}\gamma\epsilon - \tfrac{1}{2}\pi i,$$

and $\log \gamma = 0.5772157\dots$ is Euler's constant.

A solution is assumed of the form

$$(11) \qquad F_2(v) = f_0 + f_1\epsilon + f_2\epsilon^2 + \dots,$$

where the f_n depend only on v, α, and $\log \epsilon$. (For normal incidence, $f_{2n+1} = 0$.) If the above expansions are inserted into eq. (6), the equating of like powers of ϵ leads to the following infinite set of integral equations:

$$(12) \quad \begin{cases} \displaystyle\int_0^\pi f_0\psi_0\, dv = \pi, \\[2ex] \displaystyle\int_0^\pi f_1\psi_0\, dv = i\pi \cos \alpha \cos u, \\[2ex] \displaystyle\int_0^\pi f_2\psi_0\, dv = -\tfrac{1}{2}\pi \cos^2 \alpha \cos^2 u - \int_0^\pi f_0\psi_1\, dv, \\[2ex] \displaystyle\int_0^\pi f_3\psi_0\, dv = -\frac{i\pi}{6} \cos^3 \alpha \cos^3 u - \int_0^\pi f_1\psi_1\, dv, \\[2ex] \displaystyle\int_0^\pi f_4\psi_0\, dv = \frac{\pi}{24} \cos^4 \alpha \cos^4 u - \int_0^\pi f_2\psi_1\, dv - \int_0^\pi f_0\psi_2\, dv, \\[2ex] \displaystyle\int_0^\pi f_5\psi_0\, dv = \frac{i\pi}{120} \cos^5 \alpha \cos^5 u - \int_0^\pi f_3\psi_1\, dv - \int_0^\pi f_1\psi_2\, dv, \\[2ex] \displaystyle\int_0^\pi f_6\psi_0\, dv = -\frac{\pi}{720} \cos^6 \alpha \cos^6 u - \int_0^\pi f_4\psi_1\, dv - \int_0^\pi f_2\psi_2\, dv - \int_0^\pi f_0\psi_3\, dv. \\ \vdots \qquad\qquad \vdots \qquad\qquad \vdots \qquad\qquad \vdots \end{cases}$$

If it is now assumed that

(13)
$$\begin{cases} f_{2n} = \sum_{\nu=0}^{n} b_{2n,\nu} \cos 2\nu v, \\[2mm] f_{2n+1} = \sum_{\nu=0}^{n} b_{2n+1,\nu} \cos (2\nu+1) v, \qquad n = 0, 1, 2, \ldots, \end{cases}$$

with $b_{n,m}$ independent of v, then, since ψ_0 possesses the expansion

(14)
$$\psi_0 = p - 2 \sum_{m=1}^{\infty} \frac{\cos mu \cos mv}{m},$$

it is found, after the evaluation of certain integrals (see Appendix), that

(15)
$$\begin{cases}
b_{0,0} = \frac{1}{p}, \qquad b_{1,0} = -i \cos \alpha, \qquad b_{2,0} = \frac{\sin^2 \alpha}{4p}, \\[3mm]
b_{2,1} = \frac{1}{2} \cos^2 \alpha - \frac{1}{4}\left(1+\frac{1}{2p}\right), \qquad b_{3,0} = \frac{i}{8} \cos^3 \alpha - \frac{i}{4}(p+\tfrac{1}{4}) \cos \alpha, \\[3mm]
b_{3,1} = \frac{i}{8} \cos^3 \alpha - \frac{i}{16} \cos \alpha, \\[3mm]
b_{4,0} = \frac{\cos^4 \alpha}{64p} + \left(1-\frac{3}{2p}\right)\frac{\cos^2 \alpha}{32} + \frac{1}{128}\left(\frac{1}{p^2}+\frac{3}{2p}-2\right), \\[3mm]
b_{4,1} = -\frac{\cos^4 \alpha}{24} + \left(\frac{1}{3}+\frac{1}{2p}\right)\frac{\cos^2 \alpha}{16} + \frac{1}{16}\left(\frac{1}{3}-\frac{1}{2p}\right), \\[3mm]
b_{4,2} = -\frac{\cos^4 \alpha}{48} + \frac{\cos^2 \alpha}{96} + \frac{1}{384}\left(1+\frac{3}{4p}\right), \\[3mm]
b_{5,0} = -\frac{i \cos^5 \alpha}{192} + \frac{i}{32}(p+\tfrac{1}{3}) \cos^3 \alpha - \frac{i}{16}\left(p^2-\frac{1}{4}p+\frac{13}{48}\right) \cos \alpha, \\[3mm]
b_{5,1} = -\frac{i \cos^5 \alpha}{128} + \frac{i \cos^3 \alpha}{256} + \frac{i}{128}(p+\tfrac{3}{8}) \cos \alpha, \\[3mm]
b_{5,2} = -\frac{i \cos^5 \alpha}{384} + \frac{i \cos^3 \alpha}{768} + \frac{i \cos \alpha}{3072}, \\[3mm]
b_{6,0} = -\frac{\cos^6 \alpha}{2304p} - \left(1-\frac{1}{p}\right)\frac{\cos^4 \alpha}{384} + \left(1+\frac{3}{4p}-\frac{3}{2p^2}\right)\frac{\cos^2 \alpha}{768} \\[2mm]
\qquad\qquad\qquad\qquad\qquad + \frac{1}{768}\left(1-\frac{29}{12p}+\frac{3}{2p^2}\right), \\[3mm]
b_{6,1} = \frac{\cos^6 \alpha}{768} - \left(\frac{1}{p}+\frac{1}{3}\right)\frac{\cos^4 \alpha}{512} + \left(p-\frac{49}{24}+\frac{3}{2p}\right)\frac{\cos^2 \alpha}{256} \\[2mm]
\qquad\qquad\qquad\qquad\qquad - \frac{1}{512}\left(p-\frac{13}{8}+\frac{5}{16p}\right), \\[3mm]
b_{6,2} = \frac{\cos^6 \alpha}{960} - \frac{\cos^4 \alpha}{1920} - \left(\frac{1}{p}+\frac{4}{15}\right)\frac{\cos^2 \alpha}{2048} + \frac{1}{2048}\left(\frac{1}{p}-\frac{4}{5}\right), \\[3mm]
b_{6,3} = \frac{\cos^6 \alpha}{3840} - \frac{\cos^4 \alpha}{7680} - \frac{\cos^2 \alpha}{30720} - \frac{1}{73728p} - \frac{1}{61440}.
\end{cases}$$

Equation (2) (or eq. (3)) for ϕ_1 may be solved in a similar manner. If

$$(16) \qquad \epsilon F_1(v) = \phi_1(a \cos v, 0),$$

and a solution is assumed of the form

$$(17) \qquad F_1(v) = g_0 + g_1\epsilon + g_2\epsilon^2 + \ldots,$$

where

$$(18) \qquad \begin{cases} g_{2n} = \displaystyle\sum_{\nu=0}^{n} a_{2n,\nu} \sin (2\nu+1)v \\[2mm] g_{2n+1} = \displaystyle\sum_{\nu=0}^{n} a_{2n+1,\nu} \sin (2\nu+2)v, \qquad n = 0, 1, 2 \ldots, \end{cases}$$

it is found that

$$(19) \quad \begin{cases}
a_{0,0} = -i \sin \alpha, \qquad a_{1,0} = \tfrac{1}{4} \sin \alpha \cos \alpha, \\[2mm]
a_{2,0} = \dfrac{i}{4} \sin \alpha (p - \tfrac{3}{4} + \tfrac{1}{2} \cos^2 \alpha), \\[2mm]
a_{2,1} = \dfrac{i \sin \alpha}{24} (\tfrac{1}{2} + \cos^2 \alpha), \qquad a_{3,0} = \dfrac{\sin^3 \alpha \cos \alpha}{48}, \\[2mm]
a_{3,1} = -\dfrac{\sin \alpha \cos \alpha}{192} (\tfrac{1}{2} + \cos^2 \alpha), \\[2mm]
a_{4,0} = -\dfrac{i \sin \alpha}{16} \left[p^2 - p\left(\dfrac{5}{4} - \tfrac{1}{2} \cos^2 \alpha\right) + \dfrac{7}{16} - \dfrac{\cos^2 \alpha}{3} + \dfrac{\cos^4 \alpha}{12} \right], \\[2mm]
a_{4,1} = -\dfrac{i \sin \alpha}{128} \left(p - \dfrac{5}{8} + \dfrac{\cos^2 \alpha}{6} + \dfrac{\cos^4 \alpha}{3} \right), \\[2mm]
a_{4,2} = -\dfrac{i \sin \alpha}{5120} \left(1 + \dfrac{4}{3} \cos^2 \alpha + \dfrac{8}{3} \cos^4 \alpha \right), \\[2mm]
a_{5,0} = -\dfrac{\sin \alpha \cos \alpha}{512} \left(p - \dfrac{9}{8} + \dfrac{5}{6} \cos^2 \alpha - \dfrac{1}{3} \cos^4 \alpha \right), \\[2mm]
a_{5,1} = -\dfrac{\sin \alpha \cos \alpha}{7680} (3 - \cos^2 \alpha - 2 \cos^4 \alpha), \\[2mm]
a_{5,2} = \dfrac{\sin \alpha \cos \alpha}{23040} (\tfrac{3}{8} + \tfrac{1}{2} \cos^2 \alpha + \cos^4 \alpha), \\[2mm]
a_{6,0} = \dfrac{i \sin \alpha}{256} \left[4p^3 - 7p^2 + \dfrac{109}{24} p - \dfrac{607}{576} + \left(2p^2 - \dfrac{9}{4} p + \dfrac{23}{32}\right) \cos^2 \alpha \right. \\[2mm]
\qquad\qquad\qquad \left. + \left(\dfrac{p}{3} - \dfrac{19}{120}\right) \cos^4 \alpha + \dfrac{\cos^6 \alpha}{36} \right], \\[2mm]
a_{6,1} = \dfrac{i \sin \alpha}{512} \left[p^2 - \dfrac{9}{8} p + \dfrac{29}{96} + \left(\dfrac{p}{2} - \dfrac{19}{80}\right) \cos^2 \alpha + \dfrac{\cos^4 \alpha}{60} + \dfrac{\cos^6 \alpha}{30} \right], \\[2mm]
a_{6,2} = \dfrac{i \sin \alpha}{61440} \left(5p - \dfrac{35}{12} + \dfrac{1}{2} \cos^2 \alpha + \dfrac{2}{3} \cos^4 \alpha + \dfrac{4}{3} \cos^6 \alpha \right), \\[2mm]
a_{6,3} = \dfrac{i \sin \alpha}{322560} \left(\dfrac{5}{16} + \dfrac{3}{8} \cos^2 \alpha + \dfrac{1}{2} \cos^4 \alpha + \cos^6 \alpha \right).
\end{cases}$$

FAR-FIELDS AND TRANSMISSION COEFFICIENTS

In the following, attention will be confined to the far-field region. However, it may be noted in passing that, for $\sqrt{(y^2+z^2)} > a$, it is legitimate to expand the Hankel functions appearing in eqs. (1) and (4) in powers of ϵ, and so representations of ϕ_1, ϕ_2 in this region may be found.

Let a point in the far-field region be specified by polar co-ordinates (ρ,θ), where θ is measured from the positive y-axis. Then, according to eq. (1),

$$(20) \quad \phi_1(y,z) \sim \frac{e^{-\frac{1}{4}\pi i}}{\sqrt{(2\pi)}} \frac{e^{ik\rho}}{\sqrt{(k\rho)}} \epsilon \sin\theta \int_0^\pi \sin v \; \phi_1(a\cos v,0) e^{-i\epsilon \cos\theta \cos v} \, dv,$$

or, in terms of the quantities introduced in eqs. (16), (17), and (18),

$$(21) \quad \phi_1(y,z) \sim \left(\frac{2\pi}{k\rho}\right)^{\frac{1}{2}} e^{ik\rho+\frac{1}{4}\pi i} \sum_{n=0}^\infty T_{2n+1}^{(1)}(\alpha,\theta;p)\epsilon^{2n+2},$$

where

$$(22) \quad \begin{aligned}
T_1^{(1)} &= -\frac{i}{4}\, a_{0,0} \sin\theta, \\[4pt]
T_3^{(1)} &= \frac{\sin\theta}{4}\left(\frac{i}{8}\, a_{0,0}\cos^2\theta - \frac{a_{1,0}}{2}\cos\theta - ia_{2,0}\right), \\[4pt]
T_5^{(1)} &= -\frac{\sin\theta}{4}\left[\frac{i}{192}\, a_{0,0}\cos^4\theta - \frac{a_{1,0}}{24}\cos^3\theta - \frac{i}{8}\,(a_{2,0}+a_{2,1})\cos^2\theta \right. \\
&\qquad\qquad\qquad\qquad\qquad\qquad \left. +\frac{a_{3,0}}{2}\cos\theta + ia_{4,0}\right], \\[4pt]
T_7^{(1)} &= \frac{\sin\theta}{4}\left[\frac{i}{9216}\, a_{0,0}\cos^6\theta - \frac{a_{1,0}}{768}\cos^5\theta \right. \\
&\qquad -\frac{i}{64}\left(\frac{a_{2,0}}{3}+\frac{a_{2,1}}{2}\right)\cos^4\theta + \frac{1}{24}\left(a_{3,0}+\frac{a_{3,1}}{2}\right)\cos^3\theta \\
&\qquad \left. +\frac{i}{8}\,(a_{4,0}+a_{4,1})\cos^2\theta - \frac{a_{5,0}}{2}\cos\theta - ia_{6,0}\right].
\end{aligned}$$

The plane-wave transmission coefficient $t^{(1)}(\alpha)$, defined to be the ratio of the energy transmitted through the slit per unit area to the energy flux in the incident field per unit area normal to the direction of propagation, is given by

$$(23) \quad t^{(1)}(\alpha) = -\frac{\pi}{\epsilon}\,\mathrm{Im}\left[\sum_{n=0}^\infty T_{2n+1}^{(1)}(\alpha,\alpha;p)\epsilon^{2n+2}\right]$$

so

$$(24) \quad t^{(1)}(\alpha) = \frac{\pi^2\epsilon^3}{32}\sin^2\alpha\left\{1+\frac{5}{16}\epsilon^2\left(1-\frac{8}{5}\delta-\frac{4}{5}\cos^2\alpha\right)+\frac{\epsilon^4}{8}\left[\frac{5}{24}\cos^4\alpha\right.\right.$$
$$\left.\left. -\left(\frac{17}{32}-\delta\right)\cos^2\alpha+\frac{1}{192}\left(109-336\delta+288\delta^2-24\pi^2\right)\right]+\ldots\right\}$$

where $\delta = \log\frac{1}{4}\gamma\epsilon$.

NOTE: The transmission coefficient may also be obtained by a direct calculation of the energy flow across a semicircular cylindrical surface in the far-field region. Here ϕ_1 is of order ϵ^2 as ϵ tends to zero, and this method of calculation, together with equations (22), will yield one more term in the series for $t^{(1)}(\alpha)$ than appears in eq. (24).

In a similar manner it may be shown that

$$(25) \qquad \phi_2(y,z) \sim \left(\frac{2\pi}{k\rho}\right)^{\frac{1}{2}} e^{ik\rho+\frac{1}{4}\pi i} \sum_{n=0}^{\infty} T_{2n}^{(2)}(\alpha,\theta;p)\epsilon^{2n},$$

where

$$(26) \quad \begin{vmatrix} T_0^{(2)} = -\frac{1}{2} b_{0,0}, \\[2mm] T_2^{(2)} = \frac{b_{0,0}}{8} \cos^2\theta + \frac{i}{4} b_{1,0} \cos\theta - \frac{1}{2} b_{2,0}, \\[2mm] T_4^{(2)} = -\frac{b_{0,0}}{128} \cos^4\theta - \frac{i}{32} b_{1,0} \cos^3\theta + (b_{2,0}+\frac{1}{2} b_{2,1}) \frac{\cos^2\theta}{8} \\[4mm] \qquad\qquad\qquad\qquad\qquad\qquad +\frac{i}{4} b_{3,0}\cos\theta - \frac{1}{2} b_{4,0}, \\[4mm] T_6^{(2)} = \frac{b_{0,0}}{4608} \cos^6\theta + \frac{ib_{1,0}}{768} \cos^5\theta - \left(\frac{3}{2} b_{2,0}+b_{2,1}\right) \frac{\cos^4\theta}{192} \\[4mm] \qquad -i(3b_{3,0}+b_{3,1}) \frac{\cos^3\theta}{96} + (2b_{4,0}+b_{4,1}) \frac{\cos^2\theta}{16} + \frac{i}{4} b_{5,0}\cos\theta - \frac{1}{2} b_{6,0}. \end{vmatrix}$$

The transmission coefficient, $t^{(2)}(\alpha)$, is given by

$$(27) \qquad t^{(2)}(\alpha) = -\frac{\pi}{\epsilon} \operatorname{Im}\left[\sum_{n=0}^{\infty} T_{2n}^{(2)}(\alpha,\alpha;p)\epsilon^{2n} \right],$$

so

$$(28) \quad t^{(2)}(\alpha) = \frac{\pi^2}{\epsilon q}\left\{ 1 - \frac{\epsilon^2}{4} \cos 2\alpha + \frac{3}{256} \epsilon^4 \left[1 + \frac{16}{3}\frac{\delta}{q} + \frac{8}{3}(q-3)\cos^2\alpha + 8\cos^4\alpha \right] \right.$$
$$\left. -\frac{\epsilon^6}{64}\left[\frac{29}{144} - \frac{\delta}{q} + \left\{\frac{q-1}{8} - \left(q-\frac{2}{q}\right)\delta\right\}\cos^2\alpha + \left(q-\frac{5}{3}\right)\frac{\cos^4\alpha}{2} + \frac{5}{9}\cos^6\alpha \right] + \ldots \right\}$$

with $q = \pi^2 + 4\delta^2$.

The first two terms of eq. (24), and the first three terms of eq. (28), have been found, for $\alpha = \frac{1}{2}\pi$, by Bouwkamp (1953), and Müller and Westpfahl (1953); see also Bouwkamp (1954). Nomura and Katsura (1957) have found, for normal incidence, the first two terms of eq. (24), and the first term of eq. (28). Hoop (1955) has calculated $t^{(1)}(\alpha)$ to the same order in ϵ as eq. (24), and $t^{(2)}(\alpha)$ up to and including terms of relative order ϵ^4.

The variation of the transmission coefficients, $t^{(1)}(\alpha)$ and $t^{(2)}(\alpha)$, with α and ka is exhibited in Figs. 1 and 2. For $ka \leqslant 1$, the curves are determined by eqs. (24) and (28); for larger ka, the asymptotic values (Millar 1958) are plotted. As a standard of comparison, the curves of Morse and Rubenstein (1938) for $\alpha = 0°$ and $90°$ have been included.

It is apparent that eq. (24) for $t^{(1)}(\alpha)$ is a good approximation for $ka < 1$; agreement is less satisfactory in the case of $t^{(2)}(\alpha)$. For fixed ka, the accuracy of approximation in both cases appears to decrease as α decreases from $90°$
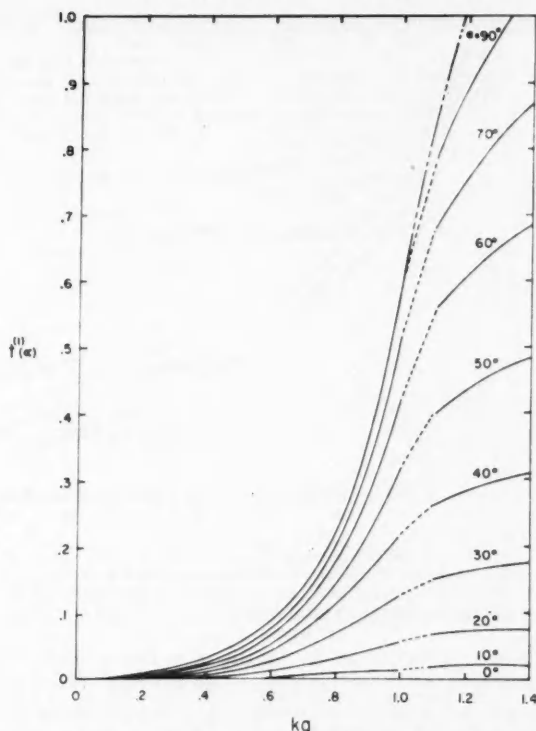
FIG. 1. Transmission coefficient $t^{(1)}(\alpha)$ as a function of the angle of incidence, α, and ka.
————— Present theory for small ka; asymptotic theory for larger ka.
— — — — Theory of Morse and Rubenstein for $\alpha = 90°$.

and, in the so-called "resonance region", near $ka = 1$, neither the present nor the asymptotic method appears to be particularly well suited to the analysis of the problem.

The question of the convergence of series such as those which appear in eqs. (24) and (28) is still a matter for conjecture. Because of the presence of log ka in the coefficients of powers of ka, it is possible that the expressions given above are only asymptotic as $ka \to 0$.

DIFFRACTION OF A CYLINDRICAL WAVE

Diffraction of a cylindrical wave by the slit may be treated in the same manner as the case of an incident plane wave. Suppose a line source whose location is specified by polar co-ordinates (r,ϕ) radiates, from $z < 0$, a field $H_0^{(1)}(kR)$, where R is the distance from the source. Then the equations obtained are once again (2) and (5), with the right-hand sides replaced by

$$2i \frac{\partial}{\partial z} H_0^{(1)}(kR) \bigg|_{z=0} \qquad \text{and} \qquad 2i H_0^{(1)}(kR) \bigg|_{z=0}$$
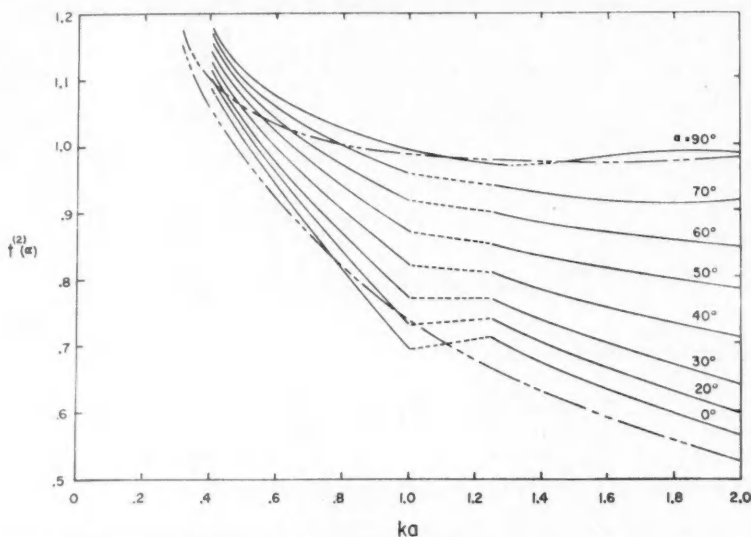
FIG. 2. Transmission coefficient $t^{(2)}(\alpha)$ as a function of the angle of incidence, α, and ka.
——————   Present theory for small ka; asymptotic theory for larger ka.
— – – –   Theory of Morse and Rubenstein for $\alpha = 0°$ and $\alpha = 90°$.

respectively. These functions may be rewritten as $2ikr \sin \phi \, H_1^{(1)}(kS)/S$ and $2iH_0^{(1)}(kS)$, with $S^2 = r^2 + y^2 - 2ry \cos \phi$ and $-a \leqslant y \leqslant a$. If $r > a$, it is permissible to expand each function as a convergent power series in $\epsilon \, (= ka)$, the coefficients of which depend on kr, $\cos \phi$, $\cos u(= y/a)$, and the analysis proceeds as before. For example,

$$H_0^{(1)}(kS) = H_0^{(1)}(kr) + \cos u \cos \phi \, H_1^{(1)}(kr)\epsilon + \dots$$

and, if $kr \gg 1$,

$$H_0^{(1)}(kS) \sim \left(\frac{2}{\pi kr}\right)^{\frac{1}{2}} e^{ikr - \frac{1}{4}\pi i}(1 - i \cos u \cos \phi \cdot \epsilon + \dots) .$$

If

$$2i \lim_{kr \to \infty} \left(\frac{\pi kr}{2}\right)^{\frac{1}{2}} e^{-ikr + \frac{1}{4}\pi i} H_0^{(1)}(kS)$$

is formed, and ϕ is equated to $\pi + \alpha$, then the power-series expansion of the right-hand side of eq. (5) is obtained.

ACKNOWLEDGMENT

REFERENCES

BOUWKAMP, C. J. 1953. Diffraction theory, a critique of some recent developments. New York University Mathematics Research Group, Research Report No. EM-50.
——————   1954. Repts. Progr. in Phys. **17**, 35.

HOOP, A. T. DE. 1955. Proc. Koninkl. Ned. Akad. Wetenschap. B, **58**, 401.
MILLAR, R. F. 1958. Proc. Cambridge Phil. Soc. **54**, 479.
MORSE, P. M. and RUBENSTEIN, P. J. 1938. Phys. Rev. **54**, 895.
MÜLLER, R. and WESTPFAHL, K. 1953. Z. Physik, **134**, 245.
NOMURA, Y. and KATSURA, S. 1957. J. Phys. Soc. Japan, **12**, 190.
SOMMERFELD, A. 1954. Optics: Lectures on theoretical physics, Vol. IV (Academic Press, Inc., New York), p. 276.

APPENDIX

EVALUATION OF CERTAIN INTEGRALS

$$\int_0^\pi \psi_0 \, dv = p\pi,$$

$$\int_0^\pi \psi_0 \cos mv \, dv = -\pi \cos mu / m \qquad\qquad m \geqslant 1,$$

$$\int_0^\pi \psi_1 \, dv = -\tfrac{1}{8}\pi[2p + (p + \tfrac{1}{2})\cos 2u],$$

$$\int_0^\pi \psi_1 \cos v \, dv = \tfrac{1}{4}\pi[(p + \tfrac{1}{4})\cos u + \tfrac{1}{12}\cos 3u],$$

$$\int_0^\pi \psi_1 \cos 2v \, dv = -\frac{1}{16}\pi\left[p + \frac{1}{2} + \frac{2}{3}\cos 2u - \tfrac{1}{12}\cos 4u\right],$$

$$\int_0^\pi \psi_1 \cos mv \, dv = \frac{1}{8}\pi\left[\left(\frac{1}{2m} - \frac{1}{m+1} + \frac{1}{2m+4}\right)\cos (m+2)u\right.$$
$$\left. + \left(\frac{2}{m} - \frac{1}{m+1} - \frac{1}{m-1}\right)\cos mu + \left(\frac{1}{2m} - \frac{1}{m-1} + \frac{1}{2m-4}\right)\cos (m-2)u\right] \quad m \geqslant 3,$$

$$\int_0^\pi \psi_2 \, dv = -\frac{\pi}{256}\left[3 - 9p + \left(\frac{4}{3} - 8p\right)\cos 2u - \left(\frac{7}{24} + \frac{p}{2}\right)\cos 4u\right],$$

$$\int_0^\pi \psi_2 \cos v \, dv = \frac{\pi}{256}\left[(3 - 12p)\cos u - \left(\frac{5}{12} + 2p\right)\cos 3u - \frac{1}{20}\cos 5u\right],$$

$$\int_0^\pi \psi_2 \cos 2v \, dv = -\frac{\pi}{256}\left[\frac{2}{3} - 4p - (\tfrac{3}{8} + 3p)\cos 2u - \frac{1}{5}\cos 4u + \frac{1}{120}\cos 6u\right],$$

$$\int_0^\pi \psi_2 \cos 3v \, dv = -\frac{\pi}{256}\left[\left(\frac{5}{12} + 2p\right)\cos u + \frac{3}{10}\cos 3u - \frac{1}{30}\cos 5u + \frac{1}{420}\cos 7u\right],$$

$$\int_0^\pi \psi_2 \cos 4v \, dv = \frac{\pi}{1280}\left[\frac{35}{48} + \cos 2u - \frac{1}{4}\cos 4u + \frac{1}{21}\cos 6u - \frac{1}{224}\cos 8u\right],$$

$$\int_0^\pi \psi_3 \, dv = \frac{\pi}{18432}\left[30 - 50p + \left(\frac{465}{16} - \frac{225}{4}p\right)\cos 2u + \left(\frac{39}{20} - 9p\right)\cos 4u\right.$$
$$\left. - \left(\frac{37}{240} + \frac{p}{4}\right)\cos 6u\right],$$

$$\int_0^\pi \psi_3 \cos 2v \, dv = \frac{\pi}{36864}\left[\frac{465}{16} - \frac{225}{4}p + \left(\frac{49}{2} - 60p\right)\cos 2u - \left(\frac{3}{8} + \frac{15}{2}p\right)\cos 4u\right.$$
$$\left. - \frac{3}{14}\cos 6u + \frac{1}{224}\cos 8u\right].$$

THE RADAR CROSS SECTION OF A SEMI-INFINITE BODY[1]

H. BRYSK[2]

ABSTRACT

The concept of cross section as applied to a semi-infinite scattering body seems to require some clarification. The need for careful formulation of the problem arises because of the simultaneous occurrence of two characteristic lengths tending to infinity: the range from the radar to the target, and the size of the target. The infinite range assumption in the definition of the cross section allows the incident wave to be approximated as a plane wave in the case of a finite scatterer. For a semi-infinite body, it is customary to retain the plane-wave incidence, and introduce *ad hoc* arguments to dispose of the awkwardness due to the infinite extent of the scatterer. A return to the basic definition of a cross section, and examination of its motivation, lead here to an unequivocal formulation for the cross section of a semi-infinite body. Its consequences are pursued in the physical optics approximation. In particular, the nose-on backscattering from a body of revolution is exhibited, and results are computed for the paraboloid and the cone (which turn out to agree with the traditional ones). The broadside backscattering from a cylinder is also calculated, and the difference in this case between monostatic backscattering and the return in the backward direction from an incident plane wave is discussed.

I. CONCEPT

The return backscattered from a radar target is expressed formally by the range equation

$$(1) \qquad P_r/P_t = G_r G_t \lambda^2 \sigma/(4\pi)^3 R^4$$

where P_r = power scattered into the receiver,
P_t = power transmitted,
$G_{r,t}$ = gain of receiver, transmitter,
λ = wavelength,
R = range (minimum distance from radar to target),
σ = radar cross section.

(The discussion will be restricted to monostatic operation in order to simplify the mathematical manipulations; the generalization to bistatic operation does not involve any additional conceptual problems.) Equation 1 can be applied with great generality provided that the possibility is admitted that the gains and the cross section vary with the range. It is most commonly used to describe scattering by a finite target at very long range, in which case the gains and the cross section become range independent and the factors in equation 1 separate naturally as distinct physical entities. The concept of a cross section is usually referred to the long range limit. From the above definition, it then follows that the cross section is

(2)
$$\sigma = \lim_{R \to \infty} 4\pi R^2 |\mathbf{S}^s / \mathbf{S}^i|$$

where

$\mathbf{S}^{s,i}$ = scattered, incident Poynting vector

or, using the relationship between the electric and magnetic field vectors in free space,

(3)
$$\sigma = \lim_{R \to \infty} 4\pi R^2 |\mathbf{H}^s / \mathbf{H}^i|^2$$

where

$\mathbf{H}^{s,i}$ = scattered, incident magnetic field.

It is customary to assume that the incident field is a plane wave; this amounts to removing the source to infinity. In fact, electromagnetic boundary-value problems are usually formulated for an incident plane wave. Instead of the limit process indicated by equation 3, what is effectively done is to go separately to the limit $R \to \infty$ for one factor in the expression (namely $|\mathbf{H}^i|^2$), and later carry out the limit for the remaining factors, as if there were two distinct and independent limits involved. This procedure simplifies the mathematical manipulations, and it can be justified provided that the range is sufficiently long compared with all the characteristic lengths of the problem (wavelength, maximum linear dimension of target, ratio of projection area of target to wavelength).

The above approximation breaks down when one dimension of the body has to be considered infinite. This need not impair the usefulness of the cross-section concept, although it does necessitate greater care in setting up the computation. The usual practice in this situation (for example, Kerr 1951) is to retain the plane-wave incidence, and to formally cut up the body into the analogue of Fresnel zones, each section then being considered as a finite body. A qualitative argument is then made for ignoring all but the first section (on the basis of approximate destructive interference from neighboring zones) and for discarding most of the contribution of the first zone (ascribing to end effects those terms that depend on a dimension of the zone and claiming that they are cancelled by corresponding end terms from the next zone). This approach has some intuitive appeal, but the reasoning is a bit inelegant.

In reality there is no such thing as a semi-infinite body. The problem can be clarified by going back to the physical situation that has impelled the imputation of an infinite dimension to the body. The motivation is that the body does not terminate sharply (for example, it has a jagged edge, or a blurred ending such as an ionized region) and the boundary surface is mathematically extended to infinity to avoid undesired end effects that would arise from a spuriously clean edge. The source of radiation and the observer have actually a well-defined position. With respect to this position, the boundary extended to infinity is receding from the radar. It is in the spirit of the infinite body

approximation that this distance variation be taken into account, in the same manner for the incident wave as for the scattered wave. Removing the plane-wave approximation for the incident wave necessitates the stipulation of the antenna pattern—which is reasonable. Thus, the limit process should be handled in a single step as per equation 3, with the incident field represented not by a plane wave but by a spherical wave with a specified angular variation of amplitude. The $R \to \infty$ limit can then be consistently attained for a semi-infinite body, as it need only mean that the range is much longer than the wavelength.

Formally, the problem is now set up in the standard way (for example, Kerr 1951) except for omission of the plane-wave approximation. The field scattered by a perfectly conducting body is given rigorously by

$$(4) \qquad \mathbf{H}^s = -(1/4\pi) \int_S (\hat{n} \times \mathbf{H}) \times \nabla (r^{-1} e^{-ikr}) dS$$

where $\hat{n}$ = unit vector normal to the surface S,
          $\mathbf{H}$ = total magnetic field at the surface,
          r = range from the radar to a point on the surface,
          k = $2\pi/\lambda$.

If $kr \gg 1$ for all r on S,

$$(5) \qquad \nabla(r^{-1} e^{-ikr}) \approx -\hat{r}\, ikr^{-1}\, e^{-ikr}$$

so that

$$(6) \qquad \mathbf{H}^s = -(ik/4\pi) \int_S \hat{r} \times (\hat{n} \times \mathbf{H})\, r^{-1}\, e^{-ikr}\, dS.$$

Equation 6 is the starting point for the physical optics approximation. In the latter, the field at an illuminated point on the surface is set equal to twice the tangential component of the incident field

$$(7) \qquad \mathbf{H} = 2[\mathbf{H}^i - (\mathbf{H}^i \cdot \hat{n})\, \hat{n}]$$

(as would be the case if the body were replaced by its tangent plane at the point), so that

$$(8) \qquad \hat{r} \times (\hat{n} \times \mathbf{H}) = -2\mathbf{H}^i\, (\hat{r} \cdot \hat{n}),$$

while the field at a surface point in the shadow is set equal to zero. The departure from the usual formulation comes in not proceeding now to the further approximations that r^{-1} be factored out of the integral in equation 6 and that $\mathbf{H}^i$ be taken as a plane wave. Instead, $\mathbf{H}^i$ will be considered as a spherical wave with a specified angular amplitude diagram. As an example, the field due to an electric dipole oriented along the x axis will be used in the illustrations below:

$$(9) \qquad \mathbf{H}^i = H_0\, (\hat{r} \times \hat{x})\, r^{-1}\, e^{-ikr}$$

leading to

$$(10) \qquad \mathbf{H}^s = (ik/2\pi)\, H_0 \int_S (\hat{r} \times \hat{x})\, (\hat{r} \cdot \hat{n})\, r^{-2}\, e^{-2ikr}\, dS.$$

II. BODIES OF REVOLUTION NOSE-ON

As the most straightforward example of scattering from a semi-infinite body, these ideas will now be applied to backscattering from a body of revolution with the dipole source located on the axis of symmetry (taken as the z axis). In cylindrical co-ordinates, z, ρ, ϕ,

$$(11) \qquad dS = \rho[1+(d\rho/dz)^2]^{\frac{1}{2}}\, d\phi\, dz,$$

$$(12) \qquad \mathbf{r} = \hat{z}\,(R+z)+\hat{x}\rho\cos\phi+\hat{y}\rho\sin\phi,$$

$$(13) \qquad r^2 = (R+z)^2+\rho^2,$$

$$(14) \qquad \hat{r}\times\hat{x} = r^{-1}\,[\hat{y}(R+z)-\hat{z}\rho\sin\phi],$$

$$(15) \qquad \int_0^{2\pi} d\phi(\hat{r}\times\hat{x}) = 2\pi\hat{y}\,r^{-1}\,(R+z).$$

The slope of the tangent to the body is $(d\rho/dz)$. The inclination with respect to the z axis of the ray to a point on the body is $\tan^{-1}[\rho/(R+z)]$. The angle γ between the incident ray and the tangent to the body is given by

$$(16) \qquad \tan\gamma = \tan\{\tan^{-1}(d\rho/dz)-\tan^{-1}[\rho/(R+z)]\}$$

$$= [(R+z)(d\rho/dz)-\rho]/[R+z+\rho(d\rho/dz)],$$

from which it follows that

$$(17) \quad \hat{r}\cdot\hat{n} = -\sin\gamma = -[(R+z)(d\rho/dz)-\rho]/\{[(R+z)^2+\rho^2][1+(d\rho/dz)^2]\}^{\frac{1}{2}}$$

$$= -[(R+z)(d\rho/dz)-\rho]/r[1+(d\rho/dz)^2]^{\frac{1}{2}}.$$

With these values, equation 10 becomes

$$(18) \qquad \mathbf{H}^s = -ik\,H_0\,\hat{y}\int_0^\infty dz\,\rho(R+z)[(R+z)(d\rho/dz)-\rho]\,r^{-4}\,e^{-2ikr}.$$

From equation 13,

$$(19) \qquad r\,dr = [R+z+\rho(d\rho/dz)]\,dz$$

so that

$$(20) \quad \mathbf{H}^s = -ik\,H_0\hat{y}\int_R^\infty r^{-3}dr\,e^{-2ikr}\,\rho(R+z)[(R+z)(d\rho/dz)-\rho]$$

$$\times[R+z+\rho(d\rho/dz)]^{-1}.$$

Repeated integration by parts of equation 20 yields

$$(21) \qquad \mathbf{H}^s = -(H_0/2)\,e^{-2ikR}\hat{y}\sum_{n=0}^{\infty}(2ik)^{-n}\,g^{(n)}(R)$$

where

$$(22) \qquad g(r) = r^{-3}(R+z)[(R+z)\rho(d\rho/dz)-\rho^2][R+z+\rho(d\rho/dz)]^{-1}$$

and

$$(23) \qquad g^{(n)}(r) = (d/dr)^n g(r).$$

The terms evaluated at infinity must, of course, vanish.

For a clearer view of the relative order of terms, it is helpful to change to the dimensionless quantities

$$(24) \qquad t = r/R, \qquad u = z/R, \qquad v = \rho/R, \qquad K = 2kR,$$

$$(25) \qquad G(t) = Rg(r) = t^{-3}(1+u) \,[(1+u)v(dv/du) - v^2][1+u+v(dv/du)]^{-1},$$

$$(26) \qquad G^{(n)}(t) = (d/dt)^n G(t) = R^n (d/dr)^n G(t).$$

Thus

$$(27) \qquad \mathbf{H}^s = -(H_0/2R) \, e^{-iK} \, \hat{y} \sum_{n=0}^{\infty} \, (iK)^{-n} \, G^{(n)}(1).$$

Provided the $G^{(n)}(1)$ do not differ inordinately from each other, successive terms in the series are smaller by a factor of order $(kR)^{-1}$.

Inasmuch as a surface of revolution is most naturally described by specifying ρ as a function of z, it may be more convenient to use equation 19 to write the derivatives as

$$(28) \qquad d/dt = (dz/dr)(d/du) = t[1+u+v(dv/du)]^{-1}(d/du)$$

so that equation 27 becomes

$$(29) \quad \mathbf{H}^s = -(H_0/2R) \, e^{-iK} \, \hat{y} \sum_{n=0}^{\infty} \, (iK)^{-n}[\{t[1+u+v(dv/du)]^{-1}(d/du)\}^n G]_{u=0},$$

where

$$t = [(1+u)^2 + v^2]^{\frac{1}{2}}$$

and the surface is defined by

$$v = v(u).$$

(A) *Paraboloid*

The equation of the paraboloid is

$$(32) \qquad \rho^2 = 2cz$$

or, in terms of the dimensionless variables,

$$(33) \qquad v^2 = 2cu/R.$$

Hence,

$$(34) \qquad G(1) = (c/R) \,[1+(c/R)]^{-1}$$

with all the higher-order terms finite. To lowest order, then,

$$(35) \qquad \mathbf{H}^s = -\hat{y} \, (H_0 c/2R^2) \,[1+(c/R)]^{-1} \, e^{-2ikR}$$

and according to equation 3

$$(36) \qquad \sigma = \pi c^2.$$

This is Kerr's answer (Kerr 1951) obtained directly, without resort to truncation of the paraboloid and the associated Fresnel zone argument.

(B) Cone

Use of the physical optics approximation for the infinite cone cannot be formally justified, since the tip does not satisfy the condition that the radius of curvature be greater than the wavelength. However, physical optics has often given good answers beyond its range of proved applicability, and it has accordingly been used extensively beyond this range, in particular for the cone. The equation of the curve is

$$(37) \qquad \rho = z \tan \alpha$$

where α is the cone half-angle, or

$$(38) \qquad v = u \tan \alpha.$$

In this case,

$$(39) \qquad G(1) = 0$$

$$(40) \qquad G'(1) = \tan^2 \alpha$$

with all the higher-order terms finite. Hence, to lowest order,

$$(41) \qquad \mathbf{H}^s = i\hat{y} \, (H_0 \tan^2 \alpha / 4kR^2) \, e^{-2ikR}$$

and

$$(42) \qquad \sigma = (\pi/4k^2) \tan^4 \alpha = (\lambda^2/16\pi) \tan^4 \alpha.$$

This answer was obtained by Kerr's approach in Siegel and Alperin (1952).

III. BROADSIDE SCATTERING

The attractiveness of the concept of a cross section stems from the assumption that, if the source and observer are sufficiently distant from the scattering body, the scattered intensity will be independent of the range except for the geometrical factor R^{-4}. There are configurations for which this is not true (i.e. for which the scattered intensity at large distances does not fall off as R^{-4}). For instance, certain bodies have an R^{-3} dependence for broadside incidence; heuristically, this is identified with a dependence of the scattering on the size of the first Fresnel zone. For these cases, the formulation of the cross section as the infinite range limit does not apply; in fact, equation 3 would give an infinite answer. Nonetheless, the term "cross section" is often used to denote the quantity that would have to be used in the radar range equation to describe the scattering at large distances, even though the "cross section" so defined differs from the more common variety in containing a dependence on the range (no matter how great the latter be). The extension of equation 3 to cover this contingency involves replacing the limit $R \to \infty$ by the more intricate statement that R be taken sufficiently large (albeit finite) that in an expansion in powers of R only the highest-order term need be retained. The normal situation then corresponds to this highest-order term being independent of R (in which case the two definitions are equivalent), while in the present instance the leading term will be linear in R.

(*A*) *Circular Cylinder*

As an example, the "cross section" of an infinite circular cylinder for broadside backscattering is computed from equation 10. The axis of the cylinder is taken as z axis, the normal from the cylinder axis to the source as y axis, and the polarization direction as x axis. Then

$$(43) \qquad\qquad dS = \rho\, d\phi\, dz,$$

$$(44) \qquad\qquad \mathbf{r} = -\hat{y}(R+\rho)+\hat{z}z+\hat{\rho}\rho,$$

where

$$(45) \qquad\qquad \hat{\rho} = \hat{x}\cos\phi+\hat{y}\sin\phi = \hat{n},$$

so that

$$(46) \qquad\qquad \mathbf{r} = \hat{x}\rho\cos\phi-\hat{y}[R+\rho(1\text{-}\sin\phi)]+\hat{z}z,$$

$$(47) \qquad\qquad r^2 = z^2+R^2+2\rho(R+\rho)(1-\sin\phi),$$

$$(48) \qquad\qquad \hat{r}\times\hat{x} = r^{-1}\{\hat{z}[R+\rho(1-\sin\phi)]+\hat{y}z\},$$

$$(49) \qquad\qquad \hat{r}\cdot\hat{n} = -r^{-1}[R\sin\phi-\rho(1-\sin\phi)].$$

At long ranges $(R\gg\rho)$, ϕ in the illuminated region extends from 0 to π. The z component of the integrand is symmetric in z, the y component antisymmetric. Hence,

$$(50) \quad \mathbf{H}^s = -(ik\rho/\pi)H_0\hat{z}\int_0^\pi d\phi[R^2\sin\phi-\rho(R+\rho)(1-\sin\phi)^2]\int_0^\infty dz r^{-4}\,e^{-2ikr}.$$

Subject to $R\gg\rho$, r can be expanded:

$$(51) \qquad r = (z^2+R^2)^{\frac{1}{2}}+\rho(R+\rho)(z^2+R^2)^{-\frac{1}{2}}(1-\sin\phi)-2^{-1}\rho^2(R+\rho)^2(z^2+R^2)^{-3/2}$$
$$\times(1-\sin\phi)^2+\ \ldots\ .$$

The third term can be neglected in the phase if

$$(52) \qquad\qquad (k\rho/R) \ll 2\pi,$$

which is the usual Fresnel far-zone requirement

$$(53) \qquad\qquad R \gg (\rho^2/\lambda).$$

Only the first term of equation 51 need be retained for the r^{-4} factor. A couple of ρ's can also be consistently dropped in other factors, reducing equation 50 to

$$(54) \quad \mathbf{H}^s = -(ikR^2\rho/\pi)\,H_0\hat{z}\int_0^\infty dz(z^2+R^2)^{-2}\exp\{-2ik[(z^2+R^2)^{\frac{1}{2}}$$
$$+R\rho(z^2+R^2)^{-\frac{1}{2}}]\}\times\int_0^\pi d\phi[\sin\phi-(\rho/R)(1-\sin\phi)^2]$$
$$\times\exp[2ikR\rho(z^2+R^2)^{-\frac{1}{2}}\sin\phi].$$

The first term in the ϕ integration is

$$(55) \quad \int_0^\pi d\phi \sin \phi \exp[2ikR \rho (z^2+R^2)^{-\frac{1}{2}} \sin \phi]$$

$$= \int_0^\pi d\phi \sin\phi \cos[2kR\rho(z^2+R^2)^{-\frac{1}{2}}\sin\phi] + i\int_0^\pi d\phi \sin\phi \sin[2kR\rho(z^2+R^2)^{-\frac{1}{2}}\sin\phi]$$

$$= \pi E_1[2kR\rho(z^2+R^2)^{-\frac{1}{2}}] + i\pi J_1[2kR\rho(z^2+R^2)^{-\frac{1}{2}}]$$

where E_1 and J_1 are the Weber and Bessel functions of order one, respectively (Watson 1952). The second term yields the same functions of orders zero, one, and two. The contribution of the second term is thus smaller than that of the first by a factor of the order of magnitude of (ρ/R), and it will henceforth be neglected. Then

$$(56) \quad \mathbf{H}^s = -ikR^2\rho H_0\hat{z} \int_0^\infty dz(z^2+R^2)^{-2}\{E_1[2kR\rho(z^2+R^2)^{-\frac{1}{2}}]$$

$$+iJ_1[2kR\rho(z^2+R^2)^{-\frac{1}{2}}]\} \times \exp\{-2ik[(z^2+R^2)^{\frac{1}{2}}+R\rho(z^2+R^2)^{-\frac{1}{2}}]\}.$$

Equation 56 can be evaluated by stationary phase. To highest order in R outside the phase factor, the result is

$$(57) \quad \mathbf{H}^s = -i2^{-1}\pi^{\frac{1}{2}}R^{-3/2}\rho H_0\hat{z}[E_1(2k\rho)+iJ_1(2k\rho)] \exp\{-i[2k(R+\rho)+(\pi/4)]\},$$

which leads to

$$(58) \quad \sigma = \pi^2 kR\rho^2|E_1(2k\rho)+iJ_1(2k\rho)|^2.$$

The polarization has been assumed above to be transverse to the cylinder axis. For longitudinal polarization, there would correspond to equation 48

$$(59) \quad \hat{r}\times\hat{z} = -r^{-1}\{\hat{x}[R+\rho(1-\sin\phi)]+\hat{y}\rho\cos\phi\}.$$

To leading terms in R, this would lead only to the change $\hat{z} \rightarrow -\hat{x}$ in equation 57 and leave equation 58 unchanged. Thus, the far-zone intensity of the field scattered by an infinite circular cylinder shows no polarization dependence in the physical optics approximation.

In the course of this calculation, explicit use has been made of several requirements that the range exceed other characteristic dimensions. An additional condition that occurs in the derivation of the physical optics approximation (although there has been much pragmatic success in using the method despite its violation) is that the wavelength be smaller than the radii of curvature of the surface, hence that $2k\rho \gg 1$. If this last inequality be also satisfied, the Weber and Bessel functions can be replaced by their asymptotic values (Watson 1952):

$$(60) \quad E_1(2k\rho) = -Y_1(2k\rho)+0[(2k\rho)^{-2}] = -(\pi k\rho)^{-\frac{1}{2}} \sin[2k\rho-(3\pi/4)] +0[(2k\rho)^{-3/2}],$$

$$(61) \quad J_1(2k\rho) = (\pi k\rho)^{-\frac{1}{2}} \cos[2k\rho-(3\pi/4)]+0[(2k\rho)^{-3/2}],$$

$$(62) \quad E_1(2k\rho)+iJ_1(2k\rho) = i(\pi k\rho)^{-\frac{1}{2}} \exp\{i[2k\rho-(3\pi/4)]\}.$$

Equation 57 now reduces to

(63) $\mathbf{H}^s = -2^{-1}R^{-3/2}\rho^{\frac{1}{2}}H_0\hat{z}\ e^{-2ikR}$

and equation 58 to

(64) $\sigma = \pi R\rho.$

It is interesting to note that the cylinder "cross section" obtained above (equations 58 and 64) is a factor of two smaller than would be obtained with the usual assumption of an incident plane wave. Thus, tampering with the limit processes can alter the answer.

The limiting value of the "cross section" given by equation 64 is easy to grasp intuitively. The geometric optics cross section of a conducting body for specular backscattering is usually given by

(65) $\sigma = \pi R_1 R_2$

where R_1 and R_2 are the principal radii of curvature at the specular point, and both are large compared with the wavelength. In the case of the cylinder, one of these radii of curvature is infinite (the longitudinal one) and the expression breaks down. A bit of care in tracing through the derivation of the geometric optics formula elicits the fact that it is the relative curvature of the body and wavefront which is pertinent. Ordinarily, the curvature of the wavefront at a large distance from the radar is negligible compared with that of the body, and equation 65 results. In the present case, the opposite is true along one axis and then the radius of curvature of the wavefront enters instead of the radius of curvature of the body, leading to equation 64. On the other hand, the assumption of plane-wave incidence takes this relative curvature into account going one way and not the other, thus underestimating the effective curvature (overestimating the effective radius of curvature).

REFERENCES

KERR, D. E. 1951. Propagation of short radio waves (McGraw-Hill Book Co., Inc., New York).
SIEGEL, K. M. and ALPERIN, H. A. 1952. University of Michigan Report UMM-87.
WATSON, G. N. 1952. A treatise on the theory of Bessel functions, 2nd ed. (Cambridge University Press).

MEASUREMENT OF RADIATIVE CAPTURE RESONANCE INTEGRALS IN A THERMAL REACTOR SPECTRUM, AND THE THERMAL CROSS SECTION OF Pu-240[1]

W. H. WALKER, C. H. WESTCOTT, AND T. K. ALEXANDER

ABSTRACT

An apparatus is described which detects γ-rays emitted by a thin target placed in a well-defined neutron beam. It has been used to determine the Cd ratios of Au and Pu-240, from which the ratio of the resonance integral to the 2200 m/s cross section for radiative neutron capture in Pu-240 has been deduced, using Au as a reference standard. Using this ratio and previously measured values of the resonance integral of Pu-240 and its effective cross section in two positions in the NRX reactor, three separate estimates of the 2200 m/s cross section of Pu-240 have been made. The mean value is 270 ± 17 barns.

In an auxiliary experiment to indicate the shape of the epithermal spectrum of the neutron beam, the activation Cd ratios of Mn and In were compared with that of Au. These results, combined with the known 2200 m/s capture cross sections of these nuclides, yield new values of the radiative capture resonance integrals for both Mn and In.

1. INTRODUCTION

When this experiment was started, the existence of a strong resonance in Pu-240 at about 1 ev was known, but accurate values of resonance parameters and thermal cross section were not available. Initially therefore, this investigation was primarily directed at measuring the cadmium ratio for the capture of reactor neutrons in Pu-240, using an apparatus which was also intended to be used with other nuclides such as fission products.

Although the results for Pu-240 have been given in an earlier paper (Westcott *et al.* 1958) a full description seems worth while, especially as the techniques used for observing neutron capture have not been widely used except in conjunction with time-of-flight work where the expected background counting rates are much lower than in our conditions. In this connection it may be interesting to note that the three NaI (Tl) crystals used as γ-ray detectors were originally arranged close to the Pu target foil to provide maximum efficiency in case coincidence measurements were required. Heavy shielding was necessary to protect these counters from the radiation near the reactor and a considerable effort was required to develop a suitable collimator for the neutron beam.

In the course of calibrations, incidental determinations were required of resonance integrals for two nuclei commonly used as standards. As these did not confirm the accepted values, details of the work and its conclusions are presented in addition to results on Pu-240.

The relation between cadmium ratios and the ratio of resonance integrals to thermal cross sections is also more fully expounded in the present paper

than has been done in earlier publications (Westcott 1956; Westcott, Walker, and Alexander 1958). It may be noted that the neutron spectrum in the moderator at the center of a large thermal reactor, such as the NRX reactor at Chalk River, is well suited for the application of this theory.

Several recently published time-of-flight measurements (Fluharty 1957; Côté *et al.* 1958; Leonard *et al.* 1958) of the resonance parameters of Pu-240 are in agreement, and predict a 2200 m/s cross section which has been confirmed by a measurement with a crystal spectrometer (Pattenden 1958). By combining our value for the ratio of the resonance integral to the 2200 m/s cross section with determinations of the effective Pu-240 capture cross sections for positions in NRX, we obtain a value of 270 barns for the 2200 m/s cross section, in agreement with the spectrometer results. However, it should be noted that other recently published results on the resonance parameters (Egelstaff *et al.* 1958) and thermal cross section and resonance integral (Rose *et al.* 1958) differ appreciably from this value.

2. BEAM COLLIMATION, SHIELDING, AND γ-RAY DETECTION

The essential components of the experimental arrangement used to detect capture γ-rays are an intense, well-collimated beam of neutrons, a thin film of target material in the beam, and efficient γ-ray detectors placed around the target position. These are shown in Fig. 1. The neutron beam is obtained from a graphite scatterer in an "instrument" hole which is tangential to the wall of the NRX calandria, as shown in the inset sketch. The 11-ft collimator unit extends outwards from a point $7\frac{1}{2}$ ft inside the pile shielding to the detector cavity inside the main experimental shield. The collimating hole is placed above the center line of the instrument hole so that a rotating steel cylinder located 2 ft inside the pile face can be used as a gate to shut off the beam. The main shielding is contained by walls of welded $\frac{1}{4}$-in. steel plate, mounted on two 4-wheeled carriages running on rails as shown in Fig. 1. The sections adjacent to the counter cavity and beam path are filled with lead, the remainder with boron-loaded gelatin. The forward section, which carries the detectors, preamplifiers, and pump, normally remains in position against the pile face, and the rear carriage is moved back when it is necessary to gain access to counters or target.

In its initial form the collimating hole was 1 in. in diameter over its entire length. Alternation of short sections of graphite, B_4C powder in aluminum cans, and Pb served to slow down and capture neutrons, and to reduce γ-ray intensities outside the beam. The background due to capture of scattered neutrons in the NaI (Tl) detectors and the materials surrounding them proved to be greater than expected. This background was reduced to a low level by evacuating the beam path near the counters and using a collimator insert. The evacuated section extends from near the filter position to the B_4C beam stopper while the insert starts near the fission chamber at the left-hand margin of Fig. 1 and ends at the end of the original collimator. The beam is reduced by the first (tapered) portion of the insert to a diameter of 0.5 in. at a point 2 ft in front of the target position, while from this point on, the insert
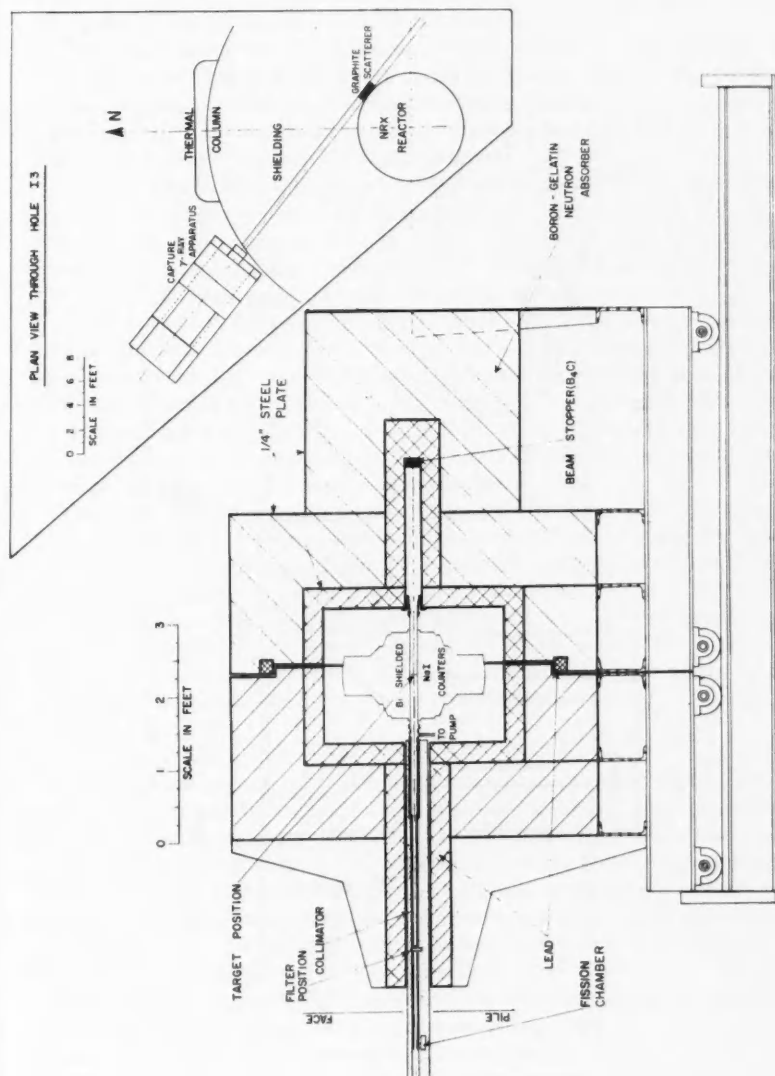
Fig. 1. Arrangement of apparatus for counting neutron capture gamma rays.

NaI CRYSTAL
4" DIA X 2"

NaI
CRYSTALS
2" DIA X 2"
(2 - END TO END)

NaI CRYSTAL
4" DIA X 2"

SECTION
SHOWN
AT LEFT

DRY B₄C ABSORBER
IN AL CANS

EVACUATED
AL TUBE

0   1   2   3
SCALE IN INCHES

MUMETAL
SHIELD

STEEL

EVACUATED
AL TUBE

TO
PREAMPLIFIER

5819

LUCITE

NaI
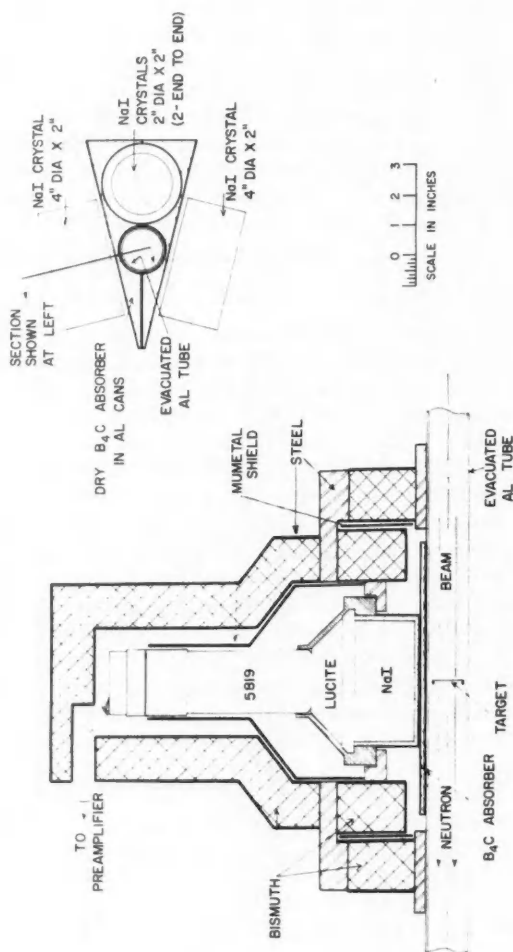
BEAM

BISMUTH

NEUTRON
B₄C ABSORBER   TARGET

FIG. 2.   Counter arrangement and shielding.

has an internal diameter of $\frac{3}{4}$ in., large enough to clear the neutron beam, but small enough to shield the scintillators from neutrons penetrating or scattering from the constricted $\frac{1}{2}$-in. section. Thus no neutron scattered only once from the walls of the collimator can enter the detectors.

The target material is deposited on a .0003-in. thick Al foil mounted on a 1-in. diameter Al ring. Both the ring and the holder used to place it in the target position are clear of the neutron beam. The aluminum-canned B_4C shown in Fig. 2 surrounding the target tube helps reduce the background in the detectors due to scattered thermal neutrons.

Capture γ-rays from the target are detected in three NaI (Tl) scintillation counters arranged about the target position as shown in Fig. 2. Two of the counters are 4-in. diameter by 2-in. thick NaI (Tl) crystals mounted with lucite light pipes on 2-in. RCA 5819 photomultiplier tubes. The section through one of these and its bismuth shielding is shown.

Photomultipliers with a small photocathode area were chosen in preference to 5-in. diameter types because the latter had a poor gain-stability characteristic under changing counting rates. After counting at high rates, the gain returned to its low counting rate value exponentially with a half-life of about 28 minutes, confusingly similar to the half-life of the I-128 activation induced by neutron capture in the iodine of the crystal. The use of a light pipe instead of direct coupling entailed some loss in resolution.

The third counter consists of two independently sealed 2-in. diameter by 2-in. long NaI (Tl) crystals placed end to end and viewed separately by two RCA 5819 photomultiplier tubes. The collector outputs are added at the input to a cathode follower preamplifier. The gains were equalized by adjustment of the voltage across the dynode resistor chains until the counters gave optimum photopeak resolution when detecting Na-22 γ-rays.

To reduce the effect of stray magnetic fields on the gain of the photomultipliers, they were surrounded by mu-metal shields.

3. ELECTRONIC APPARATUS

To record the γ-rays emitted from the target, a counting system was required in which the pulses from the scintillation counters, after pulse height discrimination, can operate either a 0.1-μsec coincidence circuit or scalers. The design of the circuits ensured that the rise time of the pulses at the output of a linear amplifier and the time jitter of triggering of the discriminators were less than 0.1 μsec. Hence it was only necessary to shape the output pulses of the discriminator, by clipping, into pulses with 0.1-μsec half-width. These shaped pulses then operated a diode coincidence gate.

Figure 3 shows a block diagram of the counting system and demonstrates one typical mode of operation. The current pulses from the photomultiplier tubes are integrated (time constant $\gg 0.25$ μsec, the time constant of NaI (Tl)) at the input of the cathode follower and shaped to pulses with approximately 0.1-μsec rise time and 0.5-μsec decay time constant at the output of the cathode follower. The pulses are amplified with a maximum gain of 20 and passed directly to the input of a discriminator which triggers from negative
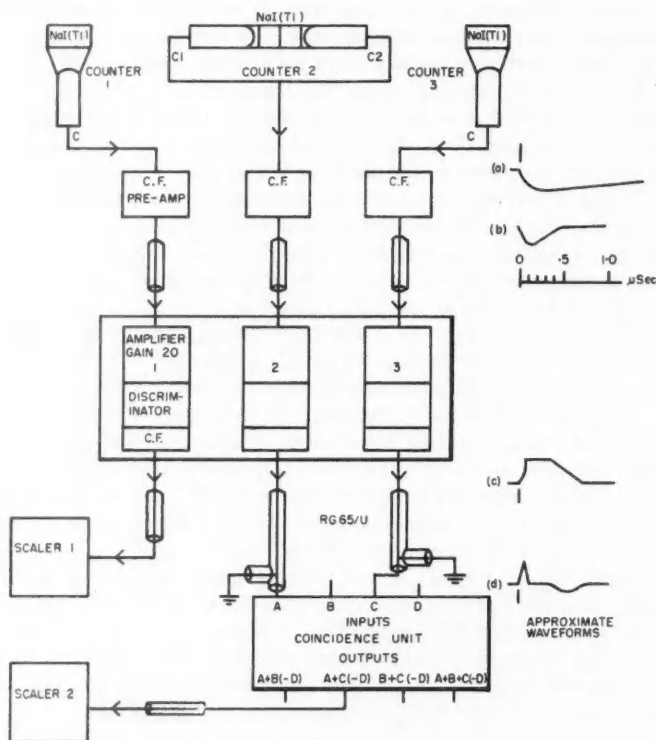
Fig. 3. Block diagram of the counting system showing a typical mode of operation.

pulses in the range 0.1 to 1 volt. The discriminator produces a positive, 10-volt, fast-rising pulse when triggered. The dead time of the discriminator is 0.7 μsec.

The output pulses of the discriminator operate a scaler or, if coincidences are to be recorded, these pulses are clipped with a 0.05-μsec shorted delay line to give pulses 0.1 μsec wide. This width then determines the resolving time of the coincidence circuits.

The coincidence unit, shown in Fig. 4, has four inputs A, B, C, and D. Four diode gates impulsed through ferrite-cored pulse transformers make up the coincidence gates to provide outputs A+B (−D), A+C (−D), B+C (−D), and A+B+C (−D), where + indicates coincidence and (−D) indicates optional anticoincidence. If all diodes in a given gate are cut off, the current flowing then charges the stray capacity on the input of the shaper and triggers it to produce a 15-volt output pulse.

The resolving time was checked experimentally by measuring the chance coincidence rates when independent Co-60 γ-ray sources irradiated each crystal separately. The measured value was 0.12 μsec ±5%.
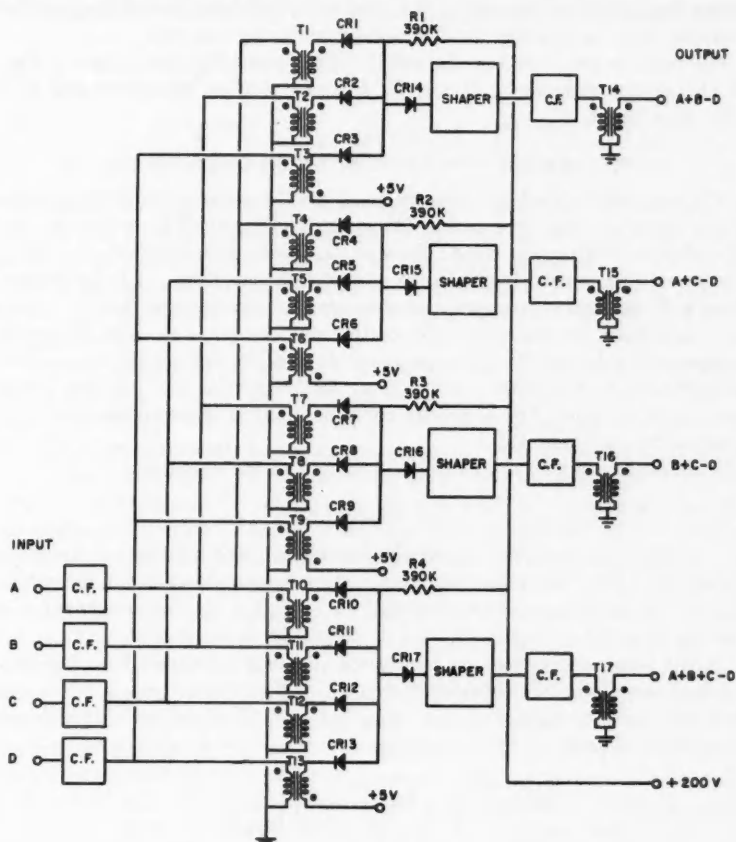
FIG. 4.   Circuit diagram of coincidence circuits.

4. COUNTING CAPTURE γ-RAYS

The capture rate in the target foil may be measured by either single or multiple counting of capture γ-rays. The range of γ-ray energies used in single counting is limited by the growth of I-128 in the scintillator due to the capture of stray thermal and resonance neutrons. Since this nuclide decays with a 25-minute half-life, emitting a 2-Mev β-particle in 93% of the disintegrations, and a 1.6-Mev β-particle in coincidence with a 0.4-Mev γ-ray in the remainder, all counts below 2 Mev are usually biased out in single counting in order to avoid a time variation of the background.

With multiple-coincidence counting, the rates are much lower, and the signal-to-background ratio higher. In double-coincidence counting, the low γ-ray energy limit is again set by the I-128 decay; in this case, however,

pulses from all γ-rays exceeding 0.4 Mev are acceptable. In triple-coincidence counting there is no lower limit to acceptable γ-ray energies.

The beam is monitored by the small U-235 fission chamber shown in Fig. 1, which counts neutrons scattered by a lucite ring at the inner end of the collimator insert.

5. THEORETICAL INTERPRETATION OF CADMIUM RATIOS

The treatment developed here is based on the convention for cross section and neutron flux first proposed by Westcott (1956) and adopted since by many laboratories (Pattenden 1958; Rose et al. 1958; Eastwood et al. 1958); a similar scheme is used by Halperin and Stoughton (1958). It is applicable to large well-moderated reactors, and assumes that the neutron flux is composed of Maxwellian (or thermal) and epithermal components. The Maxwellian component is defined by a temperature T, and the epithermal component is proportional to dE/E with a cutoff at μkT, where $\mu = 5$ for heavy-water-moderated reactors. The appendix contains a list of the symbols used in this paper with their definitions.

The development of the definitions leading to the equation

$$(1) \qquad\qquad \hat{\sigma} = \sigma_0(g+rs)$$

can be found in an earlier paper (Westcott et al. 1958). In this reference it is shown that, for a detector with cross section proportional to $1/v$ below about 0.5 ev, the quantity s is proportional to $\sqrt{(T/T_0)}$. In the treatment which follows the invariant quantity $s\sqrt{(T_0/T)}$ will be denoted by s_0.

In the present paper we are concerned with the interpretation of cadmium ratios. For an infinitely thin detector in which the cross section is nearly equal to $\hat{\sigma}_M(v_0/v)$ between μkT and E_{Cd}, the equation of Westcott et al. (1958) written in terms of s_0 and $r\sqrt{(T/T_0)}$ becomes

$$(2) \qquad\qquad R_{Cd} = \left\{ \left(r\sqrt{\frac{T}{T_0}} \right)^{-1} + \frac{s_0}{g} \right\} \left\{ \frac{s_0}{g} + \frac{1}{K} \right\}^{-1}.$$

The parameter K is a function of the thickness of Cd, tabulated by Westcott et al. (1958) for both a normally incident neutron beam and for isotropic incidence on one side of a Cd foil, as required for a "sandwich" detector inside a reactor. If a sharp cutoff at an energy E_{Cd} is assumed for the neutrons transmitted through the Cd, then

$$K = \frac{1}{4} \sqrt{\frac{\pi E_{Cd}}{E_0}}.$$

For application to the present case, equation (2) needs further refinement. The term $\{r\sqrt{(T/T_0)}\}^{-1}$ mainly represents the contribution of thermal neutrons; if the Cd is thin enough a fraction of these can pass through the Cd, so that it is necessary to add to the denominator the term $h\{r\sqrt{(T/T_0)}\}^{-1}$, where h is the transmitted fraction of the neutron density for the initially Maxwellian component.

The resonance capture contribution, s_0/g, is defined by the equation

$$(3) \quad \frac{s_0}{g} = \frac{2}{\sqrt{\pi}} \int_{\mu k T}^{\infty} \left(\frac{\sigma}{g \sigma_0} - \sqrt{\frac{E_0}{E}} \right) \frac{dE}{E}$$

$$= \frac{2}{\sqrt{\pi}} \int_{\mu k T}^{E_{Cd}} \left(\frac{\sigma}{g \sigma_0} - \sqrt{\frac{E_0}{E}} \right) \frac{dE}{E} + \frac{2}{\sqrt{\pi}} \int_{E_{Cd}}^{\infty} \left(\frac{\sigma}{g \sigma_0} - \sqrt{\frac{E_0}{E}} \right) \frac{dE}{E}.$$

The second integral is, for our cases, essentially invariant with respect to T and the first term is a small correction, W say, arising in those cases where σ is not proportional to $1/v$. Values of W have been estimated for Au, In, Mn, and Pu-240, assuming that the cross section between $\mu k T$ and E_{Cd} is all due to the first resonance; they are $W_{Au} = 0.027$, $W_{In} = 0.245$, $W_{Mn} = 0$, and $W_{Pu\text{-}240} = 0.35$.

The last integral of equation (3) is reduced by resonance self-shielding in the target foils and by the attenuation of resonance neutrons in the Cd filter. The first of these factors can be calculated using the method of Roe (1945) for predominantly capturing resonances if their parameters are known. For the target thickness of Au, In, and Pu-240 used in these experiments self-shielding is important for only one resonance, while in the case of Mn, where the resonance is predominantly scattering and the method of Roe does not apply, the targets are sufficiently thin that self-shielding is negligible.

The attenuation of the resonance neutrons in the Cd filter is a function of cadmium thickness (N atoms/cm²), neutron energy, and angle of incidence. For the beam irradiations this reduction is given by the factor $\exp\{-\sigma_{total} \times N(.030 \text{ in.})\}$, while for those in the pneumatic carrier it is given by the exponential integral function $E_2\{\sigma_{capture} N(.015 \text{ in.})\}$. In the latter case it is assumed that the foil sandwich approximates an infinite slab and the effect of potential scattering ($\sim$5 barns) is negligible. The slopes of these functions change sufficiently slowly with neutron energy that the value at the resonance peak energy (E_r) may be used as the filter reduction factor. This assumption is valid for narrow resonances in the region of 1 ev such as Pu-240, but would not apply to those for which the width Γ was appreciably larger.

It is therefore necessary to multiply the resonance capture contribution in the numerator (s_0/g) by G_1, and that in the denominator $\{(s_0/g) - W\}$ by FG_1, where "F" is the reduction factor due to the cadmium filter and "G_1" is Roe's self-shielding factor for the dominant absorption resonance of the target. Equation (2) then becomes

$$(4) \quad R_{Cd} = \left\{ \left(r \sqrt{\frac{T}{T_0}} \right)^{-1} + G_1 \frac{s_0}{g} \right\} \left\{ FG_1 \frac{s_0}{g} + \frac{1}{K} - W + h \left(r \sqrt{\frac{T}{T_0}} \right)^{-1} \right\}^{-1}$$

using the approximation $W = FG_1W$.

Since all materials are to be compared with Au, a more useful equation is

$$(5) \quad \frac{(FR_{Cd} - 1)_z}{(FR_{Cd} - 1)_{Au}} = Z_z \left[\frac{\{(G_1 s_0)/g\}_{Au} + (1/F_{Au})\{(1/K) - W_{Au} + h(r\sqrt{T/T_0})^{-1}\}}{\{(G_1 s_0)/g\}_z + (1/F_z)\{(1/K) - W_z + h(r\sqrt{T/T_0})^{-1}\}} \right],$$

where

$$(6) \quad Z_x = \frac{(r\sqrt{T/T_0})^{-1}(1/F_x)\{(1/-K)-W_x+h(r\sqrt{T/T_0})^{-1}\}}{(r\sqrt{T/T_0})^{-1}-(1/F_{Au})\{(1/K)-W_{Au}+h(r\sqrt{T/T_0})^{-1}\}}$$
$$\approx 1+W_x\,r\sqrt{T/T_0},$$

since $h \ll 1$, $W_{Au} \ll 1$, and $K \gg r\sqrt{(T/T_0)}$. In these experiments $r\sqrt{(T/T_0)}$ is equal to 0.025 to the degree of accuracy required, so that $Z_{Mn} = 1.0$, $Z_{In} = 1.006$, and $Z_{Pu-240} = 1.009$.

6. CADMIUM RATIO MEASUREMENTS WITH GOLD

In the measurements reported in this paper gold has been used as a reference standard. The gold target used is a deposit of 1 mg/cm² evaporated on a 0.3-mil Al foil. Table I lists recent measured values for the 2200 m/s capture

TABLE I

Gold cross sections

Reference	σ_0	σ_s(th)	Σ'	
			4.9-ev resonance	Other resonances
Carter, Palevsky, Myers, and Hughes (1953)	98.7±0.6	—	—	—
Egelstaff (1954)	98.4±0.9	9±2	—	—
Allen, Stephenson, Stanford, and Bernstein (1954)	—	8.7±0.9	—	—
Gould, Taylor, Rustad, Melkonian, and Havens (1957)	98.8±0.3	—	—	—
Seidl et al. (1954)	—	—	—	42±15
Wood, Landon, and Sailor (1955)	—	—	1470±37	—
Argonne (1955)	—	—	—	55±12

cross section, the thermal scattering cross section σ_s(th), and the capture resonance integral. The capture resonance integrals Σ' have been calculated from published resonance parameters since it can be shown that, for a single Breit–Wigner resonance,

$$(7) \quad \Sigma' = (\pi/2)\sigma_r\Gamma_\gamma/E_r$$

provided $E_r \gg \mu kT$, so that σ is proportional to $1/v$ in the region of μkT.

Values adopted in this paper are $\sigma_0 = 98.6$ barns, $\sigma_s = 9$ barns, and $\Sigma' = 1525$ barns, so that $(s_0)_{Au} = 17.45$.

The validity of using capture γ-ray counting to measure the Cd ratio of Au has been established by comparison with activation results. Agreement to 1% and better was obtained between all three counters, singly and in coincidence, taken over a range of biases. For single counts the range investigated was between 1.5 and 3.0 Mev. In addition Cd ratios obtained by activations in the beam agreed within the experimental error of 2% with values obtained in the same experiment by single counting of capture γ-rays. No appreciable contaminant was detected in the activation experiment.

7. SELF-FILTERING WITH GOLD

A further test of the reliability of the detection method used in these experiments is a measurement of the epi-Cd neutron transmission through Au filters, using a thin Au detector. If $\eta_f = \sigma_r t_f$ and $\eta_t = \sigma_r t_t$, where t_f and t_t are the thicknesses of the filter and target foil respectively, in atoms/cm², and σ_r is the resonance peak cross section in square centimeters, then it can be shown (Roe 1954, p. 32) that the transmission for this resonance is given by

$$(8) \qquad T \cong \frac{(\eta_f + \eta_t)G_1(\eta_f + \eta_t) - \eta_f G_1(\eta_f)}{\eta_t G_1(\eta_t)}$$

$$= \frac{1}{(G_1(\eta_t))} \frac{\partial}{\partial \eta} \left\{ \eta_f G_1(\eta_f + \tfrac{1}{2}\eta_t) \right\}$$

Here "$G_1\eta$" is the self-shielding factor referred to in Section 5. The approximation in equation (8) introduces a negligible error in the cases of gold and Pu-240.

If it is assumed that the signals received by the counters from the various resonances are in proportion to their resonance capture integrals, the over-all calculated transmission is the sum of the contributions from each resonance, i.e.

$$(9) \qquad T_{\text{calc}} = \frac{\Sigma_1' T_1 + \Sigma_2' T_2 + \Sigma_3' T_3 \ldots}{\Sigma'}$$

where Σ_n' is the resonance integral contribution of the nth resonance and $\Sigma' = \Sigma_1' + \Sigma_2' + \ldots$.

In Table II the results of measurements of epi-Cd neutron transmissions with their statistical errors are compared with calculated values. The error

TABLE II

Transmission of epi-Cd neutrons

Au filter thickness, mg/cm²	T_{calc}	T_{meas}	$(T_{\text{meas}} - .030)/0.97$
4.67	0.816±0.010	0.810±0.005	0.803
9.48	0.673±0.010	0.673±0.003	0.662
14.15	0.573±0.010	0.578±0.002	0.564
22.93	0.434±0.010	0.459±0.002	0.442
32.41	0.359±0.010	0.380±0.001	0.360
1490	0.050±0.005	0.079±0.004	0.050

assigned the latter is estimated and is due primarily to errors in reading the curves. The last measurement (very thick filter) was done separately, in conjunction with the temperature measurement reported in the next section.

The two sets of transmissions show a monotonic divergence which is well outside the limits of error for the thicker filters. This can be accounted for by assuming a constant signal in the counters from the target, equal to 3% of the epi-Cd signal with no Au filter, as indicated in the last column. Such a signal could arise from resonant capture in unidentified high-energy resonances,

from capture in the detectors of potential-scattered neutrons, or from capture in a contaminant in the target. The first possibility is improbable since it would require a contribution to Σ' equal to that from all the identified resonances other than the one at 4.9 ev. A scattering signal of 3% is not consistent with the agreement to better than 2% between in-beam and activation comparisons of the Cd ratio of Au, as described in Section 6. Since the presence of a contaminant cannot be similarly ruled out nor its effect on the Cd ratio calculated, it is only possible to say that the Cd ratio of Au determined by capture γ-ray counting is correct to 2% or better.

8. THE "TEMPERATURE" OF THE BEAM NEUTRONS

To determine the temperature of the Maxwellian component of the beam neutrons a measurement was made of the transmission through a 1.49 g/cm² gold filter, of neutrons having energies less than the Cd cutoff, using the standard gold foil as detector, with single counting. The measured transmission was 0.645.

Values for transmission using $1/v$ filters and a thin $1/v$ detector have been calculated as a function of filter thickness and neutron temperature. Corrections were made for scattering in gold, for the departure of the gold cross section from $1/v$ ($g = 1.01$ at 130° C) (Westcott 1958) and for $1/v$ capture due to nitrogen ($\sigma_0 = 1.88$ barns) (Hughes and Harvey 1955) in the flight path.

The temperature corresponding to the corrected transmission was $130 \pm 10°$ C where the assigned error in the measurement is due chiefly to the uncertainty in the scattering cross section of Au.

This result is in good agreement with thermocouple measurements in the graphite outside the calandria, and with other measurements of neutron temperature in the graphite at two self-serve positions (Bigham 1958).

The effect of the nitrogen in the 5-meter flight path between the graphite scatterer and the filter position is made up of two parts, a scattering effect causing a loss of about 20% for neutrons of all energies, and the capture of neutrons in the (n,α) reaction. At a neutron temperature of 130° C the latter effect is estimated to be a signal reduction of $3\frac{1}{2}$% for Maxwellian neutrons, and of 1% for epi-Cd neutrons. No correction is required if the results are treated using equation (5).

9. THE EPITHERMAL SPECTRUM OF THE BEAM NEUTRONS

In the derivation of equation (5) it is assumed that the epithermal spectrum is proportional to dE/E, the distribution function predicted by neutron diffusion theory for epithermal neutrons in the moderator near the center of a well-moderated reactor with a large resonance escape probability such as NRX. The irradiation station of the NRX pneumatic carrier is located in an empty lattice position in the median plane of the reactor near the central axis. Unfortunately, the absence of fuel in this position depresses the neutron spectrum at higher energies below the $1/E$ distribution which occurs elsewhere in the moderator. A calculation of the flux at this location in the region of the

lowest Mn resonance (337 ev) and near the gold resonance (5 ev), assuming
Fermi age distributions about line sources of 3-Mev neutrons, indicates that
the former is 14% smaller than the $1/E$ extrapolation of the latter. Although
the higher Mn resonance will be affected to a greater extent, corrections for
the various simplifying approximations made and for the resonance capture in
U-238 in the fuel will tend to reduce this discrepancy, so that 14% may be
considered an upper limit. The deviation from $1/E$ predicted between 1 ev
and 5 ev was less than 1%.

The epithermal spectrum of the beam neutrons was compared with that in
the pneumatic carrier position in the moderator by measuring the Cd ratios
of Au, In, and Mn. All measurements were made by activating the target
materials, with the exception of those for Au in the beam. In this case capture
γ-rays were counted before and after the beam activations of Mn and In.
Pertinent information on the activation targets is given in Table III.

TABLE III

Activation targets

Irradiation position	Target element	Target thickness, $\mu g/cm^2$	Cd thickness, inches	Irradiation period, min		Activity measured
				No Cd	Cd	
Pneumatic carrier	Mn	240	.015	1.00	10.0	Mn-56 (2.6 hr)
Pneumatic carrier	In	60	.015	1.00	3.00	In-116 (54 min)
Pneumatic carrier	Au	80	.015	In same capsules as Mn and In		Au-198 (2.7 days)
Beam	Mn	3500*	.030	5.0	60.0	Mn-56
	In	840*	.030	10.0	29.0	In-116

*Mounted on 1-in. diameter Al ring and irradiated in regular target position (see Fig. 2).

The activation counting was done in the same geometry in all cases. The
detector was a 2-in. ×2-in. NaI (Tl) crystal coupled to an RCA 6655 phototube,
and shielded by 2 inches of Pb. To give the largest signal-to-background ratio,
only the region about the photopeak was counted, using a single-channel
analyzer. Corrections for the activity of the aluminum backings were measured
by counting foils which were irradiated with the targets.

The relative masses of the target materials used in the pneumatic carrier
irradiations were measured by activation counting following subsequent
irradiations in which the pairs of foils were placed face to face, separated only
by a thin foil of Al. The relative masses of the beam targets were measured by
comparing the capture γ-rays from each pair. The values obtained for R_{Cd} in
these measurements are listed in Table IV.

From equation (5) it can be seen that $\{(FR_{Cd} - 1)_x\}/\{(FR_{Cd} - 1)_{Au}\}$
will be sensibly independent of the epithermal flux density if $h = 0$ and s_0
remains constant, i.e. if the shape of the epithermal flux spectrum remains
constant. Auxiliary conditions are that G_1, $g(T \, ^\circ C)$, $1/K$, and F (on the left-

TABLE IV

Measured values of R_{Cd}. Corrected values of $\{(FR_{Cd}-1)_x\}/\{(FR_{Cd}-1)_{Au}\}$

Irradiation position	Target element	R_{Cd} (measd.)	Shielding factors		Normalization factor	$\{(FR_{Cd}-1)_x\}/\{(FR_{Cd}-1)_{Au}\}$ (normalized)
			F	G_1		
Beam	Mn	39.4 ± 0.7	0.98	1.00	1.034	15.80 ± 0.5
	Au	3.53 ± 0.07	0.98	0.978		
Beam	Mn	37.3 ± 0.55	0.98	1.00	1.034	15.70 ± 0.5
	Au	3.41 ± 0.07	0.98	0.978		
Pneumatic carrier	Mn	31.1 ± 0.4	1.00	1.00	1.060	15.64 ± 0.2
	Au	3.04 ± 0.01	1.00	1.00		
Beam	In	3.20 ± 0.05	0.96	0.966	0.974	0.895 ± 0.035
	Au	3.32 ± 0.07	0.98	0.978		
Pneumatic carrier	In	2.955 ± 0.018	0.95	1.00	1.000	0.886 ± 0.015
	Au	3.04 ± 0.01	1.00	1.00		

hand side of the equation) remain the same. In the present experiment these factors vary and "h" is not always zero, but since their values can be calculated it is possible to normalize the measured ratios to a standard condition. The shielding factors F and G_1 are listed in Table IV; the thermal neutron penetration factor, "h", is 0.0025 for the thickness of Cd used in the pneumatic carrier irradiation and zero for the beam; $1/K = 0.522$ for the thickness of Cd and direction of neutron incidence in the beam, 0.502 in the pneumatic carrier; for the beam, with $T = 130°$ C, $g_{Au} = 1.012$, $g_{Mn} = 1.000$, and $g_{In} = 1.041$; for the pneumatic carrier, with $T = 38°$ C, $g_{Au} = 1.006$, $g_{Mn} = 1.000$, and $g_{In} = 1.022$ (Westcott 1958). The standard conditions chosen are: $h = 0$; $F = G_1 = 1.00$ for every case; $1/K = 0.522$; and $T = 20°$ C. The normalization factors are listed in Table IV, as are the normalized values for $\{(FR_{Cd}-1)_x\}/\{(FR_{Cd}-1)_{Au}\}$.

The similarities of the values in Table IV for both Mn and In for the two locations indicate that the epithermal spectra of the beam and in the vacant lattice position have substantially the same form within the energy range 1 ev to 1000 ev.

10. THE ACTIVATION RESONANCE INTEGRALS OF Mn-55 AND In-115

The values of s_0 for Mn-55 and In-115 can be obtained directly from the weighted mean values of $\{(FR_{Cd}-1)_x\}/\{(FR_{Cd}-1)_{Au}\}$ of Table IV using equation (5) and the values of g, F, G_1, and $1/K$ given above for the standard conditions. The resonance integrals, Σ', can also be obtained since the thermal capture cross sections of both Mn-55 and In-115 are known (Hughes and Harvey 1955; Rose et al. 1958). Values of s_0, σ_0, and Σ' are given in Table V. The value of 7.2 ± 0.2 obtained for Mn on this basis has been adjusted to the value given in the table to allow for the depletion of the flux at 337 ev relative to that at 5 ev discussed in the previous section, the error quoted having been increased to allow for uncertainties in this correction.

TABLE V

Values of s_0 and Σ' for Mn, In

Target	g, 20° C	s_0	σ_0, barns	Σ', barns
Au	1.005	17.45		
Mn	1.00	0.615±0.015	13.2±0.4	7.8±0.8
In	1.017	20.2	198±2	3530±100

Values previously reported for the Mn resonance integral include one of 5 barns quoted by Macklin and Pomerance (1956), 4.5±2.5 barns (Rose, Cooper, and Tattersall 1958), and 8.2 barns (Dancoff *et al.* 1947). For the In-115 resonance integral our value is to be compared with the value of 2640 barns quoted by Macklin and Pomerance (1956) and one of 3500±250 barns obtained for naturally occurring In by Rose *et al.* (1958) using a pile oscillator. Using resonance parameters from the 1958 edition of BNL-325 the calculated value of Σ' is 3050±150 barns.

11. PREPARATION AND CALIBRATION OF Pu SOURCES

Neutron capture in Pu-240, as in Au-197, is dominated by a single large resonance. The method of determining the Cd ratio by counting capture γ-rays should therefore be applicable to Pu-240. The isotopic composition of the Pu samples used in the measurement of the Cd ratio of Pu-240 are given in Table VI. The Pu-239/241 sample was especially prepared to have the same ratio of Pu-239 to Pu-241 atoms as the Pu-240-enriched sample.

TABLE VI

Isotopic abundances of Pu target material
(in atom per cent)

Sample designation	Isotopes				Ratio, Pu-239/Pu-241
	239	240	241	242	
Pu-240	11.46	88.01	0.49	0.034	23.4
Pu-239/241	92.13	3.86	3.95	0.06	23.3

TABLE VII

Alpha counting of plutonium targets

Target designation	α-Emitting area, cm²	Geometric efficiency of chamber	Counting rate, c.p.m.	Specific activity, d.p.m./mg	Target thickness, μg/cm²
Pu-240(A)	1.267	8.306×10⁻⁵	11,750	4.66×10⁵	240
	2.85	8.306×10⁻⁵	26,590	4.66×10⁵	241
Pu-240(B)	1.267	8.460×10⁻⁵	12,160	4.66×10⁵	243
	2.85	8.460×10⁻⁵	27,320	4.66×10⁵	243
Pu-239/241(A)	1.267	8.757×10⁻⁵	597	1.50×10⁵	35.9
	2.85	8.757×10⁻⁵	1380	1.50×10⁵	36.9
Pu-239/241(B)	1.267	8.757×10⁻⁵	405	1.50×10⁵	24.3
	2.85	8.757×10⁻⁵	910	1.50×10⁵	24.3

Two targets of each sample were used. The Pu-240 targets were scanned with a "pinhole" α-probe and found to be uniform within $\pm15\%$. Alpha counting was carried out in a low-geometry ionization chamber to determine the absolute and relative amounts of the deposits. As an additional check on deposit uniformity the emission areas were restricted by disks with circular apertures of $\frac{1}{2}$-in. diameter and $\frac{3}{4}$-in. diameter. The results are shown in Table VII.

The α-spectra of both Pu samples were investigated to determine the proportion of Pu-238 present. Concentrations were negligible in both cases, of the order of .01 at.%.

12. DETERMINATION OF THE Cd RATIO OF Pu-240

Several measurements were made using single counting. In addition to the Pu targets and the standard Au target a .00031-in. foil of Al was inserted to measure background counting rates. The Pu counting rates had to be corrected for the contributions of Pu-239 and Pu-241, as well as those of the background and the Al mounting foil. This contribution can be estimated from the net Pu-239/241 target counting rates (i.e. less Al foil and background rates) by multiplying by a factor equal to the ratio of the relative abundance of the Pu-239 and Pu-241 in the Pu-239/241 target to that in the Pu-240 target multiplied by the ratio of the Pu thicknesses ($\mu g/cm^2$) in the two targets. This factor is of the order of unity for both Pu-240(A) and Pu-240(B). The results of all runs are shown in Table VIII.

TABLE VIII

Cadmium ratios of Pu-240 and Au-197

	Pu targets used		Cadmium ratios		
Run No.	Pu-240	Pu-239/241	Au-197	Pu-240	$(s_0)_{Pu-240}$
1	A, B	A	3.31 ± 0.066	2.28 ± 0.025	36.9 ± 1.2
2	B	A	3.38 ± 0.067	2.31 ± 0.035	36.9 ± 1.3
3	A, B	A, B	3.33 ± 0.067	2.31 ± 0.030	36.3 ± 1.2
4	B	B	3.41 ± 0.068	2.34 ± 0.040	36.7 ± 1.4

Equation (5) is used to calculate the values of s_0 for Pu-240 shown in the last column. For $T = 130\pm10°$ C the tabulated value of "g" for Pu-240 (Westcott 1958) is 1.060 ± 0.003; it is dependent only on the location of the large resonance ($E_r = 1.056$ ev). For the thicknesses of Pu-240 used in this experiment the self-shielding factor "G_1" is approximately 1 and is not too sensitive to the resonance parameters. The value used in calculating s_0 was $(G_1)_{Pu-240} = 0.983$. The factor calculated for shielding by the .030-in. cadmium filter at the Pu-240 resonance energy (F) is 0.94. The mean value of s_0 is 36.7 ± 0.7.

If neutron capture takes place predominantly through a single energy state, as in Au, the energy distribution of the γ-rays should not change when the Cd filter is inserted. For gold this was verified by comparing the Cd ratios determined by capture γ-ray counting at various biases and by activation; for

Pu-240 only a check at different biases is possible. The Cd ratios were found to be constant within experimental error for single γ-ray counting at several biases ranging from 2 Mev upwards. (The mean value of these measurements is shown as run No. 4 in Table VIII.)

13. THE THERMAL CROSS SECTION, RESONANCE INTEGRAL, AND RESONANCE PARAMETERS OF Pu-240

Our value of s_0 for Pu-240 can be combined with other measurements involving irradiations in NRX to yield a value of σ_0, the 2200 m/s cross section for Pu-240. The epi-Cd resonance integral, Σ_{Cd}, has been measured by Cornish and Lounsbury (1956) as 8700 ± 800 barns. For the thickness of Cd used in their experiment $\Sigma' = \Sigma_{Cd} - 0.45\sigma_0$, so that

$$\sigma_0 = \frac{2}{\sqrt{\pi}} \cdot \frac{(\Sigma_{Cd} - 130)}{s_0} = 264 \text{ barns.}$$

In addition, two measurements of the effective capture cross section for Pu-240 have been made; one in an empty fuel rod position (Fields $et\ al.$ 1956) ($\hat{\sigma} = 530 \pm 50$ barns), the second inside a fuel rod (Craig $et\ al.$ 1958) ($\hat{\sigma} = 1000 \pm 50$ barns). The values of $r\sqrt{(T/T_0)}$ for these two positions are known to be 0.026 ± 0.002 and 0.070 ± 0.006 respectively. The thermal neutron temperature is taken to be that of the moderator, 38° C, for which $g = 1.03$ (Westcott 1958). The two values of σ_0, calculated using equation (1), are listed in the last two lines of column 5, Table IX.[2]

TABLE IX

Pu-240 parameters

Source	Γ, milli-ev	σ_{res}, kilobarns	σ_0, barns	Σ', kilobarns	Σ'/σ_0
Fluharty (1957)	34.5 ± 3	176^*	295†	8.5†	28.9†
Coté $et\ al.$ (1958)	34.5 ± 3	173	290†	8.4†	29.9†
Leonard, Seppi, and Friesen (1958)	32.3 ± 1.5	—	—	—	30.8†
Egelstaff $et\ al.$ (1958)	40 ± 3	130 ± 5	300†	7.45†	24.8†
Ioffe and Okun (1956)	42	190^*	480†	11.3†	23.6†
Krupchinsky (1957)	—	—	460 ± 45	10.0 ± 2.8	21.7
Rose, Cooper, and Tattersall (1958)	—	—	370 ± 40	11.3 ± 1.0	30.5
Cornish and Lounsbury (1956)	—	—	—	$8.5_7 \pm 0.8$	—
Pattenden (1958)	—	—	273 ± 8	—	—
Halperin and Stoughton (1958)	—	—	285 ± 25	—	—
This paper	$30.6 \pm 0.6^*$	—	264 ± 30‡ 278 ± 30§ $268 \pm 30\|$	—	32.5 ± 0.6

*Calculated from other parameters.

†Calculated from resonance parameters, including contributions from higher resonances (see text).

‡Derived from measured value of Σ'/σ_0, using Σ' from Cornish and Lounsbury (1956).

§Derived from Σ'/σ_0 and $\hat{\sigma}$ (Pu-240) $= 1000 \pm 50$ barns in an NRX fuel rod ($r\sqrt{T/T_0} = 0.070 \pm .006$). See Craig $et\ al.$ (1958).

$\|$Derived from Σ'/σ_0 and $\hat{\sigma}$ (Pu-240 $= 530 \pm 50$ in an NRX empty lattice position ($r\sqrt{T/T_0} = .026 \pm .002$). See Fields $et\ al.$ (1956).

[2]This table supersedes that given by Westcott $et\ al.$ (1958); some of the corrections (notably F) described in Section 5 above had not then been applied to the results.

The mean value for the 2200 m/s capture cross section is

$$\sigma_0 = 270 \pm 17 \text{ barns}$$

and for the resonance capture integral is

$$\Sigma' = 32.5 \times 270 = 8.78 \pm 0.55 \text{ kilobarns.}$$

If a single resonance dominates capture in both the thermal and epithermal region it can be shown that

$$(10) \qquad \sigma_0 = \frac{\sigma_r \Gamma \Gamma_\gamma}{4 \, E_r^{3/2} \, E_0^{1/2} \{1 - (E_0/E_r)\}^2}.$$

Combining equations (10) and (7) for the 1.056-ev resonance,

$$(11) \qquad s_0 = \frac{2}{\sqrt{\pi}} \cdot \frac{\Sigma'}{\sigma_0} = \frac{4\sqrt{\pi E_r \, E_0}}{\Gamma} \left(1 - \frac{E_0}{E_r}\right)^2,$$

$$(s_0)_{1.056 \text{ ev}} = \frac{1.104}{\Gamma}.$$

It is known, however, that other resonances contribute to Σ' and σ_0. Using published parameters for these resonances (Fluharty 1957) their contributions were calculated to be 150 ± 50 barns and 1 barn respectively. Thus

$$s_0 = \frac{2}{\sqrt{\pi}} \left(\frac{\Sigma'_{1.056} + \Sigma'_{\text{rem}}}{\sigma_0} \right) = (s_0)_{1.056} + (s_0)_{\text{rem}}$$

so that $(s_0)_{1.056} = 36.7 - 1/\sqrt{\pi} = 36.1$ and $\Gamma = 30.6 \pm 0.6$ milli-ev for the 1.056-ev resonance.

In Table IX our values for Σ'/σ_0 and the derived parameters and cross sections are compared with recently published values. The first five lines give results of parameter measurements. In estimating Σ' and Σ'/σ_0 from these parameters the 150-barn contribution from higher resonances has been added. We only obtain full agreement with the time-of-flight measurements of the three groups of American workers (Fluharty 1957; Côté et al. 1958; Leonard et al. 1958), and with the values of σ_0 obtained by Pattenden (1958) and Halperin and Stoughton (1958).

14. SELF-FILTERING WITH Pu-240

A portion of the Pu-240-enriched material (Table VII) was alloyed with pure aluminum and from this stock two disks $\frac{3}{4}$ inch in diameter were fabricated for use as filters. Chemical analysis showed that the alloy was 12.6% Pu by weight, and that the thickness of the two disks corresponded to 13.0 mg/cm² and 27.4 mg/cm² of Pu-240.

A number of measurements were made of the epi-Cd counting rates with either or both of these filters inserted at the filter position, and with Al filters having a similar aluminum content. The self-filtering transmissions for Pu-240 resulting from these measurements are compared in Table X with values

TABLE X

Self-filtering in Pu-240

Filter thickness, mg/cm² of Pu-240	Transmissions	
	T_{meas}	T_{calc}
13.0	0.247 ± 0.015	$0.26_5 \pm 0.01$
27.4	0.165 ± 0.010	0.16 ± 0.01
40.4	0.134 ± 0.008	$0.13_5 \pm 0.01$

calculated using equations (8) and (9), taking into account contributions from all known resonances (Fluharty 1957). For the 1.056-ev peak the values adopted were $\Gamma_\gamma = 0.032$ ev and $\Gamma_n = 0.00245$ ev.

The agreement between T_{meas} and T_{calc} gives added support to the parameter measurements of the three groups of American workers. It also indicates that there is no scattering or contaminant contribution of appreciable magnitude, as was the case with Au.

ACKNOWLEDGMENTS

REFERENCES

ALLEN, R. G., STEPHENSON, T. E., STANFORD, C. P., and BERNSTEIN, S. 1954. Phys. Rev. **96**, 1297.

ARGONNE FAST CHOPPER. 1955. *Quoted in* Brookhaven National Laboratory Report BNL-325. Unpublished data.

BIGHAM, C. B. 1958. The thermal neutron temperature in NRX self-serve positions S-3-5 and S-6-3, Chalk River Report CRRP-765.

CARTER, R. S., PALEVSKY, H., MYERS, V. W., and HUGHES, D. J. 1953. Phys. Rev. **92**, 716.

CÔTÉ, R. E., BOLLINGER, L. M., BARNES, R. F., and DIAMOND, H. 1958. Slow neutron cross sections of Pu-240, Pu-242 and Am-243, Second Geneva Conference, A/Conf. 15/P/685.

CORNISH, F. W. and LOUNSBURY, M. 1956. Cross sections of Pu-239 and Pu-240 in the thermal and epi-Cd regions, Atomic Energy of Canada Report CRC-633.

CRAIG, D. W., HANNA, C. G., HURST, D. G., KUSHNERIUK, S. A., LEWIS, W. B., and WARD, A. G. 1958. Long irradiation of natural uranium. The zero irradiation extrapolation is used for σ (Pu-240), Second Geneva Conference, A/Conf. 15/P/205.

EASTWOOD, T. A. *et al.* 1958. Radiochemical methods applied to the determination of cross sections of reactor interest, Second Geneva Conference, A/Conf. 15/P/203.

EGELSTAFF, P. A. 1954. J. Nuclear Energy, **1**, 57.

EGELSTAFF, P. A., GAYTHER, D. B., and NICHOLSON, K. P. 1958. J. Nuclear Energy, **6**(1), 303.

FIELDS, P. R., PYLE, G. L., INGHRAM, M. G., DIAMOND, H., STUDIER, M. H., and MANNING, W. M. 1956. Nuclear Sci. and Eng. **1**, 62.

FLUHARTY, R. G. 1957. Recent total cross section measurements, Proceedings of the International Conference on the Neutron Interactions with the Nucleus, Columbia University, TID 7547 (Cu-175), p. 42.

GOULD, F., TAYLOR, T. I., RUSTAD, B. M., MELKONIAN, E., and HAVENS, W. W., Jr. 1957.
    Bull. Am. Phys. Soc. 2(II), 42.
HALPERIN, J. and STOUGHTON, R. W. 1958. Some cross sections of heavy nuclides
    important to reactor operations, Second Geneva Conference, A/Conf. 15/P/1072.
HUGHES, D. J. and HARVEY, J. A. 1955. Neutron cross sections, Brookhaven National
    Laboratory Report BNL-325.
IOFFE, B. L. and OKUN, L. B. 1956. J. Nuclear Energy, 4(II), 371 (translated from Atomaya
    Energiya, 1, 80 (1956)).
KRUPCHINSKY, P. A. 1957. J. Nuclear Energy, 6(II), 155 (translated from Atomaya
    Energiya, 2, 240 (1957)).
LEONARD, B. R., Jr., SEPPI, E. J., and FREISEN, W. J. 1959. Nuclear Sci. and Eng. 5, 32.
PATTENDEN, N. J. 1958. Some neutron cross sections of importance to reactors, Second
    Geneva Conference, A/Conf. 15/P/11.
ROE, G. M. 1954. The absorption of neutrons in Doppler broadened resonances, Knolls
    Atomic Power Laboratory Report KAPL-1241.
ROSE, H., COOPER, W. A., and TATTERSALL, R. B. 1958. The use of the pile oscillator in
    thermal reactor problems, Second Geneva Conference, A/Conf. 15/P/14.
SEIDL, F. G. P., HUGHES, D. J., PALEVSKY, H., LEVIN, J. S., KATO, W. Y., and SJOSTRAND,
    N. G. 1954. Phys. Rev. 95, 476.
WESTCOTT, C. H. 1956. The specification of neutron flux and effective cross sections in
    reactor calculations, Atomic Energy of Canada Limited, AECL 352.
────── 1958. Effective cross section values for well-moderated thermal reactor spectra,
    Atomic Energy of Canada Limited, AECL 670.
WESTCOTT, C. H., WALKER, W. H., and ALEXANDER, T. K. 1958. Effective cross sections
    and cadmium ratios for the neutron spectra of thermal reactors, Second Geneva Con-
    ference, A/Conf. 15/P/202.
WOOD, R. E., LONDON, H. H., and SAILOR, V. L. 1955. Phys. Rev. 98, 639.

APPENDIX—SYMBOLS USED AND THEIR DEFINITIONS

Symbol   Definition

v_0 neutron velocity of 2200 m/s.

E_0 energy of a neutron with velocity v_0 (.0253 ev).

E_{Cd} the "effective" cutoff energy for a cadmium filter.

E_r the energy at the peak of a Breit–Wigner resonance.

$\sigma(E)$ absorption cross section for neutrons with energy E.

σ_0 absorption cross section for a neutron with velocity v_0 (the 2200
               m/s cross section).

$\hat{\sigma}$ $\hat{\sigma} = \sigma_0 (g+rs)$, effective cross section in a flux having both Maxwel-
                lian and epithermal components.

$\hat{\sigma}_M$ the effective cross section in a pure Maxwellian flux distribution for
                  a given temperature.

σ_r the total resonance cross section (i.e. excluding potential scattering)
               at the peak of a Breit–Wigner resonance.

g $$g = \hat{\sigma}_M/\sigma_0 = \frac{1}{\sigma_0} \sqrt{\frac{4kT}{\pi E_0}} \int_0^\infty \sigma(E) \left(\frac{E}{kT}\right) \exp\left(-\frac{E}{kT}\right) d\left(\frac{E}{kT}\right).$$

Σ $$\Sigma = \int_{\mu kT}^\infty \sigma(E) \frac{dE}{E}, \text{ the resonance absorption integral.}$$

Σ' $$\Sigma' = \Sigma - g\sigma_0 \int_{\mu kT}^\infty \sqrt{\frac{E_0}{E}} \frac{dE}{E}, \text{ the resonance absorption integral}$$

in excess of the effective Maxwellian cross section.

Σ_{Cd} $$\Sigma_{Cd} = \Sigma - \int_{\mu kT}^{E_{Cd}} \sigma(E) \frac{dE}{E}, \text{ the resonance absorption integral under}$$

a cadmium filter.

r $r = f \sqrt{(\pi\mu/4)}$ is the epithermal density index, where f is the fraction of the total neutron density in the epithermal distribution.

R_{Cd} the ratio of the reaction rate in an unfiltered neutron flux to the reaction rate in a Cd-filtered neutron flux.

s $s = \sqrt{\dfrac{4T}{\pi T_0} \dfrac{\Sigma'}{\sigma_0}}$.

s_0 $s_0 = s \sqrt{\dfrac{T_0}{T}} = \sqrt{\dfrac{4}{\pi} \dfrac{\Sigma'}{\sigma_0}}$.

T_0 $T_0 = E_0/k = 293.6°\,K$ (20.44° C), "temperature" of a neutron with velocity v_0 (k is Boltzmann's constant).

K $K = R_{Cd}\, r\sqrt{(T/T_0)}$ for a $1/v$ detector ($g = 1$, $s_0 = 0$) (see text).

Γ the full-width of the resonance peak $\sigma(\text{total}) = \sigma_r/2$.

Γ_γ, Γ_n the partial widths for radiative capture and resonance scattering ($\Gamma = \Gamma_\gamma + \Gamma_n$ if no other processes are involved).

ANALYSIS AND SYNTHESIS OF RADIATION PATTERNS FROM CIRCULAR APERTURES[1]

A. ISHIMARU AND G. HELD

ABSTRACT

Part I considers the problem of determining the source distribution over a circular aperture required to produce a prescribed radiation pattern. In particular, the problem of optimizing the narrow broadside pattern from a circular aperture is discussed in detail and an improved design method over Taylor's for line source is devised. Numerical examples are given.

Part II deals with the analysis of the radiation pattern from a circular aperture from r_1 to r_2 with the traveling wave type source functions. Expressions suitable to the analysis and the synthesis are obtained and the narrow-beam and shaped-beam synthesis are discussed.

INTRODUCTION

The problem of determining the source field over an aperture in order to produce a required radiation pattern has been considered for the rectangular aperture by Woodward in 1946. Taylor (1955) extended the method to include a design which approaches the optimum pattern. However, the synthesis of circular apertures has not yet been discussed except for the method outlined by Johnk (1954), who employed the conventional source function of the form $(1-r^2)^p$ and as a consequence, had to use the Schmidt orthogonalization process, which is rather difficult to apply to an actual synthesis problem.

In this paper we investigate the synthesis problem for circular apertures by proposing to represent the source function by a series of Bessel or Hankel functions. This representation yields the radiation pattern in a form similar to the one encountered in the rectangular aperture case, and a technique similar to Woodward's and Taylor's may be employed for the circular aperture case. For broadside antenna we devised a method to improve Taylor's design of optimum pattern. For radiation at an arbitrary angle, we employ the traveling wave type sources and discuss the required modifications.

In Part I, we discuss the constant phase broadside pattern by representing the source by a series of Bessel's functions and we clarify the relationship between the radiation field and the circular aperture source and develop the general form of the radiation function. We then define the optimum pattern for aperture antenna, formulate this optimum condition, and devise a method to realize this optimum pattern. Numerical examples are given and compared with the conventional design and Taylor's design.

In Part II, we discuss the radiation from a source composed of traveling wave type modes. The source is expressed by a series of Hankel functions over the range from r_1 to r_2. The radiation field from this source is investigated in terms of sidelobe level, beamwidth, and the choice of r_1 and r_2. The synthesis of narrow beam and shaped beam is also discussed.

PART I. CONSTANT PHASE

1. Source Function and Radiation Pattern

The radiation pattern from a circular aperture is given (Silver 1949) by

$$(1) \qquad g(u) = \int_0^1 f(r) J_0(ur) \, r dr$$
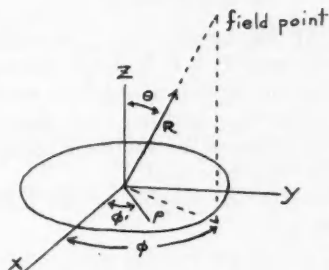
for a source independent of ϕ', where (see Fig. 1)

FIG. 1.   Circular aperture source (ρ, ϕ') and the field point (R, θ, ϕ).

$g(u)$ = radiation pattern,

$f(r)$ = aperture field distribution,

$$(2) \qquad u = \frac{2\pi a}{\lambda} \sin \theta,$$

$$r = \frac{\rho}{a}, \qquad a = \text{radius of the aperture.}$$

The source function which has been employed in the past (Silver 1949; Johnk 1954) is of the form

$$f(r) = (1-r^2)^p, \qquad\qquad p = 0, 1, 2 \ldots .$$

This function yields the radiation pattern of the form

$$g(u) = 2^p p! \frac{J_{p+1}(u)}{u^{p+1}}.$$

From the viewpoint of the synthesis, this pattern is quite inconvenient since this is a non-orthogonal function and the only way of utilizing this is through the Schmidt orthogonalization process which is hardly practical (Johnk 1954). Also this offers no means of optimizing the pattern which is the main concern of this Part I.

For the purpose of synthesis, we use the source function of the form

$$(3) \qquad f(r) = \sum_{n=0}^{N} a_n J_0(u_n r) \qquad \text{for } 0 \leqslant r \leqslant 1,$$

$$= 0 \qquad \text{for } r > 1.$$

Each term of (3) is chosen to satisfy the homogeneous boundary condition at $r = 1$. Thus

$$(4) \qquad u_n J_0'(u_n) + h J_0(u_n) = 0$$

where h is a constant. It may be seen that if $h \rightarrow$ infinite, each term of (3) approaches zero at $r = 1$ and $f(1) = 0$. If $h = 0$, each term of (3) has maxima or minima at $r = 1$. As will be shown later, the optimum pattern requires $h = 0$, and this case will be discussed in detail. However, physical structure of an antenna sometimes requires the vanishing source field at the edge and in this case, $h \rightarrow$ infinite should be used.

Substituting (3) into (1) and employing the Lommel integral formula (Jahnke and Emde 1945),

$$\int J_0(u_n r) J_0(ur) \, r dr = \frac{r}{u_n^2 - u^2} [u J_0(u_n r) J_0'(ur) - u_n J_0'(u_n r) J_0(ur)],$$

we obtain

$$(5) \qquad g(u) = \sum_{n=0}^{N} a_n \frac{J_0(u_n)}{u_n^2 - u^2} [u J_0'(u) + h J_0(u)].$$

The value of a_n to produce $g(u)$ can be determined by the value of $g(u)$ at $u = u_n$ in the following manner:

If u approaches one of u_n, say u_k, then the function

$$\frac{u J_0'(u) + h J_0(u)}{u_n^2 - u^2}$$

is zero except when $u_k = u_n$. When $u_k = u_n$, this function becomes

$$J_0^2(u_n) \frac{h^2 + u_n^2}{2u_n^2}.$$

Therefore, a_n is determined by $g(u_n)$ by the following equation:

$$(6) \qquad a_n = \frac{2u_n^2}{(h^2 + u_n^2) J_0^2(u_n)} g(u_n).$$

In order to utilize eq. (6) and to determine the proper a_n to produce a desired pattern $g(u)$, it is necessary to investigate in what form $g(u)$ should be represented.

For this purpose let us write (5) in the following form:

$$(7a) \qquad g(u) = [uJ_0'(u) + hJ_0(u)] \sum_{n=0}^{N} a_n \frac{J_0(u_n)}{u_n^2 - u^2},$$

$$(7b) \qquad = [uJ_0'(u) + hJ_0(u)] \frac{P_N(u^2)}{\prod_{n=0}^{N} \left[1 - \left(\frac{u}{u_n}\right)^2\right]},$$

$$(7c) \qquad = \frac{[uJ_0'(u) + hJ_0(u)] \prod_{n=1}^{N} \left[1 - \left(\frac{u}{u_n + t_n}\right)^2\right]}{h \prod_{n=0}^{N} \left[1 - \left(\frac{u}{u_n}\right)^2\right]}.$$

$P_N(u^2)$ in (7b) is a polynomial in u^2 of order N and can be determined by the location of its N zeros. The N zeros of P_N are expressed by $u_n + t_n$, $n = 1$, $2, \ldots N$ in (7c). The constant is chosen to normalize $g(u)$ such that $g(0) = 1$.

2. Optimum Pattern

In order to obtain an optimum pattern, we list the following statements:

(a) t_n Must Be Real for an Optimum Pattern

It is well known (Silver 1949) that the best pattern can be obtained only when all the zeros lie on the real axis, and that any complex zeros tend to produce higher sidelobe levels and broader beamwidth. Therefore, the zeros of P_N must be real, and since u_n is real, t_n is also real.

(b) The Constant h Must Be Zero for an Optimum Pattern

In (7c), we note that for the range $u \geqslant u_{N+1}$, the zeros of $g(u)$ are u_n, $n = N+1, N+2, \ldots$ in eq. (4). In the range $u < u_{N+1}$, we wish to place N zeros $u_n + t_n$ so as to produce a desired pattern. Now, the optimum pattern requires the minimum beamwidth for a given sidelobe level. This can be achieved only when the zeros are placed as near to the origin as possible while keeping the sidelobes at a given level.

It can easily be seen from eq. (4) that as h becomes smaller, the zeros u_n for $n \geqslant N+1$ move towards the origin. But the negative values of h can not be used because the first zero is lost and the nth zero for $h < 0$ is farther from the origin than the nth zero for $h > 0$. Thus, the optimum condition requires $h = 0$ and the first zero u_0 coincides with the origin.

The radiation pattern (7c) must be written then as

$$(7d) \qquad g(u) = \frac{2J_1(u) \prod_{n=1}^{N} \left[1 - \left(\frac{u}{u_n + t_n}\right)^2\right]}{u \prod_{n=1}^{N} \left[1 - \left(\frac{u}{u_n}\right)^2\right]}$$

where u_n is a positive root of $J_1(u) = 0$.

It may be noted from eq. (3) that the source field is finite at the edge $r = a$ for the case $h \neq \infty$. If $h \to \infty$ may be used, the source field always approaches zero as $r \to a$.

(c) Definition of Optimum Pattern

Optimum pattern is defined as the one having a minimum beamwidth for
a given sidelobe ratio (or a maximum sidelobe ratio for a given beamwidth)
for a given N where $N-1$ is the number of terms used to describe the source
function as in (3). The significant difference in the definition of the optimum
pattern between the linear array and the aperture lies in this additional
condition concerning N for the latter. For a given N, we have a freedom
of choosing N zeros or u_n+t_n in (7d) to make the pattern optimum. Since
we have only N zeros to adjust, the best we can hope to obtain is the equal
level for the first N sidelobes. The rest of the sidelobes are tapered down
according to the equation (7d) and we have no control over those sidelobes
(see Fig. 2).
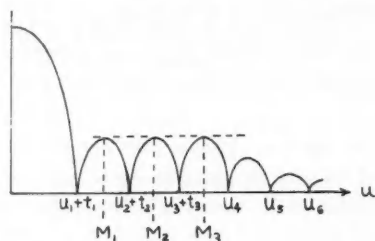
Fig 2.   Optimum pattern ($N=3$). Equal level for the first N sidelobes. Tapered sidelobes
for $u > u_{N+1}$.

(d) N Must Be Finite

It may be obvious from Fig. 2 that the larger the N, the closer the zeros
u_n+t_n can be chosen towards the origin for a given sidelobe level. It seems then
that the infinite N or the infinite series for the source would achieve the truly
optimum pattern. That this infinite series is physically impossible was shown
by Van Der Maas (1954) and Taylor (1955) for the line source. It is shown
in the Appendix that a similar argument can be made for the circular aperture.
If the source function is an infinite series, the equal sidelobes are extended
in all the region $u_1 < u \le \infty$ and this requires the value of the source function
$f(r)$ at the edge $r = 1$ to become infinite. Therefore in order for $f(r)$ to be
finite, N must be finite.

(e) Minimum and Maximum N, Supergain

In order to find the practical range of N, let us consider a pattern as shown
in Fig. 3. Let us consider the design for 30-db sidelobe level. If we employ
$N = 2$, we can choose the first two zeros to get 30-db level for the first two
sidelobes. However, the third sidelobe cannot be controlled and though the
level may be slightly lower than 28 db, the third lobe may remain above
30 db. Therefore N must be at least 3, for then the fourth lobe has 31 db or
lower and the situation that all the sidelobes are equal to or below 30 db is
established. In general, the minimum N must be chosen such that the $(N+1)$th
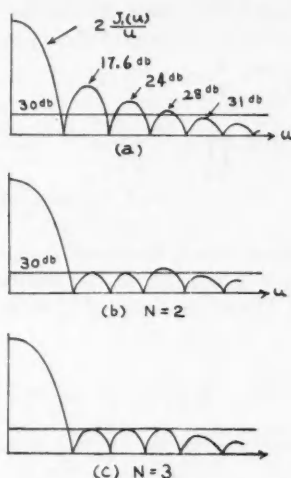sidelobe of $2J_1(u)/u$ has the level below the desired sidelobe level.

FIG. 3.   Choice of N. For 30 db, $N = 2$ is not enough, $N = 3$ is minimum.

The maximum N is determined mainly by the supergain consideration. If N is chosen so large that u_n lies in the invisible region, then $g(u)$ in the region $(2\pi a/\lambda) < u < u_{N+1}$ must be increased to attain the prescribed sidelobe level. Thus, this leads to larger reactive power and a supergain antenna. Therefore the maximum N must be such that u_N is in the visible region.

In fact if u_N is in the invisible region, we can place all N zeros in the visible region, thus obtaining a smaller beamwidth than the optimum design in this paper for the same sidelobe level. However, since this requires excessively large reactive power in the region $(2\pi a/\lambda) < u < u_{N+1}$ this antenna is not practical.

Between the above two limits, N must be determined by practical considerations such as the amount of computational labor (later it will be shown that the solution of N linear equations is required) and the physical characteristics of the source, which may not be able to produce too high an harmonic.

3. Optimum Condition and Solution

Our next task is then to find a method to determine the zeros $u_n + t_n$ in (7d) in order to realize the optimum pattern. To this end, we formulate the optimum condition in the following manner. It is seen from the previous section and Fig. 2 that there are N sidelobes in the region $u_1 < u < u_{N+1}$. Assume that the peaks of those sidelobes occur at $u = M_n$, $n = 1, 2, 3, \ldots N$ (see Fig. 2). Then the optimum condition is expressed by the following N equations:

$$(8) \qquad |g(M_1)| = |g(M_2)| = |g(M_3)| = \ldots = |g(M_N)| = b$$

where b is the sidelobe level and $g(u)$ is shown in (7d). M_n are functions of $t_1, t_2, \ldots t_n$. Therefore, this is a system of N equations for N unknowns $t_1, t_2, \ldots t_n$.

The solution of (8) seems rather difficult, but the following procedure is found quite effective in solving a problem of this type. Let us write equation (7d) in the following manner:

$$(9) \qquad g(u) = \frac{2J_1(u)}{u} \prod_{n=1}^{N} \frac{\left[1 + \dfrac{2u_n}{u_n^2 - u^2} t_n + \dfrac{1}{u_n^2 - u^2} t_n^2\right]}{\left[1 + \dfrac{2}{u_n} t_n + \dfrac{1}{u_n^2} t_n^2\right]}.$$

Let us for a moment assume that t_n are small compared with u_n, and that t_n^2 terms are negligible. Now in eq. (8), M_n are located at about the middle point between u_n and u_{n+1}. Therefore, for small t_n, we approximate the product in (9) by a series,

$$(10) \qquad g(M_m) = \frac{2J_1(M_m)\left[1 + \displaystyle\sum_{n=1}^{N} \frac{2u_n}{u_n^2 - M_m^2} t_n\right]}{M_m\left[1 + \displaystyle\sum_{n=1}^{N} \frac{2}{u_n} t_n\right]}.$$

Therefore, eq. (8) becomes

$$(11) \qquad \sum_{n=1}^{N} a_{mn} t_n = C_m, \qquad\qquad m = 1, 2, \ldots N,$$

$$(12) \qquad a_{mn} = \frac{2u_n}{u_n^2 - M_m^2} - \left|\frac{M_m b}{2J_1(M_m)}\right| \frac{2}{u_n},$$

$$c_m = \left|\frac{M_m b}{2J_1(M_m)}\right| - 1.$$

The equation (11) seems to be N linear equations for N unknowns. However, there are two points which must be clarified in order for (11) to be treated as a linear equation.

(a) t_n Must Be Small

The equation (10) holds only for small t_n. However, this is not an essential difficulty, because this process can be repeated and after the repeated process, t_n becomes so small that equation (10) holds almost exactly. The repeated process is as follows:

Suppose we solved (11) and found t_n; $g(u)$ in (7d) is not yet optimum because t_n may not be small. To find the pattern closer to optimum, let the zeros be given by the $u_n + t_n + t_n^1$. Then

$$(13) \qquad g(u) = g_1(u) \frac{\displaystyle\prod_{n=1}^{N}\left[1 - \left(\frac{u}{u_n + t_n + t_n^1}\right)^2\right]}{\displaystyle\prod_{n=1}^{N}\left[1 - \left(\frac{u}{u_n + t_n}\right)^2\right]}.$$

where

$$(14) \qquad g_1(u) = \frac{2J_1(u) \prod_{n=1}^{N} \left[1 - \left(\frac{u}{u_n + t_n} \right)^2 \right]}{u \prod_{n=1}^{N} \left[1 - \left(\frac{u}{u_n} \right)^2 \right]} .$$

$g_1(u)$ is obviously an improvement over $2J_1(u)/u$. And if we compare (13) with (7d), we see that (13) has the same form except that $[2J_1(u)]/u$ and u_n in (7d) are replaced by $g_1(u)$ and $u_n + t_n$ respectively in (13). Therefore, to get the better pattern we use

$$(15) \qquad \sum_{n=1}^{N} a_{mn} t_n^1 = c_m, \qquad\qquad m = 1, 2, \ldots N$$

where a_{mn} and c_m are shown in (12) with u_n and $2J_1(M_m)/M_m$ replaced by $u_n + t_n$ and $g_1(M_m)$.

Solving (15), we obtain t_n^1 and we get the improved pattern

$$(16) \qquad g_2(u) = \frac{2J_1(u) \prod_{n=1}^{N} \left[1 - \left(\frac{u}{u_n + t_n + t_n^1} \right)^2 \right]}{u \prod_{n=1}^{N} \left[1 - \left(\frac{u}{u_n} \right)^2 \right]} .$$

The further improved pattern may be obtained by letting the zeros be given by $u_n + t_n + t_n^1 + t_n^{11}$ and solving the equation similar to (15) for t_n^{11}, and theoretically this process can be repeated indefinitely to obtain the truly optimum pattern. However, for practical purpose, t_n^1 usually gives satisfactory results.

(b) *Choice of M_m*

The above discussion concerning the linear equation for t_n is valid only when M_m is independent of t_n. But M_m is actually a function of t_n. This difficulty can be avoided by assuming M_m independent of t_n. One such choice is

$$(17) \qquad M_m = \frac{u_m + u_{m+1}}{2} .$$

This assumes that the peak point of the sidelobe is at the midpoint between zeros. This causes an error but the error for the sidelobe of the pattern $[2J_1(u)]/u$ is less than 0.4 db. Considering the great simplification made possible by the assumption (17), this unavoidable error of 0.4 db is certainly tolerable.

4. *Numerical Example*

As an example, let us consider a design with a sidelobe level of 25 db. As is seen from Fig. 3, the minimum N is 2. However, since three linear equations can be easily solved, we take $N = 3$. Obviously, the higher N will give the better pattern. Now we employ the following constants for eqs. (11) and (12).

$$
(18) \quad
\begin{array}{ll}
u_n = \text{zeros of } J_1(u) & M_m = \text{maximum point of } J_1(u)/u \\
u_1 = 3.83 & M_1 = 5.33 \\
u_2 = 7.016 & M_2 = 8.53 \\
u_3 = 10.173 & M_3 = 11.70
\end{array}
$$

$$
b = \frac{1}{17.78} \ (25 \text{ db down})
$$

Solving the linear eq. (11) we get $g_1(u)$ in (14)

$$
(19) \quad g_1(u) = \frac{2 J_1(u) \left[1 - \left(\dfrac{u}{4.1625} \right)^2 \right] \left[1 - \left(\dfrac{u}{6.652} \right)^2 \right] \left[1 - \left(\dfrac{u}{9.620} \right)^2 \right]}{u \left[1 - \left(\dfrac{u}{3.83} \right)^2 \right] \left[1 - \left(\dfrac{u}{7.016} \right)^2 \right] \left[1 - \left(\dfrac{u}{10.173} \right)^2 \right]} .
$$

This $g_1(u)$ exhibits the obvious improvement as shown in Fig. 4, but its first sidelobe is still higher than the desired 25 db. This is because of the relatively
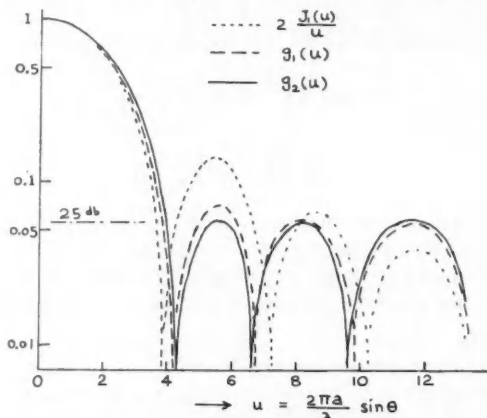
FIG. 4.   Example of synthesis for 25-db sidelobe level.

large t_n for which the equations (10) and (11) hold only approximately. The next attempt in (15) must improve this pattern considerably, because t_n^1 is now very small.

After computing t_n^1 in (15) we obtain the improved pattern

$$
(20) \quad g_2(u) = \frac{2 J_1(u) \left[1 - \left(\dfrac{u}{4.2885} \right)^2 \right] \left[1 - \left(\dfrac{u}{6.561} \right)^2 \right] \left[1 - \left(\dfrac{u}{9.576} \right)^2 \right]}{u \left[1 - \left(\dfrac{u}{3.83} \right)^2 \right] \left[1 - \left(\dfrac{u}{7.016} \right)^2 \right] \left[1 - \left(\dfrac{u}{10.173} \right)^2 \right]} .
$$

In Fig. 4, the improved pattern $g_1(u)$ and the further improved pattern $g_2(u)$ are shown together with the pattern $2 J_1(u)/u$. The half-power beamwidth can be approximately given by

$$(21) \qquad \theta < 1.02 \frac{\lambda}{D} \frac{u_1 + t_1 + t_1^1}{u_1} \text{ radians.}$$

In Fig. 5, the synthesized pattern is shown with the conventional 24.6-db pattern $8J_2(u)/u$. Both have the same sidelobe level, but the marked improve-
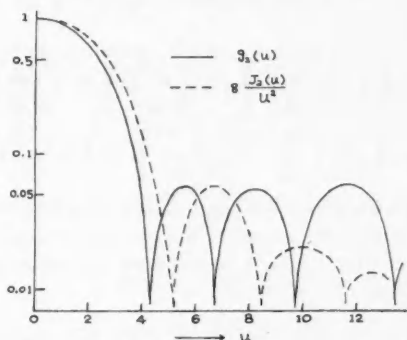

FIG. 5. Comparison between the optimum and the conventional pattern for the same sidelobe level of 25 db.

ment of the synthesized pattern is obvious in the reduction of the beamwidth. The source function can be found by (6). Thus

$$(22) \qquad \begin{aligned} f(r) &= 1 + 0.912\, J_0(3.83\, r), \\ &\quad + 0.595\, J_0(7.016\, r), \\ &\quad - 0.987\, J_0(10.173\, r) \qquad \text{for } 0 \leqslant r \leqslant 1, \\ &= 0 \qquad\qquad\qquad\qquad\quad \text{for } r > 1. \end{aligned}$$

5. Comparison with Taylor's Design

Taylor's design procedure for a line source can be adapted to the circular aperture in the following manner:

For $u \geqslant u_{N+1}$, the zeros are roots of $J_1(u)$.

For $u < u_{N+1}$, we employ the zeros which are similar to that of the ideal pattern

$$(23) \qquad g(u) = \frac{\cos \sqrt{(u^2 - A^2)}}{\cosh A}, \qquad \cosh A = \text{sidelobe ratio.}$$

Thus

$$(24) \qquad u_n = \sigma \sqrt{[A^2 + (n - 1/2)^2 \pi^2]} \quad \text{for } n = 1, 2, \ldots N,$$

where

$$(25) \qquad \sigma = \frac{u_{N+1}}{\sqrt{\{A^2 + [(N+1) - 1/2]^2 \pi^2\}}}.$$

For the example of the previous section,

$$N = 3, \qquad A = 3.57, \qquad \sigma = 1.11.$$

So, we obtain

$$(26) \qquad \begin{aligned} u_1 &= 4.34, \\ u_2 &= 6.57, \\ u_3 &= 9.58. \end{aligned}$$

The pattern is given by

$$(27) \qquad g_T(u) = \frac{2 J_1(u)\left[1-\left(\dfrac{u}{4.34}\right)^2\right]\left[1-\left(\dfrac{u}{6.57}\right)^2\right]\left[1-\left(\dfrac{u}{9.58}\right)^2\right]}{u\left[1-\left(\dfrac{u}{3.83}\right)^2\right]\left[1-\left(\dfrac{u}{7.016}\right)^2\right]\left[1-\left(\dfrac{u}{10.173}\right)^2\right]}.$$

The first zero is at 4.34 while the optimum design yields 4.2885 which gives a narrower beam and this improvement of the optimum design over Taylor's design is due to the fact that Taylor's design does not insure the equal side-lobe level for the range $u_1 < u < u_{N+1}$.

PART II. TRAVELING WAVE TYPE MODES

1. Formulation of the Problem

Let us consider a circular aperture in a perfectly conducting plane (Fig. 6). The electric field is assumed to lie in a plane of aperture and to be directed in ϕ_0 direction. Furthermore, we assume no variation of field in ϕ_0 and the
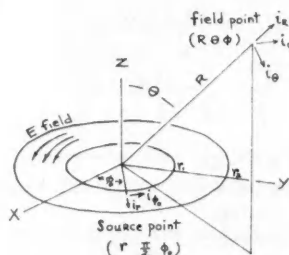
FIG. 6.   Source and field points.

fields are functions of radius only. This choice of field configuration is made on the basis of a recent experimental investigation on a radial surface wave antenna that was performed in our Antenna Laboratory. However, the method to be described in this paper can be applied equally well to other configurations with little modifications.

The Huygens' principle of the electromagnetic vector problem gives the necessary relationship between the source electric field and the radiation fields. The electric field produced by a given electric field over an aperture in a conducting plane is given by (Lewin 1951)

$$(1) \qquad E = \frac{1}{2\pi} \nabla \times \int_s (n \times E) \frac{e^{-jkR}}{R} \, ds.$$

The far-zone radiation field is then given by

$$(2) \qquad E_\theta = -\frac{jk}{2\pi R_0} e^{-jkR_0} \int_s (-\mathbf{n}\times\mathbf{E})\cdot\mathbf{i}_\phi\, e^{jkr\,\mathbf{1}_r\cdot\mathbf{1}_R}\, ds$$

$$(3) \qquad E_\phi = -\frac{jk}{2\pi R_0} e^{-jkR_0} \int_s (\mathbf{n}\times\mathbf{E})\cdot\mathbf{i}_\theta\, e^{jkr\,\mathbf{1}_r\cdot\mathbf{1}_R}\, ds$$

where $\mathbf{n}$ is a unit vector outward normal to the surface S, and $\mathbf{i}_r$, $\mathbf{i}_R$, $\mathbf{i}_\theta$, $\mathbf{i}_\phi$ are unit vectors as shown in Fig. 6. Since $\mathbf{E} = E\mathbf{i}_{\phi0}$, we have

$$(4) \qquad E_\theta = \frac{jk}{2\pi R_0} e^{-jkR_0} \int_s E \sin(\phi-\phi_0)\, e^{jkr\cos\gamma}\, ds$$

$$(5) \qquad E_\phi = \frac{jk}{2\pi R_0} e^{-jkR_0} \int_s E \cos\theta \cos(\phi-\phi_0)\, e^{jkr\cos\gamma}\, ds$$

where

$$(6) \qquad \cos\gamma = \sin\theta\cos(\phi-\phi_0)$$

$$ds = r\, dr\, d\phi_0.$$

Since E is a function of r only, the integration with respect to ϕ_0 can be readily performed to yield

$$E_\theta = 0$$

$$(7) \qquad E_\phi = \frac{jk}{2\pi R_0} e^{-jkR_0} \cos\theta\, g(\theta)$$

$$(8) \qquad g(\theta) = \int_{r_1}^{r_2} f(r)\, J_1(kr\sin\theta)\, rdr$$

where $f(r) = E(r)$ is used to conform with the notation in Part I. It is seen that the radiation pattern is a product of $\cos\theta$ and the function $g(\theta)$. Our problem of synthesis is then that of finding the source function $f(r)$ required to produce a prescribed radiation function.

2. Source Functions

Two different forms of the source functions may be considered and each one demands a different approach to our synthesis problems. One is a source function with constant phase and varying amplitude. The other is the function with varying phase and varying amplitude. Both functions are capable of producing the desired beam at an arbitrary angle, and some general aspects of these problems will be discussed here.

(a) Constant Phase

The source function $f(r)$ takes a form

$$(9) \qquad \begin{aligned} f(r) &= \sum_n a_n J_1(\alpha_n r) && \text{for } 0 < r < a \\ &= 0 && \text{for } r > a \end{aligned}$$

where α_n are real. Each term is similar to the different modes in a circular guide. In general, the choice of α_n may be made such that

$$(10) \qquad \alpha_n a J_1'(\alpha_n a) + h J_1(\alpha_n a) = 0.$$

The magnitude of the source function at the edge depends on h as in Part I. This problem will not be treated in this paper since the situation is similar to the Part I.

(b) *Varying Phase*

It is often desired that the source is composed of the traveling wave type modes. Our particular choice is

$$(11) \qquad\qquad f(r) = \sum_n a_n N_n H_1^{(2)}(\alpha_n r) \qquad\qquad \text{for } r_1 \leqslant r \leqslant r_2,$$

$$= 0 \qquad\qquad \text{for } r < r_1,$$

$$r > r_2.$$

The Hankel function $H_1^{(2)}$ is chosen because of our choice of time variation $e^{j\omega t}$, so that $H_1^{(2)}$ represents a traveling wave in a positive r direction. N_n is a complex number which gives the phase shift between each term and also serves to normalize the radiation pattern; a_n is a real number representing the strength of field contained in each term.

In the subsequent sections, an analysis and a synthesis procedure for the sources represented by (11) will be explained in detail.

3. *Analysis of Radiation Pattern*

We wish to examine the radiation function

$$(12) \qquad\qquad g(\theta) = \int_{r_1}^{r_2} f(r) J_1(kr \sin\theta)\, r\, dr$$

for the sources given by eq. (11). First, we take one term of the series in eq. (11). Then, we get

$$(13) \qquad\qquad g(\theta) = a_n N_n \int_{r_1}^{r_2} H_1^{(2)}(\alpha_n r) J_1(kr \sin\theta)\, r\, dr.$$

At this point let us choose r_1 or α_n such that

$$(14) \qquad\qquad\qquad \alpha_n r_1 > 1.$$

This does not restrict the applicability of our solution, because as will be seen later, $H_1^{(2)}(\alpha_n r)$ yields the main beam at θ_n where $k \sin\theta_n = \alpha_n$, and we can always choose r_1 to satisfy (14). Under this condition (14), the Hankel function in (13) can be approximated by its asymptotic form whenever it is convenient.

The integration in (13) can be easily performed by the Lommel integral formula. However, this integration does not give us a form suitable to our analysis and synthesis problems for the useful range of θ. Thus, we consider two cases, one dealing with the useful range of θ, $\theta_d < \theta < \pi/2$, and the other dealing with the angle θ nearly equal to zero, $0 \leqslant \theta < \theta_d$.

(a) $\theta_d < \theta < \pi/2$

In this range of θ, we employ the form

$$(15) \qquad\qquad g(\theta) = e^{jp(\theta)}[g_1(\theta) + e^{-jq(\theta)}g_2(\theta)],$$

$$(16) \qquad e^{jp} g_1(\theta) = \frac{a_n N_n}{2} \int_{r_1}^{r_2} H_1^{(2)}(\alpha_n r) H_1^{(1)}(kr \sin \theta) \, r \, dr,$$

$$(17) \qquad e^{j(p-q)} g_2(\theta) = \frac{a_n N_n}{2} \int_{r_1}^{r_2} H_1^{(2)}(\alpha_n r) H_1^{(2)}(kr \sin \theta) \, r \, dr,$$

where we employed the relation

$$(18) \qquad J_1(x) = \tfrac{1}{2}[H_1^{(1)}(x) + H_1^{(2)}(x)]$$

and the phase functions $p(\theta)$ and $q(\theta)$ are inserted to simplify the expressions later and are independent of n. The integration in eqs. (16) and (17) can be readily performed, and if we choose θ_d such that

$$(19) \qquad kr_1 \sin \theta_d > 1$$

then all the Hankel functions can be approximated by their asymptotic forms.

The results can be written as

$$(20) \qquad g_1(u) = a_n \sqrt{\frac{u_n}{u} \frac{\sin (u - u_n)}{u - u_n}},$$

$$(21) \qquad g_2(u) = a_n \sqrt{\frac{u_n}{u} \frac{\sin (u + u_n)}{u + u_n}},$$

$$(22) \qquad p(\theta) = \frac{2\pi}{\lambda} r_0 \sin \theta,$$

$$(23) \qquad q(\theta) = \frac{4\pi}{\lambda} r_0 \sin \theta + \frac{\pi}{2},$$

where

$$r_0 = 1/2(r_1 + r_2),$$

$$r_d = 1/2(r_2 - r_1),$$

$$(24) \qquad u = \frac{2\pi}{\lambda} r_d \sin \theta,$$

$$u_n = \alpha_n r_d,$$

and the normalizing constant N_n in (16) and (17) has been chosen as

$$(25) \qquad N_n = \frac{\alpha_n \pi}{r_2 - r_1} e^{j\alpha_n r_0}.$$

The visible region of u is then

$$(26) \qquad 0 < u \leqslant \frac{2\pi r_d}{\lambda}.$$

It is important to note that there is a one-to-one correspondence between the intensity a_n and the value of $g_1(u)$ at $u = u_n$:

$$(27) \qquad g_1(u_n) = a_n.$$

The physical interpretations of eqs. (20) and (21) may be made by considering the radiation pattern produced by a traveling wave on a rectangular aperture. It is well known that the aperture field in a rectangular aperture expressed by

$$(28) \qquad f_1(x) = e^{-j\alpha_n x}, \quad -x_d < x < x_d$$

produces the radiation pattern

$$(29) \qquad g_1(u) = \frac{\sin (u - u_n)}{u - u_n}$$

where

$$u = \frac{2\pi}{\lambda} x_d \sin \theta, \qquad u_n = \alpha_n x_d.$$

We can see that eq. (20) has exactly the same form as (29) except $\sqrt{(u_n/u)}$. Therefore, $g_1(u)$ is similar to the radiation from the source wave traveling in a direction of the observation point. Similarly, $g_2(u)$ represents the radiation from the source wave traveling in the opposite direction.

The radiation from the circular aperture is a combination of these two $g_1(u)$ and $g_2(u)$ as in eq. (15). It is understandable that since the field over the aperture travels in all directions around the axis $r = 0$, $g(u)$ must be a sum of two waves traveling in opposite directions. (Fig. 7).

$g_1(u)$ behaves like a $\sin x/x$ shifted by u_n except for $\sqrt{(u_n/u)}$, and has a main beam at u_n; $g_2(u)$ is relatively small in the range $0 < u < u_n$ (see Fig. 8 (a))
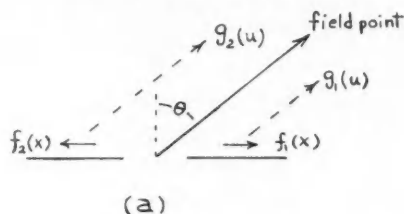
(a)
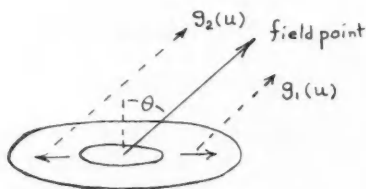
(b)

Fig. 7. Similarity between two rectangular apertures and circular aperture.
(a) Two rectangular apertures. The one on the right side carries the source wave $f_1(x)$ traveling to the right. The aperture on the left carries $f_2(x)$ traveling to the left.
(b) Circular aperture produces the radiation pattern similar to $g_1(\theta)$ and $g_2(\theta)$ from two rectangular apertures. The phase difference is $(2\pi/\lambda)(2r_0) + (\pi/2)$.

Therefore, the first approximation for $g(u)$ may be given by neglecting $g_2(u)$:

$$(30) \qquad |g(u)| \approx |g_1(u)|.$$

The maximum error introduced by (30) may be given by the maximum value of $g_2(u)$ which is

$$(31) \qquad a_n \sqrt{\frac{u_n}{u}} \frac{1}{u+u_n}.$$

For u near u_n or peak point, this error will be approximately
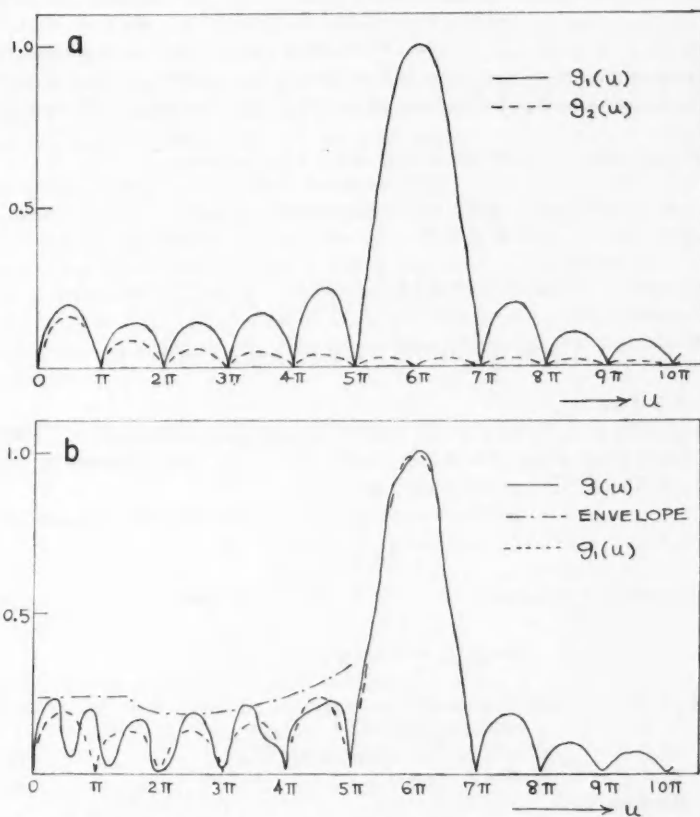
$$(32) \qquad a_n \frac{1}{2u_n}.$$

Fig. 8. (a) Radiation functions $g_1(\theta)$ and $g_2(\theta)$.
$r_1 = \lambda,$ $r_2 = 7.92\,\lambda,$ $r_d = 3.46\,\lambda,$
$\theta_n = 60°,$ $u_n = 6\pi,$ visible range of $u \leqslant 6.92\,\pi.$
(b) Radiation pattern $g(\theta)$ of eq. (34) and envelope.

The detailed shape of the pattern $g(u)$ may be found by considering

$$(33) \qquad |g(u)| = \{|g_1(u)|^2 + |g_2(u)|^2 + 2|g_1 g_2 \cos \psi|\}^{\frac{1}{2}}$$

where ψ is the phase difference between g_1 and g_2. This phase difference is a function of u so that ψ increases by 2π as u increases by the amount $(r_d/r_0)\pi$ as is seen from eqs. (15) and (23). Since $r_d < r_0$, as u varies by π, ψ undergoes at least a complete cycle of 2π or more.

Therefore, the radiation function $g(u)$ consists mainly of $g_1(u)$ and the effect of $g_2(u)$ is the small high-frequency components superimposed on $g_1(u)$, and $g(u)$ varies between $|g_1| + |g_2|$ and $||g_1| - |g_2||$ (see Fig. 8 (b)).

(b) $0 \leqslant \theta < \theta_d$

In this range of angle, the asymptotic form for Hankel functions no longer holds and we must investigate the original equation (13). We note that for this range, $g_1(u)$ and $g_2(u)$ arrive at the observation point with almost the same magnitudes and little phase difference and it is no longer advantageous to treat the radiation field as composed of two waves traveling in the opposite directions.

The integration in (13) yields after some manipulation

$$(34) \qquad g(\theta) = \frac{a_n V_n}{\beta^2 - \alpha_n^2} \sqrt{\frac{2\alpha_n r_2}{\pi}}\, e^{-j(\alpha_n r_2 - \frac{\pi}{4})}(A - B)$$

$$(35) \qquad A = J_1(\beta r_2) - j\frac{\beta}{\alpha_n} J_0(\beta r_2)$$

$$(36) \qquad B = \sqrt{\frac{r_1}{r_2}}\, e^{j\alpha_n(r_2 - r_1)}[J_1(\beta r_1) - j\frac{\beta}{\alpha_n} J_0(\beta r_1)]$$

where $\beta = k \sin \theta$.

In eq. (35), β/α_n is very small and A is approximately equal to $J_1(\beta r_2)$, which has a peak value of 0.582 at $\beta r_2 = 1.84$. In eq. (36), the second term is also small and B is approximately given by

$$(37) \qquad |B| \approx \sqrt{\frac{r_1}{r_2}}\, J_1(\beta r_1).$$

The approximate maximum value of $|A - B|$ will be then

$$(38) \qquad |A - B|_{max} \approx 0.582 + 0.92 \left(\frac{r_1}{r_2}\right)^{3/2}.$$

Therefore, the approximate maximum value of $g(u)$ near $\theta = 0$ is given by

$$(39) \qquad a_n \sqrt{\frac{\pi}{2u_n}} \sqrt{\frac{r_2}{r_d}}\left[0.582 + 0.92 \left(\frac{r_1}{r_2}\right)^{3/2} \right].$$

(c) Dividing Line

The angle θ_d can be found by equating the peak value of (15) and (39). Thus

$$(40) \quad a_n \sqrt{\frac{u_n}{u}}\left[\left|\frac{1}{u - u_n}\right| + \left|\frac{1}{u + u_n}\right| \right] = a_n \sqrt{\frac{\pi}{2u_n}} \sqrt{\frac{r_2}{r_d}}\left[0.582 + 0.92 \left(\frac{r_1}{r_2}\right)^{3/2} \right].$$

From this, we obtain approximately

$$(41) \qquad u_d \approx 1.2\,\pi\,\frac{1}{1+\dfrac{r_1}{2r_d}} \qquad\qquad \text{for } r_1 \ll r_2.$$

(d) Analysis of Pattern

It may be interesting to investigate the detailed shape of the pattern in view of the above analysis. In Fig. 8(a), $g_1(\theta)$ and $g_2(\theta)$ are plotted for $r_1 = \lambda$ and $r_2 = 7.92\lambda$ and $\theta_n = 60°$. In Fig. 8(b), the exact pattern computed from eq. (34) is shown together with $g_1(\theta)$ and the envelope given by

$$\sqrt{\frac{u_n}{u}}\left[\frac{1}{|u-u_n|}+\frac{1}{|u+u_n|}\right] \qquad\qquad \text{for } \theta > \theta_d$$

and eq. (39) for $0 < \theta < \theta_d$.

It may be seen that the actual pattern consists mainly of $g_1(\theta)$ and the effect of $g_2(\theta)$ is the high-frequency components of small amplitude. The total pattern never exceeds the envelope given above.

4. Source Function which Vanishes at the Edges

Since we are considering the aperture on a conducting plane, it is required that the electric field at r_1 and r_2 be zero. In this section, we wish to examine such a source distribution and the radiation pattern it produces.

Each term of the source function given by (11) does not vanish at r_1, and r_2, but a suitable combination of the terms will produce this vanishing field.

Let us approximate eq. (11) by using the asymptotic form of Hankel function

$$(42) \qquad \begin{aligned} f(r) &= \sum_n a_n \frac{1}{r_2-r_1}\sqrt{\frac{2\pi\alpha_n}{r}}\,e^{-j\alpha_n(r-r_0)+j\frac{3}{4}\pi} \qquad \text{for } r_1 < r < r_2, \\ &= 0 \qquad\qquad\qquad\qquad\qquad\qquad\quad \text{for } 0 \leqslant r < r_1,\quad r_2 < r. \end{aligned}$$

We combine the nth and the mth terms and letting

$$(43) \qquad \begin{aligned} \frac{\alpha_n+\alpha_m}{2} &= \alpha_p \\ \frac{\alpha_m-\alpha_n}{2} &= \alpha_k \end{aligned}$$

and choosing α_n and α_k in such a manner that

$$(44) \qquad \begin{aligned} a_n\sqrt{\alpha_n} &= a_m\sqrt{\alpha_m} = a_k\sqrt{\alpha_p} \\ \alpha_k &= (2k+1)\,\frac{\pi}{2}\,\frac{1}{r_d}\,, \qquad\qquad k = 0, 1, 2, \ldots \end{aligned}$$

we get

$$(45) \qquad f(r) = K\,\frac{e^{-j\alpha_p r}}{\sqrt{r}}\sum_k a_k \cos\,(2k+1)\,\frac{\pi}{2}\,\frac{r-r_0}{r_d}$$

where

(46)
$$K = \text{constant},$$

$$= \frac{2\sqrt{2\pi\alpha_p}}{r_2 - r_1} e^{j\alpha_p r_0 + j_4^2 \pi}.$$

The series in eq. (45) is symmetric about $r = r_0$ and vanishes at r_1 and r_2. If a_k is real, eq. (45) represents a traveling wave with a constant velocity and its amplitude varies approximately as $1/\sqrt{r}$.

The radiation field arising from such a source distribution can be easily obtained:

(47)
$$g_1(u) = \sum_k a_k \sqrt{\frac{u_p}{u}} \frac{2(2k+1)\frac{\pi}{2}(-1)^{k+1}\cos(u-u_p)}{(u-u_p)^2 - \left[(2k+1)\frac{\pi}{2}\right]^2},$$

(48)
$$g_2(u) = \sum_k a_k \sqrt{\frac{u_p}{u}} \frac{2(2k+1)\frac{\pi}{2}(-1)^{k+1}\cos(u+u_p)}{(u+u_p)^2 - \left[(2k+1)\frac{\pi}{2}\right]^2}.$$

There is a one-to-one correspondence between a_k and the value of $g_1(u)$ at $u = u_p \pm (2k+1)\pi/2$.

(49)
$$g_1\left[u_p \pm (2k+1)\frac{\pi}{2}\right] = a_k \sqrt{\left[\frac{u_p}{u_p \pm (2k+1)\frac{\pi}{2}}\right]}.$$

Also, $\sqrt{u}\, g_1(u)$ is an even function of $(u-u_p)$.

5. *Narrow Beam*

If we desire a narrow beam directed at an angle θ_p, it is most convenient to choose

(50)
$$\alpha_p = \frac{2\pi}{\lambda}\sin\theta_p, \qquad u_p = \alpha_p r_d.$$

The general form of the radiation pattern $g_1(u)$ can then be written as

(51)
$$g_1(u) = \sqrt{\frac{u_p}{u}} \cos(u - u_p) \frac{P_N[(u-u_p)^2]}{\prod_{k=0}^{N}\left[1 - \left(\frac{u-u_p}{(2k+1)\frac{\pi}{2}}\right)^2\right]}$$

where $P_N[(u-u_p)^2]$ is a polynomial in $(u-u_p)^2$ of order N. This can also be written using the locations of zeros as follows:

(52)
$$g_1(u) = \sqrt{\frac{u_p}{u}} \cos(u - u_p) \frac{\prod_{k=1}^{N}\left[1\left(-\frac{u-u_p}{v_n}\right)^2\right]}{\prod_{k=0}^{N}\left[1\left(-\frac{u-u_p}{(2k+1)\frac{\pi}{2}}\right)^2\right]}$$

where v_n are zeros of $g_1(u)$.

Since the magnitudes of $g_2(u)$ are relatively small as compared with $g_1(u)$, we can neglect $g_2(u)$ as a first approximation. Then equation (52) is similar to the radiation pattern (7d) of Part I, and the same technique may be used to optimize the radiation pattern. It is also possible to include the effect of $g_2(u)$ by considering the radiation pattern $|g_1(u)| + |g_2(u)|_{max}$ in such a manner that the actual sidelobe level is always equal to or lower than the prescribed level. The detail of the treatment of this point is given in the previous report by Ishimaru and Held (1959).

(a) *Sidelobe Level*

If the source function consists of one term for $k = 0$ in eq. (45) we have

$$(53) \qquad f(r) = a_0 K \frac{e^{-j\alpha_p r}}{\sqrt{r}} \cos \frac{\pi}{2} \frac{r - r_0}{r_d} .$$

This is the simplest case and the source field is $1/\sqrt{r}$ times the half sine wave.

The first sidelobe level is approximately at $u = u_p \pm 2\pi$ and the maximum magnitude is given by

$$(54) \qquad |g_1(\theta)| + |g_2(\theta)|_{max} = a_0 \sqrt{\frac{u_p}{u}} \pi \left[\frac{1}{(u - u_p)^2 - \left(\frac{\pi}{2}\right)^2} + \frac{1}{(u + u_p)^2 - \left(\frac{\pi}{2}\right)^2} \right].$$

If $u \gg u_p$, then this becomes

$$(55) \qquad a_0 \pi \left[\frac{4}{15\pi^2} + \frac{1}{4u_p^2} \right].$$

The sidelobe ratio is

$$(56) \qquad \frac{1}{15} + \frac{1}{4u_p^2} \left(\frac{\pi}{2}\right)^2.$$

As u_p becomes large, this ratio approaches $1/15$, which is 23.52 db.

(b) *Beamwidth*

When θ_p is not near $\pi/2$ and the beam is sufficiently narrow, $\cos \theta$ in eq. (7) is practically constant. We obtain from the equation

$$(57) \qquad \frac{\cos (u - u_p)}{1 - \left[\dfrac{u - u_p}{\dfrac{\pi}{2}}\right]^2} = \frac{1}{\sqrt{2}}$$

the beamwidth in terms of u,

$$(58) \qquad \Delta u = 3.74.$$

The beamwidth in terms of θ is

$$(59) \qquad \Delta \theta = \frac{3.74}{\dfrac{2\pi r_d}{\lambda} \cos \theta_p}$$

If θ is near $\pi/2$, it becomes more difficult to obtain the sharp beam. The beamwidth must be computed from

$$(60) \qquad \frac{\cos \theta}{\cos \theta_p} \frac{\cos (u - u_p)}{1 - \left[\dfrac{u - u_p}{\dfrac{\pi}{2}} \right]^2} = \frac{1}{\sqrt{2}} .$$

(c) *Choice of r_1 and r_d*

r_1 must be sufficiently large so that eq. (14) holds

$$(61) \qquad\qquad\qquad k r_1 \sin \theta_p > 1.$$

r_d must be chosen so as to give a desired narrow beamwidth. From (59)

$$(62) \qquad\qquad\qquad \frac{r_d}{\lambda} > \frac{3.74}{2 \pi \cos \theta_p \cdot \Delta\theta}$$

where $\Delta\theta$ is a desired beamwidth.

6. *Shaped Beam*

As stated in Section 4, $\sqrt{u}\, g_1(u)$ is an even function of $(u - u_p)$. Therefore, by the source function described in Section 4, it is not possible to obtain an arbitrary function of u. For example, if we wish to obtain the cosecant pattern

$$(63) \qquad | \cos \theta g(\theta) | = \operatorname{cosec} \left(\frac{\pi}{2} - \theta \right) \qquad\qquad \text{for } \theta_1 < \theta < \theta_2,$$

$$= 0 \qquad\qquad 0 \leqslant \theta < \theta_1 \text{ and } \theta_2 < \theta < \frac{\pi}{2},$$

we cannot choose u_p arbitrarily. Instead, we must choose u_p so as to produce this desired pattern. It is possible to choose u_p such that

$$(64) \qquad\qquad\qquad u_p = \frac{2 \pi r_d}{\lambda} .$$

Then, all the visible region of u is on one side of u_p and we could assign any prescribed arbitrary pattern in this region. Of course, the other side of u_p is in the invisible region of u and this would tend to increase the reactive power.

If we neglect $g_2(u)$ in (63), we can find the source function to approximate the radiation pattern in exactly the same manner as the Woodward method (1946).

CONCLUSIONS

In Part I, the synthesis of circular aperture antenna is considered with particular emphasis on the optimum pattern. Taylor's narrow-beam synthesis technique for a line source is applied to a circular aperture and the improvement over Taylor's design is shown together with the definition and the limitations of the optimum pattern.

In Part II, the circular aperture with sources composed of traveling wave modes is analyzed and its similarity with rectangular apertures is discussed in detail. Some considerations are given to narrow-beam and shaped-beam synthesis.

APPENDIX

N must be finite.

Let us consider the radiation pattern for circular and rectangular apertures:

(1)
$$g_c(u) = \frac{2 J_1(u) \prod_{n=1}^{N} \left[1 - \left(\frac{u}{u_n + t_n} \right)^2 \right]}{u \prod_{n=1}^{N} \left[1 - \left(\frac{u}{u_n} \right)^2 \right]},$$

(2)
$$g_r(u) = \frac{\sin u \prod_{n=1}^{N} \left[1 - \left(\frac{u}{n\pi + t_n} \right)^2 \right]}{u \prod_{n=1}^{N} \left[1 - \left(\frac{u}{n\pi} \right)^2 \right]}.$$

If N becomes infinite, both equations approach

$$\prod_{n=1}^{\infty} \left[1 - \left(\frac{u}{u_n + t_n} \right)^2 \right].$$

Therefore, we have the same ideal (but unrealizable) optimum pattern

(3)
$$g_i(u) = \frac{\cos \sqrt{(u^2 - A^2)}}{\cosh A}$$

where $\cosh A$ is a sidelobe ratio.

If this $g_i(u)$ is to be realized, the source function must be given by

$$a_k = \frac{2}{J_0(u_k)^2} g_i(u_k).$$

For large k,

$$u_k \approx k\pi + \frac{\pi}{4} \quad \text{and} \quad g_i(u_k) \approx \frac{(-1)^k}{\sqrt{2} \cosh A}.$$

The source function is a series of $a_k J_0(u_k r)$ and this will become at $r = 1$

$$a_k J_0(u_k) \rightarrow \frac{\sqrt{(\pi u_k)}}{\cosh A}.$$

As $u_k \rightarrow \infty$, the term becomes infinite and $f(r)$ at $r = 1$ is divergent.

ACKNOWLEDGMENTS

REFERENCES

ISHIMARU, A. and HELD, G. 1959. University of Washington, Electrical Engineering, Technical Report No. 33.
JAHNKE, E. and EMDE, F. 1945. Tables of functions (Dover Publications, New York), p. 146.
JOHNK, C. T. A. 1954. University of Illinois, Engineering Experiment Station, Technical Report No. 1.
LEWIN, L. 1951. Advanced theory of waveguides (Iliffe and Sons), p. 123.
SILVER, S. 1949. Microwave antenna theory and design (McGraw-Hill Book Co., Inc.), p. 194.
TAYLOR, T. T. 1955. IRE Trans., PGAP-3, 16.
VAN DER MAAS, G. J. 1954. J. Appl. Phys. 25, 121.
WOODWARD, P. M. 1946. J. Inst. Elect. Engrs. 93 (IIIA), 1554.

THE FREEZING POINTS OF HIGH PURITY METALS AS PRECISION TEMPERATURE STANDARDS

V. THERMAL ANALYSES ON 10 SAMPLES OF TIN WITH PURITIES GREATER THAN 99.99+%[1]

E. H. McLaren and E. G. Murdock

ABSTRACT

Extensive thermal analyses have been made on 10 samples (suppliers' analyzed impurity contents <0.2 to <100 p.p.m.) of high purity tin, including zone-refined metal; liquidus points have been intercompared with a precision of about 0.0002° C and alloy melting ranges have been examined following different types of freezing with and without overnight anneals near the solidus temperature. Samples of nominal 99.9999% purity tin were found to have such narrow alloy melting ranges that any ambiguity, arising from unknown impurity concentrations, in specifying the liquidus point of pure tin is well inside 0.001° C; a value of 231.913° C (Int. 1948) was found for the standard liquidus point of pure tin. An account is given of the supercooling that was observed on the bulk samples and of anomalous structures that were found on melting curves. An appendix gives the results of long-term intercomparisons of the temperatures realized in four water triple point cells.

INTRODUCTION

Earlier work* (Part II, 1957b) has shown that, with appropriate experimental conditions, it is possible to obtain highly reproducible plateaux that have nearly constant (within 0.0001° C) temperatures for long durations on the cooling curves of high purity samples of tin. The purpose of the present investigation was to increase our knowledge of the tin point by examining samples of the highest purity tin available from several refiners and to determine a value for the liquidus point of pure tin on the International Temperature Scale.

MATERIAL

Table I lists the origin, grade, and form of the tin metal as received and Table II shows the chemical analyses supplied by the sources. Attempts to estimate the expected lowerings of the liquidus from that of the pure element and the alloy melting ranges of the samples using these chemical analyses and known phase diagrams were abandoned due to the uncertainties in locating the liquidus for the tin–iron system at the tin-rich end and to the usual difficulties in locating the solidus for very dilute alloys. Campbell *et al.* (1949) report a eutectic transformation at about 0.003% Fe with the eutectic temperature not more than 0.1° C lower than the freezing temperature of the pure element; precision thermal analyses on a series of tin–iron alloys in this concentration range should yield an accurate determination of this liquidus.

TABLE I

Identification of the tin samples

Sample	Origin	Grade	Form
Sn.9	Vulcan Detinning Co. Sewaren, N.J.,	Spectrographic, VS-52SP(1–5) (zone refined)	Bar, 1.2×0.7×7.5 cm
Sn.8	U.S.A.	Spectrographic, VS-52SP(51–55) (zone refined)	Bar, 1.2×0.7×7.5 cm
Sn.6	Vulcan Detinning Co. Sewaren, N.J.,	Extra Pure, VS-65 (electrolytic)	Bar, 2.2×1.5×18.5 cm
Sn.3	U.S.A.	Extra Pure, VS-24 (electrolytic)	Bar, 2.2×1.5×18.5 cm
Sn.13	The Consolidated Mining and Smelting Co.	Special Research (34–37, 42) (electrolytic)	Bar, 250 g
Sn.7	Trail, B.C., Canada	High Purity, MR139 (electrolytic)	Bar, 2.5×2.5×25 cm
Sn.11	Johnson, Matthey and Co. Ltd., London, E.C.1, England	Specpure. J.M. 530	Rod, 0.6 diam.×16 cm
Sn.2*	National Bureau of Standards, Washington 25, D.C., U.S.A.	Standard Sample 42d	Cast ingot, 3.8 diam.×8.0 cm
Sn.12†	Philipp Bros. (Canada) Ltd., Montreal 25, Que.,	Zone Refined (received Feb. 1959)	Rod, 1.6 diam.×22 cm
Sn.10†	Canada	Zone Refined (received Nov. 1958)	Rod, 1.6 diam.×22 cm

*See Scribner (1952).
†Japanese zone-refined tin.

TABLE II

Impurity contents of the tin samples supplied by the sources

Sample	Weight, p.p.m.									
	Pb	Fe	Cu	Ni	Bi	In	Ca	As	Mg	Al
Sn.9	0.3	<0.5	n.d.	<0.1						
Sn.8	0.3	<0.5	n.d.	<0.1						
Sn.6	0.2	0.6								
Sn.3	5	1	0.2	0.1				n.d.		
Sn.13	<0.2		<0.2							
Sn.7	1					tr.				
Sn.11	5	n.d.	<1	n.d.	2	n.d.	<1	n.d.	n.d.	n.d.
Sn.2	<50	<56	6							
Sn.12*	tr.	v.w.	v.w.		tr.				tr.	tr.
Sn.10*	tr.	v.w.	v.w.		tr.				tr.	tr.

NOTE: n.d., not detected; tr., trace; v.w., very weak.
*Qualitative spectrochemical analysis only.

EXPERIMENTAL

In the earlier investigation (Part II, 1957b) thermal analyses were made on only two samples of tin, Sn.2 and Sn.3; the liquidus point of Sn.3 was found to be about 0.008° C higher than Sn.2 and alloy melting ranges were found to depend both on the type of freeze and the duration of anneal prior to remelting.

(A) Thermal Survey

The apparatus and techniques used in the thermal analyses have been described previously (Parts I–IV, 1957a, b; 1958a, b); dry nitrogen atmospheres are now always used over the 1100-g tin melts which are contained in high purity graphite crucibles (manufactured and purified after fabrication by United Carbon Products Co., Bay City, Michigan, U.S.A.).

Resistance thermometry for this survey was based on measurements of the 2-ma resistance (R_{Sn}^2) of the thermometer at 15 cm mid-point immersion in the liquid metal corrected to 1 atmosphere nitrogen pressure (for pressure corrections see McLaren 1959) and single daily determinations of the zero current resistance (R_{TP}^0) at the triple point of water. For plotting and correlating results in this type of thermal survey it is a convenience to work with temperatures in arbitrary ratio units defined as $R_{\mathrm{Sn}}^2/R_{\mathrm{TP}}^0$; for the Meyers thermometer, S155, used in this study 37×10^{-8} ratio units $\simeq 10^{-4\circ}$ C.

Figure 1 shows typical cooling curves (Sn.3) that are obtained when a sample of high purity tin transforms under different rates and types of freezing.
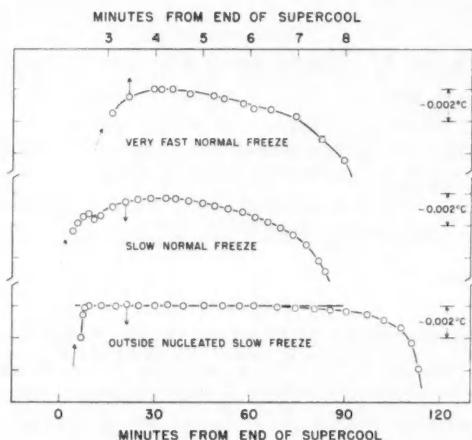
FIG. 1.   Typical freezing curves obtained on high purity tin.

The very fast normal freezes are made by extracting the pyrex tubes holding the crucibles of molten tin from the furnace and allowing solidification to take place in room air. Slow normal freezes are obtained when undisturbed freezing takes place in a slowly cooling block furnace; cooling curves from such freezes are characterized by well-rounded contours, a consequence of the large amount of supercooling found on freezing high purity tin, which rule out their use for precision-fixed temperature points. The bottom curve in Fig. 1 illustrates the type of cooling curve that is obtained by nucleating (technique described in Part II, 1957b) the melt in the throat of the furnace and then immediately lowering it into a slowly cooling furnace block; this outside nucleated slow freeze results in a plateau of nearly constant temperature on the cooling curve

which serves as an excellent index for a temperature standard and, as an additionally desirable feature, this type of freezing has very short recalescent periods.

In this survey, estimates of the melting ranges of the samples were determined from heating curves after very fast freezes and after outside nucleated slow freezes, and in addition the ranges of freezing temperatures were estimated for all samples from the cooling curves obtained on outside nucleated slow freezes; only freezes, and melts after freezes, that had a supercooling of $> 4°$ C are used in this survey. Table III gives the approximate durations and trans-

TABLE III

Transformation conditions for the thermal survey

Transformation	Type	Designation	Figure	Freeze duration		
Freeze	Very fast normal	—	1	10 min		
Freeze	Outside nucleated slow	a	1, 2(a), 3	2 hr		
				Prior freeze duration	Solid anneal	Melting duration
Melt	After outside nucleated slow freeze	b_1	2(b_1), 4	2 hr	2 hr	2 hr
Melt	After outside nucleated slow freeze with overnight anneal	b_2	2(b_2), 5	2 hr	17 hr	2 hr
Melt	After very fast normal freeze	c_1	2(c_1), 6	10 min	2 hr	2 hr
Melt	After very fast normal freeze with overnight anneal	c_2	2(c_2), 7	10 min	17 hr	2 hr

formation conditions for several series of cooling and heating curves from which estimates of the alloy ranges of transformation temperatures were made for the 10 samples of high purity tin; samples were annealed at $215 \pm 5°$ C.

Resistance balances were estimated to the nearest micro-ohm and times were recorded to the nearest second. From direct time–temperature (in ratio units) plots of these measurements the percentage of the total transition time spent in equal temperature intervals was derived* and the information was then used in two ways to make effective comparisons of the alloy transition ranges of the 10 samples.

First, histograms of the percentage time vs. temperature were plotted from which the temperature widths at the 1% level of the total transition time were estimated for all samples. Figure 2 shows a set of these histograms that were obtained for sample Sn.9 from Vulcan Detinning Spectrographic grade tin. Since this material was found to be the purest† tin that was examined in

*This operation approximates the temperature derivative of the direct time–temperature curve; a plot of these time increments against temperature is referred to as the derived inverse (or inverse-rate) transition curve (see Hume-Rothery *et al.* 1952).

†Purest sample is used in the thermal sense; narrow alloy ranges are taken to show that the associated samples contain dissolved impurities in amount and kind that place the least strain on the solvent lattice and hence their solid solutions most closely approximate an ideal pure tin.
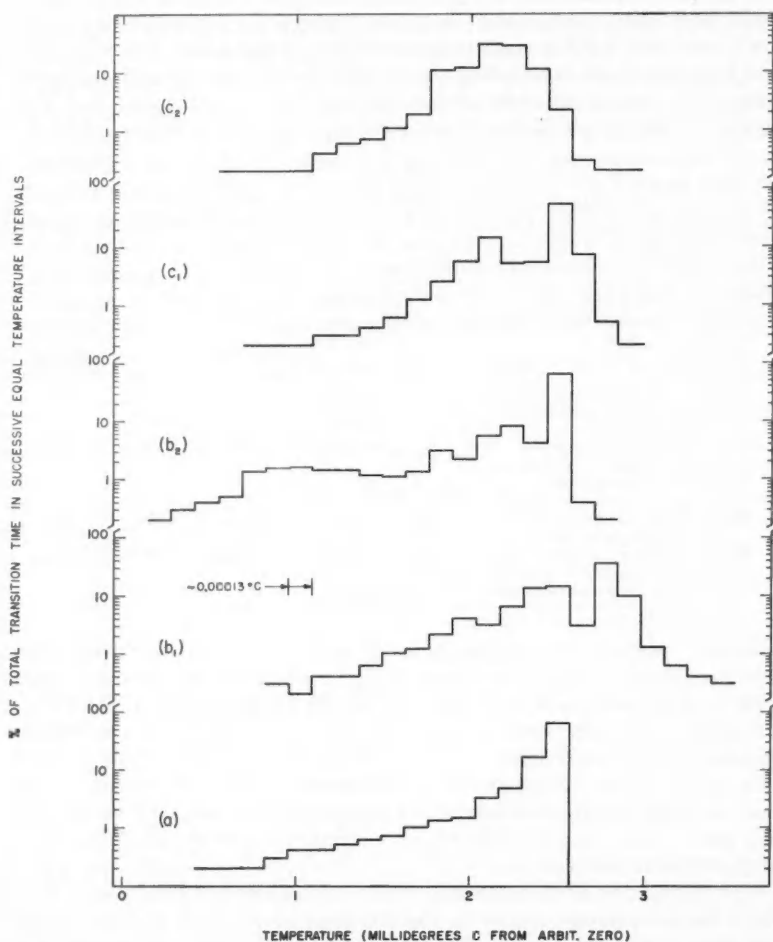
FIG. 2. Inverse transition curves derived for Sn.9: a, outside nucleated slow freeze; b_1, b_2 melts after slow freezing; c_1, c_2 melts after fast freezing; subscripts 1, 2 refer to melting following 2-hour or overnight solid anneals respectively.

this investigation, these inverse curves were derived from percentage time in temperature intervals of $\sim 0.00013°$ C (i.e. 50×10^{-8} ratio units) and hence show alloy transition ranges of the purest tin under the highest temperature resolution that was used in this survey. In Fig. 2 temperatures are plotted directly from arbitrary ratio units; the plateau temperature on the outside nucleated slow freeze was not selected as the arbitrary temperature zero on these plots because temperature differences from histogram to histogram may be uncertain to $0.0005°$ C due to the shortened temperature measurement plan and the approximate differentiation operation used in the survey.

For the wider examination of all the samples durations in temperature intervals of $\sim 0.00027°$ C (i.e. 100×10^{-8} ratio units) were used in plotting the histograms from which the values of the widths at the 1% level of the total transformation time listed in Table IV were obtained. The estimates (Table IV)

TABLE IV

Width at the 1% level of the total transition time (°C)

Sample	a	b_1	b_2	c_1	c_2
Sn.9	0.0013	0.0023	0.0022	0.0015	0.0015
Sn.8	0.0013	0.0023	0.0016	0.0015	0.0015
Sn.13	0.0013	0.0030	0.0011	0.0047	0.0026
Sn.6	0.003	0.004	0.004	0.003	0.003
Sn.3	0.003	0.008	0.005	0.004	0.002
Sn.7	0.003	0.006	0.006	0.005	0.006
Sn.2	0.004	0.008	0.012	0.007	0.008
Sn.11	0.006	0.009	0.014	0.006	0.006
Sn.12	0.006	0.011	0.019	0.006	0.005
Sn.10	0.008	~ 0.02	~ 0.03	~ 0.01	~ 0.02

NOTE: Alloy transformation ranges: a, outside nucleated slow freeze; b_1, b_2 melts after slow freezing; c_1, c_2 melts after fast freezing; subscripts 1, 2 refer to transformations following 2-hour and overnight solid anneals respectively.

of the widths at the 1% level, with the exception of samples Sn.9, Sn.8, and Sn.13, are given only to the nearest millidegree, since variations of this amount were found for this melting range parameter on repeated transformations of the same type on the samples of lower purity tin.

The temperature widths at the 1% level of the total melting time from similar histograms have been used previously as useful indexes for comparing the alloy transformation ranges of temperature among several samples of zinc and cadmium but they must be used with some reservations with tin. The large and variable amount of supercooling found with high purity tin makes it very difficult to arrange nearly identical freezing environments for different tin samples. Although the furnaces may be adjusted to give the same rates of cooling on the samples prior to extraction into room air or into the furnace throat, depending on the type of freeze, it was not possible to have identical initial crystallization conditions exist in the different melts on the same types of freezes, or, indeed, in a single sample on repeated freezes of the same kind. A consequence of this failure to duplicate the thermal environment at the moment of primary crystallization results in a diversity of growth conditions

which causes variations in the initial segregations of soluble impurities even on the same type of freeze. These variable segregations on freezing in turn give rise to variable secondary arrests on melting that last well over 1% of the total melting time and make the 1% level melting range parameter much too sensitive for comparing other than very pure tin samples (i.e. samples with alloy ranges of $\leqslant 0.002°$ C).

For these reasons the derived information "% duration vs. temperature interval" obtained from direct time–temperature curves was used in an alternative manner to make reliable comparisons of the transition ranges of all the samples. The percentage of duration was incremented* to 95% of the total transition time beginning at and incrementing in both directions from the temperature interval having the maximum percentage of duration (i.e. the temperature
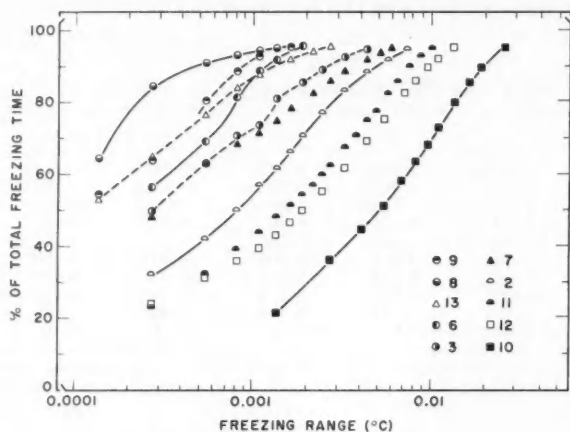
Fig. 3.   Fraction of the total freezing time spent in given freezing ranges on outside nucleated slow freezes: derived from 'a' curves.

range in which the greatest amount of the sample transformed). The summations were cut off at 95% of the total transition time for two reasons: the estimations of the total transition times may be in error by a few per cent and also the initial and final few per cent of the total time of a melting or freezing curve may reflect curvatures, caused by thermal lag in the furnace block, that might not be quite identical from melt to melt because the final adjustments on furnace powers are made only 10 or 15 minutes before the arrest.

The total transition time is arbitrarily estimated by selecting the duration that appears to encompass the complete transformation on the direct time–temperature plot. With the exception of samples Sn.9 and Sn.8, difficulty was sometimes experienced in accurately identifying the time for the liquidus break

*This operation approximates an integration of the inverse transition curve between specified limits; by summing in both directions from the intervals having maximum durations on all samples, melting range comparisons are based on the heart of the melting range information and variable end effects are minimized.

especially on b_1 type (see Table III) melting curves; the temperature would quickly break upward for a few tenths of a degree from the liquidus point but during the next few minutes it would intermittently rise, drop, or remain nearly steady before positively following an all liquid heating curve.

This erratic behavior is likely caused by the movement of remaining small amounts of solid still dispersed in the liquid melt. It is probably significant that this phenomenon is most pronounced on melting shortly after the slow freezing which appears to cause the greatest amount of segregation of the dissolved solutes in the ingot.

Figures 3–7 inclusive show the results of plotting the "% duration" sum-
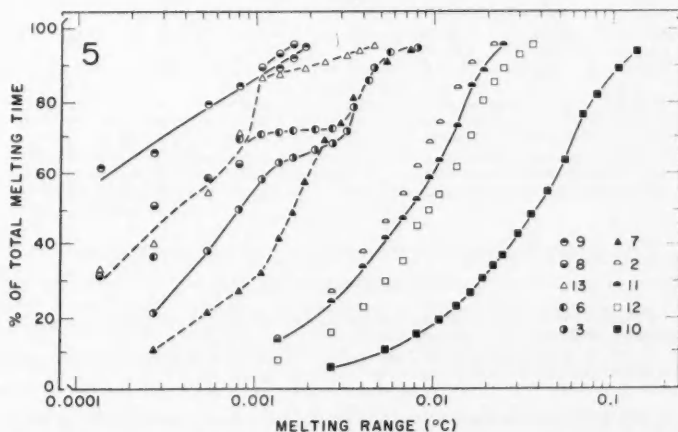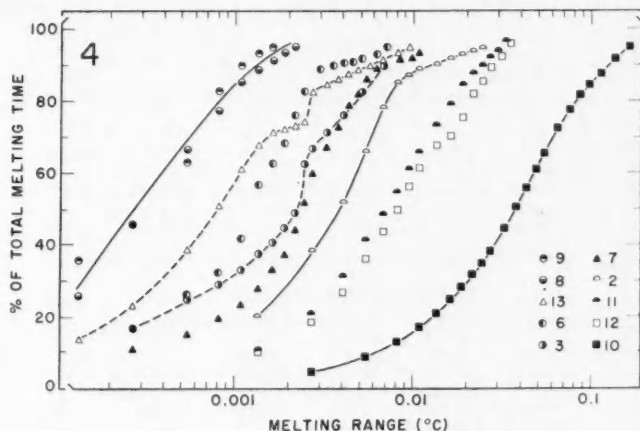
FIG. 4.   Fraction of the total melting time spent in given melting ranges following outside nucleated slow freezes with 2-hour solid anneals: derived from 'b_1' curves.

FIG. 5.   Fraction of the total melting time spent in given melting ranges following outside nucleated slow freezes with 17-hour solid anneals derived from 'b_2' curves.

mated in the above manner against transition range for the several series of
freezes and melts on the 10 samples of high purity tin; trend lines instead of
proper histograms are drawn on these plots to reduce any confusion in following
particular samples.

Several observations may be made on the results shown in Figs. 3–7.
Narrowest* alloy transition ranges for all the samples were found on the outside
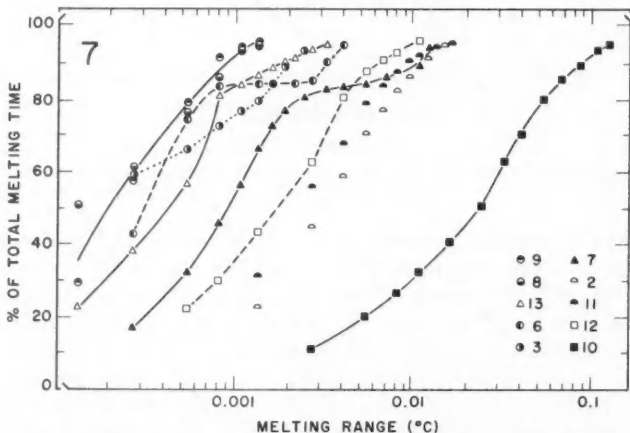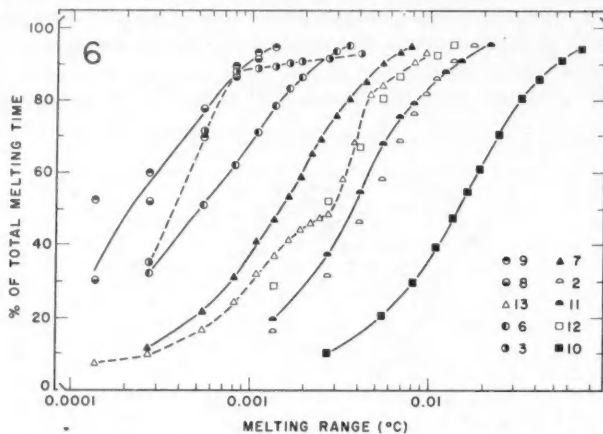
FIG. 6.   Fraction of the total melting time spent in given melting ranges following very fast
normal freezes with 2-hour solid anneals: derived from 'c_1' curves.
FIG. 7.   Fraction of the total melting time spent in given melting ranges following very fast
normal freezes with 17-hour solid anneals: derived from 'c_2' curves.

*Narrow and wide alloy ranges are used here to denote temperature ranges over which the
bulk of the individual samples transformed; undoubtedly there are regions in each ingot (e.g.
near grain boundaries and the small volume immediately adjacent to the thermometer well)
where segregated solutes (see Weinberg 1959; Kishkin and Bokstein 1955) become so concen-
trated that these regions have solidus temperatures that are very much lower than the tem-
perature at which general melting of the bulk of the particular sample begins.

nucleated slow freezes (Fig. 3); widest alloy ranges were found on remelting after these freezes allowing only short anneals near the solidus temperature (Fig. 4). By inspection of these curves it is easy to grade the samples on the basis of the width of their alloy transition ranges; the fact that their relative positions in an array based on increasing alloy range vary following different types of freezing and amounts of annealing is probably the result of variations in the distributions of different impurity solutes between grain volume and grain boundary regions. In order to illustrate these differences and to obtain numbers for specific comparisons among the samples, the alloy ranges corresponding to 50% of the total transition times were obtained from Figs. 3–7; these estimations are given in Table V, the final column of which anticipates results from the intercomparison of plateau freezing temperatures.

TABLE V

Temperature range (°C) for 50% duration

Sample	a	b_1	b_2	c_1	c_2	Liquidus point rel. to Sn.9, °C
Sn.9	0.0001	0.0003	0.0001	0.0003	0.0002	0.0
	(-7)	(-20)	(-7)	(-16)	(-13)	
Sn.8	0.0001	0.0003	0.0002	0.0003	0.0002	0.0
	(-17)	(-17)	(-17)	(-18)	(-16)	
Sn.13	0.0001	0.0008	0.0003	0.0028	0.0004	-0.0004
	(-7)	(-14)	(-7)	(-14)	(-6)	
Sn.6	0.0002	0.0012	0.0004	0.0005	0.0003	$+0.0009$
	(-12)	(-12)	(-10)	(-10)	(-14)	
Sn.3	0.0003	0.0020	0.0008	0.0004	0.0002	-0.0012
	(-5)	(-4)	(-6)	(-6)	(-13)	
Sn.7	0.0003	0.0022	0.0015	0.0015	0.0009	-0.0010
	(-7)	(-6)	(-7)	(-8)	(-11)	
Sn.2	0.0008	0.004	0.005	0.004	0.003	-0.0090
	(-7)	(-7)	(-5)	(-6)	(-9)	
Sn.11	0.002	0.007	0.007	0.004	0.002	-0.0025
	(-6)	(-8)	(-6)	(-9)	(-8)	
Sn.12	0.002	0.008	0.009	0.003	0.0015	-0.0048
	(-5)	(-11)	(-5)	(-8)	(-5)	
Sn.10	0.005	0.04	0.04	0.015	0.003	-0.0132
	(-4)	(-6)	(-4)	(-9)	(-9)	

NOTE: Temperature ranges (°C) in which the samples spent 50% of their total transition times: a, outside nucleated slow freeze; b_1, b_2 melts after slow freezing; c_1, c_2 melts after very fast freezing; subscripts 1, 2 refer to transformations following 2-hour or overnight solid anneals respectively. The amounts (°C) of supercooling prior to solidification are given in parentheses beneath the respective transition ranges; for ready reference, a summary of the liquidus point intercomparison is given in the final column.

The Vulcan Detinning Spectrographic tin (Sn.9 and Sn.8) has the narrowest alloy ranges of all the samples examined; further, the transition range of this metal is not greatly affected by the type of transformation or amount of solid anneal. Tables IV and V show that the samples which have liquidus points within 0.001° C of that of Sn.9 have alloy ranges which are both wider and more sensitive to transformation conditions than are transition ranges of Vulcan's zone-refined material. The relatively poor showing of the Japanese[*]

[*]We have examined a sample of nominal 99.9999% zone-refined lead from this source and found it to compare quite favorably with lead (not zone-refined) of this purity from other refiners.

zone-refined tin (Sn.12 and Sn.10) would suggest that these samples contain dissolved solutes that are not efficiently carried out with a moving zone. From this investigation it appears that for gauging alloy transformation ranges for tin in the purity range 99.99% to 99.9999%, the estimates (Table V) of the alloy ranges corresponding to 50% of the total transition times are probably more useful than the temperature widths (Table IV) at the 1% level from inverse curves because the latter parameter is too sensitive to minor variations in segregations of dissolved solutes on solidification following the large and variable supercooling. However, the 1% level parameter has the necessary sensitivity to detect significant differences in the alloy ranges of samples of the highest purity (i.e. samples with alloy ranges of ≤0.002° C).

(a) *Supercooling*

During the course of these thermal analyses some knowledge was gained of factors affecting the supercooling of high purity bulk tin melts (mass, 1.1 kg; size, 3.5 diameter×19 cm) contained in machined graphite crucibles.

A high degree of supercooling is particularly important in the attainment of the plateau temperatures on outside nucleated slow freezes; it is essential that, when a melt strikes, the rates of nucleation and grain growth are sufficiently great to provide the release of enough latent heat of fusion to immediately raise the sample temperature to its liquidus point. For the 10 samples used in our experimental arrangement a supercooling of 4° C or greater provided large enough rates of nucleation and growth to assure attainment of the plateau temperature; for Vulcan Spectrographic grade tin the plateau temperatures could be obtained with only 2° C supercooling.

The degree of supercooling attained before melts strike appears to depend on a combination of many variables of which the following general observations were made:

(i) Least pure samples, Sn(2, 11, 12, 10), tended to supercool <10° C.

(ii) It is best to handle high purity tin under an inert atmosphere and to omit topping the melts with the usual graphite powder, as an oxide inhibitor. Inadequate (<1° C) supercooling* was experienced, even with Vulcan Detinnings' Spectrographic grade tin, when graphite powder (200 mesh) became distributed throughout a sample; on loading Sn.8 for the second time some of this powder from the first loading became dispersed through the liquid metal and gave rise to difficulties in attaining the desired 4° C supercool on outside nucleated slow freezes. Thereafter graphite powder topping was omitted when the samples were loaded.

A sample that has been contaminated with graphite powder in the above manner may be cleaned by heating the sample ∼50° C above its liquidus point and allowing time for the powder to float to the surface where it may be spooned off with a pyrex ladle; cycling the sample through a few freezes and melts also appears to aid in clearing out the external nucleating agents.

(iii) The extent of the supercool appeared to depend on the amount and

---

*These experiences on bulk samples appear to be contrary to that reported by Pound and LaMer (1952); they found that powdered graphite did not catalyze the nucleation rate in finely divided tin droplets (diameters, 1–30 microns).

duration of the previous overheat; melts that were held 10° C above their liquidus points overnight nearly always supercooled more than the same melts when refrozen <2 hours after melting. Further, when melts were held <2° C above the liquidus points for <2 hours and then refrozen the observed supercooling was usually <4° C. These trends became accentuated when using the least pure samples, Sn.2, 10, 11, 12, to such an extent that we conclude that the supercooling of samples having alloy melting ranges of, say >0.01° C definitely exhibits a dependence on the thermal history of the liquid sample. In many respects, these observations are similar to the effect of thermal history on the supercooling phenomena on tin observed by Webster (1933), the existence of which, Turnbull (1950, 1953) attributes to the presence of crystal nucleation catalyst particles in the liquid. Webster does not give either the mass or the purity of the bulk tin used in his experiments: his tin was contained in quartz crucibles open to the air.

(iv) On many freezes the rate of cooling was observed to slow up and indeed even stop and reverse slightly, in the temperature range up to 4° C undercool, before increasing rapidly to a final momentary arrest before general nucleation. At this temporary arrest* in the region up to 4° C supercool significant nucleation must be occurring to release enough latent heat to stop the cooling of the 1.1-kg melts that was observed. When the samples were in this rather indecisive but sensitive state, general nucleation could apparently be triggered by a loud noise near the furnace. In contrast, when the melts had safely cooled below this sensitive region vibration and noise appeared to have no further effect on nucleation; nor did 10 r/min γ-rays from a Co⁶⁰ beam therapy unit. Whether the nucleating agents present in the 0–4° C range are different from the ones active in the general nucleation is not known.
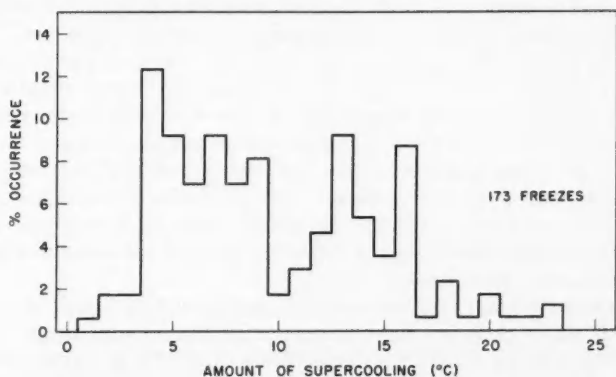
Fig. 8. Histogram of the amount of supercooling attained before general nucleation on freezing all samples.

*These observations refer only to supercooling in freezes when the melts are extracted into the furnace throat or into room air (i.e. relatively rapid supercooling >1° C/min). When this type of nucleation occurs on a normal slow freeze (i.e. rate of supercooling <0.1° C/min) the melt temperature has been observed to rise and fall in this 4° C range several times before general nucleation begins; similar indecision in the recalescent state was noted on normal slow freezes in high purity zinc (see Fig. 5, McLaren 1957b).

Webster (1933) found that his samples supercooled either 3 to 4° C or 20 to 25° C and he reported only one observation between these two ranges; the information given in Fig. 8 includes supercooling data obtained for all samples using the freezes that were made in both the thermal survey and in the precision intercomparison of the liquidus points.

(b) Anomalous Structures on the Front End of Melting Curves

In our earlier work* examples were presented of anomalous structures that were found on the front ends of many melting curves on high purity tin. These were sudden discontinuities on the melting contours in which the melt temperature abruptly rises a few millidegrees and may or may not then decrease 0.002° C before completing the transformation with either a long alloy slope of steadily increasing temperature or a nearly constant plateau-like feature, presumably dependent on the concentration ranges of the associated dissolved solute in the solid that is being melted. Figure 9 shows a selection of similar front end structures (usually found during the first quarter of the melting time) that were observed in this investigation. Neither the prominence nor the form of the structure appeared to correlate with the amount of supercool or the type of the prior freeze; on the other hand, perhaps the most interesting structures were found on melting curves made on ingots following overnight solid anneals.

The most significant observation on these structures made in the present investigation was that no marked evidence of front end structures was found on the melting curves on Sn.9 and Sn.8. Since these samples also had the narrowest alloy melting ranges we conclude that the front end structures are probably associated with impurity segregations† in the ingots. The lack of a correlation of these effects with prior supercool and type of freeze seems to militate against a strain anneal explanation whereas impurity diffusion might account for the greater frequency of these structures on melting curves following overnight anneals. We speculate that a possible cause of the anomalous superheating that is observed might be a decrease in internal stress in the solid following a rapid diffusion of impurity atoms at the liquidus temperature; further, because these effects were not observed on samples Sn.9 and Sn.8 we consider that instrumental causes similar to those discussed by Smit (1957) are unlikely in our experimental arrangement. The latter observation also appears to rule out the possibility of changes in internal stress (and hence variations in the melting temperatures) with a release of trapped gas since all samples were solidified under dry nitrogen.

A final observation was that the maximum temperature attained on a front end anomaly never exceeded the temperature of the liquidus break on the melting curve; this factor clearly differentiates this type of apparent overheating from the superheating of 1 to 2° C found by Haykin and Bénet (1939) on melting large single crystals of high purity tin. After completion of the

---

*Part II (1957b): In Fig. 13 of this reference the curves labelled (d) and (b) should have read (b) and (d) respectively.

†Doping Vulcan's Spectrographic grade tin with radioactive solutes and correlating autoradiographs of solidified ingots with their corresponding thermal analyses should test this conclusion and provide information on the thermal effects and distributions of specific impurities.
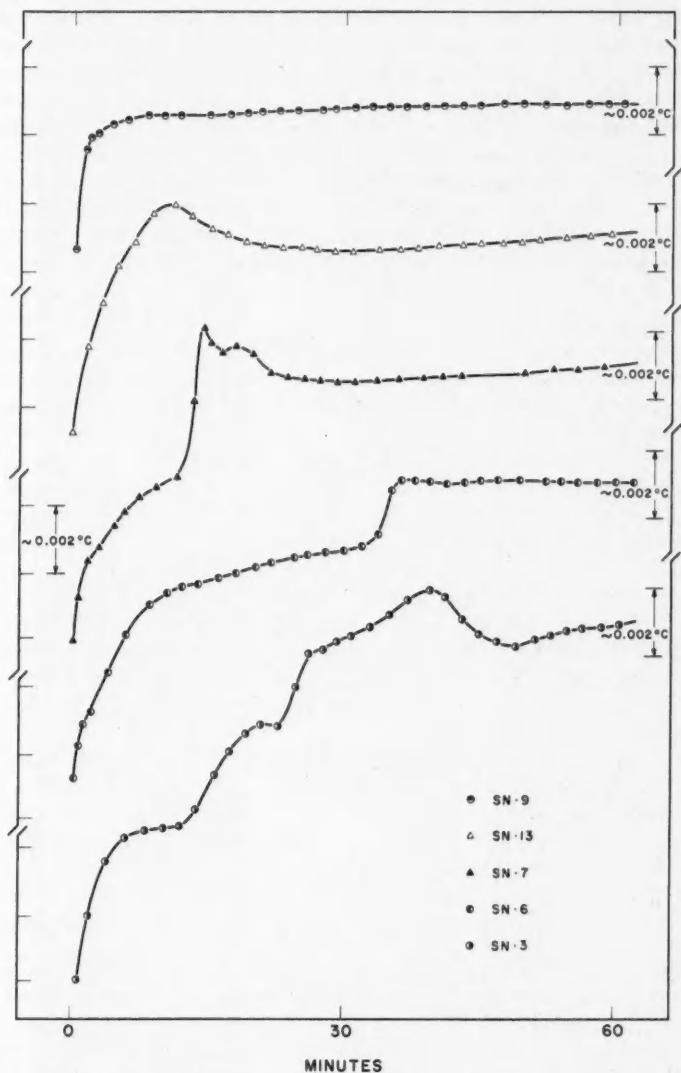
FIG. 9.   Portions of melting curves showing anomalous front end structures. Types of melting curves: Sn.9(c_2), Sn.13(b_1), Sn.7(c_2), Sn.6(b_2), Sn.13(b_2).

thermal survey a melt (Vulcan Extra Pure from Lot VS-65) was decanted 30 minutes after striking on a slow outside nucleated freeze; prior supercool was 11° C and the furnace was adjusted for a ~2-hour freeze. Figure 10 shows a photograph of the sectioned shell that remained in the crucible on decanting; a smooth interface, containing many dendrites, appears to have advanced in a nearly uniform fashion (grain size, irregular 5–20 mm) from the walls of the crucible. The dendrites* that project ahead of the smooth interface undoubtedly grew very quickly in the minute or so after general nucleation as the melt recovered from the large supercool (see Weinberg and Chalmers 1951, 1952). Cylindrical shells have previously been found on decanting zinc melts that were partly solidified in the block furnace; they provide an ideal environment for the sensing coil of the resistance thermometer by both enclosing and shielding it with the freezing interface.

(B) Intercomparison of Liquidus Points

A careful intercomparison of the plateau freezing† temperatures attained on outside nucleated slow (~3 hours) freezes on the 10 samples of tin was made; the measuring sequence was similar to that used in the intercomparison of samples of high purity zinc (Part III, 1958a). For such measurements it is normal to compare the liquidus points of two samples at nearly the same time with a single thermometer in order to minimize the effects of any short-term systematic variations in bridge, thermometer, or water triple cell temperature during the comparison. The fully corrected zero current resistances at the liquidus points of a single Meyers thermometer, S155, at 15 cm mid-point immersion corrected to 1 atmosphere dry nitrogen pressure over the melts were determined; corresponding resistances at the triple point of water (triple cell 29) were used to baseline all measurements. Figure 11 gives the results of comparing samples Sn.8 and Sn.13 against Sn.9, eight determinations being made on each sample; Table VI summarizes the intercomparisons that were made on all the samples.

Sn.9 and Sn.8, Vulcan-Detinning's zone-refined tin, had the narrowest alloy transition ranges and for this reason are considered to be the samples which have purities nearest to an ideal 'pure' tin; and since the bulk of these samples transformed in <0.002° C under a variety of transition conditions (Figs. 3–7) it is very probable that their liquidus points are <0.0005° C from that of pure tin. Further, since a value of 231.9119° C (Int. 1948) for the liquidus point of Sn.3 under a total pressure of 1 atmosphere was determined previously

*We do not discount the melting of the material in these dendrites as a possible cause of the anomalous structures observed on the front end of melting curves; since they grow during a period of very rapid freezing their average impurity concentration is thought to be considerably greater than that of material that solidifies at the plateau freezing temperatures.

†Plateau freezing temperatures are used synonymously with the liquidus points of the alloys; plateau freezing temperatures are invariably closely associated with the temperature of the liquidus breaks on melting curves. It is thought that, on the appropriate phase diagrams for these samples, the liquidus for the range of concentrations that solidify at the plateau freezing temperature is so close to horizontal that the resistance thermometer is unable to detect its slope; and in addition, the material freezing out at the plateau freezing temperature has a nearly constant composition which closely approximates the equilibrium concentration in the solid at the liquidus temperature.
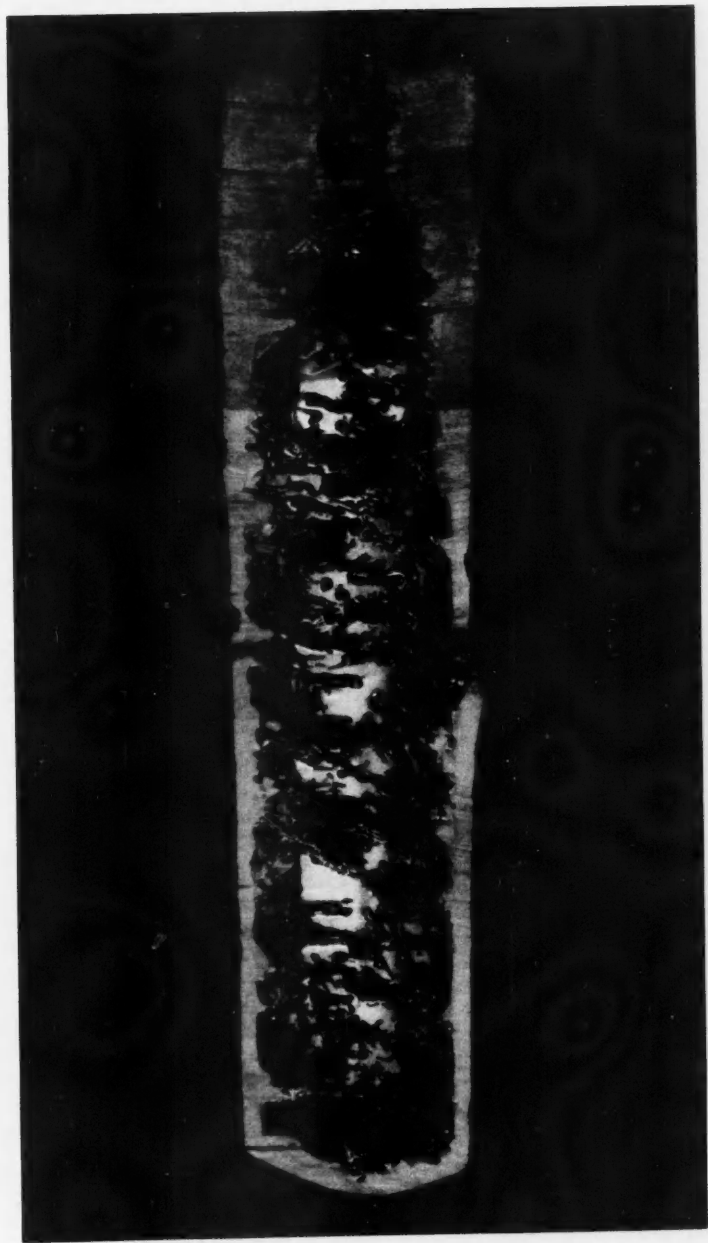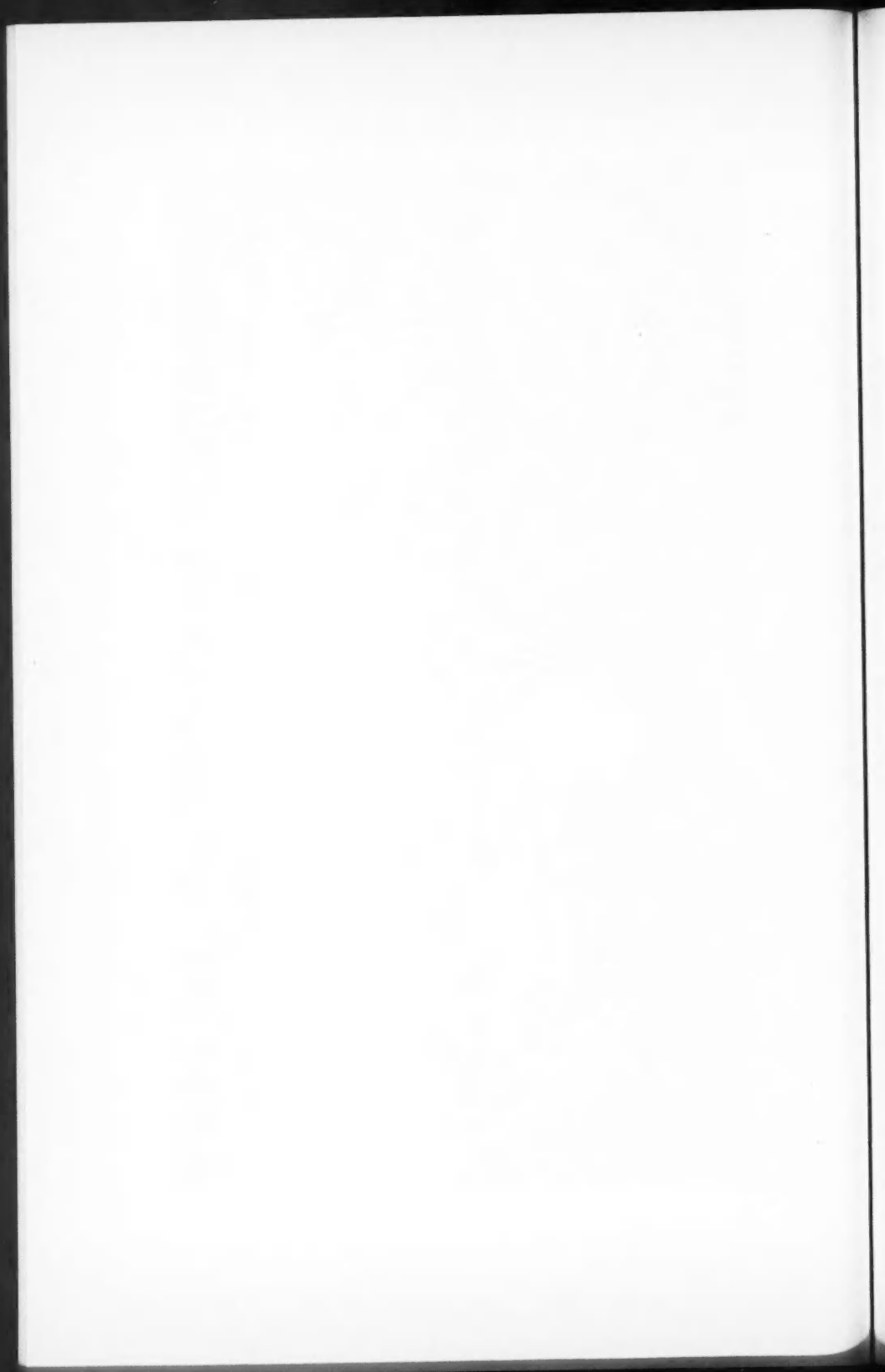
PLATE I

FIG. 10 Photograph of a sectioned shell of tin remaining in the crucible on decanting the melt after partial freezing.
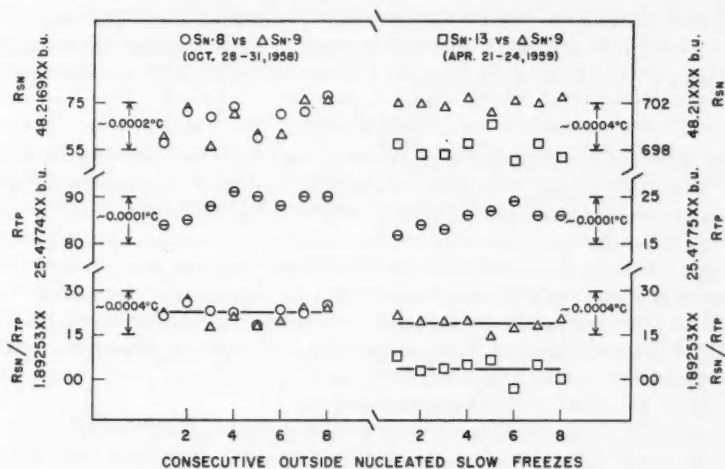
McLaren and Murdock—Can. J. Phys.

FIG. 11.   Intercomparison of plateau temperatures of Sn.8 and Sn.13 with Sn.9; R_{TP} and R_{Sn}, zero current fully corrected resistances of the thermometer at the triple point of water and the tin point respectively.

TABLE VI

Intercomparison of plateau temperatures

Mean date	Sample	No. of freezes	Ratio R_{Sn}/R_{TP}		Reproducibility (equivalent 10^{-4}° C)		Plateau temp. rel. to Sn.9, °C
			Mean	$10^8 \times$ std. dev.	Std. dev.	Spread	
12.6.58	Sn.3	5	1.89252821	±51	±1.4	3.2	−0.00123
	Sn.6	5	3605	±20	±0.5	1.3	
28.8.58	Sn.7	8	1.89252877	±33	±0.9	2.4	−0.00105
	Sn.6	8	3593	±37	±1.0	3.3	
11.9.58	Sn.6	8	1.89253525	±54	±1.5	4.1	+0.00088
	Sn.8	8	3205	±33	±0.9	2.1	
30.10.58	Sn.8	8	1.89253227	±24	±0.6	2.2	+0.00002
	Sn.9	8	3220	±31	±0.8	2.4	
21.11.58	Sn.2	4	1.89249855	±20	±0.5	1.2	−0.00898
	Sn.9	4	53188	±24	±0.6	1.5	
3.12.58	Sn.10	4	1.89248301	±215	±5.8	13.7	−0.0132
	Sn.9	4	53212	±29	±0.8	1.6	
27.1.59	Sn.11	4	1.89252282	±10	±0.3	0.5	−0.00246
	Sn.9	4	3196	±17	±0.5	1.1	
3.3.59	Sn.12	4	1.89251428	±44	±1.2	2.8	−0.00479
	Sn.9	4	3206	±25	±0.7	1.5	
23.4.59	Sn.13	8	1.89253034	±35	±0.9	2.7	−0.00042
	Sn.9	8	3189	±22	±0.6	1.9	
29.4.59	Sn.3	8	1.89252819	±46	±1.2	3.6	−0.00119
	*Sn.9	8	3262	±30	±0.8	2.5	

*The average R_{Sn}/R_{TP} for the 56 freezes on Vulcan Detinnings' Spectrographic grade tin (Sn.9, Sn.8) was 1.89253215 with a standard deviation equivalent to ±0.00009₂° C and a spread of 0.00044° C; this reproducibility is comparable with that of any fixed temperature point on the International Temperature Scale.

(McLaren 1959) from measurements with 11 standard thermometers, it is deduced, from the additional information given in Table VI, that the standard liquidus points of samples Sn.9 and Sn.8 have a value 231.9131° C (Int. 1948).

DISCUSSION

The selection of samples of highest purity metal on the basis of narrowest alloy transition ranges was used to establish precision thermometric fixed points at the standard liquidus points of zinc, cadmium, and indium; in the particular samples that were examined in the zinc and cadmium investigations the ones with the narrowest alloy melting ranges also happened to have the highest liquidus temperatures. An interesting difference has been found in this study on high purity tin: Sn.6 was found to have a liquidus point that is 0.0009° C higher than that of the metal with the narrowest transition range. The explanation of this difference undoubtedly lies in the nature of the specific impurities contained in the respective samples.

On solution, solutes which are more soluble in liquid than solid alloy lower the liquidus points of their alloys from that of the pure solvent; conversely solutes more soluble in solid than liquid alloy raise liquidus temperatures on solution (for a discussion on these points see Pfann (1958)*). Therefore to explain the value of the liquidus point that was found for sample Sn.6 we look for a solute that raises the liquidus temperature on solution in tin; antimony appears to be the most likely impurity on two counts. Firstly, Vulcan Detinning's† Extra Pure grade tin is prepared by further electrolytic refining of selected samples of Vulcan 99.99% Electrolytic tin which contains about 20 p.p.m. antimony. The Vulcan Spectrographic grade tin is prepared by zone-refining selected lots of the Extra Pure grade tin which further effects a partial removal of any remaining antimony and substantially reduces the level of other impurity solutes. On analysis the limit of detection of antimony in the final products is thought to be about 5 p.p.m. Secondly, since a reasonable suspicion of antimony in Sn.6 has been established it is also significant that 6 p.p.m. antimony in tin would raise the liquidus point by the observed 0.0009° C (phase diagram, Metals Handbook 1948).

CONCLUSIONS

This investigation on 10 samples of the highest purity tin that could be obtained has provided the broad evidence required to confirm the results of the earlier investigation, namely, that the liquidus point of high purity tin is a thoroughly reliable thermometric fixed point of the highest reproducibility and experimentally may be simply and quickly realized in any well-equipped laboratory. This study has shown that alloy melting range parameters are sufficiently sensitive to enable the purest samples of tin to be easily selected.

*Pfann (1958) also gives references to the purification of tin by zone refining; Aleksandrov *et al*. (1956) give a thorough account of the purification of tin by zone-melting techniques and in addition report on the effectiveness of continuous heating under high vacuum for the elimination of highly volatile impurities.
†We are indebted to Robert H. Taylor of the Vulcan Detinning Co., Sewaren, N.J., U.S.A., for this information.

A value of 231.913° C (Int. 1948) was found for the standard liquidus point of pure tin; samples that melt over a range of ≤0.002° C will have liquidus points within 0.001° C of this value.

The three fixed points, triple point of water and the standard liquidus points of high purity tin and zinc, provide a ready means for any industrial, university, or institutional laboratory to quickly and reliably carry out high precision calibrations (for interpolation considerations see McLaren (1959)) of resistance thermometers for subsequent use in the range 0 to 630° C (Int.).

ACKNOWLEDGMENTS

REFERENCES

ALEKSANDROV, B. N., VERKIN, B. I., and LAZAREV, B. G.   1956.   Fiz. Metal. i Metalloved. Akad. Nauk S.S.R. **2** (I) No.1, 93; **2** (II) No. 1, 100.
CAMPBELL, A. N., WOOD, J. H., and SKINNER, G. B.   1949.   J. Am. Chem. Soc. **71**, 1729.
HAYKIN, S. E. and BÉNET, N. P.   1939.   Compt. rend. (Doklady) acad. sci. U.R.S.S., **23**, 31.
HUME-ROTHERY, W., CHRISTIAN, J. W., and PEARSON, W. B.   1952.   Metallurgical equilibrium diagrams (The Institute of Physics, London), Chap. 11.
KISHKIN, S. T. and BOKSTEIN, S. Z.   1955.   International Conference on the Peaceful Uses of Atomic Energy A/Conf. 8/P/703.
McLAREN, E. H.   1957a.   Can. J. Phys. **35**, 78.
———   1957b.   Can. J. Phys. **35**, 1086.
———   1958a.   Can. J. Phys. **36**, 585.
———   1958b.   Can. J. Phys. **36**, 1131.
———   1959.   Can. J. Phys. **37**, 422.
METALS HANDBOOK.   1948.   (The American Society for Metals, Cleveland, Ohio), p. 1239.
PFANN, W. G.   1958.   Zone melting (John Wiley & Sons, Inc., New York), Chap. 2.
POUND, G. M. and LaMER, V. K.   1952.   J. Am. Chem. Soc. **74**, 2327.
SCRIBNER, B. F.   1952.   Symposium on Tin, Special Technical Publication No. 141 (American Society for Testing Materials, Philadelphia), p. 105.
SMIT, W. M.   1957.   Purity control by thermal analysis (Elsevier Publishing Co., New York), p. 33.
TURNBULL, D.   1950.   Trans. Am. Inst. Mining Met. Engrs. **188**, 1147.
———   1953.   Progress in metal physics, Vol. 4 (Pergamon Press Ltd., London), p. 358.
WEBSTER, W. L.   1933.   Proc. Roy. Soc. A, **140**, 653.
WEINBERG, F.   1959.   Grain boundaries in metals. To be published in Progress in metal physics, Vol. 8 (Pergamon Press Ltd., London).
WEINBERG, F. and CHALMERS, B.   1951.   Can. J. Phys. **29**, 382.
———   1952.   Can. J. Phys. **30**, 488.

APPENDIX

During March 1959 an intercomparison of the temperatures realized in six water triple point cells was carried out with the same measuring scheme that was used in earlier intercomparisons (Part I, 1957a). This laboratory has retained four of the National Research Council cells, namely triple cells 29, 24, 21, 31, that were included in the former surveys and recently has added two more cells, 203 and 204, prepared by the J. and J. Instrument Co., Silver Spring, Maryland, U.S.A.; this group of cells now constitutes the grid for assessing our realization of the triple point of water and for gauging changes in particular cells. Table VII gives the results of the present intercomparison;

TABLE VII

ΔR_{TP} of cells relative to T.C. 29. The limiting uncertainty in a
difference measurement is of the order of $3\ \mu\Omega : 10\ \mu\Omega \equiv 0.0001°$ C

Cell	Nov. Dec./1954, $\mu\Omega$	Apr. May/1956, $\mu\Omega$	March 1959, $\mu\Omega$	
			1st week	2nd week
29	0	0	0	0
24	+5	+3	+2	+2
21	+1	+1	+1	
31	−19	−16	−37	
203				+11
204				+10

each entry was determined from the average of 15 independent determinations
of the annealed* zero current resistance at the triple point of water, R_{TP}, made
on each cell during a 4-day interval. Table VII shows that triple cells 29, 24,
and 21 have maintained their relative triple point temperatures during the
past 3 years while that of triple cell 31, already considered substandard, has
decreased another $0.0002°$ C. As in the earlier investigations no systematic
measurable (i.e. $>3\mu\Omega$) change of cell temperature with age of the ice mantles
was found from the second to the fifth day.

*All thermometers were annealed to stability at 450° C prior to each 4-day intercomparison.

THE RADIATION CHARACTERISTICS OF A SINUATE ANTENNA[1]

S. C. LOH[2]

ABSTRACT

Rigorous expressions for the radiation field of an antenna of sinusoidal shape are derived on the assumption of a travelling-wave type of current distribution along the conductor. In order to illustrate the derived results an endfire antenna is designed and some calculations of radiation field are presented.

INTRODUCTION

The zigzag antenna described first by Cumming (1955) is characterized by two significant properties: namely, the moderate bandwidth in the V.H.F. and U.H.F. ranges, and the strong axial beam of radiation with very low side lobes. In order to derive the far-field expressions, Cumming treated the structure as an array of V-shaped elements. Assuming a travelling-wave type of current distribution along the conductor the two electric field components are determined for one turn. Considering the single turn as one element in an array, the antenna radiation pattern is obtained by multiplying the unit pattern by an array factor appropriate to the number of turns and the turn spacing of the antenna. The radiation properties of a single zigzag antenna were further investigated and reported in a recent article by Sengupta (1958).

A different and somewhat more rigorous method of solving the radiation problem of the zigzag antenna has been presented by Wong and Loh (1959). Assuming a travelling-wave type current distribution, the field components are formulated in terms of a vector potential. The total vector potential, and consequently the radiation field of the antenna, are determined by integrating the appropriate integrals over the length of the antenna.

In the present paper, the radiation problem of an antenna of sinusoidal shape (see Fig. 1), which is very similar to the zigzag antenna mentioned above, is investigated. Expressions for the radiation field are derived by using the method similar to the one employed by Wong and the author. In order to illustrate the derived results, an endfire antenna of six turns is designed for a frequency of 2650 Mc/s and some calculations of the radiation pattern are presented. The theoretical values calculated from the derived expressions agree quite well with the measured pattern.

DERIVATION OF THE RADIATION FIELD

The study was made on an antenna having the configuration shown in Fig. 1. The co-ordinate system is chosen in such a way that the antenna lies entirely on the x–z plane, the axis of the antenna being along the z axis.
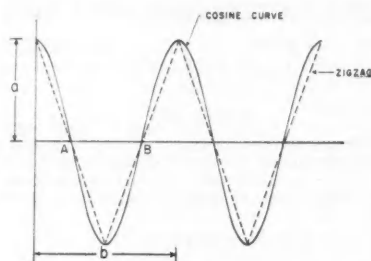
FIG. 1. The sinuate and the zigzag antennae.

Neglecting the effect of the ground screen backing the antenna, it was assumed that the antenna would carry a current distribution of the travelling-wave type with constant amplitude, and that the reflections from corners and the unterminated end of the wire would have no effect on the radiation pattern.

The problem will be formulated in terms of a Hertzian vector potential. In order to facilitate the analysis, the vector potential will be determined in rectangular components, and by applying the appropriate rectangular–spherical co-ordinate transformation equations, the field is expressed in terms of a single spherical component. In the following analysis, the rationalized M.K.S. system of units is employed, and the time variation, $\exp(i\omega t)$, is understood.

We shall first write down the parametric equations for the antenna:

$$
\begin{aligned}
x &= a \cos t \\
y &= 0 \qquad\qquad 0 < t < t_0, \\
z &= (b/2\pi)\, t
\end{aligned}
$$

(1)

where a is the amplitude of the cosine curve and b the turn spacing.

The element of arc length, ds, along the conductor is given by

$$
\text{(2)} \qquad
\begin{aligned}
ds &= \sqrt{(dx^2 + dz^2)} \\
&= (a/m)\sqrt{(1 - m^2 \cos^2 t)}\, dt
\end{aligned}
$$

where

$$
m = \frac{1}{\sqrt{[1 + (b^2/4\pi^2 a^2)]}}.
$$

Thus the arc length s is

$$
\text{(3)} \qquad s = \frac{a}{m} K(m,t)
$$

where

$$
K(m,t) = \int_0^t \sqrt{(1 - m^2 \cos^2 t)}\, dt
$$

is an elliptic integral of the second kind.

The function $K(m,t)$ can easily be expressed in an approximate form given by

(4)
$$K(m,t) \doteqdot c_1 t - c_2 \sin 2t$$

where

$$c_1 = 1 - \left(\frac{m^2}{4} + \frac{3}{64} m^4 + \frac{5}{256} m^6 + \ldots \right),$$

$$c_2 = \frac{m^2}{8} + \frac{m^4}{32} + \frac{15}{1024} m^6 + \ldots \;.$$

To determine the radiation field of an arbitrarily shaped radiator, we shall employ an expression for the Hertzian vector potential. Let us examine the vector potential at point P, distant R from the origin of the co-ordinates.
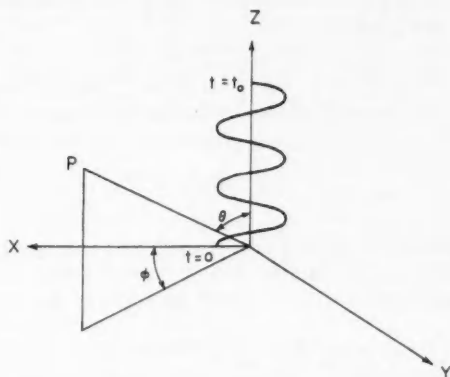
FIG. 2. Sinuate antenna located at the origin of the co-ordinate system.

With reference to Fig. 2, the Hertzian vector potential is

(5)
$$\overline{\Pi} = \frac{1}{4\pi\epsilon i\omega} \frac{\exp(-ikR)}{R} \int \overline{I}(s) \exp(ik\overline{r}\cdot\overline{p}) \, ds,$$

where

  ϵ is the permittivity of free space,
  $k = (2\pi/\lambda)$, where λ is the wavelength in free space,
  $\overline{I}(s)$ is the current in an element of length ds,
      located at a point denoted by the vector $\overline{r}$,
  $\overline{p}$ is a unit vector in the direction of R.

Writing in terms of the co-ordinate system shown in Fig. 2, we can expand eq. (5) as follows:

(6)
$$\overline{\Pi} = \frac{1}{4\pi\epsilon i\omega} \frac{\exp(-ikR)}{R} \int \overline{I}(s) \exp[ik(x\cos\phi\sin\theta + y\sin\phi\sin\theta$$
$$+ z\cos\theta)] \, ds.$$

Let us assume the current distribution along the conductor is a travelling wave of constant amplitude and is given by

$$(7) \qquad I(s) = I_0 \exp\left(-i\frac{k}{p}s\right)$$

where I_0 is the amplitude and p is the phase velocity of the current along the conductor relative to the velocity of light in free space.

Referring now to the rectangular components of the Hertzian vector potential Π, it is seen that the expression for Π_z is given by

$$(8) \qquad \Pi_z = \frac{-aI_0}{4\pi\epsilon i\omega}\frac{\exp(-ikR)}{R}\int_0^{t_0}\exp\left(-i\frac{k}{p}s\right)\exp[ik(x\cos\phi\sin\theta+z\cos\theta)] \\ \times \sin t\, dt.$$

In terms of the parametric equations (1), one can obtain upon substitution in eq. (8) the following result:

$$(9) \qquad \Pi_z = \frac{-aI_0}{4\pi\epsilon i\omega}\frac{\exp(-ikR)}{R}\int_0^{t_0}\sin t\Big\{\exp ik\Big[-\frac{a}{pm}K(m,t)+a\cos t\cos\phi\sin\theta \\ +\frac{b}{2\pi}t\cos\theta\Big]\Big\}dt.$$

Simplifying eq. (9), we get

$$(10) \qquad \Pi_z = \frac{-aI_0}{4\pi\epsilon i\omega}\frac{\exp(-ikR)}{R}\int_0^{t_0}\sin t\{\exp[i\alpha t+i\beta\sin 2t+i\gamma\sin t]\}dt,$$

where we introduce

$$\alpha = \left(\frac{kb}{2\pi}\cos\theta-\frac{ka}{pm}c_1\right),$$

$$\beta = \frac{ka}{pm}c_2,$$

and

$$\gamma = ka\sin\theta\cos\phi.$$

In order to obtain a series expansion for eq. (10), we shall use the following well known Fourier–Bessel expansions,

$$(11) \qquad \exp(ix\sin\theta) = \sum_{n=-\infty}^{\infty}J_n(x)\exp(in\theta),$$

$$\exp(ix\sin 2\theta) = \sum_{n=-\infty}^{\infty}J_n(x)\exp(i2n\theta).$$

Utilizing the above expressions, eq. (10) becomes

$$(12)\ \Pi_z = \frac{-aI_0}{4\pi\epsilon i\omega}\frac{\exp(-ikR)}{R}\sum_m\sum_n J_m(\beta)J_n(\gamma)\int_0^{t_0}\sin t\exp[i\alpha t+i2mt+int]dt.$$

The above integral can easily be evaluated by expressing $\sin t$ in terms of its exponential equivalent; therefore

$$(13) \quad \Pi_z = \frac{aI_0}{8\pi ei\omega} \frac{\exp(-ikR)}{R} \sum_m \sum_n J_m(\beta) J_n(\gamma) \left\{ \frac{\exp[i(\alpha+n+2m+1)t_0]-1}{\alpha+n+2m+1} \right.$$
$$\left. + \frac{\exp[i(\alpha+n+2m-1)t_0]-1}{\alpha+n+2m-1} \right\}.$$

The z component of the Hertzian vector potential can be derived in exactly the same way. It is obvious that there is no y component. The expression for Π_z is given by

$$(14) \quad \Pi_z = \frac{-bI_0}{8\pi^2\epsilon\omega} \frac{\exp(-ikR)}{R} \sum_m \sum_n J_m(\beta) J_n(\gamma) \left\{ \frac{\exp[i(\alpha+n+2m)t_0]-1}{\alpha+n+2m} \right\}.$$

It is usually desirable to express the Hertzian vector potential in spherical co-ordinates. This can be easily achieved by utilizing the following transformation equations:

$$(15) \quad \begin{aligned} \Pi_r &= \Pi_x \sin\theta \cos\phi + \Pi_y \sin\theta \sin\phi + \Pi_z \cos\theta, \\ \Pi_\theta &= \Pi_x \cos\theta \cos\phi + \Pi_y \cos\theta \sin\phi - \Pi_z \sin\theta, \\ \Pi_\phi &= -\Pi_x \sin\phi + \Pi_y \cos\phi. \end{aligned}$$

Also, by using the following vector relationship, the electric field components can be derived from the Hertzian vector potential.

$$(16) \qquad \overline{E} = \omega^2 \mu\epsilon\overline{\Pi} + \nabla(\nabla\cdot\overline{\Pi})$$

where μ is the permeability of free space.

The expressions in eqs. (13) and (14) for the radiation field in the x and z directions are calculated for the sinuate antenna of six turns, for different values of p. It is found that the best-fitting pattern is obtained when $p = 0.95$.

ENDFIRE OPERATION

In order to illustrate the derived results, a sinuate antenna of endfire operation has been designed and tested. The condition which should be satisfied in order to have maximum radiation along the $\theta = 0°$ direction is as follows (see Fig. 2):

$$\frac{1}{\rho} \text{ arc length } AB - \frac{b}{2} = \frac{\lambda}{2}.$$

An experimental six-cycle array, backed by a circular ground plane, was constructed on the basis of the foregoing analysis. A design frequency of 2650 Mc/s was chosen for convenience in pattern taking; the E- and H-plane patterns were measured. Both Cumming (1955) and Sengupta (1958) investigated only the radiation characteristics of a six-element array, and their results differ somewhat in beamwidth and bandwidth. Cumming found that with the zigzag antenna a bandwidth of 50% and a beamwidth of 35° can be readily achieved. However, Sengupta observed that a sharper beam is possible and found the half-power beamwidth of 22° in E plane and 28° in H plane.

In the present paper the author has also studied the radiation characteristics of a six-cycle array. It is found that the measured E-plane pattern of the sinuate antenna shown in Fig. 3 agrees quite well with the calculated pattern
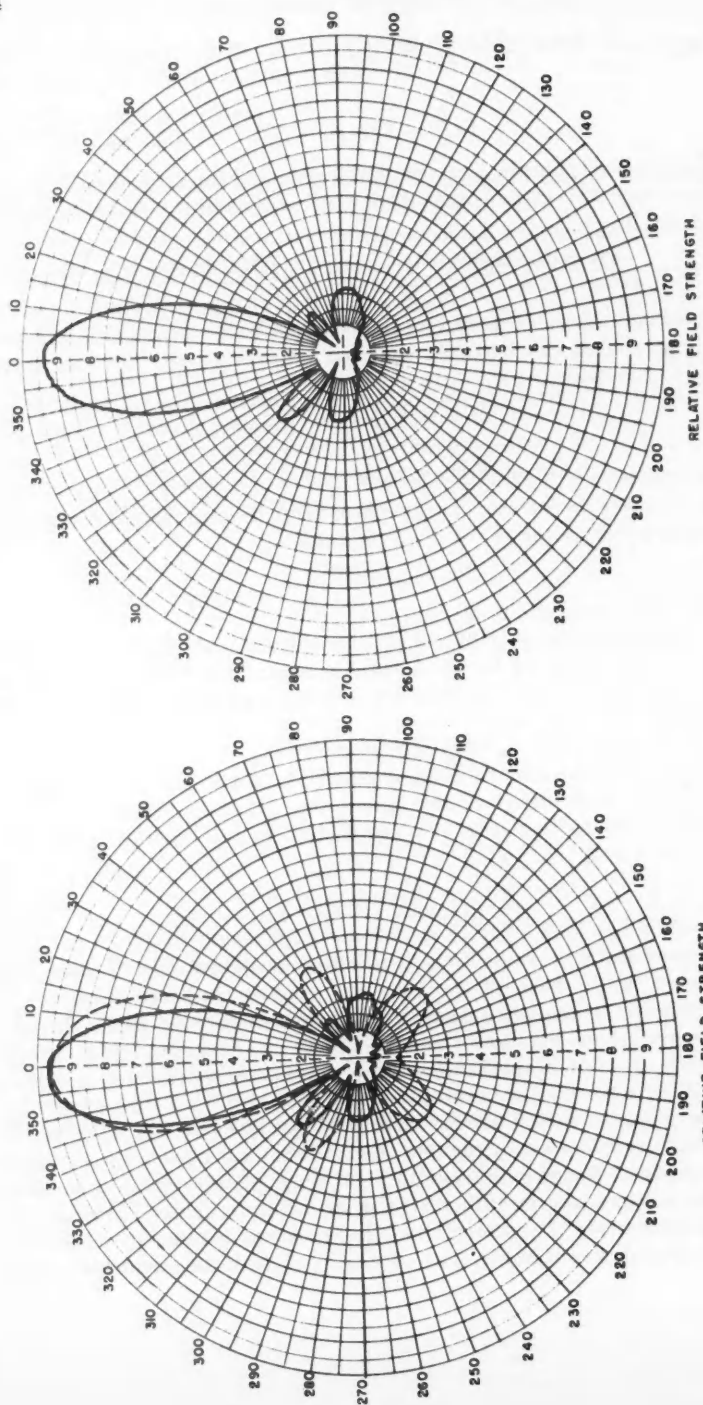
124

RELATIVE FIELD STRENGTH

Fig. 4. Measured *E*-plane pattern at 2660 Mc/s.

RELATIVE FIELD STRENGTH

Fig. 3. *E*-plane patterns at 2650 Mc/s.

RELATIVE FIELD STRENGTH
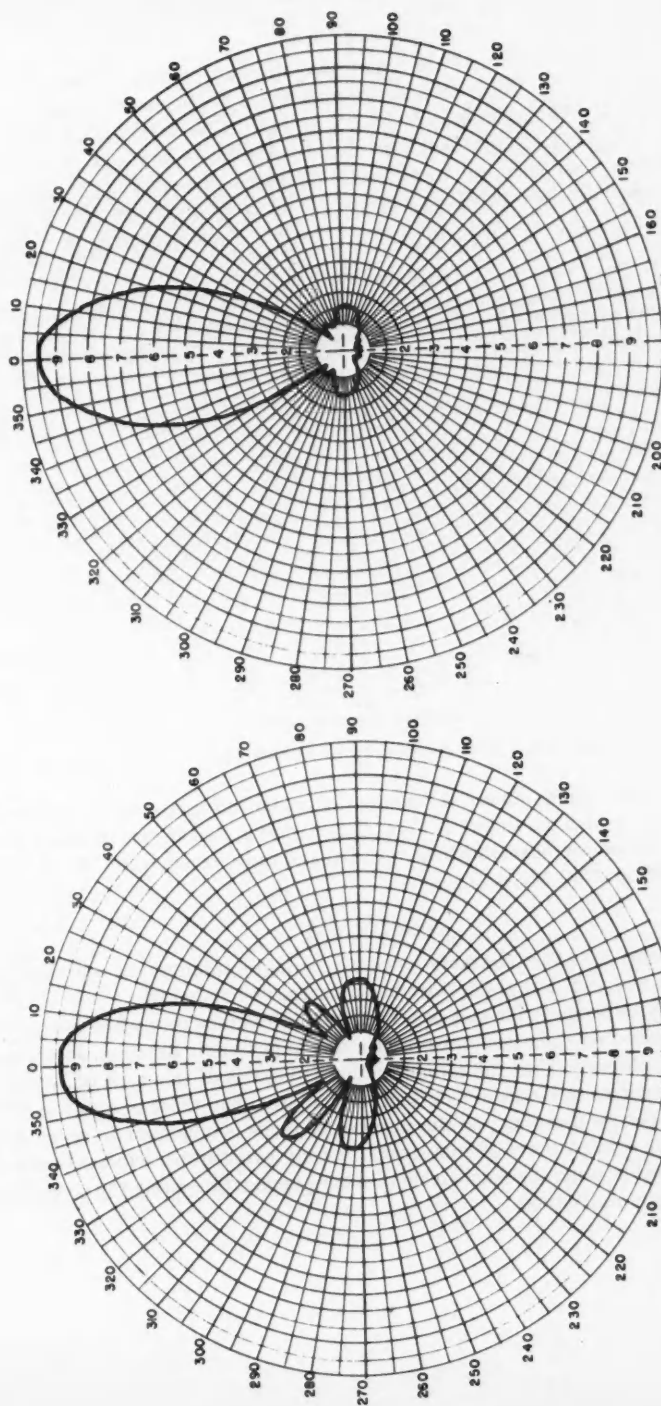
FIG. 6. Measured *H*-plane pattern at 2600 Mc/s.

RELATIVE FIELD STRENGTH
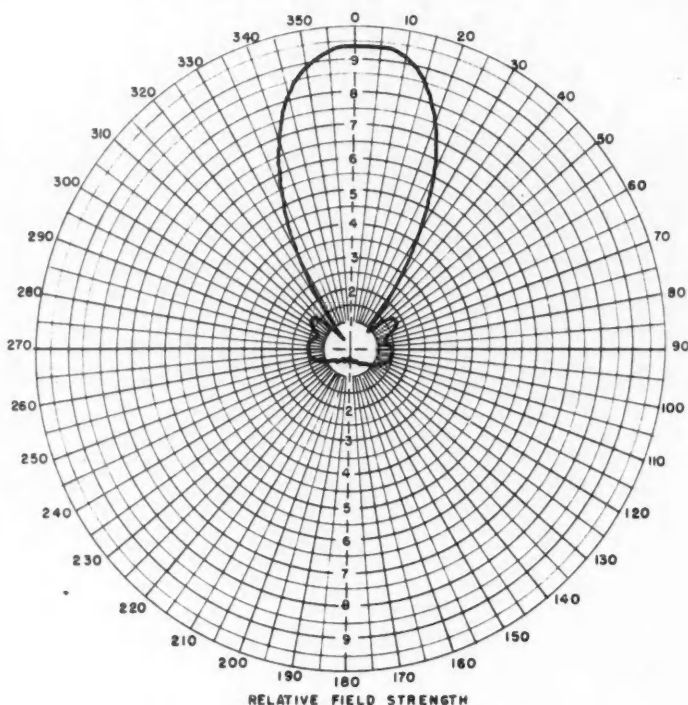
FIG. 5. Measured *E*-plane pattern at 2700 Mc/s.

FIG. 7. Measured *H*-plane pattern at 2700 Mc/s.

shown in the dotted curve. A number of radiation patterns for different frequencies are also presented in Figs. 4, 5, 6, and 7, and it can be easily seen that the half-power beamwidth in the *E* plane only varies from 28° at 2660 Mc/s to 32° at 2700 Mc/s.

CONCLUSIONS

The general radiation characteristics of a sinuate antenna are very similar to those of a zigzag, but the former has a narrower bandwidth.

The analysis presented in this paper seems quite satisfactory when compared with the measured radiation pattern of a six-cycle sinuate antenna. However, it has been observed that the radiation characteristics of this type of antenna are more sensitive to the axial length of the radiator than those of a zigzag. The endfire properties disappear as the number of turns is increased to seven and eight, but it regains them at nine turns. A fully satisfactory explanation will only be possible when the mechanism of wave propagation along the conductor is thoroughly understood.

ACKNOWLEDGMENTS

REFERENCES

CUMMING, W. A.   1955.   IRE Trans. on Antennas and Propagation, **AP-3**, 52.
SENGUPTA, D. L.   1958.   IRE Trans. on Antennas and Propagation, **AP-6**, 191.
WONG, J. Y. and LOH, S. C.   1959.   IRE Trans. on Antennas and Propagation, **AP-7**, 46.

DIFFRACTION BY A SPHEROID[1]

BERTRAM R. LEVY AND JOSEPH B. KELLER

ABSTRACT

The diffraction of a spherical scalar wave by a hard or soft spheroid is investigated theoretically. First the diffracted field is determined by the geometrical theory of diffraction. Then for comparison the corresponding boundary value problem is solved exactly in terms of a series of products of spheroidal functions. The series involves the "radial" eigenfunctions which correspond to appropriate complex eigenvalues. Asymptotic expansions are derived for these functions for large values of the variable and the parameter. When used in the series solution, these expansions yield the asymptotic form of the diffracted field for incident wavelengths small compared to the spheroid dimensions. This result coincides precisely with that given by the geometrical theory. This agreement provides another verification of that theory. The expression for the field is used to calculate the backscattering and the field on the spheroid. The electromagnetic backscattering is finally computed with the aid of a theorem which relates it to the two scalar results.

1. INTRODUCTION

A spheroid is a solid of revolution generated by rotating an ellipse about one of its axes. We consider the problem of determining the field which results when a wave is incident upon a spheroid. The customary manner of dealing with such a problem involves formulating it as a boundary value problem for the reduced wave equation. This problem is then solved by means of a series of products of spheroidal wave functions. The resulting series has been extensively studied in the literature. A compilation of the properties of the spheroidal functions contained in this series together with a complete bibliography of previous work on diffraction by a spheroid is contained in the book by Flammer (1957). However, this well-known solution is practically useless when the wavelength of the incident field is small compared to the dimensions of the spheroid. It is just this case which we treat here, and therefore we must use a different procedure. In fact, we use two different procedures, both of which yield the desired result.

Our first result, given in Section 2, is based upon the geometrical theory of diffraction (Keller 1958). This is a theory which describes the field scattered by any object directly in terms of geometrical properties of the object and certain coefficients determined from a few canonical problems. We have previously applied this theory to diffraction by convex cylinders (Keller 1956) and convex solids (Levy and Keller 1959). Whenever possible we compared the results of that theory with the asymptotic form (for wavelength small compared to object dimensions) of the solution of the corresponding boundary

value problem. In every case the agreement was perfect, including that of
the elliptic cylinder (Levy 1958). Although it has not yet been *proved* that
this agreement will always occur, we are convinced that this is the case.

In Section 3 we formulate and solve the associated boundary value problem.
Then by deriving asymptotic expansions of the spheroidal functions the
solution is asymptotically expanded. Our results closely parallel those of Ritt
and Kazarinoff (1959), who evaluated the field on the surface of the spheroid.
We find that for points off as well as on the spheroid the asymptotic expansion
of the diffracted field agrees with geometric theory given in Section 2. How-
ever, to recognize the identity of the two results for points not on the surface
of the spheroid it is necessary to utilize certain addition formulas for elliptic
integrals.

As applications of our result, we compute the field scattered back to the
source, and then find the backscattering cross section. We also evaluate the
field on the surface of the spheroid.

All of our results pertain to a prolate spheroid. The incident field is pro-
duced by a point source on the axis of revolution. The field is a scalar which
satisfies the reduced wave equation and the spheroid is either hard or soft.
In the case of backscattering, the cross section for an electromagnetic wave
hitting a perfectly conducting spheroid is also given. This calculation is based
upon a theorem proved in Appendix II. It relates the electromagnetic back-
scattering for axial incidence, on a body of revolution, to the corresponding
scalar results for hard and soft bodies.

2. GEOMETRIC CONSTRUCTION OF THE DIFFRACTED FIELD

Let us consider a prolate spheroid in a homogeneous medium, having
propagation speed c. Suppose that a point source of radiation, located on the
axis of revolution of the spheroid, emits a wave of angular frequency ω. Then
$k = \omega/c$ is the propagation constant of the medium for such a wave. When
the incident spherical wave strikes the spheroid, reflected and diffracted
fields are produced. The reflected field u_r can be constructed by the method
of geometrical optics, as described, for example, by Keller, Lewis, and Seckler
(1956). The diffracted field u_d can be constructed by means of the geometrical
theory of diffraction, as has been done by Levy and Keller (1959) for diffrac-
tion by any smooth convex scattering object. When their result is specialized
to the case of a point source on the axis of a body of revolution it becomes

$$(1) \quad u_d(P) = \frac{e^{ikR_0}}{4\pi R_0}\left[\left\{\frac{r_0\rho_1}{s_1 r_1(\rho_1 - s_1)}\right\}^{1/2} \sum_m \frac{D_m(P_1)D_m(Q_1)}{1 + \exp\left(ikT - \int_0^T \alpha_m d\tau\right)}\right.$$

$$\times \exp\left\{ik(t_1 + s_1) - \int_{Q_1}^{P_1}\alpha_m d\tau\right\} - i\left\{\frac{r_0\rho_2}{s_2 r_2(s_2 - \rho_2)}\right\}^{1/2}$$

$$\left.\times \sum_m \frac{D_m(P_2)D_m(Q_2)}{1 + \exp\left(ikT - \int_0^T \alpha_m d\tau\right)} \exp\left\{ik(t_2 + s_2) - \int_{Q_2}^{P_2}\alpha_m d\tau\right\}\right].$$

In (1) P denotes the point at which the field is evaluated. The plane containing P and the axis we will call the xy plane. Then s_1 and s_2 denote the lengths of the tangents from P to the spheroid in this plane and P_1, P_2 denote the corresponding points of tangency (see Fig. 1). The points Q_1 and
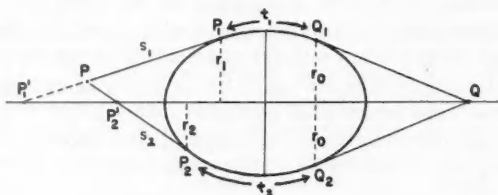

FIG. 1.   A cross section of the ellipsoid showing the source Q and a field point P. Two rays from Q are tangent to the ellipsoid at Q_1 and Q_2 where they produce diffracted surface rays. The ray from Q_1 travels a distance t_1 along the ellipsoid to the point P_1 from which it sheds a diffracted ray which passes through P. In addition it continues to encircle the ellipsoid and sheds another ray through P each time it passes P_1. The ray from Q_2 sheds rays through P each time it passes through P_2. These rays pass through the axial caustic at P_3' before reaching P.

Q_2 are the points of tangency of the tangents from the source point Q to the spheroid in this plane. The distances from the axis to P_1, P_2, and Q_1 or Q_2 are denoted by r_1, r_2, and r_0 respectively. The total arc length of the generating ellipse is denoted by T, while t_1 is the arc length along the ellipse from Q_1 to P_1 and t_2 is the arc length from Q_2 to P_2. The length of the tangent from P_1 to the point P_1' at which it intersects the axis is denoted by ρ_1, while ρ_2 denotes
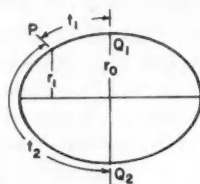

FIG. 2.   A cross section of the ellipsoid showing the points Q_1 and Q_2 at which two incident rays are tangent to it. The incident field is a plane wave coming from the right. The tangent rays produce diffracted rays which travel distances t_1 and t_2 to a point P on the surface.

the distance from P_2 to P_2'. The integrals are with respect to arc length τ along the generating ellipse. The decay coefficient $\alpha_m(\tau)$ is defined in terms of $b(\tau)$, the radius of curvature of the ellipse, by

$$(2) \qquad \alpha_m = e^{-i\pi/6}(k/6)^{1/3}q_m b^{-2/3}.$$

The constant q_m is defined in Appendix I. For the soft spheroid, $q_m \equiv q_m^{(1)}$ while for the hard spheroid $q_m \equiv q_m^{(2)}$. When it becomes necessary to distinguish between these two cases the coefficient α_m must be given the same superscript as q_m. The diffraction coefficient D_m depends upon the radius of curvature at the point at which D_m is evaluated. For the soft spheroid $D_m \equiv D_m^{(1)}$ is given by

(3) $$D_m^{(1)} = \pi^{3/4}\, 2^{1/4}\, 6^{-2/3}\, k^{-1/12}\, \{A'(q_m^{(1)})\}^{-1} e^{i\pi/24} b^{1/6}.$$

For the hard spheroid $D_m \equiv D_m^{(2)}$ is given by

(4) $$D_m^{(2)} = \pi^{3/4}\, 2^{-1/4}\, 6^{-1/6}\, k^{-1/12}\, \{q_m^{(2)1/2}\, A(q_m^{(2)})\}^{-1}\, e^{i\pi/24}\, b^{1/6}.$$

The Airy function A is defined in Appendix I.

The result (1) can be rewritten in another form by introducing prolate spheroidal co-ordinates ξ, η, ϕ. These co-ordinates are most easily defined by relating them to the Cartesian co-ordinates x, y, z. Let the axis of symmetry of the spheroid be the x axis and let the origin be at the center of the spheroid. Finally, let $2h$ denote the interfocal distance of the generating ellipse. Then the prolate spheroidal co-ordinates may be defined by

$$x = h \cosh \xi \cos \eta,$$
$$y = h \sinh \xi \sin \eta \cos \phi,$$
$$z = h \sinh \xi \sin \eta \sin \phi.$$

The angular variables η and ϕ range from 0 to π and 0 to 2π respectively, while $0 \leqslant \xi < \infty$. The spheroid may be defined by the equation $\xi = a$. The point source Q will be assumed to lie at $\eta = 0$, $\xi = \xi_0 \geqslant a$. The η co-ordinates of the points of tangency Q_1, P_1, Q_2, and P_2 will be denoted by η_1, η_2, η_3, and η_4 respectively. Their other co-ordinates are $\xi = a$ and either $\phi = 0$ or $\phi = \pi$.

The geometrical quantities in (1) can be expressed in terms of these co-ordinates. Most of them have previously been calculated by Levy (1958) and the remaining ones can be easily found. When these expressions are inserted into (1), the result for the field diffracted by the soft spheroid becomes

(5) $$u_d(P) = \pi^{1/2}\, 2^{-3/2}\, 6^{-4/3}\, e^{i\pi/12}\, k^{-1/6}\, h^{-7/6}\, (\cosh a \sinh a)^{1/6}$$

$$\times (\sinh \xi \sinh \xi_0 \sin \eta)^{-1/2} (\cosh^2 \xi_0 - \cosh^2 a)^{-1/4} \sum_{n=0}^{\infty} \{f_n(a, \eta_1, \eta_2)$$

$$- i f_n(a, -\eta_3^*, -\eta_4^*)\} \{A'(q_n^{(1)})\}^{-2} \Big[1 + \exp\Big\{ ikh \int_0^{2\pi} (\cosh^2 a - \cos^2 \eta)^{1/2}\, d\eta$$

$$+ i\tau_n^{(1)} (kh)^{1/3} (\cosh a \sinh a)^{2/3} \int_0^{2\pi} (\cosh^2 a - \cos^2 \eta)^{-1/2}\, d\eta \Big\} \Big]^{-1}.$$

In (5), $\tau_n^{(1)} = 6^{-1/3} e^{i\pi/3} q_n^{(1)}$ and $\eta_3^* = 2\pi - \eta_3$, while $\eta_4^* = \eta_4$ if the ϕ co-ordinate of P_2 is 0 and $\eta_4^* = 2\pi - \eta_4$ if the ϕ co-ordinate of P_2 is π. We assume that the ϕ co-ordinate of P is 0. The function f_n is given by

(6) $$f_n = (\cosh^2 a - \cos^2 \eta_2)^{1/4}\, \{ (\cosh \xi \cos \eta - \cosh a \cos \eta_2)^2$$

$$+ (\sinh \xi \sin \eta - \sinh a \sin \eta_2)^2 \}^{-1/4} \exp\Big[ikh \tanh \xi_0 (\cosh^2 \xi_0 - \cosh^2 a)^{1/2}$$

$$+ ikh \{ (\cosh \xi \cos \eta - \cosh a \cos \eta_2)^2 + (\sinh \xi \sin \eta - \sinh a \sin \eta_2)^2 \}^{1/2}$$

$$+ ikh \int_{\eta_1}^{\eta_2} (\cosh^2 a - \cos^2 \eta)^{1/2}\, d\eta + i\tau_n^{(1)} (kh)^{1/3} (\cosh a \sinh a)^{2/3}$$

$$\times \int_{\eta_1}^{\eta_2} (\cosh^2 a - \cos^2 \eta)^{-1/2}\, d\eta \Big].$$

For the hard spheroid (5) applies if we replace

$$\tau_n^{(1)} \quad \text{by} \quad \tau_n^{(2)} \quad \text{and} \quad \{A'(q_n^{(1)})\}^{-2} \quad \text{by} \quad 3\{q_n^{(2)}A^2(q_n^{(2)})\}^{-1}.$$

The preceding result (1) or (5) is not valid on the surface of the spheroid nor on the axis of symmetry because both of these places are caustics of the diffracted rays. However, it can easily be modified to be valid in these places by applying the appropriate caustic corrections (Levy and Keller 1959). To obtain the field on the surface, we must multiply the mth term in the first sum in (1) by the factor

$$(7) \qquad R_m = 2^{1/2}6^{1/3}\pi^{-1/2}k^{1/6}s_1^{1/2}A(q_m^{(2)})\exp(-iks_1-i\pi/12)b^{-1/3}(P_1),$$

multiply the mth term of the second sum in (1) by R_m with s_1 replaced by s_2 and P_1 replaced by P_2, and then let s_1 and $s_2 \to 0$. Upon doing this and noting that P_1, P_2, and P become identical, while $r_1 = r_2$ and $P_1 = P_2$, we find that (1) becomes on the surface of the hard spheroid

$$(8) \quad u_d(P) = e^{ikR_0}(4\pi R_0)^{-1}2^{1/2}6^{1/3}\pi^{-1/2}k^{1/6}e^{-i\pi/12}(r_0/r_1)^{1/2}b^{-1/3}(P)$$

$$\times \sum_m \frac{D_m(P)A(q_m)}{1+\exp\left(ikT-\int_0^T \alpha_m d\tau\right)}\left\{D_m(Q_1)\exp\left(ikt_1-\int_{Q_1}^P \alpha_m d\tau\right)\right.$$

$$\left. -iD_m(Q_2)\exp\left(ikt_2-\int_{Q_2}^P \alpha_m d\tau\right)\right\}.$$

For later use it is convenient to specialize (8) to the case of plane wave incidence. If the incident plane wave is given by $u_i = e^{-ikz}$ then the diffracted field is given by (8) with $e^{ikR_0}(4\pi R_0)^{-1}$ replaced by 1. The points Q_1 and Q_2 become the ends of the minor axis of the generating ellipse of the spheroid. Thus, when we write (8) in terms of spheroidal co-ordinates for plane wave incidence, we obtain

$$(9) \qquad u_d(P) = \frac{\pi(\cosh a)^{1/2}}{(\sin \eta)^{1/2}(\cosh^2 a-\cos^2 \eta)^{1/4}}$$

$$\times \sum_{m=1}^\infty \frac{\exp\{G(\pi/2, \eta)\}-i\exp\{G(\eta, 3\pi/2)\}}{[1+\exp\{G(0, 2\pi)\}]q_m^{(2)}A(q_m^{(2)})}.$$

Here we have introduced the function $G(\alpha,\beta)$ which is defined by

$$(10) \quad G(\alpha,\beta) = ikh\int_\alpha^\beta (\cosh^2 a-\cos^2 \eta)^{1/2}d\eta+i(kh)^{1/3}\tau_n^{(2)}(\sinh a \cosh a)^{2/3}$$

$$\times \int_\alpha^\beta (\cosh^2 a-\cos^2 \eta)^{-1/2}d\eta.$$

To calculate the backscattering cross section of the spheroid, we again specialize (5) to plane wave incidence with $u_{inc} = e^{-ikz}$. We then apply the method of Levy and Keller (1959) to correct u_d on the axial caustic. When this is done we find that the leading term in the expansion of $u_d(P)$ for a point on the axis becomes, for large values of x,

$$(11) \quad u_{\mathrm{d}}(P) = -\delta e^{ikz+i\pi/3} \exp\left\{ i\tau(kh)^{1/3} (\cosh a \sinh a)^{2/3} \int_{\pi/2}^{3\pi/2} (\cosh^2 a \right.$$

$$\left. -\cos^2 \eta)^{-1/2} d\eta \right\} \pi^2 k^{1/3} h (\sinh a \cosh a)^{2/3} (xq A^3 6^{1/3})^{-1}.$$

In (11), $\tau = 6^{-1/3} e^{i\pi/3} q$. The values of δ, q, and A or A' are given below for the two cases:

$$(12) \qquad \left. \begin{array}{l} \delta = 1 \\ q = 1.469354 \\ A = 1.16680 \end{array} \right\} \qquad \text{for the hard spheroid};$$

$$(13) \qquad \left. \begin{array}{l} \delta = q A^2 3^{-1} (A')^{-2} \\ q = 3.372134 \\ A' = -1.059053 \end{array} \right\} \qquad \text{for the soft spheroid}.$$

The total backscattered field u is the sum of the diffracted field $u_{\mathrm{d}}(P)$ and the geometrically reflected field $u_{\mathrm{g}}(P)$. To calculate $u_{\mathrm{g}}(P)$ we use the methods of Keller *et al.* (1956). We then obtain for the leading term in $u_{\mathrm{g}}(P)$ the result

$$(14) \qquad u_{\mathrm{g}}(P) = \pm \frac{h}{2} \frac{\cosh^2 a}{\sinh a} \exp\{ ik(x - 2h \cosh a) \}.$$

Here, the positive sign holds for the hard spheroid and the negative sign for the soft spheroid. Upon combining (11) and (14), we obtain

$$(15) \quad u(P) = \pm \frac{h}{2} \frac{\cosh^2 a}{\sinh a} \exp\{ ik(x - 2h \cosh a) \}$$

$$\left[1 - \frac{2\delta \pi^2 (kh)^{1/3} (\sinh a)^{5/3}}{q A^2 6^{1/3} (\cosh a)^{4/3}} \exp\left\{ 2ikh \cosh a + i\pi/3 \right. \right.$$

$$\left. \left. + i\tau(kh)^{1/3} (\cosh a \sinh a)^{2/3} \int_{\pi/2}^{3\pi/2} (\cosh^2 a - \cos^2 \eta)^{-1/2} d\eta \right\} \right].$$

Here, the plus sign and (12) hold for the hard spheroid and the negative sign and (13) hold for the soft spheroid.

3. ANALYTIC SOLUTION

In terms of our previously defined spheroidal co-ordinates the reduced wave equation corresponding to a point source located at $\xi = \xi_0$, $\eta = 0$ is

$$(1) \quad u_{\xi\xi} + u_{\eta\eta} + u_\xi \coth \xi + u_\eta \cot \eta + (kh)^2 (\cosh^2 \xi - \cos^2 \eta) u = \frac{\delta(\eta)\delta(\xi - \xi_0)}{2\pi h \sinh \xi_0 \sin \eta}.$$

In (1) we have made use of the fact that u is independent of ϕ. The boundary value problem to be solved is to find a solution $u(\xi, \eta)$ of (1) which satisfies the Sommerfeld radiation condition at $\xi = \infty$. On the surface of the spheroid u must satisfy either of the following boundary conditions:

(2) $u(a,\eta) = 0$ (acoustically soft spheroid)

or

(3) $u_\xi(a,\eta) = 0$ (acoustically hard spheroid).

If we replace the right-hand side of (1) by zero, the resulting equation has product solutions of the form $\Phi(\xi)\Psi(\eta)$. The functions Φ and Ψ satisfy the equations

(4) $$\frac{d^2\Phi}{d\xi^2} + \coth\xi\frac{d\Phi}{d\xi} - (kh)^2(b^2-\cosh^2\xi)\Phi = 0,$$

(5) $$\frac{d^2\Psi}{d\eta^2} + \cot\eta\frac{d\Psi}{d\eta} + (kh)^2(b^2-\cos^2\eta)\Psi = 0.$$

In (4) and (5) b is an arbitrary separation constant. We now note that for certain complex values b_n of b, (4) has outgoing solutions $V_n^{(1)}(\xi)$, which satisfy either of the conditions $V_n^{(1)}(a) = 0$ or $V_n^{(1)\prime}(a) = 0$.* Consequently, we may try to solve the boundary value problem by assuming that u has the form

(6) $$u(\xi,\eta) = \sum_{n=1}^{\infty} W_n(\eta)V_n^{(1)}(\xi).$$

If we substitute (6) into (1) and make use of the orthogonality of the $V_n^{(1)}$, we find that W_n satisfies the equation

(7) $$\frac{d^2W_n}{d\eta^2} + \cot\eta\frac{dW_n}{d\eta} + (kh)^2(b_n^2-\cos^2\eta)W_n = C_n\frac{\delta(\eta)}{\sin\eta}.$$

In (7) the constant C_n has the value

(8) $$C_n = V_n^{(1)}(\xi_0)\left[2\pi h\int_a^\infty \{V_n^{(1)}(\xi)\}^2\sinh\xi\,d\xi\right]^{-1}.$$

The orthogonality condition used in obtaining (7) is

(9) $$\int_a^\infty V_n^{(1)}(\xi)V_m^{(1)}(\xi)\sinh\xi\,d\xi = \delta_{nm}\int_a^\infty\{V_n^{(1)}(\xi)\}^2\sinh\xi\,d\xi.$$

This condition follows from (4) and the boundary conditions satisfied by the $V_n^{(1)}$. An evaluation similar to the one carried out by Levy (1958) shows that for the soft spheroid

(10) $$\int_a^\infty\{V_n^{(1)}(\xi)\}^2\sinh\xi\,d\xi = \{2(kh)^2b_n^{(1)}\}^{-1}V_n^{(1)\prime}(a)\sinh a\frac{\partial}{\partial b}V_n^{(1)}(a).$$

For the hard spheroid we obtain instead

(11) $$\int_a^\infty\{V_n^{(1)}(\xi)\}^2\sinh\xi\,d\xi = -\{2(kh)^2b_n^{(2)}\}^{-1}V_n^{(1)}(a)\sinh a\frac{\partial}{\partial b}V_n^{(1)\prime}(a).$$

*When it becomes necessary to distinguish between the sets of eigenvalues we will use $b_n^{(1)}$ to denote eigenvalues corresponding to the boundary condition (2) and $b_n^{(2)}$ to denote eigenvalues corresponding to the boundary condition (3).

In order to solve (7) we let $W_n^{(1)}(\eta)$ be a solution of the homogeneous equation obtained from (7) by setting $C_n = 0$. We require $W_n^{(1)}(\eta)$ to be regular at $\eta = 0$. A simple calculation then shows that $W_n^{(1)}(\eta)$ is an even function of η and that $W_n^{(1)}(\pi - \eta)$ is also a solution of the homogeneous equation. Since $\eta = 0$ is a singular point of (7) the subsequent analysis will be simplified by shifting the delta function to $\eta = \eta_0$ and, finally, letting $\eta_0 \to 0$. Then the conditions determining $W_n(\eta)$ are that it be regular at $\eta = 0$ and $\eta = \pi$, that it be continuous across $\eta = \eta_0$, and that $W_n'(\eta)$ have a jump of magnitude $C_n(\sin \eta_0)^{-1}$ across $\eta = \eta_0$. By applying these conditions we find that $W_n(\eta)$ is given by

$$
(12) \quad
\begin{aligned}
W_n(\eta) &= -C_n\{\sin \eta_0 \omega_n(\eta_0)\}^{-1} W_n^{(1)}(\eta_0) W_n^{(1)}(\pi - \eta), && \eta_0 \leqslant \eta \leqslant \pi; \\
W_n(\eta) &= -C_n\{\sin \eta_0 \omega_n(\eta_0)\}^{-1} W_n^{(1)}(\pi - \eta_0) W_n^{(1)}(\eta), && 0 \leqslant \eta \leqslant \eta_0.
\end{aligned}
$$

Here $\omega_n(\eta)$ is defined by

$$
(13) \qquad \omega_n(\eta) = W_n^{(1)}(\pi - \eta) W_n^{(1)\prime}(\eta) + W_n^{(1)}(\eta) W_n^{(1)\prime}(\pi - \eta).
$$

We note that ω_n is the Wronskian of two linearly independent solutions of the homogeneous equation. Therefore, a simple calculation shows that it has the value

$$
(14) \qquad \omega_n(\eta) = \frac{\omega_n(\pi/2)}{\sin \eta} = 2 W_n^{(1)}(\pi/2) W_n^{(1)\prime}(\pi/2).
$$

Upon using (14) in (12) and letting $\eta_0 \to 0$ we obtain

$$
(15) \qquad W_n(\eta) = -C_n\{2 W_n^{(1)}(\pi/2) W_n^{(1)\prime}(\pi/2)\}^{-1} W_n^{(1)}(0) W_n^{(1)}(\pi - \eta).
$$

We can obtain another expression for $W_n(\eta)$ by using (13) directly in (12). Upon doing this and using the fact that $W_n^{(1)}(\eta)$ has a logarithmic singularity at $\eta = \pi$,[*] we obtain

$$
(16) \qquad W_n(\eta) = -C_n\{\lim_{\eta_0 \to 0} \sin \eta_0 W_n^{(1)\prime}(\pi - \eta_0)\}^{-1} W_n^{(1)}(\pi - \eta).
$$

In Appendix I, equation (18), we have evaluated the limit appearing in (16). We use this result, together with (16), (10), and (8), in (6). Then, in the case of the soft spheroid, (6) becomes

$$
(17) \qquad u(\xi, \eta) = -\frac{k^2 h}{2 \sinh a} \sum_{n=1}^{\infty} \frac{b_n V_n^{(1)}(\xi_0) V_n^{(1)}(\xi) W_n^{(1)}(\pi - \eta)}{\cos\left\{ k \int_0^\pi (b_n^2 - \cos^2 \eta)^{1/2} d\eta \right\} V_n^{(1)\prime}(a) \dfrac{\partial}{\partial b} V_n^{(1)}(a)}.
$$

For the case of the hard spheroid (17) still applies if the right side is multiplied by -1 and if $V_n^{(1)}(a)$ and $V_n^{(1)\prime}(a)$ are interchanged.

We shall now obtain the asymptotic form of u for large values of kh by using the asymptotic expansions of the spheroidal functions given in Appendix I. We find, in the case of the soft spheroid, that (17) has the asymptotic form

[*]See Appendix I.

$$(18) \quad u(\xi, \eta) \sim -\pi^{1/2} 2^{-3/2} 6^{-4/3} e^{i\pi/12} k^{-1/6} h^{-7/6} (\sinh \xi \sinh \xi_0 \sin \eta)^{-1/2}$$

$$\times (\cosh a \sinh a)^{2/3} (\cosh^2 \xi_0 - \cosh^2 a)^{-1/4} (\cosh^2 \xi - \cosh^2 a)^{-1/4} (\cosh^2 a - \cos^2 \eta)^{-1/4}$$

$$\times \sum_{n=1}^{\infty} \{A'(q_n^{(1)})\}^{-2} \exp\{iF(\xi) + iF(\xi_0)\} \frac{\exp\{iG(\eta)\} - i \exp\{-iG(\eta) + 2iG(\pi)\}}{1 + \exp\{2iG(\pi)\}}.$$

In (18) we have introduced $F(\xi)$ and $G(\eta)$ which are defined by

$$(19) \quad F(\xi) = kh \int_a^{\xi} (\cosh^2 \xi - \cosh^2 a)^{1/2} - i(kh)^{1/3} \tau_n^{(1)} (\sinh a \cosh a)^{2/3}$$

$$\times \int_a^{\xi} (\cosh^2 \xi - \cosh^2 a)^{-1/2} d\xi,$$

$$(20) \quad G(\eta) = kh \int_0^{\eta} (\cosh^2 a - \cos^2 \eta)^{1/2} d\eta + i(kh)^{1/3} \tau_n^{(1)} (\sinh a \cosh a)^{2/3}$$

$$\times \int_0^{\eta} (\cosh^2 a - \cos^2 \eta)^{-1/2} d\eta.$$

In the case of the hard spheroid (18)–(20) apply if $\tau_n^{(1)}$ is replaced by $\tau_n^{(2)}$ and $\{A'(q_n^{(1)})\}^{-2}$ is replaced by $3\{q_n^{(2)} A^2(q_n^{(2)})\}^{-1}$.

It is a simple matter to show that the result for u given in (5) of Section 2, obtained by the geometric theory of diffraction, agrees precisely with (18) obtained by asymptotically expanding the exact solution. The necessary calculations are contained in Levy's work (1958). The identity of the amplitudes follow from equation (I-1) of Levy's paper, while the identity of the phases follows from (54), (55), (56), and (57) of that paper.

Let us now calculate the diffracted field at a point $P(a, \eta)$ on the surface of a hard spheroid due to an incident plane wave e^{-ikz}. To do this, we write (17) for a hard spheroid, set $\xi = a$, multiply by $4\pi h \cosh \xi_0 \exp(-ikh \cos \xi_0)$ and let $\xi_0 \to \infty$ to obtain

$$(21) \quad u(a, \eta) \sim \frac{k^{11/6} h^{11/6} \pi^{1/2} e^{i\pi/12}}{\sinh a} \sum_{n=1}^{\infty} \frac{b_n W_n^{(1)}(\pi - \eta) \exp\{ikh f(b_n)\}}{\cos\left\{ k \int_0^{\pi} (b_n^2 - \cos^2 \eta)^{1/2} d\eta \right\} \frac{\partial}{\partial b} \{V_n^{(1)'}(a)\}}.$$

Here

$$(22) \quad f(b_n) = \lim_{\xi_0 \to \infty} \left\{ \int_{\cosh^{-1} b_n}^{\xi_0} (\cosh^2 \xi - b_n^2)^{1/2} d\xi - \cosh \xi_0 \right\}.$$

Using the methods of Appendix I we find

$$(23) \quad \frac{\partial}{\partial b} V_n^{(1)'}(a) \sim -\pi^{-1} (kh)^{4/3} 2^{1/2} (\sinh a)^{-1} (\cosh a)^{1/2} e^{-2i\pi/3} q_n A(q_n).$$

The evaluation of $f(b_n)$ has been carried out in a slightly different notation by Ritt (1959) and yields the result

$$(24) \quad f(b_n) = -\int_0^{\pi/2} (b_n^2 - \cos^2 \eta)^{1/2} d\eta.$$

Using (23) and (24) in (21), together with the asymptotic expansion of $W_n^{(1)}$ contained in Appendix I, we obtain

$$(25) \quad u(a,\eta) \sim \frac{(\cosh a)^{1/2}\pi}{(\sin \eta)^{1/2}(\cosh^2 a - \cos^2 \eta)^{1/4}} \sum_{n=1}^{\infty} \frac{e^{iG(\eta)} - ie^{2iG(\tau)-iG(\eta)}}{(1+e^{2iG(\tau)})q_n^{(2)}A(q_n^{(2)})} e^{-iG(\pi/2)}.$$

Here $G(\eta)$ is defined by (20). This result (25) is identical with equation (9) of Section 2, obtained by the geometric theory.

4. CONCLUSION AND ELECTROMAGNETIC BACKSCATTERING

We have determined the scalar field diffracted by a hard or soft spheroid of dimensions large compared to the incident wavelength. This field is given by (1) or (5) at points off the spheroid surface and off the axis. On the spheroid surface it is given by (8) for the hard spheroid and by (9) if the incident field is a plane wave. The backscattered field on the axis is given by (12) for an incident plane wave. All these results have been derived by using the geometric theory of diffraction and, independently, by asymptotically expanding the solution of the appropriate boundary value problem. They are in a form which is suitable for numerical evaluation.

As an application of our results we shall now calculate the backscattered field from a perfectly conducting spheroid when a plane electromagnetic wave is incident along the axis. To do this we could apply the geometric theory of diffraction directly. However, it is simpler to utilize our previous results by means of the theorem proved in Appendix II. According to that theorem

$$(1) \qquad\qquad \mathbf{E} = \tfrac{1}{2}(u_S - u_H)\, \mathbf{E}_i.$$

Here $\mathbf{E}$ is the backscattered electromagnetic field due to the incident field $\mathbf{E}_i e^{-ikz}$. The scalar backscattered fields are u_S and u_H for the soft and hard spheroids respectively, with the field e^{-ikz} incident. Upon using (15) of Section 2 for u_S and u_H, (1) yields

$$(2) \quad \mathbf{E} = \frac{-\mathbf{E}_i}{2}\frac{h\cosh^2 a}{\sinh a} \exp\{ik(x - 2h\cosh a)\} \left(1 - \frac{\pi^2(kh)^{1/3}(\sinh a)^{5/3}}{6^{1/3}(\cosh a)^{4/3}} \right.$$

$$\times \exp\{2ikh\cosh a + i\pi/3\} \left[3^{-1}A'^{-2}\exp\left\{ i\tau_1(kh)^{1/3}(\cosh a\,\sinh a)^{2/3} \right. \right.$$

$$\times \int_{\pi/2}^{3\pi/2} (\cosh^2 a - \cos^2 \eta)^{-1/2}\,d\eta \Big\} + q_2^{-1}A^{-2}\exp\left\{ i\tau_2(kh)^{1/3} \right.$$

$$\left.\left.\left. \times (\cosh a\,\sinh a)^{2/3}\int_{\pi/2}^{3\pi/2} (\cosh^2 a - \cos^2 \eta)^{-1/2}\,d\eta \Big\} \right] \right).$$

Here A and q_2 are given by (12) of Section 2, while A' and q_1 are given by (13) of that section. The last term in the brace can usually be neglected. From (2), the electromagnetic backscattering cross section can be computed.

APPENDIX I

Asymptotic Expansions of the Spheroidal Functions

In this appendix we study the asymptotic expansions as $kh \to \infty$ of the various solutions of equations (4) and (5) in Section 3. It will be convenient to denote kh by k. To analyze equation (4) of Section 3, we set

$$(1) \qquad \Phi(\xi) = (\sinh \xi)^{-1/2} \Gamma(\xi).$$

Then we find that Γ satisfies the equation

$$(2) \qquad \Gamma'' - k^2 (b^2 - \cosh^2 \xi + 2^{-1}k^{-2} - 4^{-1}k^{-2} \coth^2 \xi) \Gamma = 0.$$

Since $\xi > a > 0$, we may apply the methods of Olver (1954) to obtain uniform asymptotic expansions of $\Gamma(\xi)$. The calculation is similar to the one carried out by Levy (1958). It yields in the present case for the outgoing solution, $V^{(1)}(\xi)$, of equation (4) of Section 3,

$$(3) \qquad V^{(1)}(\xi) \sim \zeta^{1/4} 3^{1/3} \pi^{-1} (b^2 - \cosh^2 \xi)^{-1/4} (\sinh \xi)^{-1/2} A \left(3^{1/3} e^{-i\pi/3} k^{2/3} \zeta \right).$$

In (3) ζ is defined by

$$(4) \qquad \frac{2}{3} \zeta^{3/2} = \int_{\cosh^{-1} b}^{\xi} (b^2 - \cosh^2 x)^{1/2} dx.$$

The Airy function $A(t)$ is defined by

$$(5) \qquad A(t) = \int_0^\infty \cos(z^3 - tz) dz.$$

In the case when $\xi > \cosh^{-1} b$ we can expand the Airy functions in (3) to obtain

$$(6) \qquad V^{(1)}(\xi) \sim e^{i\pi/12} k^{-1/6} 2^{-1} \pi^{-1/2} (\cosh^2 \xi - b^2)^{-1/4} (\sinh \xi)^{-1/2}$$
$$\times \exp \left\{ ik \int_{\cosh^{-1} b}^{\xi} (\cosh^2 \xi - b^2)^{1/2} d\xi \right\}.$$

The calculation of the eigenvalues, b_n, is exactly the same as in Levy (1958) and yields

$$(7) \qquad b_n \sim \cosh a + \tau_n k^{-2/3} (\sinh a)^{2/3} (\cosh a)^{-1/3}.$$

Here τ_n is defined by

$$(8) \qquad \tau_n = 6^{-1/3} e^{i\pi/3} q_n.$$

In (7) and (8) b_n, τ_n, and q_n are to have superscripts 1 for the soft spheroid and superscripts 2 for the hard spheroid where $q_n^{(1)}$ is defined by $A(q_n^{(1)}) = 0$ and $q_n^{(2)}$ is defined by $A'(q_n^{(2)}) = 0$.

To obtain the asymptotic expansion of $W_n^{(1)}(\eta)$ we must proceed in a manner different from that which we followed in the case of the corresponding elliptic cylinder function. This is due to the singularities of equation (5) of Section 3 at $\eta = 0$ and $\eta = \pi$. Accordingly, we apply a boundary layer type

of analysis to obtain the asymptotic expansion. However, we do not find it necessary to introduce a stretched independent variable because we consider only the leading term in the expansion. The use of such a variable would permit us to obtain further terms. In the neighborhood of $\eta = 0$, equation (5) of Section 3 becomes

$$(9) \qquad \psi'' + \frac{1}{\eta}\,\psi' + p^2\psi = 0,$$

where

$$(10) \qquad p^2 = k^2(b^2 - 1).$$

Thus the solution regular at $\eta = 0$ is proportional to $J_0(p\eta)$. We may normalize it to have the value 1 at $\eta = 0$. Then

$$(11) \qquad \psi \sim J_0(p\eta) \qquad\qquad \text{for } \eta \ll 1.$$

Similarly, in the neighborhood of $\eta = \pi$, equation (5) of Section 3 has the form (9) with η replaced by $\pi - \eta$. Hence, we may conclude that

$$(12) \qquad \psi \sim A\,J_0\{p(\pi - \eta)\} + BN_0\{p(\pi - \eta)\} \qquad \text{for } \pi - \eta \ll 1.$$

In (12) A and B are as yet undetermined. Away from $\eta = 0$ and $\eta = \pi$, we may apply standard W.K.B. arguments to obtain

$$(13) \qquad \psi \sim \frac{C \cos\left\{ k \int_0^\eta (b^2 - \cos^2 \eta)^{1/2} d\eta \right\} + D \sin\left\{ k \int_0^\eta (b^2 - \cos^2 \eta)^{1/2} d\eta \right\}}{(\sin \eta)^{1/2}(b^2 - \cos^2 \eta)^{1/4}}$$

The constants A, B, C, and D are obtained by matching (11) and (12) to (13) in their respective common regions of validity. To obtain C and D we set $\eta = \epsilon k^{-1/2}$. Then the argument of J_0 in (11) is large as $k \to \infty$ and we may expand J_0 asymptotically for large argument. Upon doing this and requiring that the resulting expression be identical with (13) we obtain

$$(14) \qquad C = D = (\pi k)^{-1/2}.$$

To obtain A and B we set $\eta = \pi - \epsilon k^{-1/2}$. Then upon expanding (12) asymptotically and comparing with (13) we obtain

$$(15) \qquad A = \sin\left\{ k \int_0^\pi (b^2 - \cos^2 \eta)^{1/2} d\eta \right\},$$

and

$$(16) \qquad B = -\cos\left\{ k \int_0^\pi (b^2 - \cos^2 \eta)^{1/2} d\eta \right\}.$$

Using (14) in (13) we obtain the following result, which is valid except in the neighborhoods of $\eta = 0$ and $\eta = \pi$:

$$(17) \qquad \psi(\eta) \sim (2/\pi k \sin \eta)^{1/2}(b^2 - \cos^2 \eta)^{-1/4} \cos\left\{ k \int_0^\eta (b^2 - \cos^2 \eta)^{1/2} d\eta - \pi/4 \right\}.$$

A simple calculation, using (12) and (16), shows that

$$(18) \qquad \lim_{\eta \to 0} \sin \eta \, \psi(\pi - \eta) = 2\pi^{-1} \cos \left\{ k \int_0^\pi (b^2 - \cos^2 \eta)^{1/2} d\eta \right\}.$$

We note that for $b = b_n$, $\psi(\eta) = W_n^{(1)}(\eta)$.

In order to expand equation (17) of Section 3 asymptotically, we evaluate the expansions contained in this appendix at the eigenvalues b_n. When (7) is substituted into (17), we find that

$$(19) \qquad W_n^{(1)}(\eta) \sim (2/\pi k \sin \eta)^{1/2} (\cosh^2 a - \cos^2 \eta)^{-1/4}$$

$$\times \cos \left\{ k \int_0^\eta (\cosh^2 a - \cos^2 \eta)^{1/2} d\eta + k^{1/3} \tau_n (\sinh a \cosh a)^{2/3} \right.$$

$$\left. \times \int_0^\eta (\cosh^2 a - \cos^2 \eta)^{-1/2} d\eta - \pi/4 \right\}.$$

Similarly, the substitution of (7) into (6) yields

$$(20) \qquad V_n^{(1)}(\xi) \sim e^{i\pi/12} k^{-1/6} 2^{-1} \pi^{-1/2} (\cosh^2 \xi - \cosh^2 a)^{-1/4} (\sinh \xi)^{-1/2}$$

$$\times \exp \left\{ ik \int_a^\xi (\cosh^2 \xi - \cosh^2 a)^{1/2} d\xi - ik^{1/3} \tau_n (\sinh a \cosh a)^{2/3} \right.$$

$$\left. \times \int_a^\xi (\cosh^2 \xi - \cosh^2 a)^{-1/2} d\xi \right\}.$$

Finally, we shall obtain the expansion of

$$(21) \qquad \left\{ V_n^{(1)\prime}(a) \frac{\partial}{\partial b} V_n^{(1)}(a) \right\}^{-1}.$$

To do so, we note that (3) may be differentiated with respect to both ξ and b to yield the results

$$(22) \quad V_n^{(1)\prime}(a) \sim \pi^{-1} \zeta_n^{1/4} 3^{2/3} (2\tau_n)^{-1/4} k^{5/6} (\sinh a)^{-2/3} (\cosh a)^{1/12} e^{-i\pi/3} A'(q_n) \frac{\partial \zeta_n}{\partial \xi},$$

$$(23) \quad \frac{\partial}{\partial b} V_n^{(1)}(a) \sim \pi^{-1} \zeta_n^{1/4} 3^{2/3} (2\tau_n)^{-1/4} k^{5/6} (\sinh a)^{-2/3} (\cosh a)^{1/12} e^{-i\pi/3} A'(q_n) \frac{\partial \zeta_n}{\partial b}.$$

Here ζ_n is the value of ζ at $\xi = a$, $b = b_n$. Upon differentiating (4), we find

$$(24) \qquad \frac{\partial \zeta_n}{\partial \xi} \sim -\zeta_n^{-1/2} (2\tau_n)^{1/2} k^{-1/3} (\sinh a)^{1/3} (\cosh a)^{-1/6}.$$

We also make use of the following identities:

$$(25) \qquad 2^{-1/3} k^{2/3} \zeta_n = \tau_n,$$

$$(26) \qquad \frac{\partial \zeta_n}{\partial b} = \frac{\partial \zeta_n}{\partial \tau_n} \frac{\partial \tau_n}{\partial b}.$$

From (25) and (7), we find that

$$(27) \qquad \frac{\partial \zeta_n}{\partial b} \sim 2^{1/3} (\sinh a)^{-2/3} (\cosh a)^{1/3}.$$

Upon making use of (27), (22), and (23), we obtain the desired asymptotic expansion

$$(28) \qquad \left\{ V_n^{(1)'}(a) \frac{\partial}{\partial b} V_n^{(1)}(a) \right\}^{-1} \sim \pi^2 e^{-i\pi/3} 3^{-4/3} 2^{-1/3} (\cosh a)^{-1/3} k^{-4/3}$$

$$\times (\sinh a)^{5/3} \{A'(q_n)\}^{-2}.$$

APPENDIX II

A Theorem on Backscattering

Let $\mathbf{E}$ be the electromagnetic field scattered back from a perfectly conducting body of revolution. The incident field $\mathbf{E}_1 e^{-ikz}$ is assumed to be a plane wave incident along the z axis, which is the symmetry axis of the body. We shall show that $\mathbf{E}$ can be expressed simply in terms of u_S and u_H, the scalar fields scattered back from the same body with the soft and hard boundary conditions respectively. In these cases the incident field is the plane wave e^{-ikz}. The result which we shall deduce is the backscattering theorem

$$(1) \qquad \mathbf{E} = \tfrac{1}{2}(u_\mathrm{S} - u_\mathrm{H})\mathbf{E}_1.$$

Our proof of this relation is based upon the geometrical theory of diffraction. Therefore its range of validity is the same as that of this theory.

Let us first consider the field on the reflected ray. In both scalar cases and in the electromagnetic case this field is a product of four factors. They are the value of the incident field at the point of reflection, a reflection coefficient, a geometrical or amplitude factor, and a phase factor. The latter two factors are the same in all three cases. The reflection coefficient is -1 in the soft case, $+1$ in the hard case, and -1 in the electromagnetic case. The value of this last coefficient depends upon the fact that the incident field is tangential to the surface at the point of reflection because the incident ray is normal there. From the preceding statement and the relation $-1 = \tfrac{1}{2}\{-1 -(+1)\}$, we see that (1) holds for the reflected field.

To prove that (1) also holds for the diffracted field, we first treat the case of a smooth body. According to Levy and Keller (1959), the diffracted field $\mathbf{E}_\mathrm{d}$ at any point P off the axis of the body is given by

$$(2) \qquad \mathbf{E}_\mathrm{d}(P) = \sum_{j=1}^{2} \{ (\mathbf{E}_1 \cdot \mathbf{d}_{20}^j)\, \mathbf{d}_2^j\, v_j(P) + (\mathbf{E}_1 \cdot \mathbf{d}_{30}^j)\, \mathbf{d}_3^j u_j(P) \}.$$

The unit vectors $\mathbf{d}_{20}^j$ and $\mathbf{d}_2^j$ are normal to the body at the points where the jth diffracted ray through P is initiated, and where it leaves the surface, respectively. The unit vectors $\mathbf{d}_{30}^j$ and $\mathbf{d}_3^j$ are tangent to the body and normal to the surface ray at these same points. The scalar functions v_1 and v_2 are

constructed according to the geometric theory of diffraction with the constants appropriate to a hard body, while u_1 and u_2 contain those for a soft body.

As the point P recedes from the body in a direction parallel to the axis, the points at which the rays through P leave the body tend to limiting positions. The points of initiation of these rays also tend to limiting positions. All these limiting positions lie on that cross section of the body which is normal to the axis and which has the largest radius. Let us call the plane of this section the xy plane. It is shown in Fig. 3. We have chosen the y axis
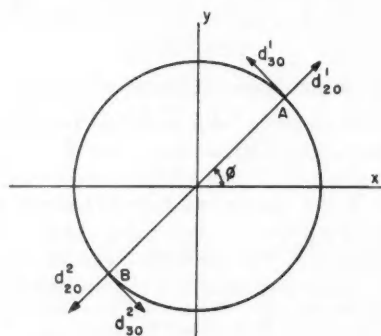
FIG. 3. A cross section of the ellipsoid through its center normal to its axis of revolution. An incident ray tangent to the surface at A travels half way around the ellipsoid to B, from which point it sheds a ray which returns to the source. The vectors $\mathbf{d}_{20}^1$ and $\mathbf{d}_{30}^1$ are respectively normal and tangential to the surface at A, and both are normal to the incident ray. The vectors $\mathbf{d}_{20}^2$ and $\mathbf{d}_{30}^2$ are associated with the ray incident at B, which sheds a ray back to the source after travelling around to A. This figure is relevant when the source is far from the ellipsoid.

to be parallel to $\mathbf{E}_1$. The angle between the xz plane and the plane which contains P and the symmetry axis we denote by ϕ. Then the limiting positions of the vectors in (2) are

(3) $\mathbf{d}_{20}^1 = -\mathbf{d}_{20}^2 = -\mathbf{d}_2^1 = \mathbf{d}_2^2 = (\cos \phi, \sin \phi, 0),$

(4) $\mathbf{d}_{30}^1 = -\mathbf{d}_{30}^2 = \mathbf{d}_3^1 = -\mathbf{d}_3^2 = (-\sin \phi, \cos \phi, 0).$

When (3) and (4) are inserted into (2), it becomes

(5) $\mathbf{E}_d(P) = -(\mathbf{E}_1 \cdot \mathbf{d}_{20}^1)\mathbf{d}_{20}^1(v_1+v_2) + (\mathbf{E}_1 \cdot \mathbf{d}_{30}^1)\mathbf{d}_{30}^1(u_1+u_2)$

$= \dfrac{E_1}{2} \{ -(u_1+u_2+v_1+v_2) \sin 2\phi, \; u_1+u_2-v_1-v_2+(u_1+u_2+v_1+v_2)$

$\times \cos 2\phi, \; 0 \}.$

As P tends to the axis of revolution, the expression for $\mathbf{E}(P)$ on the right side of (5) becomes infinite. This is because the axis is a caustic of the diffracted rays. In Keller (1957) there is a method for modifying fields which become infinite on an axial caustic. It applies to scalar wave functions which are

proportional to $\sin n\phi$ or $\cos n\phi$. Therefore it can be applied to each component of (5), provided the y component is separated into a term proportional to $\cos 2\phi$ and another independent of ϕ. To apply the method a term in $\sin n\phi$ or $\cos n\phi$ is first multiplied by the factor

$$(6) \qquad C_n = \tfrac{1}{2}(2\pi k\rho \cos \delta)^{1/2} \sec\{k\rho \cos \delta - (n+\tfrac{1}{2})\pi/2\} J_n(k\rho \cos \delta).$$

In (6) ρ is the distance of P from the axis and $\pi/2-\delta$ is the angle which the rays make with the axis. The correct finite value of the field on the axis is obtained by letting ρ tend to zero after multiplication by C_n. The result is finite because the factor $(\rho \cos \delta)^{1/2}$ in C_n cancels the singular factors in u_1, u_2, v_1, and v_2. It follows that on the axis the terms with $n \neq 0$ vanish because $J_n(0) = 0$ for $n \neq 0$. Thus only the terms with $n = 0$ in (5) remain when P is on the axis, and (5) then yields

$$(7) \qquad \mathbf{E}_\mathrm{d}(P) = \frac{E_1}{2} \left\{0, \lim_{\rho \to 0} C_0(u_1+u_2-v_1-v_2), 0\right\} = \frac{E_1}{2} \{0, u_\mathrm{S}^\mathrm{d}-u_\mathrm{H}^\mathrm{d}, 0\}$$
$$= \tfrac{1}{2}(u_\mathrm{S}^\mathrm{d}-u_\mathrm{H}^\mathrm{d})\, \mathbf{E}_1.$$

The final form of (7) is the desired result (1) for the diffracted field. In obtaining it we made use of the fact that u_S^d and u_H^d, the backscattered diffracted fields for soft and hard bodies, are given by

$$(8) \qquad\qquad\qquad\qquad u_\mathrm{S}^\mathrm{d} = \lim_{\rho \to 0} C_0(u_1+u_2),$$

$$(9) \qquad\qquad\qquad\qquad u_\mathrm{H}^\mathrm{d} = \lim_{\rho \to 0} C_0(v_1+v_2).$$

Numerical calculations of the backscattering cross section of a prolate spheroid have been carried out by Siegel *et al.* (1956). However, these calculations were limited to small values of kh and hence are not directly comparable with the values given by (7).

The same result (7) holds when the body has an edge. The proof is similar to that given above so we shall just sketch it. For simplicity we shall confine ourselves to the case of a circular disk. If Fig. 3 now represents the disk, then the field at P is again given by (5). Of course the functions u_1, u_2, v_1, and v_2 are now those appropriate to scalar diffraction by a disk. The negative sign in the first term on the right in (5) arises because the backscattered ray travels in the direction opposite that of the incident ray. Since v_1 and v_2 describe the diffraction of the tangential component of magnetic field $\mathbf{H}$, the opposite relations between $\mathbf{E}$ and $\mathbf{H}$ on the two rays introduce the negative sign. From (5) we obtain (7) as before, and thus (1) is proved.

We may also prove (7) for a body with an edge like that of a wedge, at which the two tangent planes meet at a non-zero angle. For that purpose the wedge diffraction coefficients given in equation (A10) of Keller's work (1957) must be used. The right side of that equation is missing a factor $-(2/n) \sin (\pi/n)$ due to a typographical error. Also in Keller's paper (1957) the second columns of the diffraction matrices in equations (A12) and (A13) must be multiplied by -1.

REFERENCES

FLAMMER, C. 1957. Spheroidal wave functions (Stanford University Press, Stanford, California).

KELLER, J. B. 1956. IRE Trans. on Antennas and Propagation, **AP-4**, 312.

———— 1957. J. Appl. Phys. **28**(4), 426.

———— 1958. A geometrical theory of diffraction. Calculus of variations and its applications. Proc. of Symposia in Applied Mathematics, Vol. VIII (McGraw-Hill Book Co., Inc., New York), pp. 27–52.

KELLER, J. B., LEWIS, R. M., and SECKLER, B. D. 1956. Commun. Pure and Appl. Math. **9**, 207.

LEVY, B. R. 1958. Diffraction by an elliptic cylinder, New York University, Institute of Mathematical Sciences, Division of EM Research, Research Report No. EM-121.

LEVY, B. R., and KELLER, J. B. 1959. Commun. Pure and Appl. Math. **12**(1), 159.

OLVER, F. W. J. 1954. Phil. Trans. Roy. Soc. London, A, **247**, 307.

RITT, R. K. and KAZARINOFF, N. D. 1958. Studies in radar cross sections XXX, the theory of scalar diffraction with application to the prolate spheroid, University of Michigan Research Institute, Scientific Report No. 4.

———— 1959. Ann. Phys. **6**, 227.

SIEGEL, K. M., SCHULTZ, F. V. GERE, B. H., and SLEATOR, F. B. 1956. IRE Trans. on Antennas and Propagation, **AP-4**, 266.

NOTES

A COMPLEX NON-ANALYTIC MANIFOLD AND
CONFORMAL MINKOWSKI SPACE-TIME

D. K. Sen

COMPLEX MANIFOLDS IN GENERAL

A real $2n$-dimensional manifold V_{2n} is said to admit a complex structure if it is possible to introduce co-ordinate neighborhoods in the manifold with complex co-ordinates of dimension n.

Let the co-ordinates of V_{2n} be (x^i) and let there be two co-ordinate neighborhoods connected by the co-ordinate transformation

$$(1) \qquad x^{i'} = x^{i'}(x^k); \qquad x^i = x^i(x^{k'})$$

with a non-vanishing Jacobian, where the Latin indices take the values $1, 2, \ldots n; \bar{1}, \bar{2}, \ldots \bar{n}$. Let

$$(2) \qquad \begin{cases} z^\alpha = x^\alpha + ix^{\bar{\alpha}} \\ \bar{z}^a = x^a - ix^{\bar{a}} \end{cases}$$

with its complex conjugate

where the Greek indices take the values $1, 2, \ldots n$. There is then a one–one correspondence, $(z^\alpha, \bar{z}^\alpha) \rightleftharpoons (x^i)$, and (2) may be considered as the co-ordinates of the associated n-dimensional complex manifold. Equation (1) may then be written as

$$(3) \qquad z^{\alpha'} = z^{\alpha'}(z, \bar{z}); \qquad \bar{z}^{\alpha'} = \bar{z}^{\alpha'}(z, \bar{z}).$$

The complex manifolds which have so far been studied by the mathematicians are complex analytic ones which are defined as follows.

Let N and N' be two complex co-ordinate neighborhoods and P be a point such that $P \epsilon N \cap N'$. If the co-ordinates $z^{\alpha'}$ of $P \epsilon N'$ are complex analytic functions of z^α, the co-ordinates of $P \epsilon N$, with a non-vanishing Jacobian, then the manifold is called a complex *analytic* manifold of real dimension $2n$ and complex dimension n. In case of an analytic manifold equation (3) can therefore be written as

$$(4) \qquad z^{\alpha'} = \psi^\alpha(z), \qquad \bar{z}^{\alpha'} = \bar{\psi}^\alpha(\bar{z})$$

where $\bar{\psi}^\alpha$ denotes the complex conjugate of the function $\psi^\alpha(z)$. Putting $z^{\bar{a}} = \bar{z}^\alpha$ we can write (4) as

$$(5) \qquad z^{i'} = f^i(z^k)$$

whose Jacobian is

$$(6) \qquad J = \left| \frac{\partial z^{i'}}{\partial z^k} \right| = \text{real} > 0.$$

Such a transformation is known as pseudoconformal.

All the usual concepts of tensor-calculus, such as vectors, tensors, affine connexion, and metric, can be defined in a complex manifold in the same way as in the real case.

A particular complex analytic manifold which has been studied in great detail is the Kaehler manifold (1933). A Kaehler manifold is a complex analytic manifold with a positive definite metric

$$(7) \qquad ds^2 = g_{ik}dz^i dz^k,$$

where the g_{ik} are self-adjoint and satisfy the condition

$$(8) \qquad g_{\alpha\beta} = g_{\bar{\alpha}\bar{\beta}} = 0.$$

The above condition is invariant under the pseudoconformal transformation (4). The Kaehler metric therefore reduces to the Hermetian form

$$(9) \qquad \begin{cases} ds^2 = 2\, g_{\alpha\bar{\beta}} dz^\alpha d\bar{z}^\beta, \\ g_{\alpha\bar{\beta}} = g_{\bar{\beta}\alpha} = \overline{g_{\bar{\alpha}\beta}} = \overline{g_{\beta\bar{\alpha}}}. \end{cases}$$

where

CONFORMAL MINKOWSKI SPACE–TIME

We consider a two-dimensional space–time manifold with $x^1 = x$ and $x^2 = ct$ and we introduce

$$(10) \qquad \begin{cases} z = x^1 + ix^2 \\ \bar{z} = x^1 - ix^2 \end{cases}$$

for the co-ordinate of the one-dimensional complex manifold. A proper Lorentz transformation of x^1 and x^2

$$(11) \qquad \begin{cases} x^{1'} = \gamma(x^1 - \beta x^2) \\ x^{2'} = \gamma(x^2 - \beta x^1) \end{cases} \qquad \beta = v/c,\ \gamma = (1-\beta^2)^{-\frac{1}{2}}$$

corresponds to a non-analytic transformation of z

$$(12) \qquad \begin{cases} z' = \gamma\left(z + \dfrac{\beta}{i}\,\bar{z}\right), \\[2mm] \bar{z}' = \gamma\left(\bar{z} - \dfrac{\beta}{i}\,z\right). \end{cases}$$

The transformation matrix $\begin{pmatrix} \gamma & \dfrac{\gamma\beta}{i} \\[2mm] -\dfrac{\gamma\beta}{i} & \gamma \end{pmatrix}$ is unitary with the determinant

$$J = \begin{vmatrix} \gamma & \dfrac{\gamma\beta}{i} \\[2mm] -\dfrac{\gamma\beta}{i} & \gamma \end{vmatrix} = \gamma^2(1-\beta^2) = 1.$$

The improper transformations are given by

(i) space reflection: $z' = -\bar{z}, \bar{z}' = -z, J = 1$;

(ii) time reflection: $z' = \bar{z}, \bar{z}' = z, J = -1$;

(iii) space–time inversion: $z' = -z, \bar{z}' = -\bar{z}, J = +1$.

Space–time inversion is rather distinct in the sense that it corresponds to an analytic transformation of z.

A vector $(\xi, \bar{\xi})$ transforms like $(z, \bar{z})$ and a tensor of rank two will transform as

$$(13) \qquad \xi_{i'k'} = A_{i'}^{l} A_{k'}^{m} \xi_{lm}$$

where $A_i^{i'}$ is the transformation matrix of (12).

One can introduce a metric in the complex manifold by means of a symmetric tensor g_{ik} which is in general complex:

$$(14) \qquad ds^2 = g_{ik} dz^i dz^k.$$

Since z^i takes only two values z and $\bar{z}$, we denote the corresponding metric tensors by $g_{zz}, g_{\bar{z}\bar{z}}$, and $g_{z\bar{z}}$, so that (14) can be written as

$$(15) \quad ds^2 = g_{zz} dz^2 + g_{\bar{z}\bar{z}} d\bar{z}^2 + 2g_{z\bar{z}} dz d\bar{z}$$
$$= g_{zz}(dx^2 - c^2 dt^2 + i2cdxdt) + g_{\bar{z}\bar{z}}(dx^2 - c^2 dt^2 - i2cdxdt) + 2g_{z\bar{z}}(dx^2 + c^2 dt^2).$$

The metric reduces to the conformal Minkowski form

$$ds^2 = 2g_{zz}(dx^2 - c^2 dt^2), \qquad\qquad g_{zz} \text{ real}$$

if

$$(16) \qquad\qquad g_{zz} = g_{\bar{z}\bar{z}}, \qquad\qquad g_{z\bar{z}} = 0.$$

However, one must show that the above condition is an invariant relation under Lorentz transformations. This can be seen from the transformation formula of the metric tensor. We have from (13)

$$(17) \qquad g_{z'z'} = \gamma^2 g_{zz} + \left(\frac{\gamma\beta}{i}\right)^2 g_{\bar{z}\bar{z}} + 2\gamma\left(\frac{\gamma\beta}{i}\right) g_{z\bar{z}},$$

$$(18) \qquad g_{\bar{z}'\bar{z}'} = \left(-\frac{\gamma\beta}{i}\right)^2 g_{zz} + \gamma^2 g_{\bar{z}\bar{z}} + 2\left(-\frac{\gamma\beta}{i}\right)\gamma g_{z\bar{z}},$$

$$(19) \qquad g_{z'\bar{z}'} = \gamma\left(-\frac{\gamma\beta}{i}\right) g_{zz} + \left(\frac{\gamma\beta}{i}\right)\gamma g_{\bar{z}\bar{z}} + 2\gamma^2 g_{z\bar{z}}.$$

From (17), (18), and (19) it is evident that, if

$$g_{zz} = g_{\bar{z}\bar{z}}, \qquad g_{z\bar{z}} = 0,$$

then also

$$g_{z'z'} = g_{\bar{z}'\bar{z}'}, \qquad g_{z'\bar{z}'} = 0.$$

Thus the condition (16) is Lorentz-invariant. In fact, the only condition that $g_{z\bar{z}}$ be zero in all Lorentz frames is sufficient. Because from (19) we then have

$$0 = \frac{\gamma^2 \beta}{i}\,(g_{zz} - g_{\bar{z}\bar{z}})$$

or

$$g_{zz} = g_{\bar{z}\bar{z}}.$$

And it follows therefore from (17) and (18) that

$$g_{z'z'} = g_{\bar{z}'\bar{z}'}.$$

So a sufficient condition for the metric (15) to reduce to the conformal Minkowski form is the vanishing of $g_{z\bar{z}}$ in all Lorentz frames. It is interesting to note the difference between (16) and (8), the condition for a Kaehler manifold.

In general, however, the manifold would be characterized by a non-vanishing affine connexion $\Gamma_{kl}^{t}(g_{mn})$ and curvature tensor R_{klm}^{t}.

KAEHLER, E. 1933. Abhandl. math. Sem. Hamburgischen Univ. **9**, 173.
YANO, K. and BOCHNER, C. 1953. Curvature and Betti numbers (Princeton University Press, Princeton, N.J.).

THE NUCLEAR MATRIX ELEMENT RATIO IN THE $0^- \to 0^+$ BETA TRANSITION OF Pr^{144}

J. M. PEARSON[*]

On the currently accepted view of the beta-decay interaction having the VA form, the $0 \to 0$, YES, transition is of considerable interest in that the spectrum shape is determined completely by a single nuclear matrix element ratio, $\lambda = i \langle \gamma_5 \rangle / \langle \sigma \cdot \mathbf{r} \rangle$. Such a transition is believed to take place in the ground state decay of Pr^{144}, which recently has been well measured by Graham *et al.* (1958) and by Porter and Day (1959). Both have found λ to be positive with the latter quoting $\lambda = 5 \pm 2$. Porter and Day point out that this is in clear-cut conflict with the estimate of Ahrens and Feenberg (1952), whose

*Now at the Department of Physics, Western Reserve University, Cleveland, Ohio.

method gives $\lambda \simeq -12$. The purpose of this note is to make the following two observations:

(i) Rose and Osborn (1954a) have claimed that the non-relativistic limit $\langle \gamma_5 \rangle \rightarrow -(1/M)\langle \boldsymbol{\sigma} . \mathbf{p} \rangle$, used by Ahrens and Feenberg, has an incorrect sign, whence $\lambda \simeq 12$.

(ii) Ahrens and Feenberg base their evaluation of the nuclear matrix elements (in their non-relativistic limit) on the semiempirical mass formula. The author has made an essentially different calculation in which a single-particle j–j coupling model is assumed. The same non-relativistic approximation for $\langle \gamma_5 \rangle$ is made, using the sign of Rose and Osborn and following the methods of Rose and Osborn (1954b). It is found that $\lambda = 2.5$, if the single particle potential is taken to be an infinitely deep square well. With harmonic oscillator potentials λ will still be positive, provided that the well strength of either parent or daughter does not exceed the other by a factor of 13/9. If the two well strengths are equal, then $\lambda = 8$. The two different methods of calculating the matrix elements are thus in reasonable accord as to absolute value.

The question of agreement or non-agreement between theory and experiment therefore depends essentially on the sign of the non-relativistic limit of $\langle \gamma_5 \rangle$: Rose and Osborn's form is clearly favored by experiment.

AHRENS, T. and FEENBERG, P. 1952. Phys. Rev. **86**, 64.
GRAHAM, R. L., GEIGER, J. S., and EASTWOOD, T. A. 1958. Can. J. Phys. **36**, 1084.
PORTER, F. T. and DAY, P. P. 1959. Phys. Rev. **114**, 1286.
ROSE, M. E. and OSBORN, R. K. 1954a. Phys. Rev. **93**, 1315.
———— 1954b. Phys. Rev. **93**, 1326.

DEPARTMENT OF PHYSICS,
MCMASTER UNIVERSITY,
HAMILTON, ONTARIO.

LETTERS TO THE EDITOR

Under this heading brief reports of important discoveries in physics may be published. These reports should not exceed 600 words and, for any issue, should be submitted not later than six weeks previous to the first day of the month of issue. No proof will be sent to the authors.

Frequency Measurement of Standard Frequency Transmissions[1, 2]

Measurements are made at Ottawa, Canada, using N.R.C. caesium-beam frequency resonator as reference standard (with an assumed frequency of 9 192 631 770 c.p.s.). Frequency deviations from nominal are quoted in parts per 10^{10}. A negative sign indicates that the frequency is below nominal.

Date, October 1959	MSF, 60 kc/s	GBR, 16 kc/s		KK2XEI, 60 kc/s
		7-hour average*	24-hour average	
1	−164	−171	−164	N.M.
2	−170	−167	−168	N.M.
3	−176	−171	−177	N.M.
4	−176	−177	−177	N.M.
5	−173	−168	−169	−69
6	−178	−166	−168	−63
7	−170	−167	−172	−77
8	−169	−171	−167	−73
9	−168	−170	−174	−70
10	−168	−172	−176	N.M.
11	−170	−171	−176	N.M.
12	−170	−173	−170	−72
13	−171	−175	−174	−86
14	−170	−170	−168	−76
15	−167	−168	−167	−69
16	−164	−171	−168	−83
17	−169	−170	−168	N.M.
18	−168	−172	−168	N.M.
19	−170	−171	−167	−74
20	−163	−166	−164	−76
21	−169	−163	−164	−76
22	−165	−167	−165	−75
23	−168	−165	−165	−77
24	−158	−166	−164	N.M.
25	−167	−162	−164	N.M.
26	−162	−165	N.M.	−75
27	−168	N.M.	N.M.	N.M.
28	−166	−164	−162	−74
29	−161	−159	−158	N.M.
30	N.M.	−162	−163	N.M.
31	−169	−164	−163	N.M.
Midmonthly mean	−168	−168	−168	−74
Midmonthly mean of WWV	−104			

NOTE: N.M. No measurement.
*Time of observations: 00.00 to 05.30 and 22.30 to 24.00 U.T.

S. N. KALRA

[1] Issued as N.R.C. No. 5504.
[2] Cf. Kalra, S. N. 1959. Can. J. Phys. 37, 1328, 1562.

"Spin-flip Narrowing" of Paramagnetic Resonance Lines

Copper, cobalt, and zinc potassium sulphates are isomorphous, and mixed crystals can be made with any desired proportions of copper, cobalt, and zinc. The paramagnetic resonance spectrum of the copper ions consists of four lines, with an over-all separation of some 250 gauss. These lines are broadened by spin–spin interaction so that the four lines are unresolved at all temperatures in copper potassium sulphate, and are further broadened at high temperatures by spin–lattice relaxation. In order to resolve the four lines, it is customary to reduce the spin–spin interaction by diluting the copper with diamagnetic zinc, dilutions of 1 part copper to 1000 parts zinc being usual. The paramagnetic resonance spectrum of cobalt is similar to that of copper, except that the spin–lattice relaxation times are much shorter. As a consequence of this, only a very broad line can be seen at liquid air temperature, and no line is visible at all at room temperature.

We have observed the paramagnetic resonance spectrum of copper at 3-cm wavelength at room temperature, and at liquid nitrogen temperature ($77°$ K) for the following two compounds: (5% Cu 95% Zn) $K_2(SO_4)_2.6H_2O$ and (5% Cu 95% Co) $K_2(SO_4)_2.6H_2O$. In the case of the copper–zinc specimen, a broad line, 300 gauss wide, is seen at room temperature, and at $77°$ K this line narrows somewhat and the four hyperfine components start to be resolved. For the copper–cobalt specimen, we find a line 300 gauss wide at room temperature, just as in the case of the copper–zinc specimen. On cooling the copper–cobalt specimen to $77°$ K, the copper line almost disappears, becoming very feeble and at least 2000 gauss wide.

The behavior of the copper–zinc specimen is easily understood; the line broadens at room temperature due to the shorter spin–lattice relaxation time of the copper ions. For the copper–cobalt specimen we suggest the following explanation. At $77°$ K, the copper line is broadened by the spin–spin interaction between the copper and the cobalt ions. At room temperature, the cobalt ions have such a strong interaction with the lattice that they remain in any one spin state only for a very short time. The interaction magnetic field, produced by the cobalt ions, is thus fluctuating so rapidly that the copper ions see only its average value, which is zero. A somewhat more quantitative explanation of this effect follows from the treatment of relaxation by Pines and Slichter (1955). According to these authors, the contribution of the cobalt–copper interaction to the width of the copper line should be δH or $g\beta(\delta H)^2\tau/\hbar$ according as $\tau > $ or $ < g\beta\delta H/\hbar$ (equations 6 and 4 respectively of their paper). In these formulae δH is the average interaction field produced by the cobalt, g is the g factor for copper, β is the Bohr magneton, and τ is the correlation time for the cobalt, that is the average time for which a cobalt ion stays in any one spin state. There is a close relation between τ and the spin–lattice relaxation time T_1. (For instance in a two-level system $T_1 \simeq \tau/2$. In a calculation as crude as this, the difference between the τ's of the two states can be ignored. It should be noted, however, that τ depends on exchange as well as spin–lattice relaxation.)

We have thus demonstrated that in the case of paramagnetic resonance of compounds containing two paramagnetic ions with very different values of the spin–lattice relaxation time, the width of the line of one component decreases when the spin–lattice relaxation time of the other becomes very short, a situation analogous to motional narrowing in liquids. The study of the line breadth as a function of temperature should enable the spin–lattice relaxation time of the other component to be measured. Further, this should permit the measurement of spin–lattice relaxation times of an order of magnitude smaller than has been possible with other techniques. It is possible that there would be a resonant effect on the signal strength when the correlation time of the other component is equal to the Larmor precession time of the first. These investigations are being continued.

The apparatus which was used to measure these lines has some novel features. It is basically a 3-cm transmission cavity spectrometer with 60-cycle modulation and crystal–video display. With such a system, 60-cycle pickup can be very serious, and the 60- and 120-cycle components of the output from the crystal are usually eliminated at an early stage using two twin T filters. Such a system does not produce a faithful oscilloscope display of a broad line, since such a line has important components at low frequencies. (We may define a broad line as one whose important Fourier components in the video circuit are all below 1 kc.) To overcome this difficulty, we adopted the following system. A 15-kc square wave was applied to the reflector of the klystron to switch it on and off. The output of the crystal detector was passed through the usual twin T's and through a filter which passed only frequencies between 10 kc and 20 kc, and whose phase characteristic was linear between 14 kc and 16 kc. A simple Fourier analysis of this process shows that the output of this circuit is a 15-kc sine wave carrying the paramagnetic resonance absorption signal as an amplitude modulation. This output is then added to a 15-kc reference voltage to reduce its amplitude, amplified more, detected, and finally displayed on the oscilloscope. This system enables us to filter out the pickup without distorting the line shape. There is also, in theory, a slight enhancement of the signal/noise ratio. (A system similar to this using 1-Mc frequency modulation of the klystron and 2-Mc detection was used by Bagguley and Griffiths (1952) to enhance signal/noise ratio.)

BAGGULEY, D. M. S. and GRIFFITHS, J. H. E.   1952.   Proc. Phys. Soc.(London), A, 65, 594.
PINES, D. and SLICHTER, C. P.   1955.   Phys. Rev. 100, 1014.

RECEIVED NOVEMBER 2, 1959.   J. M. DANIELS
DEPARTMENT OF PHYSICS,   H. A. FARACH*
UNIVERSITY OF BRITISH COLUMBIA,
VANCOUVER, B.C.

*On leave of absence from the University of Buenos Aires, Buenos Aires, Argentina.

NOTES TO CONTRIBUTORS

Canadian Journal of Physics

MANUSCRIPTS

General.—Manuscripts, in English or French, should be typewritten, double spaced, on paper $8\frac{1}{2} \times 11$ in. **The original and one copy are to be submitted.** Tables and captions for the figures should be placed at the end of the manuscript. Every sheet of the manuscript should be numbered. Style, arrangement, spelling, and abbreviations should conform to the usage of recent numbers of this journal. Greek letters or unusual signs should be written plainly or explained by marginal notes. Characters to be set in boldface type should be indicated by a wavy line below each character. Superscripts and subscripts must be legible and carefully placed. Manuscripts and illustrations should be carefully checked before they are submitted. Authors will be charged for unnecessary deviations from the usual format and for changes made in the proof that are considered excessive or unnecessary.

Abstract.—An abstract of not more than about 200 words, indicating the scope of the work and the principal findings, is required, except in Notes.

References.—References should be listed **alphabetically by authors' names,** unnumbered, and typed after the text. The form of the citations should be that used in current issues of this journal; in references to papers in periodicals, titles should not be given and only initial page numbers are required. The names of periodicals should be abbreviated in the form given in the most recent *List of Periodicals Abstracted by Chemical Abstracts*. All citations should be checked with the original articles and each one referred to in the text by the authors' names and the year.

Tables.—Tables should be numbered in roman numerals and each table referred to in the text. Titles should always be given but should be brief; column headings should be brief and descriptive matter in the tables confined to a minimum. Vertical rules should not be used. Numerous small tables should be avoided.

ILLUSTRATIONS

General.—All figures (including each figure of the plates) should be numbered consecutively from 1 up, in arabic numerals, and each figure referred to in the text. The author's name, title of the paper, and figure number should be written in the lower left corner of the sheets on which the illustrations appear. Captions should not be written on the illustrations.

Line drawings.—Drawings should be carefully made with India ink on white drawing paper, blue tracing linen, or co-ordinate paper ruled in blue only; any co-ordinate lines that are to appear in the reproduction should be ruled in black ink. Paper ruled in green, yellow, or red should not be used. All lines must be of sufficient thickness to reproduce well. Decimal points, periods, and stippled dots must be solid black circles large enough to be reduced if necessary. Letters and numerals should be neatly made, preferably with a stencil (**do NOT use typewriting**) and be of such size that the smallest lettering will be not less than 1 mm high when the figure is reduced to a suitable size. Many drawings are made too large; originals should not be more than 2 or 3 times the size of the desired reproduction. Whenever possible two or more drawings should be grouped to reduce the number of cuts required. In such groups of drawings, or in large drawings, full use of the space available should be made; the ratio of height to width should conform to that of a journal page ($4\frac{3}{4} \times 7\frac{1}{2}$ in.), but allowance must be made for the captions. **The original drawings and one set of clear copies (e.g. small photographs) are to be submitted.**

Photographs.—Prints should be made on glossy paper, with strong contrasts. They should be trimmed so that essential features only are shown and mounted carefully, with rubber cement, on white cardboard, with no space between those arranged in groups. In mounting, full use of the space available should be made. **Photographs are to be submitted in duplicate;** if they are to be reproduced in groups one set should be mounted, the duplicate set unmounted.

REPRINTS

A total of 100 reprints of each paper, without covers, are supplied free. Additional reprints, with or without covers, may be purchased at the time of publication.

Charges for reprints are based on the number of printed pages, which may be calculated approximately by multiplying by 0.6 the number of manuscript pages (double-spaced typewritten sheets, $8\frac{1}{2} \times 11$ in.) and including the space occupied by illustrations. Prices and instructions for ordering reprints are sent out with the galley proof.

Contents